

INFORMATION TO USERS

This manuscript has been reproduced from the microfilm master. UMI films the text directly from the original or copy submitted. Thus, some thesis and dissertation copies are in typewriter face, while others may be from any type of computer printer.

The quality of this reproduction is dependent upon the quality of the copy submitted. Broken or indistinct print, colored or poor quality illustrations and photographs, print bleedthrough, substandard margins, and improper alignment can adversely affect reproduction.

In the unlikely event that the author did not send UMI a complete manuscript and there are missing pages, these will be noted. Also, if unauthorized copyright material had to be removed, a note will indicate the deletion.

Oversize materials (e.g., maps, drawings, charts) are reproduced by sectioning the original, beginning at the upper left-hand corner and continuing from left to right in equal sections with small overlaps. Each original is also photographed in one exposure and is included in reduced form at the back of the book.

Photographs included in the original manuscript have been reproduced xerographically in this copy. Higher quality 6" x 9" black and white photographic prints are available for any photographs or illustrations appearing in this copy for an additional charge. Contact UMI directly to order.

U·M·I

University Microfilms International
A Bell & Howell Information Company
300 North Zeeb Road, Ann Arbor, MI 48106-1346 USA
313 761-4700 800 521-0600

Order Number 9121901

**Particle simulations of magnetic field reconnection and
applications to flux transfer events**

Ding, Da-Qing, Ph.D.

University of Alaska Fairbanks, 1990

U·M·I
300 N. Zeeb Rd.
Ann Arbor, MI 48106

NOTE TO USERS

**THE ORIGINAL DOCUMENT RECEIVED BY U.M.I. CONTAINED PAGES
WITH SLANTED AND POOR PRINT. PAGES WERE FILMED AS RECEIVED.**


THIS REPRODUCTION IS THE BEST AVAILABLE COPY.

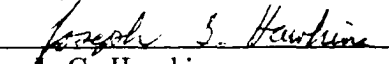
PARTICLE SIMULATIONS OF MAGNETIC FIELD RECONNECTION
AND APPLICATIONS TO FLUX TRANSFER EVENTS


by

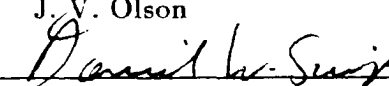
Da-Qing Ding

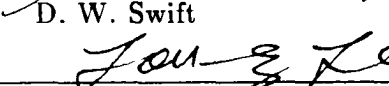
RECOMMENDED:

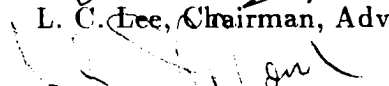

S-I Akasofu


J. G. Hawkins

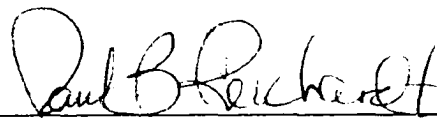

J. V. Olson

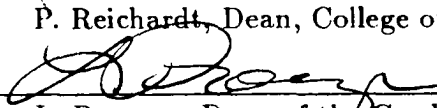

D. W. Swift


L. C. Lee, Chairman, Advisory Committee


J. L. Morack, Head, Physics Department

APPROVED:


P. Reichardt, Dean, College of Natural Sciences


L. Proenza, Dean of the Graduate School

12/1/90
Date

PARTICLE SIMULATIONS OF MAGNETIC FIELD RECONNECTION
AND APPLICATIONS TO FLUX TRANSFER EVENTS

A
THESIS

Presented to the Faculty
of the University of Alaska Fairbanks
in Partial Fulfillment of the Requirements
for the Degree of

DOCTOR OF PHILOSOPHY

By
Da-Qing Ding, B.S., M.S.

Fairbanks, Alaska
December 1990

Abstract

Basic plasma processes associated with driven collisionless magnetic reconnection at the Earth's dayside magnetopause are studied on the basis of particle simulations. A two-and-one-half-dimensional ($2\frac{1}{2}$ -D) electromagnetic particle simulation model with a driven inflow boundary and an open outflow boundary is developed for the present study. The driven inflow boundary is featured with a driving electric field for the vector potential, while the open outflow boundary is characterized by a vacuum force free condition for the electrostatic potential. The major findings are as follows. (1) The simulations exhibit both quasi-steady single X line reconnection (SXR) and intermittent multiple X line reconnection (MXR). The MXR process is characterized by repeated formation and convection of magnetic islands (flux tubes or plasmoids). (2) Particle acceleration in the MXR process occurs mainly in O line regions as particles are trapped within magnetic islands, not in X line regions. The MXR process results in a power law particle energy spectrum of $f(E) \sim E^{-4}$. (3) Field-aligned particle heat fluxes and intense plasma waves associated with the collisionless magnetic reconnection process are also observed. (4) When applied to the dayside magnetopause, simulation results show that the MXR process tends to generate a simultaneous magnetic field perturbation on both sides of the dayside magnetopause, resembling the observed features of two-regime flux transfer events (FTEs). (5) An intrusion of magnetosheath plasma bulge into the magnetosphere due to the formation of magnetic islands may lead to the layered structures observed in magnetospheric FTEs. (6) In the current sheet, the enhanced tearing mode instability caused by the driving force applied at the driven inflow boundary creates an energy source at a specific wavenumber range with $k_z L \sim 0.3$ in the modal spectrum of the magnetic field B_x component. An inverse cascade of

the modal spectrum of B_x leads to the formation of the large-scale ordered magnetic island structures observed in the simulations. (7) In addition, the results of a theoretical study show that the tearing mode instability, and hence the magnetic reconnection at the dayside magnetopause, do not exhibit strong dependence on the magnetosheath β values.

Table of Contents

	Page
Abstract	iii
Table of Contents	v
List of Figures	vii
Acknowledgments	xv
CHAPTER 1 Introduction	1
CHAPTER 2 An Overview of Magnetic Field Reconnection and Flux Transfer Events	10
2.1 Historical Development of the Concept of Magnetic Field Reconnection	10
2.2 Observational Features and Theoretical Models of FTEs	26
2.3 Necessity of Particle Simulation for Magnetic Field Reconnection Study	42
2.4 Summary	49
CHAPTER 3 Collisional and Collisionless Tearing Mode Instabilities	52
3.1 Linear Theory of the Collisional Tearing Mode Instability	55
3.2 Theoretical Study of the Collisionless Tearing Mode Instability	62
3.3 The β -Dependence of Tearing Mode Instabilities	79
CHAPTER 4 A Particle Simulation Model for Driven Magnetic Reconnection	96
4.1 An Introduction to Particle Simulation in Plasma Physics	96
4.2 A Darwin Model Using Hamiltonian Formulation	102
4.3 A $2\frac{1}{2}$ -D Particle Simulation Model for Magnetic Reconnection	107
4.4 Initial Conditions	113
4.5 Boundary Conditions Necessary for Driven Reconnection	116
4.6 Summary	134

CHAPTER 5 One-Component Simulation of Driven Collisionless Magnetic Reconnection	135
5.1 A Particle Simulation of MXR Process	137
5.2 A Comparison of Particle Simulation of MXR and Flux Transfer Events	154
5.3 A Particle Simulation of Quasi Steady SXR Process	156
5.4 Summary and Discussion	162
CHAPTER 6 Simulations of Driven Reconnection Based on a Full Particle Code	166
6.1 Driven Collisionless Reconnection in a Symmetric Current Sheet	168
6.2 Driven Collisionless Reconnection in an Asymmetric Current Sheet	199
6.3 Self-organization in Driven Collisionless Magnetic Reconnection	213
6.4 Summary	219
CHAPTER 7 Particle Acceleration in Driven Collisionless Magnetic Reconnection	222
7.1 An Introduction to Particle Acceleration in Magnetic Reconnection	223
7.2 Particle Trajectories in Driven Collisionless Magnetic Reconnection	230
7.3 Summary and Discussion	244
CHAPTER 8 Summary and Discussion	247
References	253

List of Figures

	Page
Fig. 1.1 Basic geometry for the magnetic field reconnection process [Sonnerup, 1985].	3
Fig. 1.2 The time evolution of magnetic field configuration in the laboratory reconnection experiment [Gekelman et al., 1982].	5
Fig. 2.1 A schematic diagram of the open magnetosphere model proposed by Dungey [1961], in which magnetic reconnection takes place both at the dayside magnetopause and in the nightside magnetotail.	12
Fig. 2.2 MHD reconnection models, (a) Sweet-Parker model [Parker, 1957; Sweet, 1958] and (b) Petschek model [Petschek, 1964].	15
Fig. 2.3 A unified family of models for incompressible, steady-state magnetic reconnection [Priest and Forbes, 1986].	18
Fig. 2.4 Levy et al.'s asymmetric reconnection model at the dayside magnetopause [Levy et al., 1964].	20
Fig. 2.5 Alfvén's [1968] collisionless neutral sheet model.	22
Fig. 2.6 Hill's [1975] collisionless reconnection model.	24
Fig. 2.7 An example of magnetosheath FTEs observed by ISEE 1 and ISEE 2 [Saunders et al., 1984].	28
Fig. 2.8 The elbow-shaped flux tube FTE model [Russell and Elphic, 1978, 1979].	34
Fig. 2.9 The multiple X line reconnection model [Lee and Fu, 1985].	36
Fig. 2.10 A schematic drawing of the bursty single X line reconnection model.	39

- Fig. 3.1 Change of magnetic field configuration caused by the development of the tearing mode instability, (a) unperturbed neutral sheet magnetic field configuration at $t = 0$, and (b) magnetic field configuration perturbed by the tearing mode instability at $t > 0$. 53
- Fig. 3.2 For the collisionless tearing mode instability, (a) the effective potential of the Schrödinger equation (3.67) and (b) the typical shape of the eigenfunction of the perturbed vector potential. 75
- Fig. 3.3 The normalized collisionless tearing mode growth rate as a function of normalized wave number. 77
- Fig. 3.4 The ratio of observed to theoretically predicted flow velocity change at the magnetopause as a function of β_s , the ratio of plasma pressure to magnetic pressure in magnetosheath [Paschmann et al., 1986]. 81
- Fig. 3.5 The normalized resistive tearing growth rate as a function the ratio of plasma pressure to magnetic pressure outside neutral sheet, (a) the symmetric case and (b) the asymmetric case. 85
- Fig. 3.6 Normalized collisionless tearing growth rate as a function of the ratio of plasma pressure to magnetic pressure outside a neutral sheet, (a) the symmetric case and (b) the asymmetric case. 89
- Fig. 4.1 A schematic diagram of simulation domain (blank area) and particle buffer zones (shaded area). Dashed line separates the inner buffer zone from the outer buffer zone. Arrows indicate the imposed incoming plasma flow as well as the outgoing plasma flow generated during the simulated magnetic reconnection process. 120

- Fig. 4.2 Magnetic field lines, represented by the contours of A_y , observed in the simulation with different boundary conditions at the nonperiodic open outflow boundary, (a) $\partial A_y/\partial z = 0$ at $z = \pm L_z$ and (b) $\partial^2 A_y/\partial z^2 = 0$ at $z = \pm L_z$. 124
- Fig. 4.3 Simulation results with different boundary conditions imposed for the electrostatic potential, $\partial\phi/\partial z = 0$ in the first test run and force free in the second test run. (a) Magnetic field lines, represented by the contours of A_y , and (b) contours of electrostatic potential ϕ at simulation time $t = 120\Omega_e^{-1}$. 131
- Fig. 4.4 The time history of the maximum and minimum of electrostatic potential, ϕ_{max} and ϕ_{min} , observed in the simulation, (a) the first test run with the Neumann boundary condition $\partial\phi/\partial z = 0$ and (b) the second test run with the force free boundary condition. 133
- Fig. 5.1a Magnetic field lines at various simulation times. $R_0 = 0.42$ is the imposed reconnection rate at $x = \pm L_x$. 139
- Fig. 5.1b The corresponding positions of particles and plasma flow patterns at various simulation times. The unit vectors correspond to the ion thermal speed v_{thi} . 141
- Fig. 5.2 The maximum reconnection rate in the simulation domain as a function of time. The solid line indicates the imposed reconnection rate $R_0 = 0.42$ at the driven boundary $x = \pm L_x$. 144
- Fig. 5.3 Position of the centers of three large magnetic islands A , B , and C as a function of simulation time. 145
- Fig. 5.4 The averaged power spectrum $P_A(k)$ of the vector potential A_y measured near the current sheet $x = 0$. 147

Fig. 5.5	Particle kinetic energy, magnetic energy, and total energy in the simulation domain as a function of time. The unit for energy is $T_i/2$.	148
Fig. 5.6	The average kinetic energy per particle as a function of simulation time. The unit for energy is $T_i/2$.	151
Fig. 5.7	The particle energy distribution functions $f(E)$ at $t = 0$ and $t = 150\Omega_i^{-1}$. The solid line which represents a Maxwellian energy distribution is a theoretical fit for $f(E)$ at $t = 0$.	152
Fig. 5.8	(a) The magnetic field lines, (b) the plasma flow pattern, (c) the current density contours, and (d) the magnetic tension force observed at $t = 200\Omega_i^{-1}$ in the simulation of the quasi-steady SXR process.	159
Fig. 5.9	The particle distribution in the $x - V_z$ phase space.	161
Fig. 5.10	A typical particle trajectory indicating the current sheet acceleration.	163
Fig. 6.1	(a) Magnetic field lines and (b) contours of electrostatic potential observed at various simulation times in Case A.	170
Fig. 6.2	Magnetic field lines observed at various simulation times in Case B.	174
Fig. 6.3	Time series of the magnetic energy contained at various wave modes near the current sheet region ($x \simeq 0$). Curves with squares, solid dots, and circles are for mode number $m = 1, 2,$ and $3,$ respectively.	176
Fig. 6.4	Average reconnection electric field as a function of time measured in the current sheet region ($x \simeq 0$) in the simulation Case B. The straight line indicates the imposed reconnection electric field at the driven inflow boundary ($x = \pm L_x$).	180

- Fig. 6.5 Electron energy distributions at $t = 0$ and $t = 1020\Omega_e^{-1}$ in Case B. At $t = 1020\Omega_e^{-1}$ energetic electrons with an energy spectrum of $f_e(E) \sim E^{-3.8}$ is generated by the reconnection process. 182
- Fig. 6.6 Satellite observation of high-speed plasma flows associated with FTEs at the dayside magnetopause [Smith et al., 1986]. The components of plasma flow velocity and magnetic field in the boundary normal coordinate system [Russell and Elphic, 1979] are plotted as functions of time. 184
- Fig. 6.7 High-speed plasma flow and particle heat flux generated by the driven collisionless magnetic reconnection. (a) Magnetic field lines, (b) contours of electrostatic potential, (c) ion flow pattern, and (d) ion heat flux obtained at $t = 1020\Omega_e^{-1}$ in Case B. The maximum flow speed corresponds to $\sim 1.3v_A$, where v_A is the Alfvén speed. 186
- Fig. 6.8 Ion distribution as a function of V_{\parallel} , the velocity component parallel to the magnetic field, obtained at $t = 1020\Omega_e^{-1}$ in Case B. The distribution shows the presence of a high-energy component in the region with $-2.4 \leq V_{\parallel}/v_{the} \leq -1.5$, corresponding to the presence of a particle heat flux. 189
- Fig. 6.9 Proton distribution functions associated with FTEs at the dayside magnetopause. The top panel shows a two-dimensional proton velocity distribution and the bottom panel shows an one-dimensional velocity distribution, which is obtained by cutting the two-dimensional distribution function along the direction of magnetic field (\mathbf{B}) [Thomsen et al., 1987]. 190
- Fig. 6.10 Typical power spectra of electromagnetic waves associated with the driven collisionless magnetic reconnection observed in simulation Case B. (a) Power spectrum of magnetic field component B_x obtained at $(x/\rho_e = 12, z/\rho_e = 72)$ and (b) power spectrum of electrostatic field $E = \sqrt{E_x^2 + E_z^2}$ obtained at $(x/\rho_e = 24, z/\rho_e = 0)$. 193

- Fig. 6.11 (a) Magnetic field lines and (b) contours of the self-generated magnetic field B_y component at different simulation times in Case C. In B_y contours, solid lines indicate the regions with $B_y \geq 0$ while dash lines represent the regions with $B_y < 0$. 197
- Fig. 6.12 Magnetic field data for the inbound pass on November 9, 1979, which show detections of two-regime FTEs. The heavier trace refers to measurements on ISEE 2 while the lighter trace refers to ISEE1, which is about 3817km behind ISEE 2. The main two-regime FTEs are indicated by vertical lines [Farrugia et al., 1987]. 201
- Fig. 6.13 The multilayered structure observed in a magnetospheric FTE by AMPTE/UKS satellite on October 28, 1984. (a) Magnetic field data, and (b) plasma data, where more jagged trace refers to electrons, and the second panel shows number density of energetic particles [Farrugia et al., 1988]. 202
- Fig. 6.14 Driven collisionless magnetic reconnection is an asymmetric current sheet. (a) Magnetic field lines and (b) scatter plot of electron positions at various simulation times observed in Case D. 204
- Fig. 6.15 Different FTE B_n (B_z) signatures generated by the MXR and SXR processes observed in Case D. (a) Magnetic field lines and (b) FTE B_n signatures at $t = 150\Omega_e^{-1}$ and $t = 1080\Omega_e^{-1}$. 208
- Fig. 6.16 Magnetic field strength as a function of z observed at different locations relative to the current sheet ($x \simeq 0$) when an FTE signature is generated due to the formation of magnetic island by the MXR process at $t = 150\Omega_e^{-1}$. 210
- Fig. 6.17 The power spectra of magnetic field component B_z as a function of the normalized wavenumber $k_z L$ at different simulation times observed in Case B. The peak at $k_z L \sim 0.3$ corresponds to the energy input caused by the enhanced tearing instability. The corresponding magnetic field lines are shown in Figure 6.2. 218

- Fig. 7.1 Particle trajectories in plasma neutral sheets. (a) Ion trajectories in a neutral sheet without electric field ($\mathbf{E} = 0$) and (b) ion and electron trajectories in a neutral sheet with electric field ($\mathbf{E} = E_y \mathbf{e}_y \neq 0$). 224
- Fig. 7.2 Non-adiabatic ion trajectories in a current sheet with a magnetic field B_z component, which is present due to magnetic reconnection, (a) in the neutral sheet rest frame in which $E_y \neq 0$ and (b) in the field line rest frame in which $E_y = 0$ [Speiser, 1965]. The field line rest frame moves with a speed of $\mathbf{V}_F = cE_y/B_z \mathbf{e}_x$ away from the X line region. 226
- Fig. 7.3 Magnetic field lines at different simulation times in Case C. The left column shows the magnetic field lines from $t = 210\Omega_e^{-1}$ to $t = 330\Omega_e^{-1}$ while the right column shows the magnetic field lines from $t = 480\Omega_e^{-1}$ to $t = 600\Omega_e^{-1}$. During these two periods particle trajectories were calculated. 231
- Fig. 7.4 The typical trajectory of an electron outside the current sheet obtained between $t = 210\Omega_e^{-1}$ and $t = 330\Omega_e^{-1}$. The left column shows particle trajectories projected on the $x-y$, $y-z$, and $x-z$ planes while the right column shows particle trajectories projected on the $x-v_x$, $y-v_y$, and $z-v_z$ phase spaces, and particle energy as a function of z . 233
- Fig. 7.5 The trajectory of a typical electron that becomes trapped by the magnetic island during its formation between $t = 480\Omega_e^{-1}$ and $t = 600\Omega_e^{-1}$. The format of the present figure is the same as that in Figure 7.4. 235
- Fig. 7.6 The typical trajectory of a trapped electron which streams along the closed magnetic field lines around the magnetic island in the region with $z < 0$ during the period from $t = 210\Omega_e^{-1}$ to $t = 330\Omega_e^{-1}$. The format of the present figure is the same as that in Figure 7.4. 236

- Fig. 7.7 The typical trajectory of a trapped electron which bounces rapidly inside the magnetic island formed in the $z < 0$ region between $t = 210\Omega_e^{-1}$ and $t = 330\Omega_e^{-1}$. The format of the present figure is the same as that in Figure 7.4. 238
- Fig. 7.8 The typical trajectory of a trapped electron which bounces between magnetic mirrors formed by magnetic field compression above and below the magnetic island formed in the $z < 0$ region during the period from $t = 210\Omega_e^{-1}$ to $t = 330\Omega_e^{-1}$. The format of the present figure is the same as that in Figure 7.4. 240
- Fig. 7.9 A model steady reconnection magnetic field configuration given by (7.2), with $B_{x0}/B_{z0} = 0.6$, $\lambda_x/\rho_i = 7.0$, $\lambda_z/\lambda_x = 2.0$. 242
- Fig. 7.10 A test particle calculation of ion trajectory in the model steady reconnection magnetic and electric fields given by (7.2) and (7.3). Parameters used are $B_{z0} = 1.0$, $B_{x0}/B_{z0} = 0.6$, $\lambda_x/\rho_i = 7.0$, $\lambda_z/\lambda_x = 2.0$, and $E_{y0} = 0.25$. 243

Acknowledgements

I would like to express my sincere appreciation to Dr. L. C. Lee, my thesis advisor and the chairman of my graduate advisory committee, for his guidance, advice, encouragement, support, and help in the past five years, which made the completion of this thesis possible. I am also especially grateful to the other members of my graduate advisory committee, Drs. S. -I. Akasofu, J. G. Hawkins, J. V. Olson, and D. W. Swift, for their continuous help and valuable suggestions in preparing this thesis. Particularly, I would like to thank Dr. D. W. Swift for his expertise and help in conducting particle simulation of magnetospheric plasma physics.

I am indebted to Professors Z. F. Fu and Z. X. Liu at the Center for Space Science & Applied Research of the Chinese Academy of Sciences for introducing me to the Geophysical Institute and the Department of Physics of the University of Alaska Fairbanks. Their help and encouragement are very important to the completion of my graduate study in Alaska. My gratitude also extends to many of my fellow graduate students at the Geophysical Institute and the Department of Physics who offered generous help and valuable discussions during the preparation of this thesis. Thanks particularly to Ms. A. L. LaBelle-Hamer for her help and comments on thesis writing.

This research work was supported by grants of the National Science Foundation, the Department of Energy, and the National Aeronautics and Space Administration to the University of Alaska Fairbanks. The computation work was supported by the Computer Service Center of the Geophysical Institute and the San Diego Supercomputer Center. I deeply appreciate Mr. Dick Million and Ms. Celia Rohwer at the Computer Service Center for their help in computer programming on VAX. Special thanks also extend to Ms. Doreen Fitzgerald at the Special

Publications Office of the Geophysical Institute for editing this thesis. The present thesis is typeset using TeX.

Finally, I would like to thank my parents Mr. Chong-Gao Ding and Ms. Ben-Yuan Liu, my wife Fang Li, and other family members for their continuous support, encouragement, care, love, and help, for without them, the thesis would not have been completed.

Chapter 1 Introduction

Magnetic field reconnection is believed to play a crucial role in many important plasma processes, ranging from cosmic plasma environments to controlled laboratory plasma experiments. One of the most important features of magnetic reconnection process is the release and conversion in a very short time period of huge amounts of energy stored in the magnetic field into plasma kinetic energy, accompanied by a change of magnetic field topology. For example, solar flares are a manifestation of such explosive energy release and conversion. For a typical solar flare, an energy of 3×10^{32} ergs can be released and converted within 30 minutes [e.g., Priest, 1985].

Magnetic reconnection was first proposed by solar physicists to explain solar flares [e.g., Giovanelli, 1946, 1947]. The concept of magnetic reconnection was then applied to the earth's magnetosphere to explain the geomagnetic storm and auroral activities [Hoyle, 1949; Dungey, 1961]. The magnetic reconnection process was subsequently identified in other astrophysical and interplanetary objects, e.g., Jovian magnetosphere [Nishida, 1984] and comets [Niedner, 1984], as well as in laboratory plasmas, such as tokamaks [Paré, 1984] and reversed field pinch (RFP) devices [Baker, 1984].

There are several different ways to define the magnetic reconnection process. Vasyliunas [1975] defined magnetic reconnection as a process whereby plasma flows across a surface that separates regions containing topologically different magnetic field lines. In this definition, the surface that separates different magnetic field line regions is called a separatrix and the two separatrix branches intersect at a line

called a separator [Vasyliunas, 1984; Sonnerup, 1985]. The reconnection rate refers to the amount of magnetic flux transported per unit time across a unit length of the separator. The unit for the reconnection rate is the same as the unit of electric field.

The basic reconnection geometry is illustrated in Figure 1.1. The field line a , originally located in domain 3, moves toward the separatrix surface and lies in that surface at location b . When reconnection occurs, the field lines at the separator break into components c and d , located in domains 1 and 2, respectively. In general, however, the magnetic field along the entire separator is not zero. Therefore, a field component \mathbf{B}_{\parallel} may be present along that line. The term separator is synonymous with reconnection line, merging line, or X line. The phrases neutral line and null line are also used when the magnetic field along the entire separator is zero.

Alternatively, some authors emphasize the electric field component parallel to the separator (\mathbf{E}_{\parallel}) as the distinguishing characteristic of reconnection process [e.g., Cowley, 1976; Sonnerup, 1985]. In this case, magnetic field reconnection is defined to occur in a plasma whenever \mathbf{E}_{\parallel} is present along a magnetic separator [Sonnerup, 1985]. The electric field, \mathbf{E}_{\parallel} , is proportional to the reconnection rate defined above. Finally, other authors emphasize the localized breakdown of the frozen-in field condition and the resulting changes of connection as the basis of magnetic reconnection [e.g., Axford, 1984]. They define magnetic reconnection as a process involving a violation of the magnetohydrodynamic frozen field theorem in which higher order effects such as resistivity, normally negligible in the large scale, become locally dominant with dramatic consequences in the nature of the large-scale flow and magnetic field configuration which could not be achieved otherwise.

These three definitions of magnetic reconnection are equivalent. For example, Vasyliunas [1975] argued that the plasma flow across a separatrix requires an

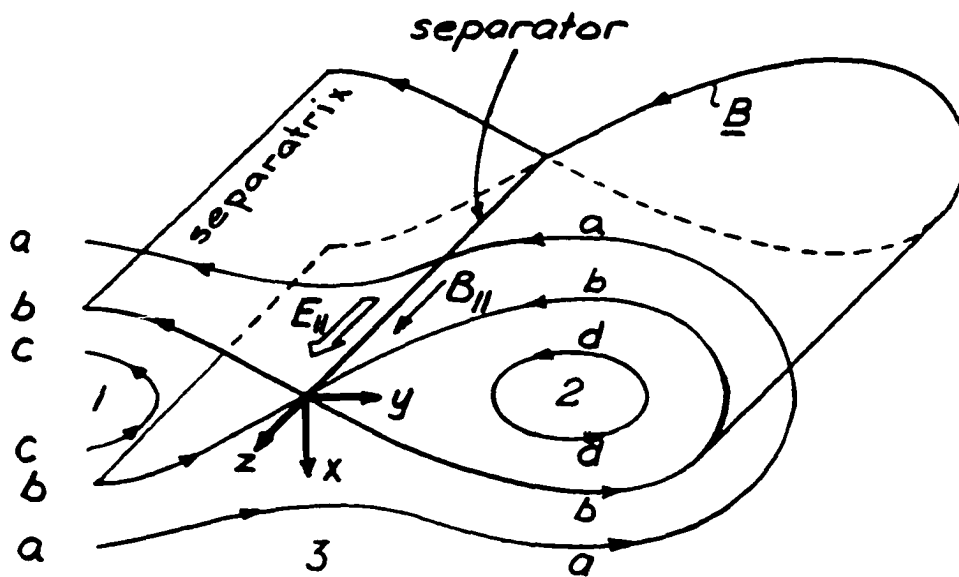


Figure 1.1 Basic geometry for the magnetic field reconnection process [Sonnerup, 1985].

electric field component \mathbf{E}_{\parallel} along the separator, which in turn implies a localized violation of ideal Ohm's law and breakdown of the frozen-in field condition [Baum and Bratenahl, 1980; Vasyliunas, 1984]. Specifically, if an electric field component \mathbf{E}_{\parallel} is present along the separator, the plasma will move across the separatrix under the influence of $\mathbf{E} \times \mathbf{B}$ force. On the other hand, the topology of magnetic field is changed when a plasma flows across the separatrix, leading to the presence of an induction electric field \mathbf{E}_{\parallel} along the separator. If a plasma is frozen-in with magnetic field, then it cannot move across any magnetic field lines; whereas, if a plasma flows across a separator that is also a part of magnetic field line, then the frozen-in field condition is violated in the vicinity of the separatrix; and vice versa.

To further illuminate the concept of magnetic reconnection, an example of the time evolution of magnetic field configuration in a laboratory reconnection experiment is shown in Figure 1.2 [Gekelman et al., 1982]. The reconnection process is illustrated by the topology change of the pair of field lines $a - a$ and $b - b$ (heavy lines). During reconnection, plasma and magnetic flux are transferred from cells 1 and 2 to cells 3 and 4. The separator is located at the center of the figure, along with the reconnection electric field \mathbf{E}_{\parallel} , is perpendicular to the plane of the paper.

As an effective mechanism for energy release and conversion, magnetic field reconnection has attracted a lot of attention among theoretical, experimental, and computational physicists [e.g., see *Magnetic Reconnection in Space and Laboratory Plasmas* ed. by Hones, 1984 and *Physics of Magnetic Flux Ropes* ed. by Russell et al., 1990]. Magnetic reconnection has been used to explain solar flares, magnetospheric storms and substorms, and many other plasma processes observed in natural and laboratory plasma environments. Magnetic field reconnection is now believed to be one of the most important processes in the transfer of solar wind mass, momentum, and energy into the earth's magnetosphere [e.g., Vasyliunas,

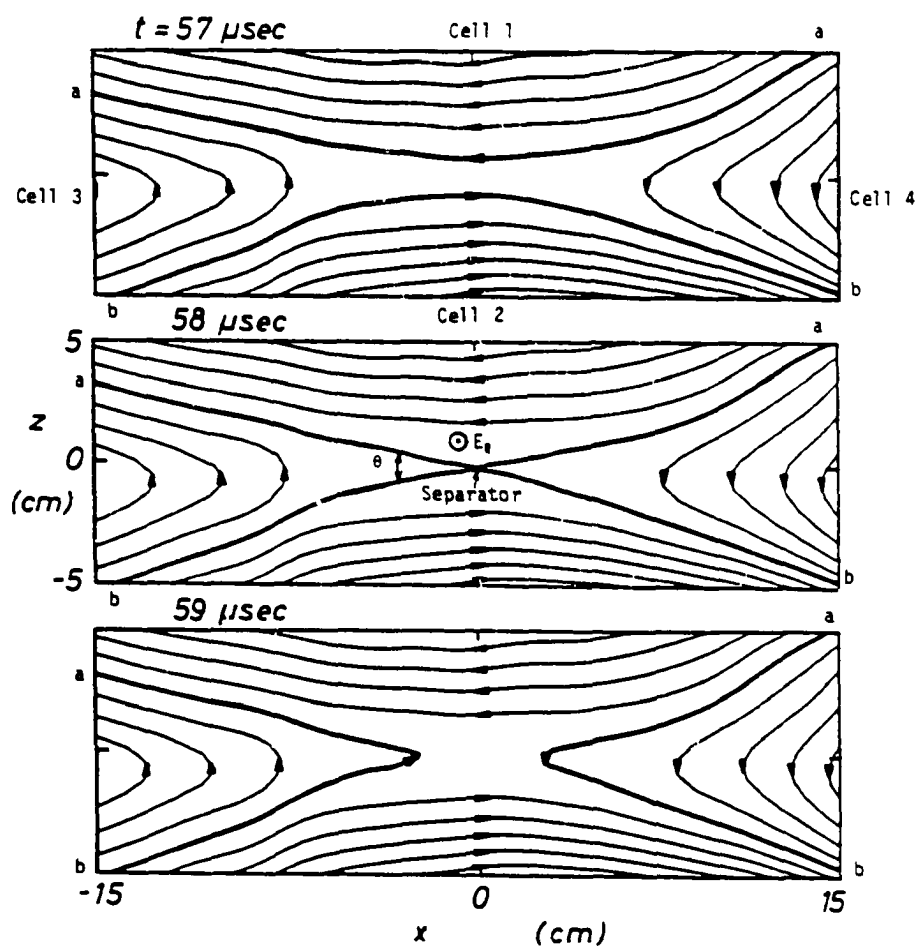


Figure 1.2 The time evolution of magnetic field configuration in the laboratory reconnection experiment [Gekelman et al., 1982].

1975; Sonnerup, 1979; Cowley, 1982; Haerendel and Paschmann, 1982; Pudovkin and Semenov, 1985; Lundin, 1988; Heikkila, 1990].

The discovery of flux transfer events (FTEs) [Russell and Elphic, 1978, 1979] provided the first observational evidence for magnetic reconnection at the earth's dayside magnetopause [Paschmann et al., 1979; Sonnerup et al., 1981]. Observations of FTEs based on ISEE 1 and ISEE 2 satellites, as well as the recent AMPTE/UKS, AMPTE/IRM, and AMPTE/CCE spacecraft, reveal many new features associated with FTEs that have dramatically changed our understanding of the reconnection process at the dayside magnetopause [see recent review by Russell, 1990; Elphic, 1990]. It is now well accepted that the dayside magnetic reconnection is an intermittent process rather than the steady-state process suggested by Dungey [1961].

Satellite observations have revealed that many distinct magnetic field and plasma characteristics are associated with FTEs. These characteristics include the bi-polar B_z signatures [Russell and Elphic, 1978, 1979; Rijnbeek et al., 1984], the high-speed plasma flows [Saunders et al., 1984], the presence of a mixture of magnetosheath and magnetospheric plasma populations [Speiser and Williams, 1982; Rijnbeek et al. 1984], and the presence of energetic particles and particle heat flux [Daly et al., 1981; Scholer et al., 1981; Sonnerup et al., 1981; Daly and Kepler, 1983; Sibeck et al., 1987; Scudder et al., 1984; Thomsen et al., 1987; Klumpar et al., 1989].

Observations of FTEs have fascinated many researchers in the space physics community. Various theoretical models have been proposed and many computer simulations have been carried out to examine the features associated with FTEs. One of the many attempts to explain the occurrence and properties of FTEs is the multiple X line reconnection (MXR) model proposed by Lee and Fu [1985] and

simulated by Fu and Lee [1985]. In the Lee-Fu model [Lee and Fu, 1985], multiple X line reconnection can be considered as a magnetic reconnection process between two approaching magnetized plasmas, carrying opposite-directed magnetic fields. Multiple X line reconnection is not a steady process. At first, the reconnected magnetic field lines form magnetic flux tubes. Then, as the magnetic flux tubes grow to a size much larger than the original current sheet thickness, the reconnection of magnetic field lines will slow down and eventually stop due to nonlinear saturation of the tearing mode instability. Subsequently, reconnection will resume when the saturated magnetic flux tubes are convected out of the reconnection region. Repeated formation and convection of magnetic flux tubes during the MXR process would lead to the observed features of FTEs at the dayside magnetopause. Fu and Lee's simulation [Fu and Lee, 1985] and other MHD simulations of MXR process performed by Lee and Fu [1986], Fu and Lee [1986], Shi et al. [1988], Fu [1989], and Fu et al. [1990] have confirmed the above speculation.

Although MHD simulations provide much useful information about the magnetic reconnection and FTEs, the plasma kinetic effects associated with the dayside magnetic reconnection process and FTEs, such as the generation of energetic particles and particle heat flux, can rarely be studied based on MHD simulations. Furthermore, in MHD simulations of the magnetic reconnection process, the anomalous resistivity that is required for reconnection to take place has to be arbitrarily assumed. The assumed spatial and temporal variations of resistivity may not be realistic in the collisionless magnetospheric plasma. For this reason, it is important to use particle simulations to study the particle kinetic features associated with collisionless magnetic reconnection process at the dayside magnetopause. The particle code has a distinct advantage over an MHD code in the simulation study of the magnetic reconnection process. In a particle code simulation, the anomalous

resistivity can be generated naturally by the non-MHD effects, such as particle inertia and/or wave-particle interaction in the collisionless plasma [Vasyliunas, 1975; Sonnerup, 1979].

This thesis reports on a series of particle simulations of the dayside magnetic reconnection process. In the simulations, both one-component (ions only) particle code and two-component (ions and electrons) particle code are used. Many features associated with the dayside magnetic reconnection process, such as the acceleration and heating of particles, the generation of energetic particle and particle heat flux, and the generation of plasma waves are examined in the simulations. The field and particle signatures obtained in the simulations are compared with the satellite observations of FTEs at the dayside magnetopause.

Specifically, this thesis is organized as follows: Chapter Two presents an overview of the historical development of the concept of magnetic field reconnection, the observational features of FTEs, and the Lee-Fu MXR model. In Chapter Three, the linear theories of collisional and collisionless tearing mode instabilities are reviewed; also examined is the effect of plasma β , the ratio of plasma pressure to magnetic pressure, on the tearing mode instabilities. Chapter Four presents the magnetoinductive particle simulation model used in the present study and the boundary conditions necessary for the simulation of the driven collisionless magnetic reconnection process. The one-component particle simulation of the dayside magnetic reconnection process is reported in Chapter Five, where application of simulation results to flux transfer events is also discussed. Based on two-component particle simulations, the driven collisionless magnetic reconnection process is examined in Chapter Six and the results are compared with satellite observations of FTEs. This chapter further examines the driven collisionless magnetic reconnection from another point of view, the perspective of self-organization. In Chapter Seven,

particle acceleration processes in the collisionless magnetic reconnection are studied based on full particle code simulations. Finally, a summary and discussion on the present thesis study is included in Chapter Eight.

Chapter 2 An Overview of Magnetic Field Reconnection and Flux Transfer Events

Since Giovanelli [1946, 1947] proposed the neutral sheet model for solar flares, magnetic reconnection process has been studied for more than four decades. After Dungey [1961] applied the concept of magnetic field reconnection to the earth's magnetosphere and Russell and Elphic [1978, 1979] discovered flux transfer events (FTEs) at the dayside magnetopause, magnetic reconnection process has been accepted as one of the prevailing mechanisms for interaction between the solar wind and the magnetosphere. In one of the many attempts to explain FTEs, Lee and Fu [1985] proposed a multiple X line reconnection model for the dayside magnetopause. This chapter contains an overview of the historical development of the study of magnetic field reconnection, the observational features of FTEs, Lee and Fu's MXR model and other theoretical FTE models, and computer simulations of the dayside magnetic reconnection.

2.1 Historical Development of the Concept of Magnetic Field Reconnection

The concept of magnetic field reconnection (magnetic field line merging, or magnetic field annihilation) was originally proposed by solar physicists to explain solar flares based on the neutral point theory. Giovanelli [1946] first proposed that the optical emission from solar flares originates from atoms excited by electrons which are accelerated in the induced electric fields near neutral points in the evolving

magnetic fields of sunspots. Fascinated by the remarkable resemblance between magnetic storms and solar flares, Hoyle [1949] suggested that the primary auroral particles which bombard the earth's polar atmosphere are accelerated at neutral points formed by the combination of an interplanetary field and the geomagnetic field.

The application of magnetic reconnection theory to the earth's magnetosphere was formally completed by Dungey [1961], who proposed an open magnetosphere model in which the interplanetary magnetic field (IMF) connects with the geomagnetic field both at the dayside magnetopause and in the nightside magnetotail. A schematic diagram of Dungey's model is sketched in Figure 2.1. Region 1 represents the earth's internal magnetic field, while region 2 is the external geomagnetic field. The thick lines are the separatrices. The open field lines in region 3 are connected to both the interplanetary magnetic field and the geomagnetic field. The field lines on the left side represent the southward IMF. Two X lines are present, indicating magnetic reconnection at both the dayside magnetopause and the magnetotail. In Dungey's model, magnetic reconnection in the earth's magnetosphere is a steady-state process.

Mathematically, magnetic field reconnection process is governed by the magnetic induction equation,

$$\frac{\partial \mathbf{B}}{\partial t} = \nabla \times (\mathbf{U} \times \mathbf{B}) + \frac{c^2 \eta}{4\pi} \nabla^2 \mathbf{B} \quad (2.1)$$

where \mathbf{B} is the magnetic field strength, t is time, \mathbf{U} is the plasma flow velocity, c is the speed of light, and η is the resistivity. This equation is derived from Maxwell's equations and Ohm's law. If the second term on the right hand side of (2.1) is much larger than the first term, then (2.1) reduces to the magnetic diffusion equation,

$$\frac{\partial \mathbf{B}}{\partial t} = \frac{c^2 \eta}{4\pi} \nabla^2 \mathbf{B} \quad (2.2)$$

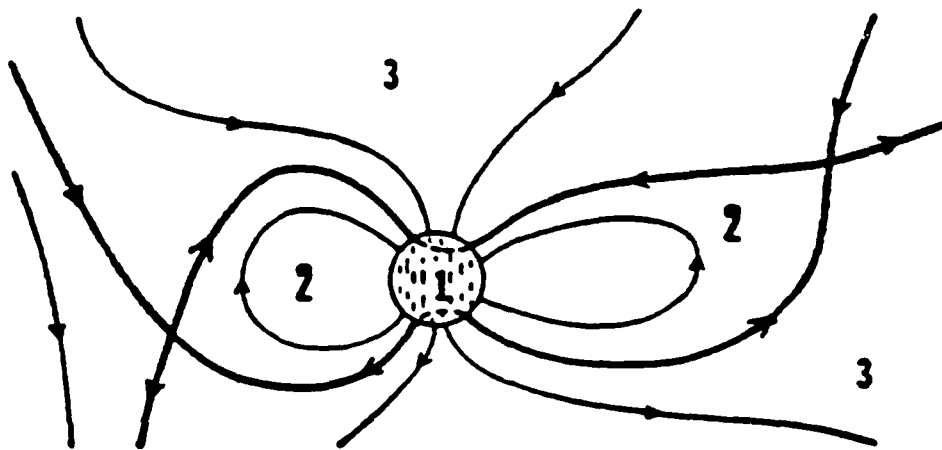


Figure 2.1 A schematic diagram of the open magnetosphere model proposed by Dungey [1961], in which magnetic reconnection takes place both at the dayside magnetopause and in the nightside magnetotail.

On the other hand, if the first term dominates, then (2.1) becomes the magnetic convection equation,

$$\frac{\partial \mathbf{B}}{\partial t} = \nabla \times (\mathbf{U} \times \mathbf{B}) \quad (2.3)$$

The ratio of the first term to the second term on the right hand side of (2.1) yields a dimensionless quantity, the magnetic Reynolds number $R_m = 4\pi UL/c^2\eta$, where U and L are respectively the characteristic speed and scale length of the physical process concerned. A large magnetic Reynolds number obviously shows that magnetic convection is important, while a small magnetic Reynolds number indicates that magnetic diffusion is dominant.

It is clear from the above that the basic magnetic field configuration for the reconnection process consists of two parts: a diffusion region and a convection region. The diffusion region is a small domain in the neighborhood of the magnetic neutral point. In the diffusion region, the scale length (L_d) is small and the resistivity (η) is important, leading to a small magnetic Reynolds number (R_m), and diffusion of magnetic fields dominates the process. The convection region is the outer part of the reconnection configuration. Here the scale length (L_c) is large and the resistivity (η) is unimportant, resulting in a large magnetic Reynolds number, and the plasma and magnetic fields are frozen-in and move together because of the negligible magnetic field diffusion.

A steady-state reconnection configuration can be obtained when magnetic field configuration does not change with time, i.e., $\partial \mathbf{B} / \partial t = 0$. To describe the steady-state magnetic reconnection process, several theoretical models have been proposed [Parker, 1957; Sweet, 1958; Petschek, 1964; Sonnerup 1970; Yeh and Axford, 1970].

As pointed out by Vasyliunas [1975], the above theoretical models are fundamentally consistent, representing different aspects of the reconnection process. Some characteristics associated with different models will be briefly described below.

The first reconnection model that describes the diffusion region in a neutral sheet was proposed by Parker [1957] and Sweet [1958]. In the Sweet-Parker model (Figure 2.2a) opposing magnetic field lines are carried by the plasma toward the diffusion region. The length of the diffusion region is $2L$ and the width is 2δ . If the inflow and outflow speeds respectively are U_1 and U_2 , then it is found from the conservation of plasma mass that $U_1L = U_2\delta$, and hence

$$U_2 = \frac{L}{\delta}U_1 \quad (2.4)$$

for an incompressible fluid with $\rho_1 = \rho_2 = \rho$. If the magnetic field outside the current sheet is B_1 , then from the momentum equation it is obtained that $B_1^2/8\pi = \rho U_2^2/2$, and hence,

$$U_2 = \frac{B_1}{\sqrt{4\pi\rho}} = V_{A1} \quad (2.5)$$

where V_{A1} is the Alfvén speed based on B_1 . In the diffusion region, the convection of the magnetic field is balanced by magnetic field diffusion. Therefore, the diffusion time ($t_d = 4\pi\delta^2/c^2\eta$) must equal the convection time ($t_c = \delta/U_1$). With $t_d = t_c$, it is obtained that

$$\frac{\delta}{L} = \frac{c^2\eta}{4\pi U_1 L} \quad (2.6)$$

During magnetic reconnection, the reconnection rate, with a unit similar to that of electric field as discussed in Chapter One, refers to the amount of magnetic flux transported per unit time across a unit length of the separator. However, a dimensionless quantity (Alfvén Mach number $M_A = U_1/V_{A1}$) is also used conventionally as a measure of the rate for reconnection process [Vasyliunas, 1975]. In the

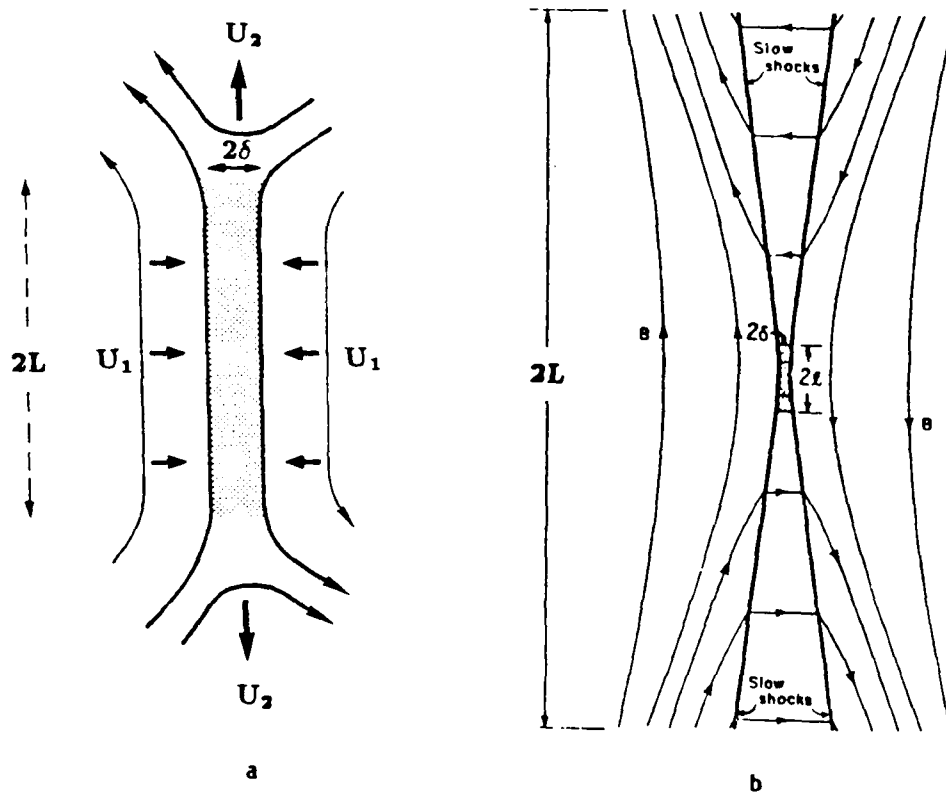


Figure 2.2 MHD reconnection models. (a) Sweet-Parker model [Parker, 1957; Sweet, 1958] and (b) Petschek model [Petschek, 1964].

following, to distinguish the dimensional reconnection rate from the dimensionless reconnection rate, reconnection electric field (E_R) refers to the reconnection rate in its dimensional unit, while the Alfvén Mach number (M_A) refers to the dimensionless reconnection rate. The relation between the Alfvén Mach number (M_A) and the reconnection electric field (E_R) can be written as $M_A = cE_R/V_{A1}B_1$. Since $U_1 = M_A V_{A1}$ is the speed of the steady-state magnetized plasma inflow toward the diffusion region, a large reconnection rate M_A , hence a large inflow speed U_1 , indicates that more magnetic energy is released and converted into plasma kinetic energy; a small reconnection rate M_A , hence a small inflow speed U_1 , indicates that less magnetic energy is released and converted. For the reconnection processes in the solar atmosphere and the earth's magnetosphere, a typical reconnection rate M_A with a value of $0.1 \sim 1.0$ is needed.

From (2.4) – (2.6) and after some straightforward algebra, it is found that the reconnection rate (M_A) in the Sweet-Parker model can be expressed as

$$M_A = \frac{U_1}{V_{A1}} = \frac{1}{\sqrt{R_m}} \quad (2.7)$$

where $R_m = 4\pi L V_{A1}/c^2 \eta$ is the magnetic Reynolds number based on the current sheet length L and the Alfvén speed V_{A1} . The typical value of the magnetic Reynolds number (R_m) for solar flares is $10^8 \sim 10^{10}$. Therefore, it is found that the reconnection rate M_A in the Sweet-Parker model is too small, by a factor of 10^{-5} to 10^{-4} , to account for the rapid energy conversion observed in solar flares. This is also true for magnetospheric substorms.

In order to increase the reconnection rate, Petschek [1964] proposed that the diffusion region is confined to a small area only, with four slow shocks attached to the central diffusion region, and the conversion of magnetic field energy into plasma kinetic energy is accomplished mainly through the acceleration and heating

of plasmas by the slow shocks. Figure 2.2b shows Petschek's model, in which the length of the diffusion region is only $2l$, while the scale length of the system is $2L$. The reconnection rate in Petschek's model is found to have a weak dependence on the magnetic Reynolds number, $M_A \sim 1/\ln(R_m)$. Therefore, a larger reconnection rate with a typical value of $0.01 \sim 0.1$ is obtained.

A new reconnection model that also contains four slow shocks was developed independently by Sonnerup [1970] and Yeh and Axford [1970]. However, as pointed out by Vasyliunas [1975], in the Sonnerup-Yeh-Axford model, the plasma flow toward the diffusion region is a divergent flow, in which the plasma experiences a slow mode expansion; in Petschek's model, the plasma flow is a convergent one, in which the plasma experiences a fast mode expansion. The upper limit of the reconnection rate obtained in the Sonnerup-Yeh-Axford model can be as large as $\sqrt{2} + 1$.

In their study of linear steady-state reconnection processes, Priest and Forbes [1986] found that magnetic reconnection configuration is very sensitive to the conditions imposed at the inflow and outflow boundaries. They obtained a unified family of models for incompressible, steady-state magnetic reconnection processes. As shown in Figure 2.3, reconnection configurations other than the Petschek and Sonnerup models, such as a slow compression model, a hybrid expansion model, and a flux pile-up model, may be obtained as different special cases in this family of models, depending on the upstream inflow boundary conditions.

Recently, Priest and Lee [1990] proposed a nonlinear model for the fast steady-state magnetic reconnection process. In the Priest-Lee model, the inflow region possesses highly curved magnetic field lines, which is different from that in the classical Petschek model, and a separatrix jet of plasma is ejected from the central diffusion region along the magnetic separatrix. It is shown in Priest and Lee [1990] that boundary conditions, both at the upstream inflow boundary and the

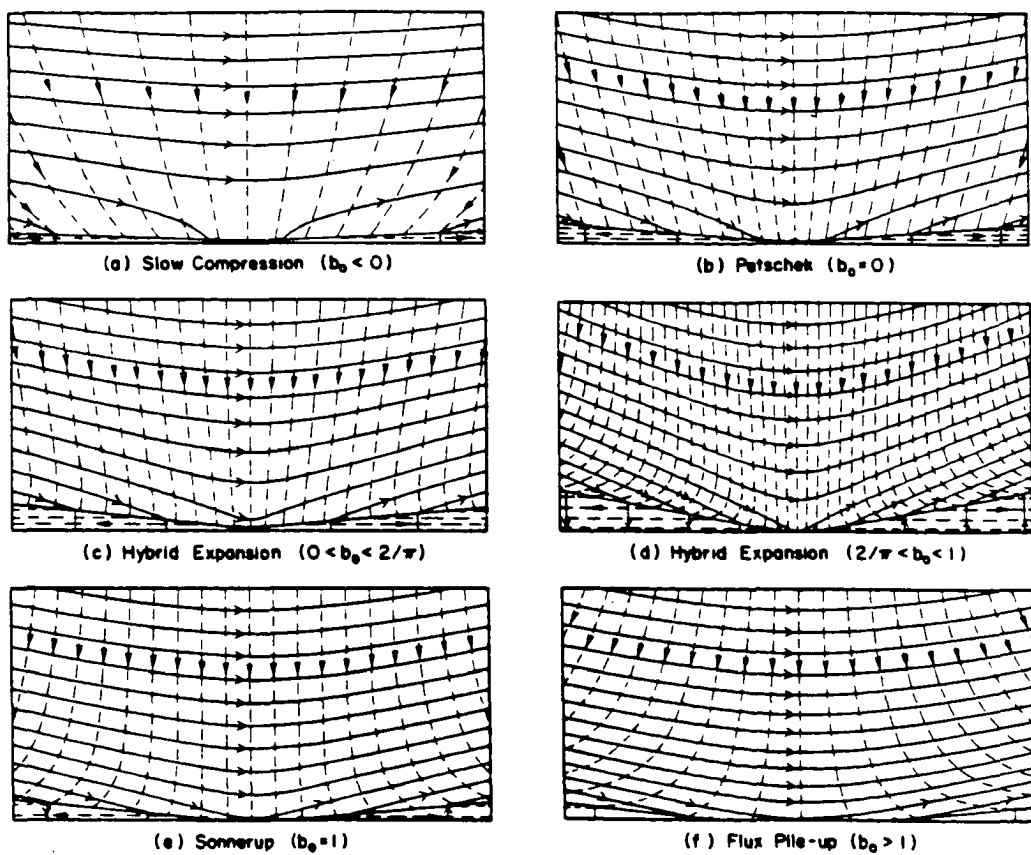


Figure 2.3 A unified family of models for incompressible, steady-state magnetic reconnection [Priest and Forbes, 1986].

downstream outflow boundary, are important in determining the reconnection configurations; and, that plasma outflow across the separatrix jet can be slowed down by fast-mode shocks or speeded up by slow-mode shocks, depending on downstream boundary conditions.

In the above reconnection models, the magnetic field configuration is symmetric about the current sheet, i.e., the magnitude of magnetic field on both sides of the current sheet is the same. At the dayside magnetopause, however, the magnetosheath field generally is smaller than the magnetospheric field. Therefore, the reconnection configuration at the dayside magnetopause would be asymmetrical. Levy et al. [1964] applied Petschek's reconnection model to the dayside magnetopause and modified Dungey's open magnetosphere model. In the model of Levy et al. [1964], shown in Figure 2.4, the magnetospheric field is larger than that in the magnetosheath side. Shocked solar wind plasma flows in from the left side only, with a vacuum condition in the magnetosphere on the right. Plasma acceleration is accomplished through a large amplitude Alfvén wave or rotational discontinuity. A slow expansion fan is formed inside the magnetopause. In Levy et al. model, the reconnection rate could reach as high as 2. Recent simulation results of Shi and Lee [1990] have shown that in asymmetric dayside reconnection configurations, intermediate shocks may also be formed in the magnetosheath region, while weak slow shocks are formed inside the magnetopause.

All the theoretical models for the steady-state reconnection process described above are two-dimensional and based on the MHD equations. Except for Sweet-Parker's model [Parker, 1957; Sweet, 1958], all other models are characterized by the presence of slow shocks [Petschek, 1964; Sonnerup, 1970; Yeh and Axford, 1970; Priest and Forbes, 1986] or large-amplitude intermediate waves and slow expansion fan [Levy et al., 1964] in the external convection region. The incoming plasma

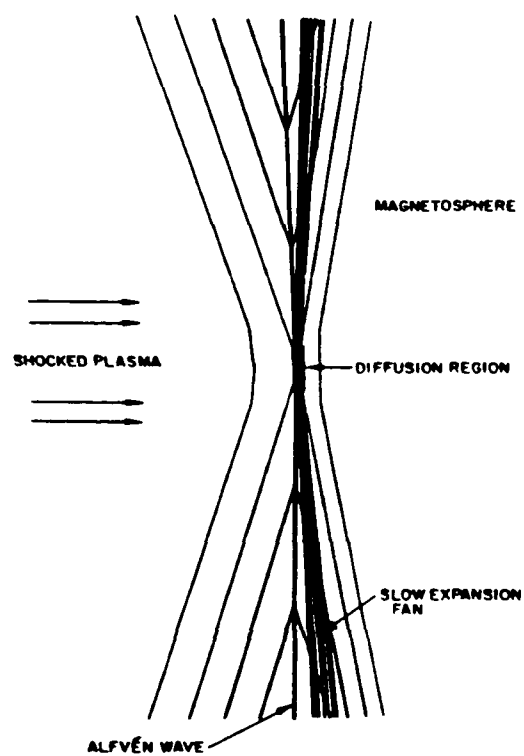


Figure 2.4 Levy et al.'s asymmetric reconnection model at the dayside magnetopause [Levy et al., 1964].

is accelerated to the Alfvén speed by the slow shocks or the Alfvén waves. The features of the reconnection process in a collisional plasma are described by these classical models based on MHD equations. However, in a collisionless plasma, the picture of the reconnection process is quite different.

The first collisionless, self-consistent neutral current sheet model was proposed by Alfvén [1968]. In Alfvén's model, shown in Figure 2.5, a neutral sheet with $\mathbf{B} = 0$ lies in the $x - y$ plane between oppositely directed magnetic fields. During the collisionless reconnection process, plasma flows from both sides toward the neutral sheet under the influence of the $\mathbf{E} \times \mathbf{B}$ drift. When they reach the neutral sheet, particles are ejected in the $\pm y$ -direction ($+y$ for ions and $-y$ for electrons). The incoming flux of plasma kinetic energy and magnetic energy are balanced by acceleration and ejection of the charged particles forming the current sheet. This current generates a self-consistent magnetic field, with a gradient across the neutral sheet. Note that in the collisionless neutral sheet model, plasma is ejected at a speed comparable with the inflow Alfvén speed along the direction of current, which is different from that in the MHD neutral sheet models. Alfvén's neutral sheet model was further developed by Dessler [1968], Speiser [1970], Eastwood [1972], Cowley [1973], and Lyons and Speiser [1985].

If the current sheet system is bounded by a plane of conducting walls separated by a distance L , then the total potential drop across the current sheet system is uniquely determined by the self-consistent requirement. The total potential drop, known as the Alfvén potential, was first derived by Alfvén [1968]. It is given by

$$\Phi_A = \frac{B^2}{4\pi N e} \quad (2.8)$$

where B is the magnetic field outside the current sheet such that the inflow plasma speed (U) is cE/B , the plasma density in the current sheet region is N , and the

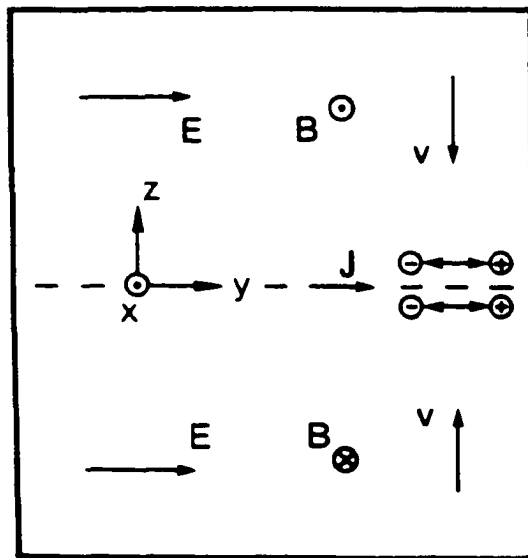


Figure 2.5 Alfvén's [1968] collisionless neutral sheet model.

magnitude of an electron charge is e . The electric field is determined by $E = \Phi_A/L$. The reconnection rate for the collisionless neutral sheet system is given by Cowley [1973] as

$$M_A = \frac{U}{V_A} = \left(\frac{\lambda_i}{L}\right) \quad (2.9)$$

where $V_A = B/\sqrt{4\pi Nm_i}$ is the inflow Alfvén speed, $\lambda_i = c/\omega_{pi}$ is the ion inertial length, and $\omega_{pi} = \sqrt{4\pi Ne^2/m_i}$ is the ion plasma frequency. For both solar flares and magnetospheric substorms, the ion inertial length λ_i is generally much smaller than the system length L . Thus, the reconnection rate given by (2.9) is very small, similar to that obtained with the Sweet-Parker model. Therefore, the above collisionless neutral sheet models describe the inner diffusion region for the collisionless reconnection process.

On the other hand, a collisionless model for the external reconnection region is provided by Hill [1975], who generalized the Alfvén-Speiser-Eastwood self-consistency condition for a current sheet to obtain collisionless reconnection configurations. A schematic picture of Hill's model is plotted in Figure 2.6. The key feature of Hill's collisionless reconnection model is that the magnetic field reversal takes place mainly along the current sheet (R). Across the four shocks (S), there is only a small amount of field line bending. The magnetic tension force associated with the central current sheet may provide most of the particle energization. Although the acceleration mechanism in Hill's model differs from that of the MHD model, its plasma flow pattern is similar to that in Petschek's model. The reconnection rate in Hill's model is closely related to the angle (χ) between the separatrix line and the field reversal plane, so that

$$M_A = \sin\chi\cos\chi \quad (2.10)$$

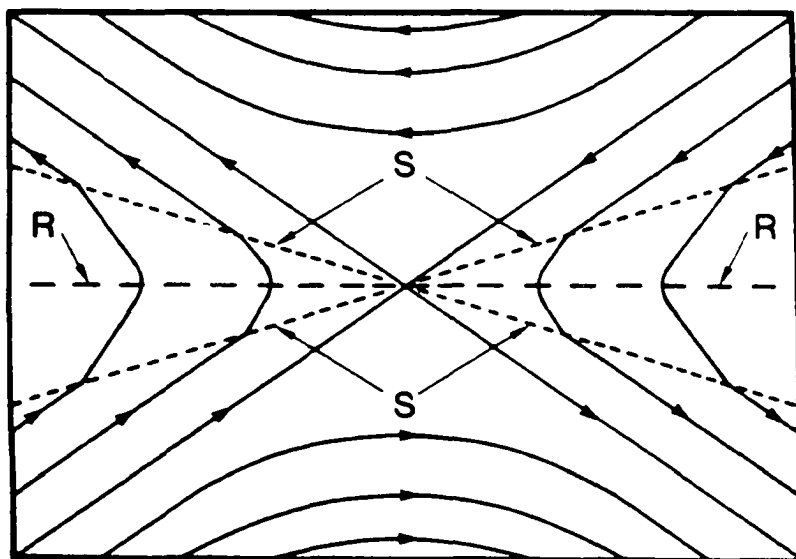


Figure 2.6 Hill's [1975] collisionless reconnection model.

Collisionless magnetic reconnection between arbitrarily oriented asymmetric magnetic fields was also discussed by Hill [1975].

In the early epoch of reconnection study, the attention of most researchers was concentrated on the simplest reconnection process, i.e., two-dimensional, symmetric or asymmetric, steady-state magnetic reconnection, based on either the MHD equations or collisionless plasma models [see reviews by Vasyliunas, 1975; Sonnerup, 1979, 1985; Cowley, 1985]. For the reconnection process at the earth's dayside magnetopause, Levy et al. [1964] pointed out that a component of magnetic field normal to the magnetopause and high-speed plasma flows should be observed at the dayside magnetopause as a consequence of dayside magnetic reconnection. The presence of the normal magnetic field component would indicate that the magnetosphere is open, whereas the presence of high-speed plasma flows would indicate that plasma acceleration occurs when the magnetic energy is converted into plasma kinetic energy during the reconnection process.

However, in the late 1960s and early 1970s, these predicted signatures of an open magnetosphere and the reconnection process at the dayside magnetopause were not observed as often as expected. Therefore, the reconnection process at the dayside magnetopause remained in doubt until the ISEE satellites provided ample observational evidence [Russell and Elphic, 1978, 1979; Paschmann et al., 1979; Sonnerup et al., 1981]. Although the satellite observations confirmed that the reconnection occurs at the dayside magnetopause, the observed characteristics of FTEs indicated that the dayside magnetic reconnection process is different from the predictions of Dungey's steady-state model. Further observations of FTEs showed that the dayside magnetic reconnection is a three-dimensional, intermittent or patchy process [see reviews by Elphic, 1990; Russell, 1990]. With these new observations, theoretical modeling study of the magnetic reconnection process entered a new era,

characterized by the three-dimensional, time-dependent reconnection models and large-scale 2-D and 3-D computer simulations of magnetic reconnections.

2.2 Observational Features and Theoretical Models of FTEs

In the late 1970s, Russell and Elphic [1978, 1979] discovered a distinct magnetic field and plasma structure in the ISEE satellite data. They identified this structure as a flux transfer event (FTE) in which magnetic flux is transferred from the solar wind into the earth's magnetosphere. Subsequently, previous observations of impulsive erosion of magnetic flux tubes [Haerendel et al., 1978] were also identified as FTEs [Rijnbeek and Cowley, 1984]. The discovery of FTEs marked a new departure in the study of the reconnection process at the dayside magnetopause. Since then, the intermittent reconnection has become one of the accepted hypotheses for the transfer of solar wind mass, momentum, and energy into the magnetosphere at the dayside magnetopause.

Over the past decade, the satellites ISEE 1, ISEE 2, and HEOS 2, have provided many valuable observations of FTEs. Recently, high resolution measurements of FTEs have become available from the AMPTE/UKS, AMPTE/IRM, and AMPTE/CCE spacecraft. So far, many observational features of FTEs have been identified and examined, including magnetic field B , electric field E , plasma waves, plasma density, plasma temperature, plasma flows, energetic particles, particle heat flux, and layered structures inside the FTEs [e.g., Russell and Elphic, 1978, 1979; Daly et al., 1981, 1984; Scholer et al., 1981, 1982; Sonnerup et al., 1981, 1987; Cowley, 1982; Berchem and Russell, 1982, 1984; Paschmann et al., 1982, 1986; Rijnbeek et al., 1982, 1984, 1987; Daly and Keppler, 1983; Rijnbeek and Cowley, 1984; Saunders et al., 1984; Scudder et al., 1984; Daily et al., 1985; Heikkila, 1986;

Chaloner et al., 1986; Smith et al., 1986; Southwood et al., 1986; Elphic and Southwood, 1987; LaBelle et al., 1987; Farrugia et al., 1987, 1988; Thomsen et al., 1987; Papamastorakis et al., 1989; Klumpar et al., 1989; Elphic, 1990; Gosling et al., 1990].

Figure 2.7 shows an example of magnetosheath FTEs observed on October 23, 1978 by ISEE 1 (heavy line) and ISEE 2 (light line) [Saunders et al., 1984]. The plasma data are plotted in the top five panels, while the magnetic field data are shown in the bottom five panels. In Figure 2.7, N_P is the total plasma density, while \bar{N}_P and \bar{N}_E are respectively the densities of energetic ions and energetic electrons. The plasma bulk flow velocity is plotted, approximately, in the geocentric solar ecliptic (GSE) coordinate system. (The origin of the GSE coordinates is located at the center of the earth, with X pointing sunward, Z northward and perpendicular to the ecliptic plane, and Y duskward and completing the right-hand orthogonal triad.) V is the magnitude of the bulk flow velocity, V_X and V_Y are the components of the bulk flow velocity. The magnetic field data are plotted in the boundary normal coordinate system, in which B_N is outward along the boundary normal, B_L is along the projection of the geocentric solar magnetospheric (GSM) Z -axis in the magnetopause plane, and B_M completes the orthogonal triad and points westward [Russell and Elphic, 1978]. (The origin of the GSM coordinates is at the center of the earth, with X pointing sunward, Z northward and in the plane determined by X and the earth's magnetic dipole, and Y duskward and completing the right-hand orthogonal triad.) The field angle in the $L - M$ plane is defined by $\alpha_{LM} = \tan^{-1}(B_M/B_L)$. ISEE 1's position is given at the base of the figure in terms of geocentric radial distance (R) in Earth radii, and GSM local time (LT_{GSM}) and latitude (LAT_{GSM}). At 1326 UT, ISEE 1 and ISEE 2 were separated by 5540 km along the N -direction with ISEE 2 leading the orbit.

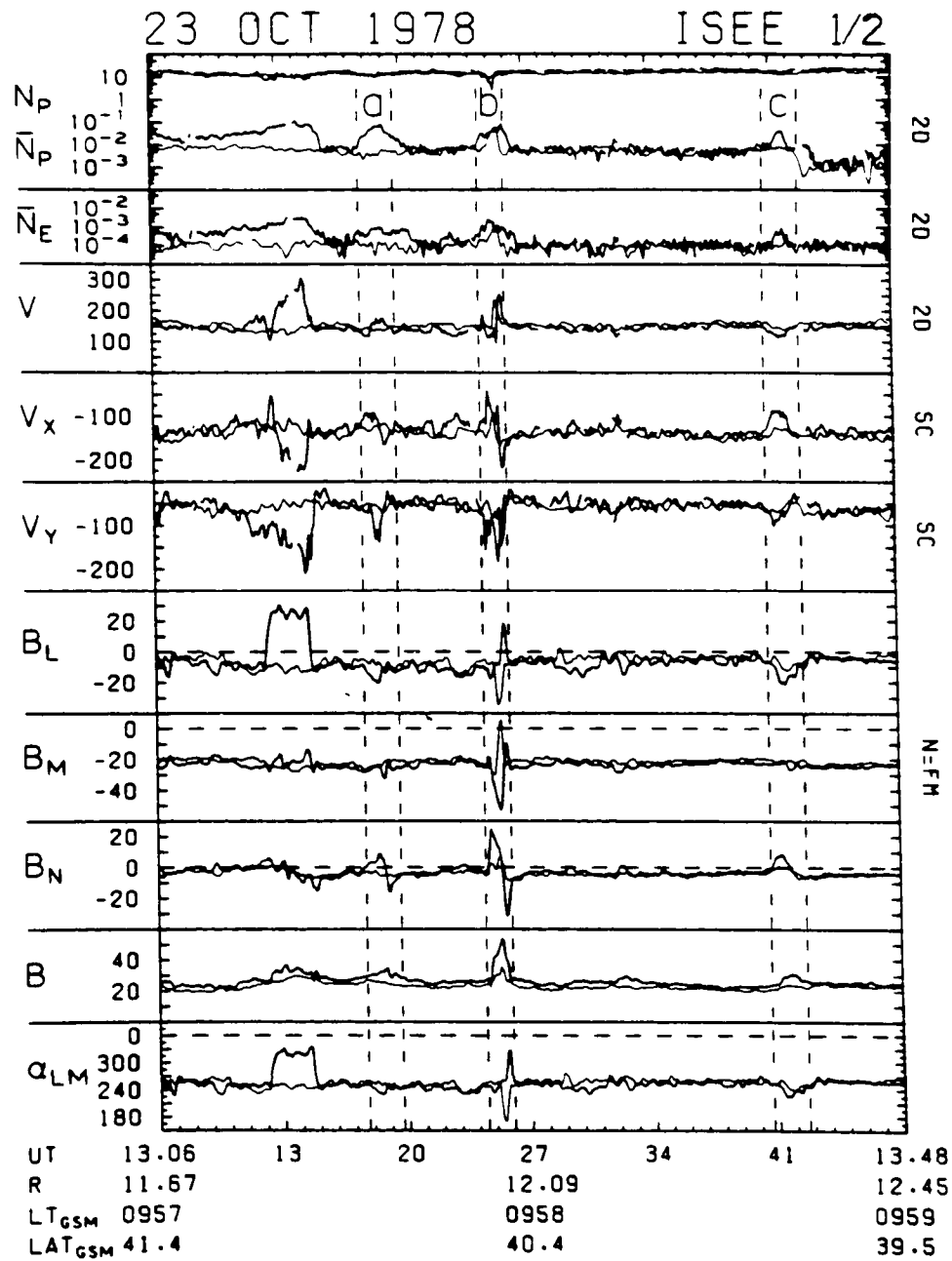


Figure 2.7 An example of magnetosheath FTEs observed by ISEE 1 and ISEE 2 [Saunders et al., 1984].

Figure 2.7 shows three magnetosheath FTEs labelled by (a), (b), and (c). During each FTE, indicated by the bi-polar signature in B_N , energetic particle density increases, while the total plasma density slightly decreases; plasma bulk flow velocity and magnetic field strength are enhanced. It is also observed that the magnetic field component and flow perturbations approximately satisfy the Walén relation [Walén, 1944]: $\Delta v = \pm \Delta v_A$, where $v_A = B/\sqrt{4\pi\rho}$ is the Alfvén speed.

In addition to magnetosheath FTEs, magnetospheric FTEs have also been observed inside the magnetopause [e.g., Daly and Keppler, 1982; Berchem and Russell, 1984; Rijnbeek et al., 1984, 1987; Farrugia et al., 1987, 1988]. Rijnbeek et al. [1984] showed that the magnetosheath FTEs and magnetospheric FTEs have similar recurrence times and similar scale sizes, and that the magnitude of the magnetospheric FTE B_N signatures is generally smaller than that of the magnetosheath FTEs. This indicates that the magnetosheath FTEs and magnetospheric FTEs are part of the same physical phenomenon at the dayside magnetopause. A summary of the observed properties of FTEs is listed below.

(1) FTEs have a strong correlation with the B_z component of the interplanetary magnetic fields (IMF). Large FTEs with a duration about 2 minutes are observed to occur repeatedly approximately every 10 minutes when the IMF has a southward B_z component.

(2) FTEs, which originate in low-latitude regions, are observed both inside and outside the magnetopause and in both the northern and southern hemispheres. Two-regime FTEs characterized by a simultaneous FTE signature both exterior and interior to the dayside magnetopause have been reported by Farrugia et al. [1987]. Simultaneous FTE signatures have also been observed at both northern and southern hemispheres [Elphic and Southwood, 1987].

(3) FTEs are distinguished by the bi-polar signature in the B_n component of the magnetic field and a strong guiding field, or core field, in the B_y component. Standard FTEs are FTEs with an outward followed by an inward (positive-negative) perturbation in the B_N component. Reverse FTEs are FTEs with an inward followed by an outward (negative-positive) perturbation in B_N component. However, irregular FTEs, with either a single inward (negative) or outward (positive) perturbation, or a more complex variation in the B_N component, have also been observed [Rijnbeek et al., 1984].

(4) Early observations show that during FTEs the magnetic field strength typically is enhanced [Russell and Elphic, 1979]. It was first pointed out by Rijnbeek et al. [1984] that the magnetic field strength during FTEs may decrease as well as increase. Crater-like FTEs with a magnetic field strength enhancement at the edges and a reduction at the center have been identified in the magnetospheric FTEs [LaBelle et al., 1987; Farrugia et al., 1988]. Penetrating deep into an FTE, satellites have also observed a magnetic cavity structure (magnetic hole) characterized by a simultaneous large decrease in the magnetic field strength and increase in plasma density with a nearly constant total pressure. [Lühr and Klöcker, 1987].

(5) Associated with FTEs, the electric field shows significant perturbations in the E_N and E_M components with an average magnitude of 3.5 mV/m, and the flux tubes move across the magnetopause plane at an average $\mathbf{E} \times \mathbf{B}$ speed of 125 km/s with respect to the ambient flow.

(6) Some dayside auroral activities are optical signatures of FTEs in the ionosphere, which are usually found at the equatorward edge of the polar cap [Cowley, 1984; Goertz et al., 1985; Sandholt et al., 1986; Lanzerotti et al., 1986; Freeman and Southwood, 1988; Lockwood et al., 1989]. The vortex-like plasma flows observed in the ionosphere associated with the field-aligned current system [e.g., Goertz et al.,

1985; Todd et al., 1986] are believed to be caused by the motion of magnetic flux tubes formed during FTEs [Southwood, 1985, 1987; McHenry and Clauer, 1987].

(7) Magnetospheric FTEs have a multilayered structure with distinct and systematic behavior in fields and charged particle populations: an outside draping field region, an inside twisting field region, and between them an intermediate boundary layer region.

(8) High-speed plasma flows and field-aligned particle heat fluxes are observed in the boundary layer region of FTEs, indicating particle acceleration and heating during the continued magnetic reconnection process. An enhancement in energetic particle densities is usually observed during magnetosheath FTEs, while a reduction in energetic particle densities is often observed during magnetospheric FTEs. Inside the FTEs, the total pressure, consisting of thermal and magnetic pressures, is usually higher than that outside the FTEs.

(9) For large FTEs, the area of the flux tube cross-section is typically $1 R_E^2$ and elongated in the L -direction of the boundary normal coordinate system, which is approximately the north-south direction in GSM. A moving deHoffmann-Teller (HT) frame of reference can be found for an FTE, in which the local plasma velocities are nearly antiparallel to the local \mathbf{B} vector and have magnitudes in the range 70% – 90% of the local nominal Alfvén speed [Papamastorakis et al., 1989].

(10) Twisted magnetic field lines are observed in the open flux tubes, indicating the presence of field-aligned currents J_{\parallel} . The field-aligned current produces the ground magnetic signatures of FTEs, e.g., unipolar and bipolar profiles of the vertical magnetic field [Goertz et al., 1985; McHenry and Clauer, 1987; Wei and Lee, 1990]. Statistical studies show a correlation between FTEs and transversely polarized Pc 4 pulsations with periods between 60 and 120s [Gillis et al., 1987]. FTEs may also contribute to certain Pc 5 magnetic variations [Lanzerotti and MacLennan,

1988]. The cusp region ultralow frequency (ULF) hydromagnetic waves associated with FTEs may be generated by the sporadic multiple X line reconnection process at the dayside magnetopause [Lee et al., 1988].

(11) Associated with FTEs, intense electrostatic and electromagnetic plasma waves are observed, ranging from below the ion gyrofrequency ($\sim 1\text{Hz}$) to above the electron plasma frequency ($\sim 50\text{kHz}$). For waves associated with FTEs, the power spectrum of electric field fluctuation is proportional to f^{-2} , and the power spectrum of magnetic field is proportional to $f^{-\alpha}$, where α is between 3.3 and 4.7.

Various observational features associated with FTEs have fascinated many researchers and attracted the attention of the solar-terrestrial space physics community. Since the discovery of FTEs at the dayside magnetopause, theoretical models for the magnetic reconnection process have undergone a significant change: from steady-state to time-dependent reconnection models [Lee, 1988]. It is now widely accepted that dayside magnetic reconnection is basically an intermittent process, even though the detailed picture of the time-dependent reconnection process remains a controversial issue, and hence an active research topic.

To explain the intermittent nature of the dayside magnetic reconnection process associated with FTEs, a number of theoretical models have been proposed. These include: (1) the elbow-shaped flux tube model [Russell and Elphic, 1978, 1979], (2) the cusp region reconnection model [Podgorny et al., 1980], (3) the tearing hole model [Sonnerup, 1984], (4) the multiple X line reconnection model [Lee and Fu, 1985], (5) the split separator line merging model [Crooker, 1985], (6) the stochastic percolation model [Galeev et al., 1986], (7) the bursty single X line reconnection model [Scholer, 1988; Southwood et al., 1988], (8) the three-dimensional tearing model [Kan, 1988], (9) the vortex induced tearing model [Liu and Hu, 1988],

(10) the turbulent reconnection model [Song and Lysak, 1989], and (11) the three-dimensional general magnetic reconnection model [Hesse et al., 1989]. Note that all the theoretical FTE models listed above are related to the magnetic reconnection process at the dayside magnetopause.

The first morphological FTE model, the elbow-shaped flux tube model of Russell and Elphic [1978, 1979] (Figure 2.8), proposes that the relaxation of the bent, elbow-shaped flux tubes intermittently formed during the patchy reconnection at the dayside magnetopause results in the observed features of FTEs. Although this model successfully explained the FTE signatures, the question of how the reconnection process leads to the intermittent formation of such flux tubes remains unsolved.

To explain the intermittent formation of the elbow-shaped flux tubes, Sonnerup [1984] proposed a tearing hole model for FTEs. In this model, the nonlinear development of the tearing mode instability at the dayside magnetopause results in patchy and intermittent reconnection, which in turn leads to the formation of elbow-shaped flux tube pairs in both the northern and southern hemispheres. The pair of elbow-shaped flux tubes form a hole structure at the dayside magnetopause. This model implies that reconnection might occur at multiple sites during the formation of the flux tube pair. Sonnerup also speculated that a threshold, other than the southward IMF B_z , might control the onset of patchy and intermittent reconnection and that under certain circumstances, quasi-steady reconnection could also be established at the dayside magnetopause.

Considering the coupling of the solar wind and the earth's magnetosphere as a driven process in which the interaction between solar wind and the magnetosphere leads to the intermittent reconnection at the dayside magnetopause, Lee and Fu [1985] proposed a multiple X line (MXR) reconnection model for FTEs. The most

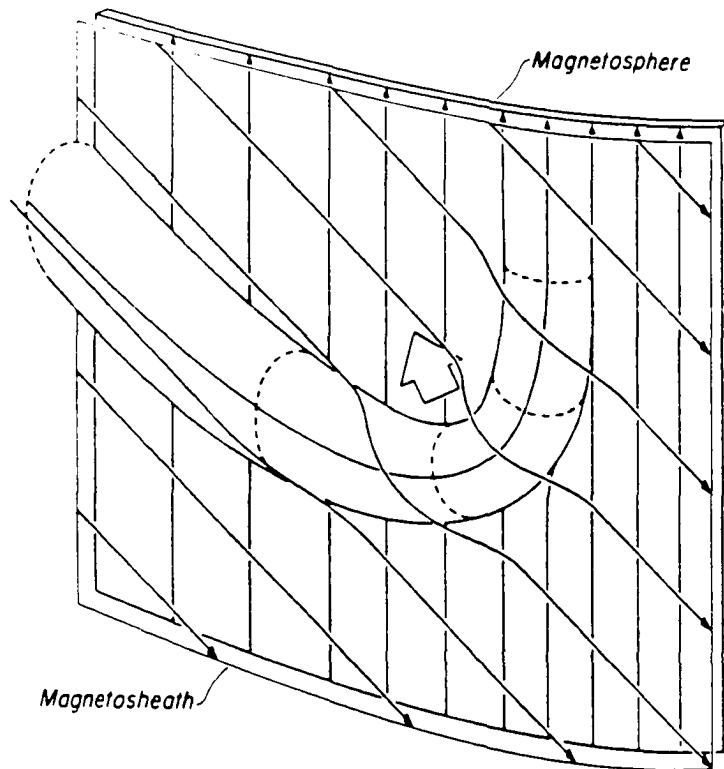


Figure 2.8 The elbow-shaped flux tube FTE model [Russell and Elphic, 1978, 1979].

important and distinguishable feature of Lee and Fu's MXR model is that the interplanetary magnetic fields (IMF) reconnect with the geomagnetic fields along several reconnection lines (X lines). Figure 2.9 is a perspective picture of the MXR model at the dayside magnetopause. In this model, the FTE signatures are generated by the convection of the magnetic flux tubes that are intermittently formed during the MXR process. The MXR process tends to occur in a system with a characteristic length (L) much larger than the characteristic thickness (l) of the current sheet. As demonstrated in the simulations [Fu and Lee, 1985, 1986; Lee and Fu, 1986; Ding et al., 1986; Shi et al., 1988], the multiple X line reconnection takes place in a highly nonlinear driven system so that the MXR process is intrinsically time-dependent. Like Sonnerup's tearing hole model, Lee-Fu's MXR model also seems to have a threshold that controls the onset and subsidence of the MXR process. Lee and Fu suggested that the threshold might be closely related to the nonlinear saturation of the tearing mode instabilities at the dayside magnetopause.

Magnetic reconnection at multiple sites was observed by Dubinin et al. [1980] and Podgorny et al. [1980] in their laboratory plasma experiments, which investigated the interaction between a supersonic or super-Alfvénic collisionless plasma flow and a magnetic dipole. These experiments showed that for a southward IMF B_z , both single X line reconnection and multiple X line reconnection may occur at the dayside magnetopause. When the solar wind Alfvén Mach number is small ($M_A \sim 1$), a single X line is formed at the low-latitude subsolar region of the magnetopause; when the solar wind Alfvén Mach number is large ($M_A \sim 10$), two X lines are formed at the high-latitude polar cleft regions and a huge O line, also called magnetic curl, is formed at the front nose of the dayside magnetopause. Inside the magnetic curl, several small magnetic islands are present due to the tearing mode instability. However, the open field lines associated with the magnetic curl

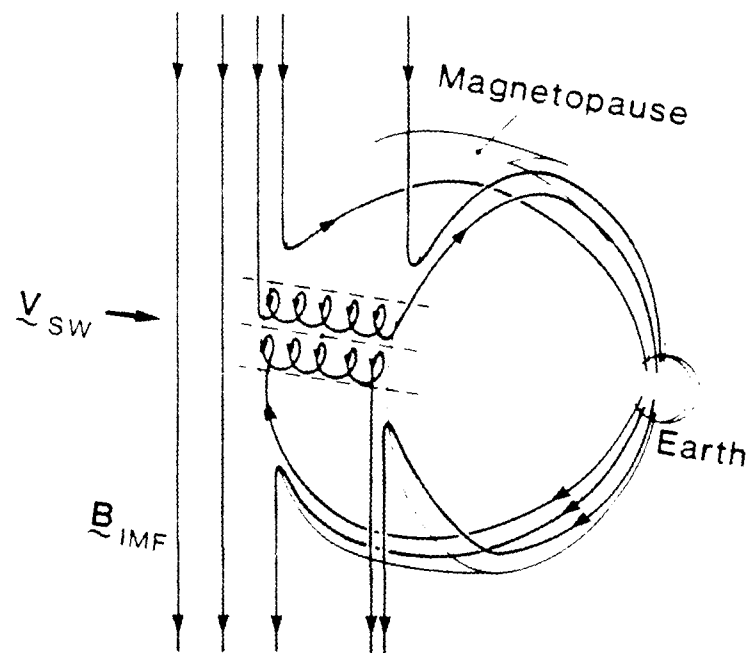


Figure 2.9 The multiple X line reconnection model [Lee and Fu, 1985].

are dragged by the solar wind in the equatorial direction. Therefore, the topology of magnetic field lines in Podgorny et al. [1980] is very different from that proposed by Lee and Fu [1985], since in the Lee-Fu model the multiple X line reconnection is allowed to occur near the subsolar point of the dayside magnetopause and the poleward convection of magnetic islands leads to the observed B_n signature of FTEs.

To obtain a unified picture that can explain both the subsolar region reconnection and the cusp region reconnection, Crooker [1985] proposed a split separator line merging model for the dayside magnetopause. In this model, the dayside magnetic field configuration is determined by the superposition of three magnetic field components that include (1) the geomagnetic dipole field, (2) the magnetic field caused by the Chapman-Ferraro current, and (3) the interplanetary magnetic field (IMF). Depending on the orientation and the magnitude of the IMF, one can obtain both multiple X line reconnection at either the subsolar region or the cusp region, and single X line reconnection at the subsolar region. In Crooker's model, the reconnection takes place at multiple merging lines. Reconnection with classical single X line geometry occurs at the outer merging lines, producing accelerated boundary layer flows. Reconnection in the subsolar region, between the separator lines, leads to the formation of magnetic islands, producing the signatures of FTEs. However, Crooker's model is mainly a topological one without any information about the dynamics, except the predicted location of accelerated boundary flow layers.

Galeev et al. [1986] pointed out that the magnetic surface at the dayside magnetopause could be destroyed by the growth and overlapping of magnetic islands. The stochastic meandering of magnetic field lines between the destroyed surfaces would result in the magnetic percolation, i.e. the appearance of a topological connection of interplanetary and geomagnetic field lines. Galeev et al. suggested that

a percolation process of this kind might lead to the patchy reconnection at the dayside magnetopause, and hence the signatures of FTEs.

To explain the intermittence of dayside reconnection, Sonnerup [1984] and Lee [1986] suggested the existence of a threshold that controls its onset and subsidence. A detailed mechanism for such a threshold was proposed in the magnetic percolation model by Galeev et al. [1986]. Based on the coupling of the drift-tearing mode to the ion-acoustic waves, Galeev et al. obtained a saturation mechanism for the magnetic percolation process: the ion-acoustic waves carry away the wave energy from the interaction region, thereby leading to the nonlinear saturation of the tearing mode inside the magnetopause current sheet, and hence, the interruption of the percolation process. However, in this model, the most favourable condition for the percolation process to occur is a magnetic field rotation of about $\theta_B = 70^\circ$ within the magnetopause, where θ_B is the angle between the magnetic fields in the magnetosheath and magnetosphere. This seems to be inconsistent with the satellite observations that FTEs occur when the IMF has a large negative B_z component, i.e. the magnetic field rotates about $\theta_B = 180^\circ$ within the magnetopause.

Recently, several authors argued that the FTE signatures may also be produced by a bursty reconnection process occurring at a single reconnection line at the dayside magnetopause [Scholer, 1988; Southwood et al., 1988]. The bursty single X reconnection (SXR) process can be caused by an enhancement and a subsequent reduction of the reconnection rate at the reconnection region. Figure 2.10 shows a schematic sketch of the bursty single X line reconnection (SXR) model, in which the bursty reconnection process leads to the formation of magnetic bulges at the dayside magnetopause. A magnetic bulge formed at the low-latitude region propagating to the high-latitude region produces magnetic perturbations and energetic particle features similar to that of FTEs. In the bursty SXR model, all of the reconnected

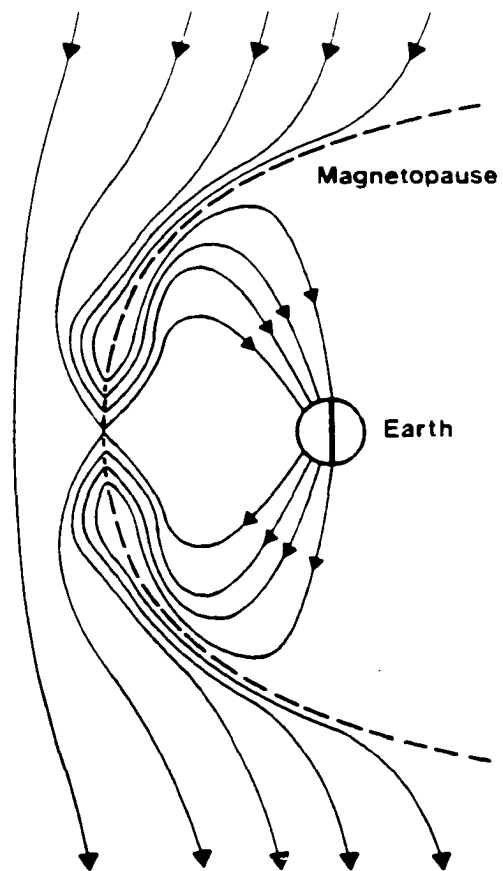


Figure 2.10 A schematic drawing of the bursty single X line reconnection model.

magnetic field lines are open field lines, a loop-like structure is produced, and no magnetic flux tubes are formed. Therefore, the footprints on the ionosphere produced by the bursty SXR are expected to be much different than those generated by the magnetic flux tubes. On the other hand, the physical mechanism that controls the bursty nature of the bursty SXR process has not been clearly identified.

Based on the argument of three-dimensional tearing of the magnetopause current sheet and three-dimensional component reconnection on the dayside magnetopause driven by the solar wind, Kan [1988] proposed a patchy and intermittent reconnection model for FTEs. In Kan's three-dimensional tearing (3DT) model, the patchiness of FTEs is caused by the structure of the three-dimensional tearing on the dayside magnetopause. The intermittent nature of the FTEs is externally controlled by the fluctuation of IMF and internally modified by the ionospheric line-tying effect. For the 3DT model, both single X line reconnection, bursty or quasi-steady, and multiple X line reconnection may take place.

At the dayside magnetopause, sheared velocity and magnetic fields have been observed. The Kelvin-Helmholtz instability may be excited due to the presence of the sheared plasma flows [e.g., Southwood, 1968; Miura, 1984; Wu, 1986]. Large scale fluid vortices may be formed because of the development of the Kelvin-Helmholtz instability. Considering such a response of magnetic field lines to the fluid vortices, Liu and Hu [1988] proposed a vortex-induced patchy reconnection model for the formation of FTEs. In this model, FTE signatures are produced by helical magnetic vortex tubes formed during the vortex-induced reconnection process that may occur at both the low-latitude region and the cusp region of the dayside magnetopause when the IMF has a large southward B_z .

Based on their study of the changing of magnetic helicities during magnetic reconnection, Song and Lysak [1989] suggested that three-dimensional magnetic

reconnection was a self-organized evolution process of a nonequilibrium dissipative system. During magnetic reconnection, the internal and external magnetic helicities are redistributed, although the total helicity is nearly conserved. A dynamo effect is introduced by a turbulent electric field that is produced by the helicity conversion. Applying their theory to the dayside magnetopause, Song and Lysak proposed a multiple-site turbulent reconnection model for FTEs. During the turbulent reconnection, fluctuating velocity and magnetic fields cause an average nonzero electric field, leading to the formation of many small twisted flux tubes. Then, the self-organization of the small twisted tubes results in a coalescence process and hence the formation of large twisted FTE flux tubes. In the Song-Lysak model, the twisted FTE flux tubes represent a mixed state with minimum energy and maximum cross helicity during the three-dimensional magnetic reconnection.

Recently, three-dimensional magnetic reconnection has attracted more and more attention in the theoretical study of reconnection process [e.g., Greene, 1988; Schindler et al., 1988; Hesse and Schindler, 1988; Fu, 1989; Fu et al., 1990]. After examining the three-dimensional topological structure of magnetic field lines in a model magnetosphere, Hesse et al., [1989] proposed a magnetic flux knot model for FTEs. They showed that a localized perturbation at the magnetopause can open a closed magnetosphere, leading to magnetic connection across the magnetopause and the formation of FTE magnetic flux tubes. However, the three-dimensional magnetic reconnection topology is different from the traditional viewpoint: the linkage of magnetic flux tubes results in the formation of a magnetic flux knot without the presence of any neutral points; and a complicated filamentary substructure of magnetic field lines is present with a decrease of magnetic shear at the magnetopause. One feature of the magnetic flux knot model is the simultaneous presence of ionospheric signatures of the same single FTE flux rope in both the southern and

and northern hemisphere, because the flux rope is connected to both hemispheres at the same time.

Many observational features associated with FTEs are summarized in this section. Various theoretical FTE models have also been reviewed. Magnetic reconnection and formation of FTEs at the dayside magnetopause are complicated. The theoretical models discussed above provide many possible explanations for dayside reconnection and FTEs. Computer simulation provides a powerful and useful tool for examining the feasibility of these theoretical models for magnetic reconnection and FTEs at the dayside magnetopause. Both MHD simulations and particle simulations have been carried out to study dayside magnetic reconnection processes and FTEs. Computer modeling of magnetic reconnection and FTEs at the dayside magnetopause is discussed in the next section.

2.3 Necessity of Particle Simulation for Magnetic Field Reconnection Study

With the development of large-scale, high-speed computer technology, computer modeling has been widely used in many research areas. Computer simulation provides a unique tool to bridge the gap between theoretical and experimental researches. Theoretical analysis, experimental observation, and computer modeling today have become three inseparable parts of scientific research. Computer simulation studies of the dayside magnetic reconnection process and FTEs have been carried out by many researchers. These studies include both MHD simulations and particle simulations.

The first two-dimensional (2-D) MHD simulation of FTEs, namely the simulation of multiple X line reconnection, was reported by Fu and Lee [1985]. Later, a

series of simulations were performed to study the intermittent MXR process based on a 2-dimensional slab model [Lee and Fu, 1986; Fu and Lee, 1986]. Both steady-state SXR and time-dependent MXR were observed. The results show that when the simulation system is long and resistivity is small, intermittent reconnection occurs at multiple sites, leading to the repeated formation of magnetic islands; otherwise, steady-state single X line reconnection take place as the system length is reduced. Lee and Fu [1986] and Fu and Lee [1986] demonstrated that for a given current sheet thickness the steady-state single X line reconnection magnetic field configurations of the Sweet-Parker model [Sweet, 1958; Parker, 1957], the Sonnerup model [Sonnerup, 1970], and the Petschek model [Petschek, 1964] can be obtained, depending on the length of the current sheet.

The simulations of Fu and Lee [1985, 1986] and Lee and Fu [1986] were based on the 2-D slab model with limited system lengths, imitating the reconnection process at the subsolar region of the dayside magnetopause. To study the dayside reconnection on a global scale, Shi et al. [1988] simulated the interaction between the interplanetary magnetic field and the earth's geomagnetic field at the dayside magnetopause when the IMF has a southward B_z component with a 2-D global MHD code. They found that when the magnetic Reynolds number (R_m) is small, the SXR process takes place; when R_m is large, MXR occurs. They also found that when the solar wind Mach number (M_A) is small, dayside reconnection takes place in the low-latitude region; when M_A is large, reconnection occurs at the high-latitude region. These results are consistent with the laboratory experiment of the dayside reconnection [Dubinin et al., 1980; Podgorny et al., 1980].

2-D MHD simulations of FTEs were also performed by Scholer [1989a, 1989b], who simulated the bursty single X line reconnection process with both symmetric and asymmetric magnetic configurations. Note that in a symmetric magnetic field

configuration, the antiparallel magnetic fields on the two sides of the current sheet have the same magnitude. The simulation results indicate that magnetic bulges can indeed be formed as a result of the bursty reconnection process. The simulation results also show that when the magnetic field is symmetric, magnetic bulges can be formed on both sides of the current sheet; when the magnetic field is asymmetric, the magnetic bulge can only be formed on the side with a weaker magnetic field, i.e., the magnetosheath.

The magnetic reconnection process in the real world is a three-dimensional phenomenon. Although the 2-D simulations have revealed many important features of the reconnection process, the lack of the third dimension definitely limits our understanding of magnetic reconnection in the 3-D environment. As large scale supercomputers became available, three-dimensional computer simulations of the FTEs at the dayside magnetopause were also carried out.

The first 3-D MHD simulation of the formation of FTEs was reported by Sato et al. [1986]. The simulation of the interaction between the solar wind, which has a southward IMF B_z component, and the earth's magnetosphere is based on a semi-global simulation model. They found that twisted magnetic flux tubes are formed as a result of repeated reconnection between the IMF and the geomagnetic field near the equatorial plane and that these flux tubes subsequently propagate to higher latitudes. The flux tube structure observed in the simulation is similar in many respect to the FTEs observed at the dayside magnetopause. Their 3-D simulation result basically confirmed the multiple X line reconnection model proposed by Lee and Fu [1985].

Another global 3-D MHD simulation of FTEs was carried out by Ogino et al. [1989]. They found that when R_m is high, the reconnection is intermittent and twisted flux tubes can be formed. The formation of flux tubes is closely associated

with the orientation of the interplanetary magnetic field. A strongly twisted and localized flux tube is formed when the IMF has a strong B_y component, whereas twin flux tubes are formed when the IMF has a small B_y component. Both of the flux tubes show characteristics similar to that observed during the FTEs. However, the magnetic flux tube is twisted due to the high viscosity used in their simulation.

Recently, Fu [1989] and Fu et al. [1990] simulated the MXR process based on a 3-D MHD model. The simulation is conducted in a local rectangular box. Under the driven boundary conditions, through which a constant plasma flow and a magnetic inflow flux are imposed, the MXR process is triggered self-consistently without using a localized resistivity enhancement. In the presence of a finite B_y , helical magnetic flux tubes can be formed as a consequence of the MXR process. At the ends of a helical flux tube, a complicated topological feature of the magnetic field lines is revealed. During the MXR process, tube-aligned plasma flows are observed inside the helical magnetic flux tubes. The simulation also showed that the magnetic flux ropes formed during the 3-D reconnection have frayed ends.

By using MHD simulation methods, the reconnection process can be imitated on a macroscopic scale. Large-scale changes of magnetic field topology, electric current distribution, plasma density, plasma flow, and plasma pressure during the reconnection process can be examined with MHD simulations. However, in MHD simulations the value of anomalous resistivity and its variations in time and space, which are crucial for the reconnection process, have to be arbitrarily assumed. For example, in Fu and Lee [1985, 1986] and Lee and Fu [1986], a uniform and constant resistivity profile was used. In Scholer [1989a, 1989b], a localized and time-dependent resistivity model was used. Other resistivity models, such as the current-enhanced resistivity model and the temperature-enhanced resistivity model were also used in the simulations [Ugai, 1983, 1984; Ogino et al., 1989]. However,

the assumed value of the anomalous resistivity, as well as its temporal and spatial distributions, may not be a realistic representation of collisionless magnetospheric plasmas.

In addition to MHD simulations, particle simulations have also been carried out to study the magnetic reconnection process and FTEs at the dayside magnetopause. One of the advantages of particle simulations of magnetic reconnection is that the anomalous resistivity can be naturally generated by particle inertia or by wave-particle interaction. Temporal and spatial variations of the resistivity therefore can be self-consistently determined during the simulation. Although MHD simulations have been successfully used to study the macroscopic properties of the reconnection process, particle simulations are more suitable for examining the microscopic features of the reconnection processes, such as particle acceleration and heating, the particle energy spectrum, particle distributions in the phase space, and nonlinear wave particle interactions. Therefore, particle simulation of magnetic reconnection is of basic importance to the study of the magnetic reconnection process at the dayside magnetopause and in the nightside magnetotail [e.g., Terasawa, 1981; Leboeuf et al., 1982; Swift, 1982, 1983, 1986; Ambrosiano et al., 1983, 1986; Ding et al., 1986; Hoshino, 1987; Lee and Ding, 1987; Swift and Allen, 1987; Hewett et al., 1988; Francis et al., 1989; Allen and Swift, 1989; Ding and Lee, 1990].

The reconnection process in a collisionless plasma is believed to be closely associated with collisionless tearing mode instabilities. Particle simulations of collisionless tearing mode instabilities contribute significantly to our understanding of the collisionless reconnection process. Terasawa [1981] investigated the collisionless tearing mode instability with one-component (ion) particle simulations and found that the simulation results, in which an explosive phase of the nonlinear tearing mode instability was observed, were consistent with analytical theories. Leboeuf

et al. [1982] studied the plasma dynamic process associated with the time-varying magnetic X points. They observed that the electrostatic field and the finite Larmor radius effects play an important role in the development of tearing mode instabilities and that hot tails are formed in the particle distribution functions during the magnetic island coalescence. The effects of a background plasma on the tearing mode instability was examined by Ambrosiano et al. [1983]. In Ambrosiano et al. [1986], it was found that the temperature anisotropy with $T_{\perp} > T_{\parallel}$ can enhance significantly the tearing instability.

Particle simulations of the dayside magnetic reconnection were also performed by Swift [1986], Hoshino [1987], and Allen and Swift [1989]. Swift [1986] and Hoshino [1987] examined the electrostatic effect on the collisionless tearing mode instability and found that the electrostatic interaction could modify the tearing growth rate. The electrostatic effect increases the tearing mode growth rate at the dayside magnetopause where the magnetic field is not antiparallel, while it decreases the tearing growth rate in the magnetotail where the magnetic field is antiparallel. Allen and Swift [1989] studied the collisionless tearing mode under conditions characteristic of the dayside magnetopause, in which the magnetic field configuration is asymmetric about the magnetopause and has a magnetic shear. They have found that the tearing growth rate is a sensitive function of θ_B , the angle between magnetic field vectors on two sides of the magnetopause and that the largest growth rate corresponds to the magnetic configuration with $\theta_B = 180^\circ$. A particle simulation study of plasma waves and particle heat fluxes associated with magnetic reconnections at the dayside magnetopause has also been carried out by Ding and Lee [1990].

In the above simulations [e.g., Leboeuf et al., 1982; Swift, 1986; Hoshino, 1987; Allen and Swift, 1989; Ding and Lee, 1990], an artificially small mass ratio

of ions to electrons ($m_i/m_e = 10 \sim 25$) was used to save computing resources and to satisfy the numerical stability requirement. Recently, particle simulation of magnetic reconnection with a realistic mass ratio of ions to electrons (m_i/m_e up to 2000) has been reported by Hewett et al. [1988] and Francis et al. [1989]. They investigated collisionless magnetic reconnection by using an implicit particle in cell (PIC) code. For large ion-electron mass ratios ($m_i/m_e > 200$), electrostatic ringing was observed in the simulation, in which electrons jetting into the magnetic O lines built up an ambipolar potential that in turn drove electrons back out of the magnetic islands. Their simulation also confirmed previous results [e.g., Allen and Swift, 1989] that the inclusion of a guiding magnetic field (magnetic shear) severely reduced the tearing mode growth rate, slowing down the initial stage of the magnetic reconnection. If the magnetic shear is large enough, the electrostatic ringing also may be totally damped out.

Although previous particle simulations of tearing mode instabilities and dayside magnetic reconnections have provided much useful information about collisionless magnetic reconnection, the periodic boundary conditions imposed in the simulations limit the long term nonlinear evolution of the magnetic islands formed during the simulations. Because of the periodic boundary conditions, the simulations would end up in an asymptotic quasi-steady configuration. Since the observations of FTEs show that the dayside reconnection is intrinsically an intermittent process, the periodic boundary conditions seem to be inappropriate for simulating the intermittent reconnection process.

Furthermore, to simulate the driven reconnection process in the collisionless magnetospheric plasma environment, a driven boundary is needed to imitate the incoming plasma and an open boundary is essential to allow the plasma to convect

out of the simulation domain. Therefore, an important part of present thesis research was the development of a particle simulation model in which both driven and open boundaries were included to simulate the driven reconnection process in the collisionless plasma. Using this particle simulation model, a series of simulations were carried out to investigate the properties associated with the driven reconnection process at the dayside magnetopause, such as the MXR and SXR processes, the generation of energetic particles and particle heat fluxes, and the characteristics of the plasma waves observed during the simulations. The simulation results are compared with FTEs observed at the dayside magnetopause.

2.4 Summary

During the past four decades, magnetic field reconnection has been applied to explain solar flares, magnetospheric substorms, flux transfer events, and other space and laboratory plasma processes. In this chapter, a historical review of magnetic reconnection and flux transfer events is presented. Both MHD reconnection models and collisionless reconnection models are discussed. Magnetic reconnection is one of the important hypotheses for the interaction between the solar wind and the earth's magnetosphere. Since the discovery of flux transfer events, magnetic reconnection has become a well-accepted mechanism at the dayside magnetopause for the transfer of solar wind mass, momentum, and energy into the magnetosphere. Satellite observations at the dayside magnetopause show that FTEs have many distinct plasma and electromagnetic field signatures. A summary of the observed FTE features is presented. Many theoretical models have been proposed to account for the occurrences and characteristics of FTEs. Since FTEs mainly occur during the period when the interplanetary magnetic field has a southward B_z component,

magnetic reconnection models of FTEs are favored. Eleven of them are discussed here. Computer simulation has provided a unique tool for modeling the dayside reconnection process and FTEs. Both MHD simulations and particle simulations of the dayside magnetic reconnection and flux transfer events are briefly reviewed. The advantages of particle simulations over MHD simulations are discussed.

Single X line reconnection and multiple X line reconnection present one of the major controversies for explaining the dayside reconnection process. Results of laboratory experiments and computer simulations indicate that single X line reconnection takes place in the subsolar region of the dayside magnetopause when the solar wind Mach number is small, whereas multiple X line reconnection occurs at the high-latitude region when the solar wind Mach number is large. It is also demonstrated that single X line reconnection takes place when the magnetic Reynolds number is small, while multiple X line reconnection occurs when the magnetic Reynolds number is large. However, as pointed out in Ding et al. [1990], single X line reconnection can be considered as one of the two extremes of the multiple X line reconnection process, in which the reconnection rate at one end of a magnetic island is dominantly larger than at another end of the magnetic island. Another extreme case of the multiple X line reconnection is where the reconnection rates at both ends of a magnetic island are equal. Generally, the reconnection rates at the two ends of a magnetic island are different.

Since magnetic field reconnection is closely related to tearing mode instabilities, a review of the linear theories of collisional and collisionless tearing mode instabilities is presented in the next chapter. Satellite observations show that more high-speed plasma flows are detected when the ratio of plasma pressure to magnetic pressure in the magnetosheath (β_s) is small, indicating that the dayside magnetic reconnection may occur preferentially for a small β_s [Paschmann et al., 1986]. This

phenomenon may be indirectly related to the tearing mode instabilities. Therefore, a survey of the β -dependence of tearing mode instabilities at the dayside magnetopause is also carried out in the next chapter.

Chapter 3 Collisional and Collisionless Tearing Mode Instabilities

As mentioned in the previous chapters, magnetic reconnection plays an important role in the interaction between the solar wind and the magnetosphere. However, the causal mechanism for magnetic reconnection has not been discussed yet. At present, it is widely believed that the magnetic reconnection process is triggered by a tearing mode instability. The tearing mode instability occurs when a finite resistivity exists in a field reversal region, leading to disruption of the magnetic surfaces, filamentation of the current sheet, and the formation of magnetic islands. If the tearing mode instability is allowed to grow, its nonlinear development results in large-scale magnetic reconnection.

As an example, the change of magnetic field configuration caused by the development of the tearing mode instability is schematically drawn in Figure 3.1. Figure 3.1a shows the unperturbed neutral sheet magnetic field configuration at $t = 0$, while Figure 3.1b shows the perturbed magnetic field configuration in the presence of the tearing mode perturbation at $t > 0$. It can be seen from Figure 3.1 that during the development of the tearing mode instability, the previously uniform current sheet is broken into filaments and magnetic islands are formed.

Finite resistivity plays an important role in the development of the tearing mode instability. According to the different mechanisms through which finite resistivity is generated, tearing mode instabilities can be divided into two categories: the collisional tearing mode instability and the collisionless tearing mode instability. For the collisional tearing mode instability, also called the resistive tearing mode

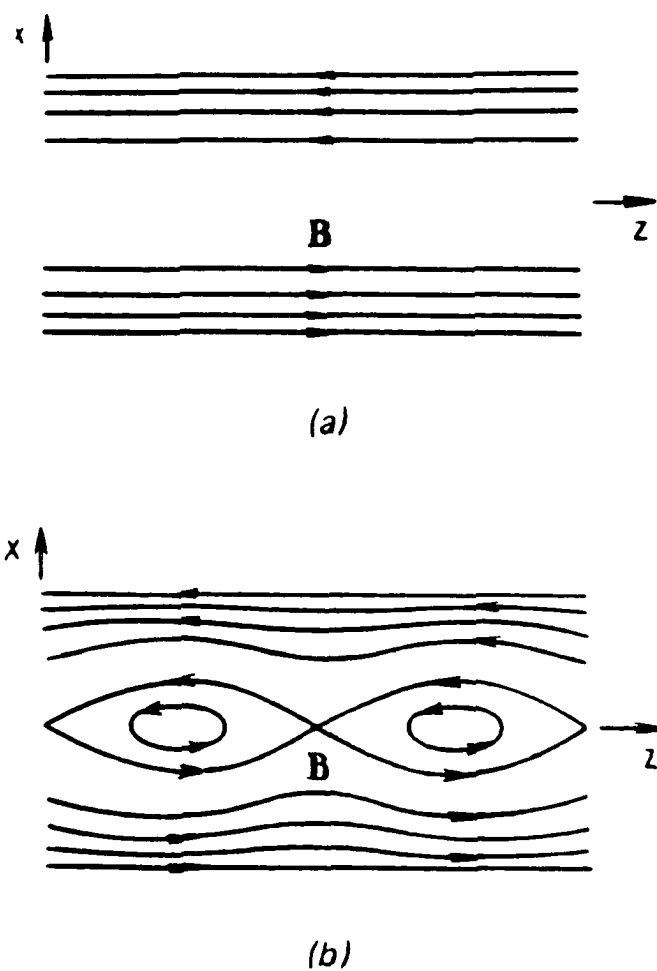


Figure 3.1 Change of magnetic field configuration caused by the development of the tearing mode instability, (a) unperturbed neutral sheet magnetic field configuration at $t = 0$, and (b) magnetic field configuration perturbed by the tearing mode instability at $t > 0$.

instability, the finite resistivity is generated by Coulomb collisions between particles, particularly between electrons and ions. For the collisionless tearing mode instability, the finite resistivity is caused by other mechanisms.

In fusion plasmas as well as space plasmas, when the plasma density becomes so low that the mean free path of electrons becomes much larger than the characteristic system length and the classical resistivity due to the Coulomb collisions becomes very small, the plasma becomes collisionless. In a collisionless plasma, the finite resistivity for the collisionless tearing mode instability may be generated due to electron inertia, pressure gradients, Hall effect, or any other terms in the generalized Ohm's law equation that are not related to the Coulomb collisions. The finite resistivity can also be generated by wave particle resonance mechanisms through inverse Landau damping in the current sheet region. Here, a brief review of collisional and collisionless tearing mode instabilities is presented and growth rates of collisional and collisionless tearing mode instabilities will be derived. Analysis of the collisional tearing mode instability is based on the MHD equations, while analysis of the collisionless tearing mode instability is based on Maxwell-Vlasov equations.

At the dayside magnetopause, the magnetospheric field is generally larger than the magnetosheath field. The magnetospheric plasma usually has a higher temperature and lower density than the magnetosheath plasma. Thus the ratio of plasma pressure to magnetic pressure changes significantly from the magnetosheath to the magnetosphere. The typical value for the ratio of plasma pressure to magnetic pressure in the magnetosphere (β_m) is $0.1 \sim 0.3$, whereas the value for the ratio of plasma pressure to magnetic pressure in the magnetosheath (β_s) can be as large as 10. Recent satellite observations at the dayside magnetopause indicate that the magnetic reconnection process may occur preferentially when the ratio of plasma

pressure to magnetic pressure in the magnetosheath has a small value ($\beta_s < 2$) [Paschmann et al., 1986]. This observational feature can be related to the development of the tearing mode instability in the asymmetric dayside magnetopause current sheet. In an attempt to explain the above observation, a study of the β -dependence of the tearing mode instability is also included in this chapter.

3.1 Linear Theory of the Collisional Tearing Mode Instability

The tearing mode instability is a long-wavelength and low-frequency, macroscopic electromagnetic instability whose source of energy is the magnetic field. It develops in a limited region where $\mathbf{k} \cdot \mathbf{B}$ is small (\mathbf{k} is the wave number vector and \mathbf{B} is the magnetic field), and finite resistivity plays an important role. Plasma diffusion then takes place across the magnetic field. The diffusion makes the plasma break up into filaments, a process which releases magnetic energy.

In an ideal MHD plasma, the plasma is frozen to the magnetic field lines [Alfvén, 1963]. Thus most instabilities involve motion of magnetic field and plasma together, and the characteristic time scale for the motion is the Alfvén time $t_A = L/v_A$, where L is the characteristic length scale and v_A is the Alfvén speed. However, in a nonideal MHD plasma, where resistivity (η) is present, the plasma can diffuse across magnetic field lines. The resistive instabilities in the nonideal plasma develop at a characteristic time scale that is a hybrid combination of the Alfvén time t_A and the diffusion time $t_d = 4\pi L^2/c^2\eta$, where c is the speed of light. Therefore, it is generally assumed that $1/t_d \ll \gamma \ll 1/t_A$, where γ is the growth rate of the resistive instabilities. The resistive instabilities were first systematically studied by Furth et al. [1963] and the tearing mode was one of the resistive instabilities they

found in their study. In the following, the growth rate for the collisional tearing mode is derived based on the linear MHD theory.

The basic equations used in the derivation are

$$\frac{\partial \rho}{\partial t} + \nabla \cdot (\rho \mathbf{u}) = 0 \quad (3.1)$$

$$\rho \frac{d\mathbf{u}}{dt} = -\nabla p + \frac{1}{c} \mathbf{J} \times \mathbf{B} \quad (3.2)$$

$$\nabla \times \mathbf{E} = -\frac{1}{c} \frac{\partial \mathbf{B}}{\partial t} \quad (3.3)$$

$$\mathbf{E} + \frac{1}{c} \mathbf{u} \times \mathbf{B} = \eta \mathbf{J} \quad (3.4)$$

$$\nabla \times \mathbf{B} = \frac{4\pi}{c} \mathbf{J} \quad (3.5)$$

$$p = p(\rho) \quad (3.6)$$

where ρ is the plasma mass density, \mathbf{u} is the plasma flow velocity, p is the plasma pressure, \mathbf{J} is the current density, \mathbf{E} is the electric field, c is the speed of light, and $d/dt = \partial/\partial t + \mathbf{u} \cdot \nabla$ is the convective derivative. With the assumption of an incompressible plasma, i.e., $\nabla \cdot \mathbf{u} = 0$, and after some straightforward algebra, the above equations are reduced to

$$\frac{\partial \rho}{\partial t} + \mathbf{u} \cdot \nabla \rho = 0 \quad (3.7)$$

$$\nabla \times (\rho \frac{d\mathbf{u}}{dt}) = \frac{1}{4\pi} \nabla \times [(\mathbf{B} \cdot \nabla) \mathbf{B}] \quad (3.8)$$

$$\frac{\partial \mathbf{B}}{\partial t} = \nabla \times (\mathbf{u} \times \mathbf{B}) + \frac{c^2 \eta}{4\pi} \nabla^2 \mathbf{B} \quad (3.9)$$

The above equations can be linearized under the assumption that $\rho = \rho_0(\mathbf{x}) + \rho_1(\mathbf{x}) \exp[i(k_y y + k_z z) + \gamma t]$, $\mathbf{B} = \mathbf{B}_0(\mathbf{x}) + \mathbf{B}_1(\mathbf{x}) \exp[i(k_y y + k_z z) + \gamma t]$, and $\mathbf{u} = \mathbf{u}_1(\mathbf{x}) \exp[i(k_y y + k_z z) + \gamma t]$, where the subscripts 0 and 1 denote the zeroth order unperturbed quantities and the first order perturbed quantities, respectively; k_y

and k_z are, respectively, the y - and z -component of the wave number vector \mathbf{k} ; and γ is the growth rate of the tearing mode instability. The linearized equations are given by

$$\gamma\rho_1 + \mathbf{u}_1 \cdot \nabla\rho_0 = 0 \quad (3.10)$$

$$\gamma\nabla \times (\rho_0 \mathbf{u}_1) = \frac{1}{4\pi} \nabla \times [(\mathbf{B}_0 \cdot \nabla)\mathbf{B}_1 + (\mathbf{B}_1 \cdot \nabla)\mathbf{B}_0] \quad (3.11)$$

$$\gamma\mathbf{B}_1 = \nabla \times (\mathbf{u}_1 \times \mathbf{B}_0) + \frac{c^2\eta}{4\pi} \nabla^2 \mathbf{B}_1 \quad (3.12)$$

The equation (3.10) can be further reduced to

$$\gamma\rho_1 + u_{1x}\rho'_0 = 0 \quad (3.13)$$

where u_{1x} is the x -component of perturbed plasma flow velocity \mathbf{u}_1 and $\rho'_0 = d\rho_0/dx$ is the derivative of the unperturbed plasma density. The equation (3.11) has three components, i.e., (3.11)_x, (3.11)_y, and (3.11)_z. By subtracting $k_y(3.11)_z$ from $k_z(3.11)_y$, a new equation is found

$$\gamma(u''_{1x} - k^2 u_{1x}) = -\frac{\gamma\rho'_0}{\rho_0} u'_{1x} + \frac{i(\mathbf{k} \cdot \mathbf{B}_0)}{4\pi\rho_0} \left[-\frac{(\mathbf{k} \cdot \mathbf{B}_0)''}{(\mathbf{k} \cdot \mathbf{B}_0)} B_{1x} + B''_{1x} - k^2 B_{1x} \right] \quad (3.14)$$

where ' denotes the derivative with respect to x and $k^2 = k_y^2 + k_z^2$. In the above manipulation, the equivalence $\nabla \cdot \mathbf{u}_1 = u'_{1x} + i\mathbf{k} \cdot \mathbf{u}_1 = 0$ and $\nabla \cdot \mathbf{B}_1 = B'_{1x} + i\mathbf{k} \cdot \mathbf{B}_1 = 0$ have been used. Similarly, by subtracting $k_y(3.12)_z$ from $k_z(3.12)_y$, another equation is obtained

$$\gamma B_{1x} = i(\mathbf{k} \cdot \mathbf{B}_0) u_{1x} + \frac{c^2\eta}{4\pi} (B''_{1x} - k^2 B_{1x}) \quad (3.15)$$

By introducing the dimensionless variables $x^* = x/L$, $\gamma^* = \gamma t_d$, $\mathbf{k}^* = \mathbf{k}L$, $\mathbf{B}^* = \mathbf{B}/\bar{B}$, $\mathbf{u}^* = -i(k^*/\gamma^*)\mathbf{u}t_d/L$, $\rho^* = \rho/\bar{\rho}$, and $F = (\mathbf{k}^* \cdot \mathbf{B}_0^*)/k^*$, the equations (3.13) to (3.15) can be written as

$$\rho_1 = -i \frac{u_{1x}\rho'_0}{k} \quad (3.16)$$

$$B_{1x} + u_{1x}F = \frac{1}{\gamma}(B_{1x}'' - k^2 B_{1x}) \quad (3.17)$$

$$(\gamma/kS)^2(u_{1x}'' - k^2 u_{1x} + \frac{\rho_0'}{\rho_0} u_{1x}') = \frac{F}{\rho_0}(-\frac{F''}{F} B_{1x} + B_{1x}'' - k^2 B_{1x}) \quad (3.18)$$

where $t_d = 4\pi L^2/c^2\eta$ is the diffusion time, $t_A = L/v_A = L\sqrt{4\pi\bar{\rho}/\bar{B}}$ is the Alfvén time, $S = t_d/t_A$ is the Lundquist number. In the above equations, the * sign, denoting the dimensionless variables, has been dropped for convenience. Since the diffusion time (t_d) is generally much larger than the Alfvén time (t_A), the Lundquist number ($S = t_d/t_A$) is much larger than unity. For example, $t_A \sim 1\text{sec}$, $t_d \sim 10^{10}\text{sec}$, and $S \sim 10^{10}$ are typical values for solar flares [Priest, 1985]. Based on the assumption discussed earlier that the resistive tearing instability develops at a characteristic time scale which is the combination of the Alfvén transit time and the diffusion time, it can be shown that the normalized growth rate of the tearing mode instability has the following property:

$$1 \ll \gamma \ll S \quad (3.19)$$

Because the tearing mode instability occurs only in a small region in which $\mathbf{k} \cdot \mathbf{B}_0 \sim 0$, the function F has the following properties: 1) $F(x_0) = 0$, where x_0 is determined by $\mathbf{k} \cdot \mathbf{B}_0 = 0$ and 2) near x_0 , the function can be expanded as $F(x) \simeq F'(x_0)(x - x_0)$, where $F' = dF/dx$ is the derivative of function F with respect to x . By introducing a new variable $\xi = x - x_0$, $F(x)$ can be written as $F(\xi) \simeq F'(0)\xi$. It is easy to verify that, with the new variable ξ , (3.16) - (3.18) remain unchanged. Therefore, for the sake of convenience, x , instead of ξ , will be used as the new variable. From now on, x is the relative distance measured from x_0 unless it is specified otherwise.

As discussed earlier, resistivity plays a crucial role in the development of the tearing mode instability. However, it is important only in the very small inner

region where the magnetic field is very small or the wave number vector (\mathbf{k}) is nearly perpendicular to the magnetic field (\mathbf{B}_0), where the magnetic field diffusion takes place, and the Ohm's law can be approximated as $\mathbf{E} = \eta\mathbf{J}$. Outside that region, the effect of the resistivity is negligible, the magnetic field convection is dominant, and Ohm's law can be approximated as $\mathbf{E} = -\mathbf{u} \times \mathbf{B}/c$. Because different terms in Ohm's law dominate in different regions, (3.16)–(3.18) have to be solved separately for both the inner region and the outer region. Then, the solutions obtained for the inner region and the outer region must be matched at the boundary that separates the two regions.

Since the resistivity is negligible in the outer region, the right hand side of (3.17) can be ignored. Because of $S \gg 1$, the left hand side of (3.18) can also be neglected. Thus, (3.17) – (3.18) become

$$B_{1x} + Fu_{1x} = 0 \quad (3.20)$$

$$B_{1x}'' - \left(k^2 + \frac{F''}{F}\right)B_{1x} = 0 \quad (3.21)$$

(3.21) can be solved for B_{1x} when the function F is specified. For simplicity, $F = \tanh(x)$ is assumed in the following analysis. By substituting $F = \tanh(x)$ into the equation, (3.21) becomes

$$B_{1x}'' - (k^2 - 2\text{sech}^2 x)B_{1x} = 0 \quad (3.22)$$

It is easy to verify that (3.22) has a solution

$$B_{1x} = \begin{cases} \exp(-kx)[1 + \frac{1}{k}\tanh x], & x \geq 0; \\ \exp(+kx)[1 - \frac{1}{k}\tanh x], & x < 0 \end{cases} \quad (3.23)$$

The solution (3.23) has a discontinuous derivative at $x = 0$, and the jump in the logarithmic derivative of B_{1x} is found to be

$$\Delta' = \frac{B_{1x}'(0^+) - B_{1x}'(0^-)}{B_{1x}(0)} = 2\left(\frac{1}{k} - k\right) \quad (3.24)$$

The jump in the logarithmic derivative of B_{1x} associated with other forms of F was also discussed by Furth et al. [1963]. For $k \ll 1$, they showed that the jump in the logarithmic derivative of B_{1x} could be approximated as

$$\Delta' = \frac{1}{k}(F'(0))^2 \left(\frac{1}{F_{-\infty}^2} + \frac{1}{F_{\infty}^2} \right) \quad (3.25)$$

where $F_{-\infty} = F(x = -\infty)$ and $F_{\infty} = F(x = +\infty)$.

Although decoupled in the outer region, (3.17) – (3.18) remain coupled in the inner region. Thus, they have to be solved together and then matched with the solutions of the outer region at the boundary. Since $x \ll 1$ in the inner region, F can be approximated as $F(x) \simeq F'(0)x$ and $B_{1x}(x)$ can be assumed as a constant, respectively. Because the tearing mode is a long wavelength instability, within the inner region $B_{1x}'' \gg k^2 B_{1x}$ and $u_{1x}'' \gg k^2 u_{1x}$ are used to further simplify the analysis. It is also assumed that the logarithmic derivative of u_{1x}' is much larger than the logarithmic derivative of ρ_0 , e.g., $u_{1x}'' \gg (\rho_0'/\rho_0)u_{1x}'$. Then, (3.17) – (3.18) can be written as

$$B_{1x}(0) + F'(0)xu_{1x} = \frac{B_{1x}''}{\gamma} \quad (3.26)$$

$$(\gamma/kS)^2 u_{1x}'' = \frac{F'(0)}{\rho_0(0)} x B_{1x}'' \quad (3.27)$$

By matching it to the outer region solution, the solution of (3.27) can be written as

$$\frac{(\gamma/kS)^2 \rho_0(0)}{F'(0)B_{1x}(0)} \int_{-\infty}^{+\infty} \frac{u_{1x}''}{x} dx = \Delta' \quad (3.28)$$

where an assumption has been made about the asymptotic behavior of u_{1x} to extend the integral to $\pm\infty$. By substituting (3.27) into (3.26), a new equation is derived as

$$xB_{1x}(0) + F'(0)x^2 u_{1x} - \frac{\rho_0(0)\gamma}{F'(0)k^2 S^2} u_{1x}'' = 0 \quad (3.29)$$

By introducing

$$x = [\rho_0(0)\gamma/(F'(0))^2 k^2 S^2]^{1/4} \xi$$

and

$$u_{1x} = [k^2 S^2 / \rho_0(0)\gamma(F'(0))^2]^{1/4} B_{1x}(0)\chi(\xi)$$

(3.29) can be simplified as

$$\chi''(\xi) - \xi^2 \chi(\xi) = \xi \quad (3.30)$$

which can be solved analytically. The solution for (3.30) can be expressed as

$$\chi(\xi) = -\frac{\xi}{2} \int_0^1 d\mu \exp(-\frac{1}{2}\xi^2 \mu)(1 - \mu^2)^{-1/4}$$

Now the Corresponding matching condition becomes

$$\gamma^{5/4} \rho_0(0)^{1/4} (F'(0))^{-1/2} k^{-1/2} S^{-1/2} \int_{-\infty}^{+\infty} \frac{\chi''}{\xi} d\xi = \Delta' \quad (3.31)$$

By substituting the solution of χ into (3.31), it is obtained

$$\gamma^{5/4} \rho_0(0)^{1/4} (F'(0))^{-1/2} k^{-1/2} S^{-1/2} \pi \frac{\Gamma(3/4)}{\Gamma(1/4)} = \Delta' \quad (3.32)$$

Thus, the growth rate for the tearing mode instability is found to be

$$\gamma = \left(\frac{\Gamma(1/4)}{\pi\Gamma(3/4)} \right)^{4/5} \rho_0(0)^{-1/5} (F'(0))^{2/5} k^{2/5} S^{2/5} (\Delta')^{4/5} \quad (3.33)$$

Notice that (3.33) is in the dimensionless form, in which the * sign denoting the dimensionless quantities has been dropped for convenience. The growth rate, in its dimensional form, is easily found as

$$\gamma = \left(\frac{\Gamma(1/4)}{\pi\Gamma(3/4)} \right)^{4/5} \left(\frac{\bar{\rho}}{\rho_0(0)} \right)^{1/5} (LF'(0))^{2/5} (kL)^{2/5} t_d^{-3/5} t_A^{-2/5} (L\Delta')^{4/5} \quad (3.34)$$

For $F = \tanh(x/L)$, the example used in calculating (3.22) - (3.24), the tearing growth rate is found to be

$$\gamma = \left(\frac{2\Gamma(1/4)}{\pi\Gamma(3/4)} \right)^{4/5} \frac{(1 - k^2 L^2)^{4/5}}{(kL)^{2/5}} \left(\frac{\bar{\rho}}{\rho_0(0)} \right)^{1/5} t_d^{-3/5} t_A^{-2/5} \quad (3.35)$$

It can be seen clearly from (3.35) that $\gamma t_d \sim S^{2/5} \gg 1$ and $\gamma t_A \sim S^{-3/5} \ll 1$. Since $t_A \ll 1/\gamma \ll t_d$, the tearing mode instability takes place at a characteristic time scale that is much larger than the Alfvén transit time and much smaller than the diffusion time. It also can be seen from (3.35) that the tearing mode instability only occurs when $kL \leq 1$. Hence, the thinner the current sheet is, or the larger the perturbation wavelength is, the easier the tearing mode becomes unstable. The preceding treatment shows that the tearing mode instability is caused by the inhomogeneity in the magnetic field, i.e., $F''/F < 0$ when resistivity is present. However, the tearing mode instability may also be modified if compressibility, thermal conductivity, and viscosity are taken into account [e.g. Coppi et al., 1966]. The above analysis is based on the linear theory that describes the initial stage in the development of the tearing mode instability. When the width of the magnetic islands becomes comparable or larger than the current sheet thickness, the nonlinear effects of the tearing mode instability must be considered, which is beyond the scope of the present review. The nonlinear theory of the tearing mode instability can be found in reviews by White [1983, 1986] and the references therein.

3.2 Theoretical Study of the Collisionless Tearing Mode Instability

The study of collisionless tearing mode instability originated from study of the stability of plasma equilibrium in a sheet pinch, where the magnetic field has a

neutral plane. Such a magnetic configuration is very important both in the controlled plasma devices and in the space plasma environment, such as the earth's magnetosphere. In the collisionless tearing mode, either the Hall current, pressure gradients, or Landau resonance mechanism replace the finite resistivity, which plays an important role in the collisional tearing mode. Electron inertia may also be responsible for the detachment of plasma from magnetic field lines. In this case, the kinetic effects of particles can no longer be properly described by MHD equations. To describe collisionless plasma, Vlasov-Maxwellian equations are necessary. In this section, a historical review of the study of the collisionless tearing mode instability is presented first. Then, the growth rate for the collisionless tearing mode is derived.

Furth [1962] was the first to discuss the stability of a collisionless neutral sheet. He used a drift Maxwellian distribution and obtained a magnetic field configuration with a neutral sheet, $B(x) = B_0 \tanh(x/L)$, where L is the width of the current sheet. He showed that originally straight magnetic field lines in the vicinity of the neutral sheet tend to connect across the neutral sheet and form magnetic islands when $kL < 1$, where k is the wave number along the magnetic field. The correctness of the marginal stability argument used by Furth [1962] was rigorously proved by Pfirsch [1962].

Using the same energy method, Laval and Pellat [1964] and Laval et al. [1966] calculated the growth rate of the collisionless tearing mode instability for both the neutral sheet magnetic field configuration and the magnetic field configuration with a magnetic shear, which is due to the presence of a guiding magnetic field along the current sheet. They found that the growth rate obtained based on the collisionless Vlasov equation is in better agreement with the experiment observations than the resistive theory of Furth et al. [1963]. The results obtained based on

the energy method were applied to the geomagnetic tail dynamics by Coppi et al. [1966]. Based on the linear Vlasov theory, Schindler [1966] used a slightly different variational method and also obtained a necessary and sufficient stability criterion for the collisionless tearing mode. Schindler and Soop [1968] included an equilibrium electrostatic field in their variational analysis of the collisionless tearing mode instability.

However, the energy method is only one of the approaches used to deal with the collisionless tearing mode instability. Another method used to analyze the instability is one which calculates the perturbed quantities by completing the integration along the unperturbed particle orbits [e.g., Laval et al., 1966; Coppi et al., 1966]. Using this method, Hoh [1966] calculated the growth rate for the collisionless tearing mode instability in the small Larmor radius limit. He found that the instability is driven by a small group of electrons located within a Larmor radius of the neutral plane and drifting about the neutral plane with zero velocity along the field lines. The kinetic energy of these particles is the energy source of the instability, which develops fastest for a critical perturbation wave length on the order of several times the sheet thickness L due to a resonance mechanism of the inverse Landau damping. Hoh's results were consistent with the previous results obtained based on the energy method [e.g., Laval et al., 1966].

Because the particle orbits used in Hoh [1966] were complicated, his final results were achieved with the supplement of numerical extrapolation. Dobrowolny [1968] demonstrated that analytical results similar to Hoh's could be obtained by using a simplified particle orbit model, in which the orbits of particles that move across the neutral sheet are approximated as pieces of straight lines, while the orbits of the particles that do not cross the neutral sheet are approximated as Larmor circles. The tearing mode instability is insensitive to the orbits of particles because the

instability is driven only by a small group of resonance electrons located in the neutral sheet region.

So far, only the linear effects of the collisionless tearing mode have been examined. The nonlinear effects of the tearing instability were first considered by Biskamp et al. [1970] based on the quasi-linear theory. They found that the nonlinear effects tend to stabilize the instability. Nonlinear effects of the tearing mode have also been investigated by Galeev and Zelenyi [1975a, 1975b]. The effects of the magnetic field component perpendicular to the current sheet, which tend to magnetize electrons in the current sheet region and hence stabilize the instability, were discussed by Biskamp et al. [1970] and Galeev and Zelenyi [1976].

Drake and Lee [1977] studied the transition of the tearing instability from the collisional to the collisionless regimes in a strong guiding field configuration by solving the Fokker-Planck equation and found a semi-collisional region for the tearing mode instability. They also examined the drift tearing mode caused by the electron and ion gradient drifts in the collisional, semi-collisional, and collisionless regimes. The collisionless drift tearing mode was also investigated by Coppi et al. [1979] and Galeev et al. [1985].

In the previous works, the collisionless tearing mode instability in both the neutral sheet configuration and the strong guiding field configuration has been examined. The collisionless tearing mode instability in the neutral sheet configuration has been applied to the magnetotail to explain the magnetic substorms [e.g., Coppi et al., 1966]. However, at the dayside magnetopause, the magnetic field configuration generally has neither a neutral sheet nor a strong guiding field, because the guiding field component (B_y) is usually less than or comparable to the antiparallel component (B_z).

Based on the OGO 5 magnetometer data, Greenly and Sonnerup [1981] found location, orientation, amplitude, and frequency of magnetic oscillations at the day-side magnetopause to be consistent with the collisionless tearing mode theory. Quest and Coroniti [1981a, 1981b] investigated the collisionless tearing mode instability for the typical magnetic field geometry and plasma parameters at the dayside magnetopause. They found that the linear growth rate of the tearing mode is a sensitive function of the IMF orientation, magnetopause thickness, and electron number density. Larger tearing growth rates tend to be obtained when the angle between the IMF and the geomagnetic field is large, the dayside magnetopause is thin, and the electron number density is low. The nonlinear evolution and the nonparallel propagation ($\mathbf{k} \times \mathbf{B} \neq 0$) of the tearing mode instability at the dayside magnetopause were further examined by Coroniti and Quest [1984] and Quest and Coroniti [1985].

The collisionless tearing mode at the dayside magnetopause was also investigated by Kuznetsova and Zelenyi [1985], Galeev et al. [1986], and Gladd [1990]. In addition to the usual tearing mode perturbations (cylindrical geometry $m \geq 2$ modes) in a slab current layer with sheared magnetic field, Kuznetsova and Zelenyi [1985] found that a set of special tearing mode perturbations (slab geometry of $m = 1$ cylindrical modes) with larger growth rates could also be excited and that the saturation mechanism caused by the coupling tearing perturbations to the ion sound waves could only affect the usual tearing modes. Based on an analytical calculation of the stability of the dayside magnetopause, Galeev et al. [1986] found that the growth and overlapping of magnetic islands due to the drift tearing mode could destroy the magnetic surfaces at the magnetopause and that the stochastic wandering of the magnetic field lines between the destroyed magnetic surfaces could lead to the magnetic field line percolation, i.e., patchy magnetic reconnection. A

magnetopause stability threshold was obtained by Galeev et al. [1986]. They also found that the drift tearing mode could be stabilized by its coupling to the ion sound waves. These analytical results were later confirmed and further extended by numerically solving the eigenmode equations [Gladd, 1990].

Thus far, most of the works mentioned above deal with the collisionless tearing mode instability in an isotropic plasma, i.e., $T_{\perp} = T_{\parallel}$, where T_{\perp} and T_{\parallel} are temperatures perpendicular and parallel to the magnetic field, respectively. However, in the collisionless plasma, the motion of particles parallel to the magnetic field is decoupled from the perpendicular motion and temperature anisotropy can be maintained even in thermal equilibrium, which may also affect the development of the tearing mode.

The collisionless tearing mode instability in the anisotropic plasma has been examined by several authors. For example, Laval and Pellat [1968] showed that the tearing mode can be stabilized by a weak electron anisotropy, in which the perpendicular temperature ($T_{e\perp}$) is smaller than the parallel temperature ($T_{e\parallel}$). Forslund [1968] found that the tearing growth rate can be enhanced when $T_{e\perp}$ is slightly larger than $T_{e\parallel}$. Chen and Davidson [1981] demonstrated that the range of wave number for unstable modes is reduced for $T_{i\perp} < T_{i\parallel}$ and is increased for $T_{i\perp} > T_{i\parallel}$ when an ion temperature anisotropy is present.

Traditionally, in calculating the growth rate for the collisionless tearing mode instability, a two-region approximation and a constant eigenfunction assumption are used. In the inner region, where particles move across the neutral sheet, the orbits of particles are assumed to be pieces of straight lines and the eigenfunction is assumed to be a constant; whereas in the outer region, particles do not cross the neutral sheet and the orbits of particles are approximated as the Larmor circles. Then, the asymptotic solutions are matched at the boundary that separates the

two regions. In the two-region approximation, the intermediate region where ions still move across the neutral sheet while electrons can no longer do so, has been neglected. For example, Dobrowolny [1968] obtained the dispersion relation of tearing mode by matching the asymptotic solutions at the boundary separating the electron inner and outer regions, while neglecting the contributions of ions to the dispersion relation.

Chen and Palmadesso [1984] studied the collisionless tearing mode instability in an anisotropic neutral sheet. They found that even though it is a good approximation for the isotropic plasma, the two-region approximation is inadequate for the anisotropic neutral sheet. They proposed a three-region approximation model for the particle orbits to include the contribution from the intermediate region. Including the ion contribution in the intermediate region, they found that an ion temperature anisotropy with $T_{i\perp} > T_{i\parallel}$ can enhance the tearing growth rate by an order of magnitude, while an ion anisotropy with $T_{i\perp} < T_{i\parallel}$ tends to strongly stabilize the instability.

An integro-differential formalism was developed by Chen and Lee [1985] to solve the collisionless tearing mode in a neutral sheet geometry. With the integro-differential formalism, the constant eigenfunction assumption is no longer needed and the orbits of particles are treated exactly. When applied to a non-Maxwellian distribution, the integro-differential method produced an enhanced tearing growth rate, which can be one or two orders of magnitude larger than that obtained from the previous best analytical approximation, the three-region approximation [Chen and Lee, 1985; Burkhart and Chen, 1989a, 1989b]. A quadratic-form analysis of the collisionless tearing mode was also reported by Chen and Lee [1988].

Previous theoretical works on the collisionless tearing mode instabilities have been reviewed above. The simulation studies of the collisionless tearing mode have

also been carried out and will be discussed later. In the following, the growth rate and the eigenfunction of the tearing mode instability in a slab neutral sheet are derived. For the calculation of the tearing growth rate and eigenfunction in a current sheet with a sheared magnetic field, readers are referred to Laval et al. [1966], Galeev and Zelenyi [1978], Quest and Coroniti [1981b], Galeev [1984], Galeev et al. [1986], Gladd [1990], and references therein.

To calculate the growth rate for the collisionless tearing mode instability, a set of Vlasov-Maxwellian equations is used. With the Coulomb gauge, $\nabla \cdot \mathbf{A} = 0$, these basic equations can be written as

$$\frac{\partial f_\alpha}{\partial t} + \mathbf{v} \cdot \frac{\partial f_\alpha}{\partial \mathbf{x}} + \frac{q_\alpha}{m_\alpha} \left(\mathbf{E} + \frac{\mathbf{v} \times \mathbf{B}}{c} \right) \cdot \frac{\partial f_\alpha}{\partial \mathbf{v}} = 0 \quad (3.36)$$

$$\nabla^2 \phi = -4\pi \sum_\alpha q_\alpha \int f_\alpha d\mathbf{v} \quad (3.37)$$

$$\nabla^2 \mathbf{A} = -\frac{4\pi}{c} \sum_\alpha q_\alpha \int \mathbf{v} f_\alpha d\mathbf{v} \quad (3.38)$$

$$\mathbf{E} = -\nabla \phi - \frac{1}{c} \frac{\partial \mathbf{A}}{\partial t} \quad (3.39)$$

$$\mathbf{B} = \nabla \times \mathbf{A} \quad (3.40)$$

where f_α is the particle distribution of the α species, q_α and m_α are, respectively, the charge and mass for a particle of the α species, \mathbf{v} is the particle velocity, $\partial/\partial \mathbf{x} = (\partial/\partial x)\mathbf{e}_x + (\partial/\partial y)\mathbf{e}_y + (\partial/\partial z)\mathbf{e}_z$, $\partial/\partial \mathbf{v} = (\partial/\partial v_x)\mathbf{e}_x + (\partial/\partial v_y)\mathbf{e}_y + (\partial/\partial v_z)\mathbf{e}_z$, ϕ is the electrostatic potential, and \mathbf{A} is the vector potential. As defined before, \mathbf{E} , \mathbf{B} , and c are, respectively, the electric field, the magnetic field, and the speed of light.

Under the assumption that

$$f_\alpha(\mathbf{x}, \mathbf{v}, t) = f_{0\alpha}(\mathbf{x}, \mathbf{v}) + f_{1\alpha}(\mathbf{x}, \mathbf{v}, t)$$

$$\phi(\mathbf{x}, t) = \phi_1(\mathbf{x}, t)$$

$$\mathbf{A}(\mathbf{x}, t) = \mathbf{A}_0(\mathbf{x}) + \mathbf{A}_1(\mathbf{x}, t)$$

where 0 denotes the zeroth order quantities in an equilibrium and 1 denotes the first order perturbed quantities, which are much smaller than the zeroth order quantities, the equations of (3.36) - (3.40) can be separated into two sets of equations, one describing the zeroth order equilibrium state and the other describing the first order perturbed state. The zeroth order equations are

$$\mathbf{v} \cdot \frac{\partial f_{0\alpha}}{\partial \mathbf{x}} + \frac{q_\alpha}{m_\alpha} \left[\frac{\mathbf{v} \times (\nabla \times \mathbf{A}_0)}{c} \right] \cdot \frac{\partial f_{0\alpha}}{\partial \mathbf{v}} = 0 \quad (3.41)$$

$$\nabla^2 \mathbf{A}_0 = -\frac{4\pi}{c} \sum_{\alpha} q_\alpha \int \mathbf{v} f_{0\alpha} d\mathbf{v} \quad (3.42)$$

$$\mathbf{E}_0 = 0 \quad (3.43)$$

$$\mathbf{B}_0 = \nabla \times \mathbf{A}_0 \quad (3.44)$$

and the linearized first order equations are

$$\begin{aligned} \frac{df_{1\alpha}}{dt} &= \frac{\partial f_{1\alpha}}{\partial t} + \mathbf{v} \cdot \frac{\partial f_{1\alpha}}{\partial \mathbf{x}} + \frac{q_\alpha}{m_\alpha} \left[\frac{\mathbf{v} \times (\nabla \times \mathbf{A}_0)}{c} \right] \cdot \frac{\partial f_{1\alpha}}{\partial \mathbf{v}} \\ &= -\frac{q_\alpha}{m_\alpha} \left[-\nabla \phi_1 - \frac{1}{c} \frac{\partial \mathbf{A}_1}{\partial t} + \frac{\mathbf{v} \times (\nabla \times \mathbf{A}_1)}{c} \right] \cdot \frac{\partial f_{0\alpha}}{\partial \mathbf{v}} \end{aligned} \quad (3.45)$$

$$\nabla^2 \phi_1 = -4\pi \sum_{\alpha} q_\alpha \int f_{1\alpha} d\mathbf{v} \quad (3.46)$$

$$\nabla^2 \mathbf{A}_1 = -\frac{4\pi}{c} \sum_{\alpha} q_\alpha \int \mathbf{v} f_{1\alpha} d\mathbf{v} \quad (3.47)$$

$$\mathbf{E}_1 = -\nabla \phi_1 - \frac{1}{c} \frac{\partial \mathbf{A}_1}{\partial t} \quad (3.48)$$

$$\mathbf{B}_1 = \nabla \times \mathbf{A}_1 \quad (3.49)$$

It is easy to verify that the self-consistent current sheet model of Harris [1962] is an equilibrium solution for the zeroth order equations, in a reference frame in which

$$\frac{U_i}{T_i} = -\frac{U_e}{T_e} \quad (3.50)$$

where U_i (U_e) and T_i (T_e) are the drift speed and temperature of ions (electrons), respectively. With the assumption that ions drift in the y -direction and electrons drift in the $-y$ -direction and that the current sheet lies at $x = 0$, the Harris solution can be written as

$$f_{0\alpha} = n(x) \frac{1}{\pi^{3/2} V_{th\alpha}^{3/2}} \exp\left[-\frac{v_x^2 + (v_y - U_\alpha)^2 + v_z^2}{V_{th\alpha}^2}\right] \quad (3.51)$$

$$n(x) = n_0 \operatorname{sech}^2\left(\frac{x}{L}\right) \quad (3.52)$$

$$\mathbf{E}_0 = 0 \quad (3.53)$$

$$\mathbf{B}_0 = B_0 \tanh\left(\frac{x}{L}\right) \mathbf{e}_z \quad (3.54)$$

where $V_{th\alpha} = \sqrt{2T_\alpha/m_\alpha}$ is the particle thermal speed for α species, $n(x)$ is the particle number density profile, which is the same for both ions and electrons, n_0 is the particle number density in the current sheet, $L = \sqrt{2c^2 T_i / 4\pi n_0 e^2 U_i^2 (1 + T_e/T_i)}$ is the current sheet thickness, and $B_0 = \sqrt{8\pi n_0 (T_i + T_e)}$ is the magnitude of magnetic field outside the current sheet. After some straightforward algebraic manipulation, it is found that for the Harris current sheet model

$$\frac{\rho_\alpha}{L} = \frac{U_\alpha}{V_{th\alpha}} \quad (3.55)$$

where $\rho_\alpha = V_{th\alpha}/\Omega_\alpha = (c/\omega_{p\alpha})\sqrt{T_\alpha/(T_i + T_e)}$, $\Omega_\alpha = eB_0/cm_\alpha$, and $\omega_{p\alpha} = \sqrt{4\pi n_0 e^2/m_\alpha}$ are, respectively, the particle gyroradius, the particle gyrofrequency, and the plasma frequency for the species α .

To solve the first order equations, further assumptions are made for the first order perturbed quantities, i.e.,

$$f_{1\alpha}(\mathbf{x}, \mathbf{v}, t) = \tilde{f}_{1\alpha}(\mathbf{x}, \mathbf{v}) \exp(ik_z z + \gamma t) \quad (3.56)$$

$$A_{1z} = 0 \quad (3.57)$$

$$A_{1y}(\mathbf{x}, t) = \tilde{A}_1(\mathbf{x}) \exp(ik_z z + \gamma t) \quad (3.58)$$

$$A_{1x} = 0 \quad (3.59)$$

$$\phi_1(\mathbf{x}, t) = \tilde{\phi}_1(\mathbf{x}) \exp(ik_z z + \gamma t) \quad (3.60)$$

where k_z is the wave number of the first order perturbation along the zeroth order magnetic field and γ is the growth rate for the collisionless tearing mode. With the above assumptions, and after some algebraic manipulation, (3.45) can be rewritten as

$$\begin{aligned} \tilde{f}_{1\alpha} = & \frac{q_\alpha}{T_\alpha} \left(\frac{U_\alpha \tilde{A}_1}{c} - \tilde{\phi}_1 \right) f_{0\alpha} \\ & - \frac{q_\alpha}{T_\alpha} \int_{-\infty}^t \frac{\partial}{\partial t'} \left\{ \left[\frac{v'_y \tilde{A}_1(\mathbf{x}')}{c} - \tilde{\phi}_1(\mathbf{x}') \right] \exp[ik_z(z' - z) + \gamma(t' - t)] \right\} f_{0\alpha}(\mathbf{x}', \mathbf{v}') dt' \end{aligned} \quad (3.61)$$

where the integration is performed along the unperturbed particle orbit and the result of (3.51) is used. For the neutral sheet with an isotropic Maxwellian distribution, described by Harris [1962], it is reasonable to assume that near $\mathbf{x} \sim 0$ the eigenfunctions are approximately constant, i.e., $\tilde{A}_1(\mathbf{x}') \simeq \tilde{A}_1(\mathbf{x})$ and $\tilde{\phi}_1(\mathbf{x}') \simeq \tilde{\phi}_1(\mathbf{x})$. Similarly, the particle density profile is approximated as $n(\mathbf{x}') = n(\mathbf{x})$. Also from $P_{y\alpha} = m_\alpha v_y + (q_\alpha/c)A_y = \text{const}$, where $P_{y\alpha}$ is the y -component of particle canonical momentum for the α species, it is found that $v'_y \simeq v_y$ in the $\mathbf{x} \sim 0$ region. It is also found that $v'_z \simeq v_z$ since $v'_z{}^2 + v'_y{}^2 = v_z^2 + v_y^2 = \text{const}$ and that $z' - z = v_z(t' - t)$

because of $v'_z = v_z = \text{const.}$ After completing the integration along the unperturbed particle orbit, (3.61) is deduced to

$$\bar{f}_{1\alpha} = \frac{q_\alpha}{T_\alpha} \left(\frac{U_\alpha \bar{A}_1}{c} - \bar{\phi}_1 \right) f_{0\alpha} + \frac{q_\alpha}{T_\alpha} \left(\frac{v_y \bar{A}_1}{c} - \bar{\phi}_1 \right) \frac{i\gamma}{k_z v_z - i\gamma} f_{0\alpha} \quad (3.62)$$

and the first order distribution function is found to be

$$f_{1\alpha} = \frac{q_\alpha}{T_\alpha} \frac{k_z v_z}{k_z v_z - i\gamma} \left(\frac{v_y A_{1y}}{c} - \phi_1 \right) f_{0\alpha} + \frac{q_\alpha}{T_\alpha} (U_\alpha - v_y) \frac{A_{1y}}{c} f_{0\alpha} \quad (3.63)$$

After substituting (3.63) into (3.46) - (3.47) and completing the integration, two coupled equations are obtained.

$$\nabla^2 \phi_1 = -4\pi n(x) \sum_\alpha \frac{q_\alpha^2 Z'(\zeta_\alpha)}{m_\alpha V_{th\alpha}^2} \left(\phi_1 - \frac{U_\alpha A_{1y}}{c} \right) \quad (3.64)$$

$$\nabla^2 A_{1y} = -\frac{4\pi}{c} n(x) \sum_\alpha \frac{q_\alpha^2}{m_\alpha} \left[\frac{U_\alpha Z'(\zeta_\alpha)}{V_{th\alpha}^2} \left(\phi_1 - \frac{U_\alpha A_{1y}}{c} \right) + \zeta_\alpha Z(\zeta_\alpha) \frac{A_{1y}}{c} \right] \quad (3.65)$$

where $\zeta_\alpha = i\gamma/k_z V_{th\alpha}$, $Z(\zeta)$ is the Fried-Conte plasma dispersion function defined as

$$Z(\zeta) = \frac{1}{\pi^{1/2}} \int_{-\infty}^{\infty} \frac{e^{-t^2}}{t - \zeta} dt$$

and $Z'(\zeta) = dZ/d\zeta = -2[1 + \zeta Z(\zeta)]$. By using the quasi-neutrality condition, i.e., $\nabla^2 \phi_1 = 0$, a linear relation can be found between for ϕ_1 and A_{1y} ,

$$\phi_1 = \left[\frac{(U_i/T_i)Z'(\zeta_i) - (U_e/T_e)Z'(\zeta_e)}{(1/T_i)Z'(\zeta_i) + (1/T_e)Z'(\zeta_e)} \right] \frac{A_{1y}}{c} \quad (3.66)$$

Since for the tearing mode instability $\zeta_\alpha = i\gamma/k_z V_{th\alpha}$ is much smaller than unity, the plasma dispersion function and its derivative can be expanded as $Z(\zeta_\alpha) \simeq i\pi^{1/2}$ and $Z'(\zeta_\alpha) \simeq -2(1 + i\pi^{1/2}\zeta_\alpha)$. With above expansions and substituting (3.66) into (3.65), it is obtained

$$\frac{d^2 \bar{A}_1}{dx^2} - [k_z^2 + V_0(x) + \sum_\alpha V_{1\alpha}(x, k_z, \gamma)] \bar{A}_1 = 0 \quad (3.67)$$

where

$$V_0(x) = -(2/L^2)\text{sech}^2(x/L)$$

$$V_{1\alpha}(x, k_z, \gamma) = \begin{cases} -i\pi^{1/2}\text{sech}^2(x/L)(\omega_{p\alpha}^2/c^2)[1 + 2(\rho_\alpha/L)^2]\zeta_\alpha & |x| \leq d_\alpha \\ 0 & |x| > d_\alpha \end{cases}$$

and $d_\alpha = \sqrt{\rho_\alpha L}$ is the estimated half-width of the singular layer near the region with $\mathbf{k} \cdot \mathbf{B} \sim 0$, where the resonant wave particle interaction takes place. For the special case considered above, the singular layer is located at $x \sim 0$. Notice that in deriving (3.67) a major assumption has been made. It is assumed that all particles of species α located within the singular layer with $|x| \leq d_\alpha$ are totally unmagnetized, meandering around the singular layer, interacting with tearing waves, and contributing to $V_{1\alpha}$; whereas other particles of species α located outside the singular layer are strongly magnetized, do not participate in the resonant wave-particle interaction and hence do not contribute to $V_{1\alpha}$. Since $V_{1i}/V_{1e} \propto \sqrt{T_e m_e / T_i m_i} \ll 1$, resonant electrons play a dominant role in the wave-particle interaction in the region with $|x| \leq d_e$. Notice that (3.67) can also be obtained if ϕ_1 is neglected in (3.65). In (3.67), V_0 represents the adiabatic perturbation of the current density due to the slow pairing of the elementary current filaments, whereas V_1 represents the perturbed current density caused by the resonant wave-particle interaction.

Equation (3.67) is a Schrödinger equation with a complicated potential $V(x)$, where $V(x) = k_z^2 + V_0(x) + \sum V_{1\alpha}(x, k_z, \gamma)$. The typical form of the effective potential $V(x)$ for the Schrödinger equation (3.67) and the typical shape of the eigenfunction of the perturbed vector potential \tilde{A}_1 of the collisionless tearing mode instability are shown in Figure 3.2. Figure 3.2a shows that the effective potential has a sharp peak caused by the resonant electrons near the singular layer ($x \sim 0$) and Figure 3.2b shows that the perturbed vector potential has a discontinuous derivative at $x = 0$.

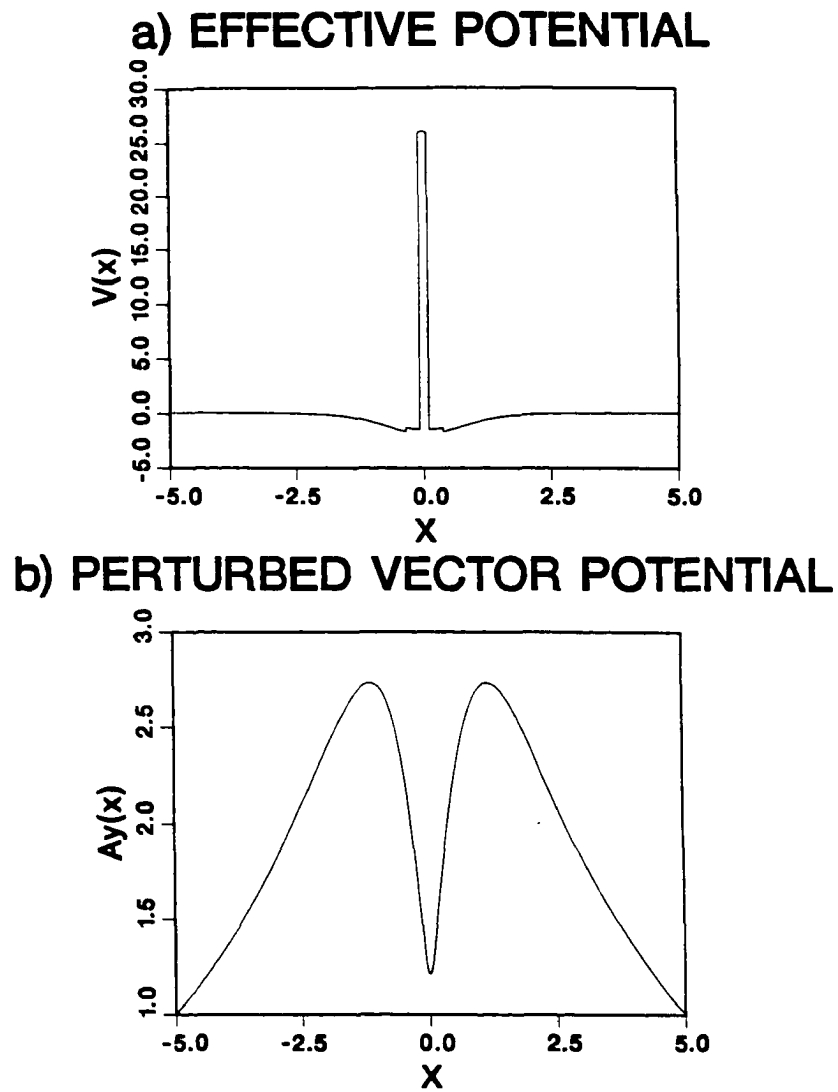


Figure 3.2 For the collisionless tearing mode instability, (a) the effective potential of the Schrödinger equation (3.67) and (b) the typical shape of the eigenfunction of the perturbed vector potential.

In general, (3.67) must be solved numerically. For example, with the assumption that the eigenfunction decreases exponentially away from the singular layer, i.e., $\tilde{A}_1 \propto \exp(-k_z|x|)$ when $x \gg 0$, (3.67) can be solved with a shooting method to obtain the eigenfunction (\tilde{A}_1) and the growth rate (γ) for a specified wave number (k_z). Plotted in Figure 3.3 is the typical curve of the normalized collisionless tearing mode growth rate γ/Ω_e as a function of normalized wave number $k_z L$ by using the shooting method. The growth rate has a maximum value when $k_z L \sim 0.3$. However, if the form of potential well can be simplified, (3.67) may also be solved analytically.

Since the contribution to $\sum V_{1\alpha}$ mainly comes from the resonant electrons in the region with $|x| \leq d_e$, it is appropriate to assume that $\sum V_{1\alpha} = V_{1e} = \text{constant}$ in the internal region ($|x| \leq d_e$) and $\sum V_{1\alpha} = 0$ in the external region ($|x| > d_e$). Notice that in the region with $d_e \leq |x| \leq d_i$, although electrons are magnetized, ions are still unmagnetized and can resonate with tearing perturbations, contributing to $\sum V_{1\alpha}$. However, in the above, V_{1i} , the contribution of ions in the region with $d_e \leq |x| \leq d_i$ is neglected. It has been shown that the above assumption is justified as long as plasma considered is isotropical [Chen and Palmadesso, 1984]. Because in the internal region $d^2 \tilde{A}_1 / dx^2 \gg k_z^2 \tilde{A}_1$ and $V_{1e} \gg V_0$, (3.67) can be simplified as

$$\frac{d^2 \tilde{A}_1}{dx^2} - V_{1e} \tilde{A}_1 = 0 \quad (3.68)$$

and the solution for (3.68) is found to be

$$\tilde{A}_{1int}(x) = \tilde{A}_{1int}(0) \cosh(\sqrt{V_{1e}} x) \quad (3.69)$$

On the other hand, in the external region, (3.67) is simplified as

$$\frac{d^2 \tilde{A}_1}{dx^2} - [k_z^2 - \frac{2}{L^2} \text{sech}^2(\frac{x}{L})] \tilde{A}_1 = 0 \quad (3.70)$$

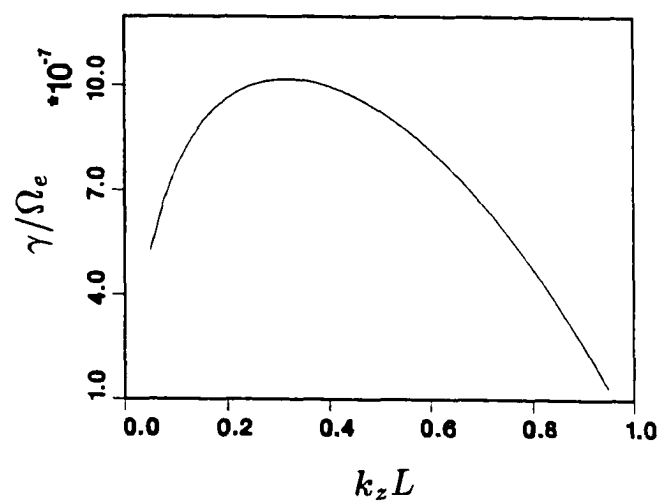


Figure 3.3 The normalized collisionless tearing mode growth rate as a function of normalized wave number.

and the solution of (3.70) is given by

$$\tilde{A}_{1ext}(x) = \tilde{A}_{1ext}(0) \left[1 + \frac{\tanh(|x|/L)}{k_z L} \right] \exp(-k_z |x|) \quad (3.71)$$

By matching the logarithmic derivative of the internal solution (A_{1int}) and the external solution (A_{1ext}) at the boundary of the singular layer ($x = d_e$), the dispersion relation for the collisionless tearing mode is obtained as

$$\sqrt{V_{1e}} \tanh(\sqrt{V_{1e}} d_e) = k_z \left[\frac{\text{sech}^2(d_e/L)}{k_z^2 L^2 + k_z L \tanh(d_e/L)} - 1 \right] \quad (3.72)$$

From the dispersion relation (3.72), after some straightforward algebraic manipulation, the well-known form of the growth rate of the collisionless tearing mode is obtained

$$\gamma = \pi^{-1/2} \Omega_e \left(\frac{\rho_e}{L} \right)^{5/2} \left(1 + \frac{T_i}{T_e} \right) (1 - k_z^2 L^2) \quad (3.73)$$

where $d_e/L \ll kL \leq 1$ is assumed. It is clear from (3.73) that the collisionless tearing mode instability occurs only when $k_z L \leq 1$, which is similar to the collisional tearing mode instability. However, in the collisionless plasma resonant wave-particle interaction instead of resistivity provides the dissipation mechanism for the instability to grow.

Equation (3.73) is obtained for special magnetic configuration, i.e., Harris' current sheet model, in which the magnitudes of the oppositely directed magnetic field on both sides of the current sheet are equal. When the current sheet is asymmetric, the growth rate of the collisionless tearing mode can be written as

$$\gamma = \pi^{-1/2} \frac{k_z V_{the}}{k_{0e}^2 d_e} \Delta' \quad (3.74)$$

where $k_{0e} = \sqrt{4\pi e^2 n(x_0)/m_e c^2}$ is the inverse collisionless skin depth, x_0 is the position of the singular layer of the asymmetric current sheet, and Δ' is the jump

in the logarithmic derivative of the perturbed magnetic field. For $k_z L \ll 1$, similar to the collisional tearing mode, Δ' can be approximated by (3.25).

When the current sheet is asymmetric, the half-width of the singular layer (d_e) can be estimated as follows. Around the singular layer x_0 , the electron orbits separate into two classes: orbits which do not cross the singular layer $x = x_0$ and are roughly gyrotropic and orbits which meander about the singular layer $x = x_0$ [Sonnerup, 1971]. The boundary that separates the two classes of orbits can be assumed at $x = x_0 \pm d_e$. Near the singular layer $x = x_0$, the magnetic field can be expanded as $B(x) \simeq B'(x_0)(x - x_0)$. For an electron with thermal speed V_{the} , its gyroradius can be written as $\rho_e(x) \simeq V_{the}(m_e c/e)/B'(x_0)(x - x_0)$. By setting $\rho_e(x_0 \pm d_e) = d_e$, the half-width of the singular layer can be estimated as

$$d_e = \sqrt{V_{the} m_e c / e B'(x_0)} \quad (3.75)$$

As a special case, for the magnetic field described by the Harris current sheet model (3.54), the half-width of the singular layer is found to be $d_e = \sqrt{\rho_e L}$, which is exactly the same as used previously in (3.67).

In the previous two sections, the growth rates for both the collisional and the collisionless tearing mode instabilities are derived. In the next section, the dependence of tearing mode instabilities on the plasma β value, the ratio of plasma pressure to magnetic pressure, will be examined.

3.3 The β -Dependence of Tearing Mode Instabilities

Magnetic reconnection has been a prevailing hypothesis for the interaction between the solar wind and the magnetosphere at the dayside magnetopause, transferring

the mass, momentum, and energy from the solar wind into the earth's magnetosphere. Tearing mode instabilities at the dayside magnetopause play an important role in the development of large-scale dayside magnetic reconnection. Recent satellite observations of high-speed plasma flows at the dayside magnetopause, which are interpreted in terms of magnetic reconnection, indicate that the magnetic reconnection process may occur preferentially when the ratio of plasma pressure to magnetic pressure in the magnetosheath has a small value ($\beta_s < 2$) [Paschmann et al., 1986].

Paschmann et al. [1986] determined for each magnetopause crossing the maximum observed velocity change $\Delta \mathbf{V}_{observed}$ and the corresponding velocity change $\Delta \mathbf{V}_{theory}$, predicted from the tangential momentum balance. Then, a dimensionless velocity change is defined as

$$\Delta V^* = \frac{\Delta \mathbf{V}_{observed} \cdot \Delta \mathbf{V}_{theory}}{|\Delta \mathbf{V}_{theory}|^2}$$

A perfect agreement between the observation and the theory would yield $\Delta V^* = 1$, whereas $\Delta V^* = 0$ would result if $\Delta \mathbf{V}_{observed}$ was either of zero magnitude or oriented at right angle to $\Delta \mathbf{V}_{theory}$. It is found that for cases with $\beta_s < 2$, the normalized flow velocity change is large, $\Delta V^* = 0.74$ on average, while for the cases with $\beta_s > 2$, the normalized flow velocity change is small, $\Delta V^* = 0.18$ on average. Therefore, the result of Paschmann et al. [1986] seems to suggest that the reconnection process at the dayside magnetopause takes place preferentially when the magnetosheath plasma β_s value (β_s) is smaller than 2. Figure 3.4 shows the original Figure 20 of Paschmann et al. [1986], in which the dimensionless flow velocity change is plotted as a function of β_s .

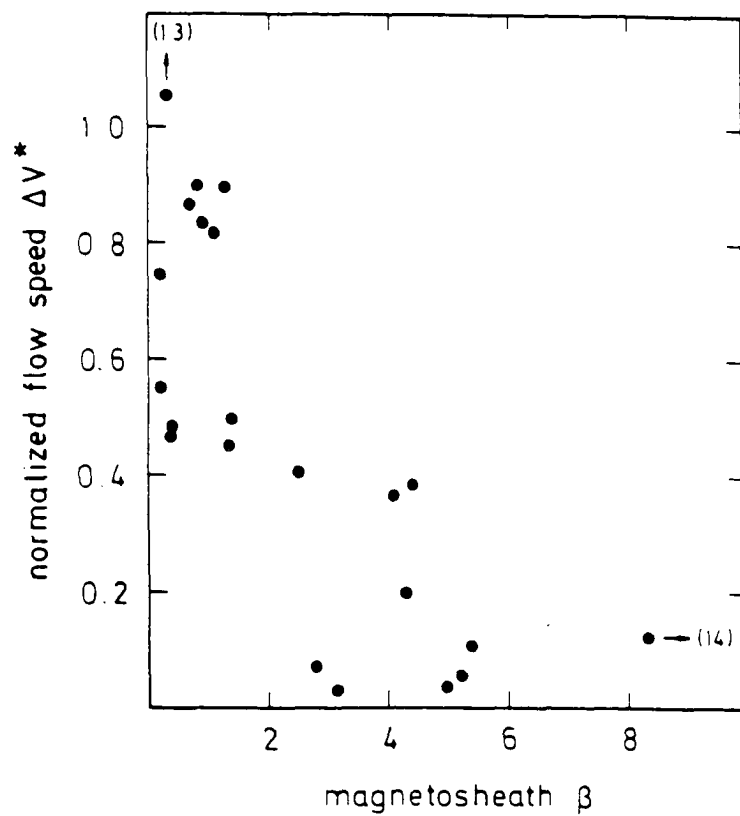


Figure 3.4 The ratio of observed to theoretically predicted flow velocity change at the magnetopause as a function of β_s , the ratio of plasma pressure to magnetic pressure in magnetosheath [Paschmann et al., 1986].

A possible explanation for the result of Paschmann et al. [1986] is that the development of the tearing mode instability triggering the onset of magnetic reconnection at the dayside magnetopause may have a dependence on the β value, the ratio of plasma pressure to magnetic pressure. The possible relationship between the tearing mode instability and the ratio of plasma pressure to magnetic pressure was discussed by Sonnerup [1974] and Quest and Coroniti [1981a]. In Sonnerup [1974], a condition of $\beta_p \leq 1$ was found for the symmetric reconnection in the magnetotail, where β_p is the ratio of perpendicular ion pressure to magnetic pressure in the inflow regions. In Quest and Coroniti [1981a], a lower electron density, hence a lower plasma β , in the current sheet was found to favor the onset of the tearing mode instability at the dayside magnetopause.

However, at the dayside magnetopause, the magnetic field configuration is usually asymmetric. Thus, the result of Sonnerup [1974] may not be applicable to the dayside magnetopause. Furthermore, the dayside magnetopause structure is essentially determined by the pressure balance between the local plasma and magnetic pressures, and the electron density in the current sheet is not allowed to vary arbitrarily once the density profile is determined by the pressure balance. Thus, the result of Quest and Coroniti [1981a] remains inconclusive. Therefore, whether or not the onset of the tearing mode instability, and hence the magnetic reconnection process, at the dayside magnetopause has a strong plasma β -dependence needs further investigation. In the following, the possible β -dependence of the tearing mode instability will be examined based on both the resistive MHD theory and the collisionless kinetic theory.

The growth rate of the resistive tearing mode is derived in section 3.1. For the resistive tearing mode developed in a current sheet with $\mathbf{k} \cdot \mathbf{B}_0(\mathbf{x}_0) = 0$, the general

dimensional form of the resistive tearing growth rate, adopted from (3.34), can be rewritten as

$$\gamma = \left(\frac{\Gamma(1/4)}{\pi\Gamma(3/4)} \right)^{4/5} \left(\frac{\bar{\rho}}{\rho_0(x_0)} \right)^{1/5} (LF'(x_0))^{2/5} (kL)^{2/5} t_d^{-3/5} t_A^{-2/5} (L\Delta')^{4/5} \quad (3.76)$$

where $F(x) = \mathbf{k} \cdot \mathbf{B}_0(x)/(k\bar{B})$ and Δ' is the jump in the logarithmic derivative of the perturbed magnetic field B_{1x} . Near x_0 , F is given, approximately, by $F(x) \simeq F'(x_0)(x - x_0)$. For $kL \ll 1$, Δ' can be written as

$$\Delta' = \frac{1}{k} (F'(x_0))^2 \left(\frac{1}{F_{-\infty}^2} + \frac{1}{F_{\infty}^2} \right) \quad (3.77)$$

Notice that in (3.76) the Alfvén transit time is defined as $t_A = L/v_A = L\sqrt{4\pi\bar{\rho}}/\bar{B}$. To examine the β -dependence of the resistive tearing mode, two cases will be considered, one involving a symmetric current sheet model and the other involving an asymmetric current sheet model. For simplicity, the plasma temperature is assumed to be a constant in the following discussion and the equilibrium magnetic field has the B_z component only.

For the symmetric neutral sheet model, the magnetic field can be written as

$$\mathbf{B}_0(x) = B_{0z} \tanh\left(\frac{x}{L}\right) \mathbf{e}_z \quad (3.78)$$

From $\mathbf{k} \cdot \mathbf{B}_0(x_0) = 0$, it is found $x_0 = 0$. From the pressure balance condition, it is obtained

$$\rho_0(x)T + \frac{B_0^2(x)}{8\pi} = \frac{B_{0z}^2}{8\pi} (1 + \beta_\infty) \quad (3.79)$$

where $\beta_\infty = 8\pi\rho_0(\infty)T/B_{0z}^2$ is the ratio of plasma pressure to magnetic pressure outside the current sheet. By defining $\bar{B} = B_{0z}$ and $\bar{\rho} = \bar{B}^2/8\pi T$, it is obtained that at the current sheet $x = x_0 = 0$

$$\rho(x_0) = \bar{\rho}(1 + \beta_\infty) \quad (3.80)$$

For the magnetic field profile (3.78), the function $F(x) = \tanh(x/L)$. Near $x_0 = 0$, $F(x) \simeq x/L$ and at $x_0 = 0$, $F'(x_0) = 1/L$. The jump in the logarithmic derivative of the perturbed magnetic field is found to be $\Delta' = 2(1 - k^2 L^2)/kL^2$. After substituting Δ' and (3.80) into (3.76), the growth rate of the resistive tearing mode in the symmetric current sheet is found to be

$$\gamma(\beta_\infty) = (1 + \beta_\infty)^{-1/5} \gamma(0) \quad (3.81)$$

where

$$\gamma(0) = \left(\frac{2\Gamma(1/4)}{\pi\Gamma(3/4)} \right)^{4/5} \frac{(1 - k^2 L^2)^{4/5}}{(kL)^{2/5}} t_d^{-3/5} t_A^{-2/5}$$

is the resistive tearing growth rate when $\beta_\infty = 0$ outside the current sheet.

In Figure 3.5a, the normalized resistive tearing growth rate $\gamma^* = \gamma(\beta_\infty)/\gamma(0)$ is plotted as a function of β_∞ , the ratio of plasma pressure to magnetic pressure outside the symmetric neutral sheet. It is shown in Figure 3.5 that the tearing growth rate only has a moderate dependence on the plasma β when the current sheet is symmetric and that the growth rate is reduced by about 40% when the plasma β outside the current sheet increases from 0 to 10.

For the asymmetric neutral sheet, the magnetic field can be written as

$$\mathbf{B}_0(x) = \frac{B_m - B_s}{2} - \frac{B_m + B_s}{2} \tanh\left(\frac{x}{L}\right) \mathbf{e}_z \quad (3.82)$$

where $B_m = B_0(-\infty)$ and $B_s = -B_0(\infty)$ are, respectively, the magnitudes of magnetic field on the two sides of the neutral sheet. From the pressure balance condition, it is found

$$\rho_0(x)T + \frac{B_0^2(x)}{8\pi} = \frac{B_m^2}{8\pi}(1 + \beta_m) = \frac{B_s^2}{8\pi}(1 + \beta_s) \quad (3.83)$$

where $\beta_m = 8\pi\rho_0(-\infty)T/B_m^2$ and $\beta_s = 8\pi\rho_0(\infty)T/B_s^2$ are, respectively, the ratio of plasma pressure to magnetic pressure at the two sides of the current sheet. From

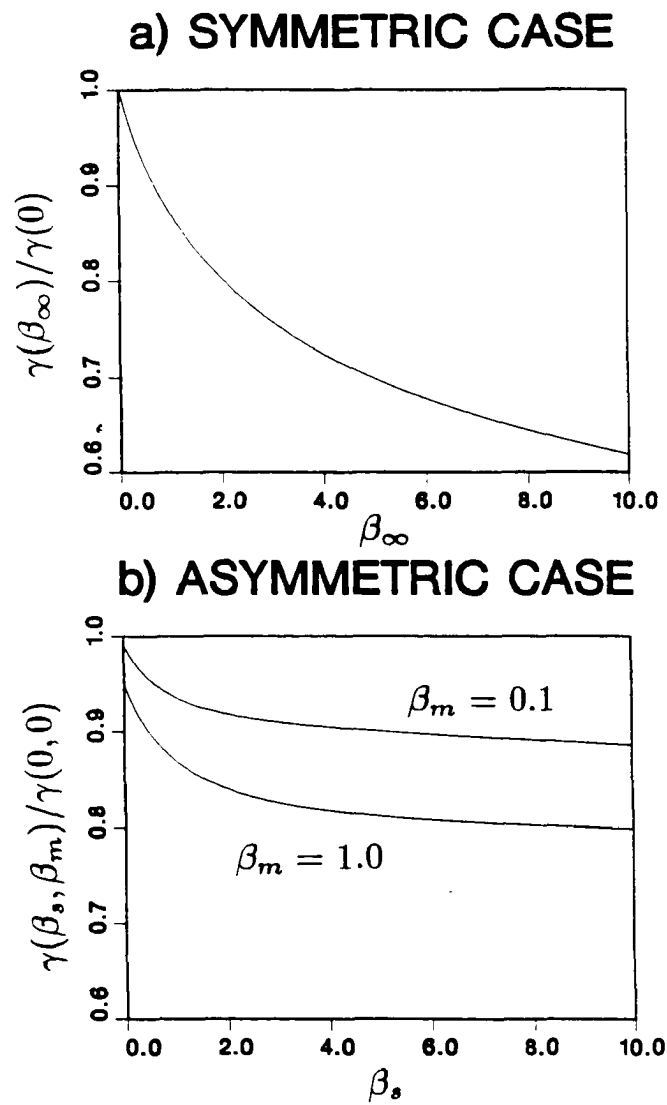


Figure 3.5 The normalized resistive tearing growth rate as a function the ratio of plasma pressure to magnetic pressure outside neutral sheet, (a) the symmetric case and (b) the asymmetric case.

$\mathbf{k} \cdot \mathbf{B}_0(x_0) = 0$, it is found that x_0 is determined by $\tanh(x_0/L) = (B_m - B_s)/(B_m + B_s)$. By defining $\bar{B} = B_m$ and $\bar{\rho} = \bar{B}^2/8\pi T$, the plasma density at $x = x_0$ can be written as

$$\rho_0(x_0) = \bar{\rho}(1 + \beta_m) \quad (3.84)$$

and the function F is found to be

$$F(x) = \frac{1 - (B_s/B_m)}{2} - \frac{1 + (B_s/B_m)}{2} \tanh\left(\frac{x}{L}\right) \quad (3.85)$$

Near x_0 , F can be approximated as

$$F(x) \simeq \frac{-2/L}{1 + (B_m/B_s)}(x - x_0) = \frac{-2/L}{1 + \sqrt{(1 + \beta_s)/(1 + \beta_m)}}(x - x_0) \quad (3.86)$$

After some straightforward algebraic manipulation, the jump in the logarithmic derivative of the perturbed magnetic field for $kL \ll 1$ is found to be

$$\Delta' = \frac{4}{kL^2} \frac{1 + (1 + \beta_s)/(1 + \beta_m)}{[1 + \sqrt{(1 + \beta_s)/(1 + \beta_m)}]^2} \quad (3.87)$$

After substituting (3.84) - (3.87) into (3.76), the growth rate of the resistive tearing mode in the asymmetric neutral sheet for $kL \ll 1$ is found to be

$$\gamma(\beta_m, \beta_s) = \frac{\gamma(0, 0)}{(1 + \beta_m)^{1/5}} \left(\frac{2}{1 + \sqrt{\frac{1 + \beta_s}{1 + \beta_m}}} \right)^2 \left(\frac{1 + \frac{1 + \beta_s}{1 + \beta_m}}{2} \right)^{4/5} \quad (3.88)$$

where

$$\gamma(0, 0) = \left(\frac{2\Gamma(1/4)}{\pi\Gamma(3/4)} \right)^{4/5} (kL)^{-2/5} t_d^{-3/5} t_A^{-2/5}$$

is the resistive tearing growth rate when $\beta_m = \beta_s = 0$ outside the current sheet.

Plotted in Figure 3.5b is the normalized resistive tearing growth rate $\gamma^* = \gamma(\beta_m, \beta_s)/\gamma(0, 0)$ as a function of β_s , the ratio of plasma pressure to magnetic pressure on one side of the asymmetric neutral sheet, for $\beta_m = 0.1$ and 1.0, the ratio

of plasma pressure to magnetic pressure on the other side of the asymmetric neutral sheet. It can be seen in Figure 3.5b that when the neutral sheet is asymmetric, the resistive tearing growth rate has a weaker β -dependence than that obtained in the symmetric neutral sheet case. For a small β_m value, $\beta_m \leq 1$, the tearing growth rate is reduced by about 20% or less when β_e increases from 0 to 10.

It is clear from the above analysis that the resistive tearing growth rate has only a weak to moderate dependence on the ratio of plasma pressure to magnetic pressure outside the current sheet. Thus, according to the resistive MHD theory, the reconnection process triggered by the development of the tearing mode instability should not be severely affected by the variations of plasma β . However, the above conclusion may not be true when the plasma becomes collisionless. Therefore, in the following, the β -dependence of the tearing mode instability will be further examined in the collisionless plasma environment.

As derived in section 3.2, the growth rate of collisionless tearing mode in a neutral sheet located at $x = x_0$ is given by (3.74), i.e.,

$$\gamma = \pi^{-1/2} \frac{k V_{the}}{k_{0e}^2 d_e} \Delta'$$

where $k_{0e} = \sqrt{4\pi e^2 n(x_0)/m_e c^2}$, $d_e = \sqrt{2V_{the} m_e c / e |B'(x_0)|}$, and for $k_z L \ll 1$ $\Delta' = [(B'(x_0))^2/k](1/B_{-\infty}^2 + 1/B_{\infty}^2)$. For simplicity, it is assumed that particle temperatures are constant. In the following discussion, both the symmetric and asymmetric neutral sheet models will be considered.

For a symmetric neutral sheet located at $x = 0$, the magnetic field profile can be written as $\mathbf{B}_0(x) = B_{0z} \tanh(x/L) \mathbf{e}_z$. From the pressure balance condition, the particle number density profile is found to be $n(x) = n_0 [\beta_{\infty} + \text{sech}^2(x/L)]$, where $n_0 = B_{0z}^2 / 8\pi(T_i + T_e)$ is the particle number density at the neutral sheet $x = 0$ when $\beta_{\infty} = 0$ and $\beta_{\infty} = 8\pi n(\infty)(T_i + T_e) / B_{0z}^2$ is the ratio of plasma pressure to

magnetic pressure outside the neutral sheet. For the symmetric neutral sheet, it is easy to verify that $n(0) = n_0(1 + \beta_\infty)$, $\Delta' = 2(1 - k_z^2 L^2)/k_z L^2$, and $d_e = \sqrt{\rho_e L}$, where $\rho_e = V_{the}/\Omega_e$ and $\Omega_e = eB_{0z}/m_e c$. By substituting the above quantities into (3.74), it is obtained

$$\gamma(\beta_\infty) = \gamma(0)(1 + \beta_\infty)^{-1} \quad (3.89)$$

where $\gamma(0) = (4/\pi)^{1/2} V_{the} (1 - k_z^2 L^2) / (\bar{k}_{0e}^2 \rho_e^{1/2} L^{5/2})$ is the collisionless tearing growth rate when $\beta_\infty = 0$ and $\bar{k}_{0e} = \sqrt{4\pi n_0 e^2 / m_e c^2}$.

The normalized collisionless tearing growth rate, $\gamma^* = \gamma(\beta_\infty)/\gamma(0)$, in the symmetric neutral sheet is plotted in Figure 3.6a as a function of β_∞ , the ratio of plasma pressure to magnetic pressure outside the neutral sheet. Figure 3.6a shows that the collisionless tearing growth rate has a strong dependence on the plasma β when the current sheet is symmetric and that the growth rate can be reduced by 90% when the β value changes from 0 to 10.

For an asymmetric neutral sheet, the magnetic field profile can be written as $\mathbf{B}_0 = 0.5[(B_m - B_s) - (B_m + B_s)\tanh(x/L)]\mathbf{e}_z$. The asymmetric neutral sheet has a singular layer at x_0 , which is determined by $\tanh(x_0/L) = (B_m - B_s)/(B_m + B_s)$. From the pressure balance condition,

$$n(x)(T_i + T_e) + \frac{B_0^2(x)}{8\pi} = \frac{B_s^2}{8\pi}(1 + \beta_s) = \frac{B_m^2}{8\pi}(1 + \beta_m)$$

the particle number density profile can be obtained. At $x = x_0$, the particle number density is given by $n(x_0) = n_{0m}(1 + \beta_m)$, where $n_{0m} = B_m^2/8\pi(T_i + T_e)$. For the magnetic configuration described above, Δ' is given by (3.87) for $k_z L \ll 1$ and $d_e = \sqrt{\rho_{em} L [1 + (1 + \beta_s)^{1/2} / (1 + \beta_m)^{1/2}] / 2}$, where $\rho_{em} = V_{the}/\Omega_{em}$ and $\Omega_{em} =$

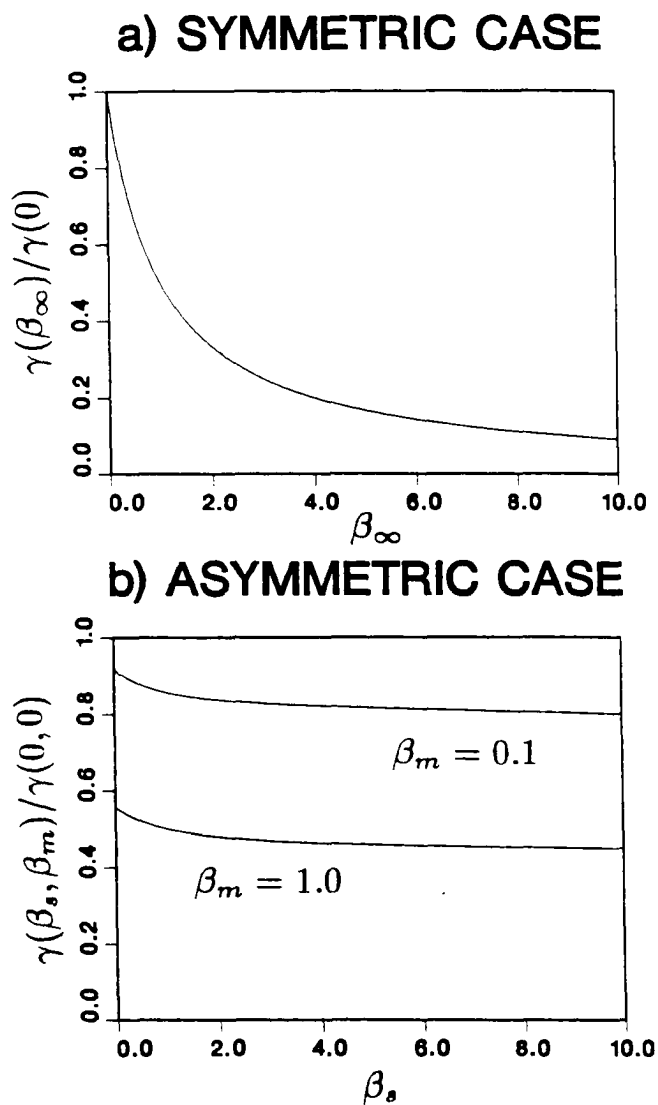


Figure 3.6 Normalized collisionless tearing growth rate as a function of the ratio of plasma pressure to magnetic pressure outside a neutral sheet, (a) the symmetric case and (b) the asymmetric case.

$eB_m/m_e c$. After substituting the above quantities into (3.74), the growth rate of collisionless tearing mode in the asymmetric neutral sheet is obtained

$$\gamma(\beta_m, \beta_s) = \frac{\gamma(0, 0)}{1 + \beta_m} \left(\frac{1 + \left(\frac{1 + \beta_s}{1 + \beta_m} \right)}{2} \right) \left(\frac{2}{1 + \sqrt{\frac{1 + \beta_s}{1 + \beta_m}}} \right)^{5/2} \quad (3.90)$$

where $\gamma(0, 0) = (4/\pi)^{1/2} V_{the} / (\bar{k}_{0em}^2 \rho_{em}^{1/2} L^{5/2})$ is the tearing growth rate when $\beta_m = \beta_s = 0$ and $\bar{k}_{0em} = \sqrt{4\pi e^2 n_{0m} / m_e c^2}$.

Plotted in Figure 3.6b is the normalized collisionless tearing growth rate $\gamma^* = \gamma(\beta_m, \beta_s) / \gamma(0, 0)$ as a function of β_s , the ratio of plasma pressure to magnetic pressure on one side of the asymmetric neutral sheet, for $\beta_m = 0.1$ and 1.0 , the ratio of plasma pressure to magnetic pressure on the other side of the asymmetric neutral sheet. It can be seen in Figure 3.6b that when the neutral sheet is asymmetric, the β -dependence of collisionless tearing instability is much weaker than when the neutral sheet is symmetric. For a small β_m value, $\beta_m \leq 1$, the tearing growth rate is reduced by about 10% or less when β_s increases from 0 to 10.

The significant differences of the β -dependence of the collisionless tearing instability between the symmetric and asymmetric neutral sheet can be easily understood. The collisionless tearing growth rate (γ) is inversely proportional to the particle number density ($n(x_0)$) in the singular layer region. Therefore, the smaller the particle number density is, the harder the system must be driven to maintain the self-consistent current. In the symmetric neutral sheet case, an increase of the ratio of plasma pressure to magnetic pressure from 0 to β_∞ outside the neutral sheet effectively changes the particle number density profile ($n(x)$) and leads to an increase of the particle number density $n(x_0)$ by $(1 + \beta_\infty)$ times, thereby significantly reducing the tearing growth rate.

However, in the asymmetric neutral sheet case, if the ratio of the plasma pressure to magnetic pressure (β_m) on one side of the neutral sheet is more or less fixed, the particle number density profile ($n(x)$) remains unchanged. Thus, an increase of the plasma beta value (β_s) on the other side of the neutral sheet only changes the magnetic field ratio (B_m/B_s) and shifts the location of the singular layer (x_0). The change of the particle number density $n(x_0)$ caused by the shifting of x_0 is generally much less than that produced by changing the particle number density profile $n(x)$ in the symmetric neutral sheet case. Therefore, the tearing growth rate is only slightly affected by the change of β_s .

The above examines the β -dependence of both the resistive tearing mode and the collisionless tearing mode. It is found that the resistive tearing mode has a moderate dependence on the ratio of plasma pressure to magnetic pressure outside the current sheet when the current sheet is symmetric and a weak dependence when the current sheet is asymmetric; and that the collisionless tearing mode has a strong β -dependence when the neutral sheet is symmetric and a much weaker β -dependence when the neutral sheet is asymmetric.

At the dayside magnetopause, the magnetosheath field (B_s) is usually smaller than the magnetospheric field (B_m). The magnetosheath plasma has a higher density (n_s) and lower temperature (T_s), while the magnetospheric plasma has a lower density (n_m) and higher temperature. The typical value of the ratio of plasma pressure to magnetic pressure in the magnetosphere (β_m) is about $0.1 \sim 0.3$, whereas the value of plasma beta in the magnetosheath (β_s) can be as large as 10 [e.g., Paschmann et al., 1986]. Thus, the dayside magnetopause current sheet is basically an asymmetric current sheet. Then, according to the results of the above survey of β -dependence, the development of the tearing mode instability, and hence the magnetic reconnection process at the dayside magnetopause, should not exhibit

a strong dependence on the ratio of plasma pressure to magnetic pressure in the magnetosheath (β_s) during the period when the interplanetary magnetic field (IMF) has a southward B_z -component, unless the magnetosheath field is enhanced to the same level as the magnetospheric field and the current sheet becomes symmetric.

At the dayside magnetopause, the magnetosheath field usually has a B_z - and a B_y -component, while the magnetospheric field has mainly a B_z -component only. Thus, during the southward IMF B_z period, the magnetic field at the dayside magnetopause is not strictly antiparallel and the magnetopause current sheet is not strictly a neutral sheet. A magnetic shear exists at the magnetopause due to the presence of the B_y -component in the magnetosheath field. The presence of magnetic shear affects the tearing mode instability and the magnetic reconnection process at the dayside magnetopause. Whether the presence of magnetic shear can cause the tearing mode instability to exhibit a strong β -dependence deserves further investigation in the future. In the following, a hypothesis is presented for the possible β -dependence of the tearing mode caused by the presence of magnetic shear. For simplicity, the plasma temperature is assumed to be a constant in this discussion and the magnetic field configuration is asymmetric.

For the resistive tearing mode, if the profile of magnetic field B_y -component is more or less uniform near the current sheet, then the profile of plasma density is mainly determined by the variation of the B_z -component. In this case, due to the presence of magnetic field component B_y , the location of the singular layer, determined by $\mathbf{k} \cdot \mathbf{B}_0(x_0) = 0$, will be shifted; the derivative of function $F(x)$, which represents the change of the angle between the wave number vector \mathbf{k} and the magnetic field $\mathbf{B}_0(x)$ at the singular layer, will be altered; and the jump condition of the logarithmic derivative of B_{z1} (Δ'), which represents the energy change, will also be changed. However, the growth rate of the resistive tearing mode and its

β -dependence is still given by (3.76), similar to what was obtained previously in the neutral sheet case. On the other hand, if the profile of B_y varies significantly across the current sheet, the plasma density profile determined by the pressure balance condition would differ significantly from that in the neutral sheet case. In this case, the magnitude and the β -dependence of the resistive tearing mode growth rate might be quite different from that discussed previously in the neutral sheet case. Especially if the location of the singular layer (x_0) is shifted toward a higher density region, the growth rate can be significantly reduced.

In the collisionless plasma, the development of the collisionless tearing mode in the sheared magnetic field configuration is quite different from that in the neutral sheet configuration [e.g., Laval et al., 1966; Drake and Lee, 1977; Galeev and Zelenyi, 1977, 1978; Quest and Coroniti, 1981a, 1981b; Galeev et al., 1986; Gladd, 1990]. Without the guiding magnetic field B_y , resonant electrons near the neutral sheet ($|x| < d_e$) meander around the neutral sheet and can be accelerated freely by the induction electric field during the development of the tearing mode. When a large magnetic field shear is present, electrons near the singular layer ($x = x_0$), determined by $\mathbf{k} \cdot \mathbf{B}_0(x_0) \sim 0$, become magnetized by the strong guiding magnetic field and a parallel electric field (E_{\parallel}) may exist, where \mathbf{B}_0 is the equilibrium magnetic field and the parallel direction is the direction of the strong guiding magnetic field at $x = x_0$. Only those electrons whose thermal speed (V_{the}) approximately equals the parallel phase speed of the tearing perturbation (γ/k_{\parallel}) can resonate with the parallel electric field E_{\parallel} , so the width of the singular layer is found to be $\delta_e = l_s \gamma / k V_{the}$, where $l_s = B_y(x_0) / |dB_z(x_0)/dx|$ is the local magnetic shear length. Notice that in the neutral sheet geometry, the width of the singular layer depends on neither the tearing growth rate (γ) nor the perturbation wave number (k).

The growth rate of the collisionless tearing mode in the sheared magnetic field [e.g., Drake and Lee, 1977; Quest and Coroniti, 1981a,b] can be written as

$$\gamma = \pi^{-1/2} \frac{k V_{the}}{k_{0e}^2(x_0) l_s} \Delta' \quad (3.91)$$

Comparing (3.91) with (3.74), it is found that the ratio of the collisionless tearing growth rate in the sheared magnetic field to the growth rate in the neutral sheet configuration is $\sim d_e/l_s$, if all other plasma parameters are held fixed. Thus the collisionless tearing growth rate tends to be reduced when the guiding field is so strong that $d_e/l_s < 1$. Since $k_{0e}^2(x_0) \propto n(x_0)$, it can be seen from (3.91) that besides the influence of l_s and Δ' , the collisionless tearing growth rate in the sheared magnetic field is also affected by the value of $n(x_0)$, which is determined by the pressure balance condition after the magnetic field profile and the plasma β values are specified. Similar to the resistive tearing case, a shift of the location of the singular layer (x_0) toward a higher density region tends to reduce the collisionless tearing growth rate. Thus, it is possible that both the resistive tearing mode and the collisionless tearing mode instabilities may exhibit strong β -dependence when the current sheet has a sheared magnetic field.

In this chapter, both the resistive and collisionless tearing mode instabilities were reviewed and a survey of the β -dependence of the tearing mode instabilities was carried out for both symmetric and asymmetric neutral sheet configurations. It was found that the resistive tearing mode exhibits a moderate dependence on β when the neutral sheet is symmetric and a weak β -dependence when the neutral sheet is asymmetric. It was also found that the collisionless tearing mode exhibits a strong β -dependence for the symmetric neutral sheet configuration and a weak β -dependence for the asymmetric neutral sheet configuration. The above results

seem to contradict the observation at the dayside magnetopause, where the magnetic field configuration is usually asymmetric, that the reconnection process, which is closely related to the tearing mode instabilities, takes place preferentially when the magnetosheath β_s value is small [Paschmann et al., 1986]. The apparent inconsistency between the above theoretical results and the observations may be caused by the omission of the magnetic shear in the theoretical model. We have speculated on the possible β -dependence of the tearing mode instabilities in a sheared magnetic field. However, a more rigorous theoretical study is needed to confirm these speculations.

Chapter 4 A Particle Simulation Model for Driven Magnetic Reconnection

The sophisticated nature of the problems encountered in fusion and space plasma physics has motivated considerable interest in computer simulation. With the rapid development of advanced computing facilities, computer simulation has become one of the most active research areas in fusion and space plasma studies [see recent review by Tajima, 1989 and references therein]. In this chapter, a brief introduction to the particle simulation methods used in fusion and space plasma physics is presented; a particle simulation model for the driven magnetic reconnection in the collisionless plasma is formulated; the initial conditions used in the present study are described; and the boundary conditions necessary for modeling the driven collisionless magnetic reconnection process are discussed. In the present model, the zero-order guiding magnetic field is assumed to be zero ($B_{0y} = 0$), which simplifies the boundary conditions necessary for the driven collisionless magnetic reconnection process. Since the inclusion of a nonzero guiding magnetic field significantly complicates the problem, the boundary conditions necessary for the driven collisionless magnetic reconnection process with $B_{0y} \neq 0$ will not be pursued in the present study.

4.1 An Introduction to Particle Simulation in Plasma Physics

In the simulation studies of fusion and space plasma processes, fluid models, kinetic models, and hybrid fluid-particle models have been developed. In the fluid simula-

tion, which is also called the magnetohydrodynamic (MHD) simulation, the MHD equations of a plasma are numerically solved with appropriate assumptions of the transport coefficients [e.g., Alder et al., 1970, 1976; Potter, 1973; Bauer et al., 1978; Gruber and Rappaz, 1985; Matsumoto and Sato, 1985; Denstrovskii and Kostomarov, 1986; Tajima, 1989]. To include more detailed models of plasma involving particle interactions through electromagnetic fields, kinetic simulation methods are developed. In the kinetic simulation, either the plasma kinetic equations, such as Vlasov or Fokker-Planck equations, are numerically solved, or the motions of a collection of charged particles that interact with each other and with the externally applied electromagnetic field are computed [e.g., Alder et al., 1970, 1976; Hockney and Eastwood, 1981; Dawson, 1983; Matsumoto and Sato, 1985; Birdsall and Langdon, 1985; Killeen et al., 1986, Greengard and Rokhlin, 1987; Tajima, 1989]. The kinetic simulation method involving calculations of charged particle motions is also categorized as particle simulation. However, the distinction between fluid and kinetic simulations has become vague since the hybrid simulation methods were introduced, in which fluid and particle treatments are applied to different components of a given plasma.

In space and astrophysical plasma physics, multi-dimensional MHD simulation codes have been successfully developed for modeling large scale phenomena, such as solar flares and prominence eruption, solar wind-magnetosphere interaction, magnetosphere-ionosphere coupling, and magnetospheric substorms. On the other hand, kinetic simulation has been particularly successful in dealing with plasma processes where particle distributions deviate significantly from a local Maxwellian distribution and where wave-particle resonance, particle trapping, or stochastic heating take place. Particle simulation and hybrid fluid-particle simulation have

also successfully modeled physical processes in collisionless plasmas in which non-MHD effects are important, such as collisionless magnetic reconnection and collisionless shocks.

Particle simulation originated from the pioneering works of Buneman [1959] and Dawson [1962] in the late 50s and early 60s. It has been shown that a relatively small system of a few thousand particles can indeed accurately simulate the collective behavior of real plasmas, if appropriate methods are used. Since then, the development of new algorithms and availability of advanced supercomputers have allowed particle simulation to progress from simple, one-dimensional, electrostatic problems to more complex and realistic situations, such as multi-dimensional electrostatic problems, magnetostatic problems, relativistic problems, and nonradiative problems, as well as electromagnetic problems. Three principal types of particle simulation models have been developed, which include the particle-particle (PP) model, the particle-mesh (PM) model, and the particle-particle-particle-mesh (PPPM or P³M) model.

The PP model, in which the forces between particles are calculated directly, can be used to simulate small systems with long-range forces or large systems with short-range forces, i.e., the forces of interaction are nonzero for only a few interparticle distances. However, due to the inefficient direct force computation, the PP model is time-consuming. Recently, a variation of the PP model, the gridless (meshless) particle model [Greengard and Rokhlin, 1987], has been proposed to speed up the force calculation in the PP model. In the gridless particle model, the forces (potentials) between particles are computed based on multipole expansions.

To speed up the force calculation in large systems with smoothly varying long-range forces, the PM model was developed. In the PM model, field quantities, such as electromagnetic fields, are defined on the mesh points; particle contributions

to the sources of field equations, such as charge density and current density, are assigned to the nearby mesh points; the differential operators, such as the Laplacian ∇^2 , are replaced by the finite-difference approximations on the mesh points; field equations are solved on the mesh points; and forces at particle positions are obtained by interpolating on the array of mesh-defined values. In the PM model, only those field variations having a wavelength longer than the spacing of the mesh can be represented by mesh values. The PM model is much faster, but generally less accurate, than the PP model. To maintain low levels of fluctuations, the number of particles in each mesh cell must be large enough, e.g., 5 ~ 10 particles per mesh cell. The PM model has been widely used in fusion and space plasma particle simulations [Hockney and Eastwood, 1981; Dawson, 1983; Birdsall and Langdon, 1985; Tajima, 1989].

The P³M model is a combination of the PP model and the PM model. In the P³M model, the interparticle forces are split into two parts: the rapid varying short-range forces and the slowly varying long-range forces. The short-range forces are computed based on the PP model, while the long-range forces are calculated based on the PM model. The resulting P³M model has the advantages of both the PP model and the PM model; it can represent close encounters as accurately as the PP model and calculate long-range forces as rapidly as the PM model. A detailed discussion of the P³M model can be found in Hockney and Eastwood [1981].

According to the algorithms used in advancing particles, the time integration schemes used in the particle simulation can be either explicit or implicit. The explicit schemes, in which the calculation of particle positions uses the fields at the preceding time, have been widely used since the beginning of the particle simulation era. The implicit schemes, in which the computation of particle positions requires knowledge of the fields at the same time, have emerged since the early 80s. With

the explicit schemes, particle simulation involving the electrostatic field requires a very large number of time steps. Otherwise, the explicit schemes become unstable when $\omega_{pe}\Delta t \geq 1.62$, where ω_{pe} is the electron plasma frequency and Δt is the simulation time step. With the implicit schemes, a larger time step ($\omega_{pe}\Delta t \gg 1$) can be used in the simulation. However, since the fields at time t_n depend on the unknown particle positions $\{\mathbf{x}^n\}$, the field and particle equations represent a very large system of coupled nonlinear equations. Therefore, to maintain the stability in implicit schemes, an accurate approximate solution for the coupled nonlinear equations is required. More discussion of the implicit schemes and other algorithms, such as electron subcycling and orbit averaging can be found in Birdsall and Langdon [1985] and references therein.

Basic electromagnetic particle simulation codes can be divided into two classes. One of them is full electromagnetic code. In a full electromagnetic code, the whole set of Maxwell equations is used and the electric and magnetic field vectors are advanced by a straightforward leapfrog scheme [Dawson, 1983; Birdsall and Langdon, 1985]. Notice that the inclusion of the transverse component of the displacement current in the full electromagnetic codes results in the hyperbolic electromagnetic field equations. The full electromagnetic codes have been used to study the plasma processes involving rapid field variations where electromagnetic radiation is important. However, as pointed out in Swift [1988], the full electromagnetic codes have two major disadvantages: (1) the numerical stability requires that the ratio of grid spacing to time stepping exceed the speed of light and (2) the electromagnetic field may reflect from simulation boundaries back into the simulation domain, interfering with the simulated plasma processes inside, if special precautions are not taken.

Many problems encountered in the fusion and space plasma environments are nonrelativistic and nonradiative in character. In the early epoch of the particle simulation of fusion and space plasma processes, nonradiative models were developed to study collisionless shock waves [Auer et al., 1961], ion-cyclotron waves [Hasegawa and Birdsall, 1964], nonlinear evolution of mirror instabilities and tearing modes [Dickman et al., 1969], and nonlinear microturbulence waves [Haber et al., 1973]. However, most of the models developed in the 60s and early 70s were either one-dimensional and electrostatic, or so complicated and specialized that they could not easily be applied to other problems in more dimensions. The first completely generalized multi-dimensional, radiation-free particle simulation algorithm was formulated by Nielson and Lewis [1976]. The nonradiative simulation model is also called the Darwin model because the Darwin approximation [Darwin, 1920], in which the transverse component of the displacement current is omitted from the Maxwell equations, has been used in the formulation. The Darwin model represents the second type of electromagnetic particle simulation codes.

With the Coulomb gauge ($\nabla \cdot \mathbf{A} = 0$), the Maxwell equations can be written as

$$\nabla^2 \phi = -4\pi\rho \quad (4.1)$$

$$\nabla^2 \mathbf{A} - \frac{1}{c^2} \frac{\partial^2 \mathbf{A}}{\partial t^2} = -\frac{4\pi}{c} \mathbf{J} + \frac{1}{c} \nabla \left(\frac{\partial \phi}{\partial t} \right) \quad (4.2)$$

where \mathbf{A} , ϕ , ρ , and \mathbf{J} are the vector potential, the electrostatic potential, the charge density, and the current density, respectively. Under the Darwin approximation, (4.2) becomes

$$\nabla^2 \mathbf{A} = -\frac{4\pi}{c} \mathbf{J} + \frac{1}{c} \nabla \left(\frac{\partial \phi}{\partial t} \right) \quad (4.3)$$

In appearance, the modified Maxwell equations under the Darwin approximation, in which the radiative term $(1/c^2)\partial^2 \mathbf{A}/\partial t^2$ is neglected, are nothing other than

an expansion of the exact Maxwell equations for the small (v/c) . However, the profound impact of the Darwin approximation is that the approximate Maxwell equations, when coupled by the particle equations through the source terms, are elliptic in character rather than hyperbolic. Thus, the modified Maxwell equations represent instantaneous action-at-a-distance without any retardation. As a matter of fact, the Darwin approximation preserves accuracy in the interaction Lagrangian up to the order of $(v/c)^2$ [Nielson and Lewis, 1976].

Since tearing mode instability and magnetic reconnection evolve on time scales of ion gyroperiods, an electromagnetic wave in such processes would propagate across the entire system on the same time scale. In these cases, the transverse displacement current is likely to be small in comparison to the conducting current, and the effect of the transverse displacement current is negligible. Thus, the Darwin model is proper for the simulation of tearing instability and magnetic reconnection. Therefore, the particle simulation model used for the present investigation of the driven magnetic reconnection process in the collisionless plasma was formulated using the Darwin approximation and the particle-in-cell (PIC) method. Notice that the electric field in the Darwin model must be advanced with other methods because the calculation of electric field directly from the displacement current term in Ampère's law could lead to significant inaccuracy [Swift, 1988].

4.2 A Darwin Model Using Hamiltonian Formulation

It has been shown by Nielson and Lewis [1976] that a particle simulation model using the Darwin approximation may be satisfactorily expressed using either Hamiltonian or Lagrangian formulation. In the Hamiltonian formulation, the force due to the transverse electric field is obtained implicitly through the equations of motion

for the particles, whereas in the Lagrangian formulation, the transverse electric field is found explicitly by using the divergence of the current transfer tensor as a source function. The calculation of electric field in the Lagrangian formulation is complicated [Nielson and Lewis, 1976] and the time derivative of the vector potential ($\partial\mathbf{A}/\partial t$) and the transverse electric field (\mathbf{E}_t) show significant differences [Swift, 1988]. The advantage of the Hamiltonian formulation is that it is not necessary to calculate \mathbf{E}_t , which is the same as $\partial\mathbf{A}/\partial t$. More comparison between the Hamiltonian and the Lagrangian formulations can be found in Swift [1988]. In the following, a particle simulation model with the Darwin approximation is formulated for the driven collisionless magnetic reconnection process in the Hamiltonian formulation.

According to the standard procedure [e.g., Goldstein, 1980], the Hamiltonian function of a system with charged particles can be written as

$$H = \sum_j \frac{1}{2m_j} (\mathbf{p}_j - \frac{q_j}{c} \mathbf{A})^2 + q_j \phi \quad (4.4)$$

where m_j , \mathbf{p}_j , and q_j are, respectively, the mass, the canonical momentum, and the charge of the j -th particle. Then, the Hamiltonian equations of motion for the j -th particle are given by

$$\frac{d\mathbf{p}_j}{dt} = -\frac{\partial H}{\partial \mathbf{x}_j} = \frac{q_j}{m_j c} (\nabla \mathbf{A}) \cdot (\mathbf{p}_j - \frac{q_j}{c} \mathbf{A}) - q_j \nabla \phi \quad (4.5)$$

$$\frac{d\mathbf{x}_j}{dt} = \frac{\partial H}{\partial \mathbf{p}_j} = \frac{1}{m_j} (\mathbf{p}_j - \frac{q_j}{c} \mathbf{A}) \quad (4.6)$$

where $\nabla \mathbf{A} = \mathbf{e}_x \partial \mathbf{A} / \partial x + \mathbf{e}_y \partial \mathbf{A} / \partial y + \mathbf{e}_z \partial \mathbf{A} / \partial z$ is a tensor and the potentials \mathbf{A} and ϕ are always evaluated at the positions of the particles.

In terms of particle variables, the charge density (ρ) and the current density (\mathbf{J}) can be written as

$$\rho = \sum_{\alpha} q_{\alpha} n_{\alpha} \quad (4.7)$$

$$\mathbf{J} = \sum_{\alpha} q_{\alpha} n_{\alpha} \langle \mathbf{v}_{\alpha} \rangle = \sum_{\alpha} \frac{q_{\alpha}}{m_{\alpha}} n_{\alpha} \langle \mathbf{p}_{\alpha} \rangle - \left(\sum_{\alpha} \frac{q_{\alpha}^2}{m_{\alpha} c} n_{\alpha} \right) \mathbf{A} \quad (4.8)$$

where α denotes particle species, q_{α} and n_{α} are, respectively, the charge and the spatial number density of species α , and $\langle \mathbf{v}_{\alpha} \rangle$ and $\langle \mathbf{p}_{\alpha} \rangle$ are the average velocity and canonical momentum for species α as functions of position and time. After inserting the source terms ρ and \mathbf{J} into (4.1) and (4.3), the field equations become

$$\nabla^2 \phi = -4\pi \sum_{\alpha} q_{\alpha} n_{\alpha} \quad (4.9)$$

and

$$\nabla^2 \mathbf{A} = -\frac{4\pi}{c} \sum_{\alpha} \frac{q_{\alpha}}{m_{\alpha}} n_{\alpha} \langle \mathbf{p}_{\alpha} \rangle + \frac{4\pi}{c^2} \left(\sum_{\alpha} \frac{q_{\alpha}^2}{m_{\alpha}} n_{\alpha} \right) \mathbf{A} + \frac{1}{c} \nabla \left(\frac{\partial \phi}{\partial t} \right) \quad (4.10)$$

By taking the divergence of (4.10), another field equation is obtained as

$$\nabla^2 \left(\frac{\partial \phi}{\partial t} \right) = 4\pi \sum_{\alpha} \frac{q_{\alpha}}{m_{\alpha}} \nabla \cdot \left(n_{\alpha} \langle \mathbf{p}_{\alpha} \rangle \right) - \frac{4\pi}{c} \left(\sum_{\alpha} \frac{q_{\alpha}^2}{m_{\alpha}} \nabla n_{\alpha} \right) \cdot \mathbf{A} \quad (4.11)$$

where the Coulomb gauge $\nabla \cdot \mathbf{A} = 0$ has been used. Notice that because of the instantaneous nature of the forces under the Darwin approximation, a direct computation of the time derivative of the electrostatic potential ($\partial\phi/\partial t$) by time differencing usually leads to numerical instability. Therefore, \mathbf{A} and $\partial\phi/\partial t$ have to be solved simultaneously with (4.10) and (4.11) by iteration, even though the electrostatic potential (ϕ) can be obtained by solving the Poisson equation (4.9) directly. Also, a supplementary operation is needed to ensure that the obtained vector potential (\mathbf{A}) satisfies the Coulomb gauge at each iteration [Nielson and Lewis, 1976].

The time differencing scheme for the equations of particle motion (4.5) and (4.6) can proceed in a variety of ways. Nielson and Lewis [1976] proposed a second order, leap-frog time differencing algorithm for the Darwin models based on

a predictor-corrector method in which the momenta of particles $\{\mathbf{p}_j\}$ are saved at half time-steps and the positions of particles $\{\mathbf{x}_j\}$ are saved at full time-steps. Thus, the equations of particle motion can be written as

$$\frac{\mathbf{P}_j^{n+1/2} - \mathbf{P}_j^{n-1/2}}{\Delta t} = \frac{q_j}{m_j c} (\nabla \mathbf{A}^n) \cdot \left(\frac{\mathbf{P}_j^{n+1/2} + \mathbf{P}_j^{n-1/2}}{2} - \frac{q_j}{c} \mathbf{A}^n \right) - q_j \nabla \phi^n \quad (4.12)$$

$$\frac{\mathbf{x}_j^{n+1} - \mathbf{x}_j^n}{\Delta t} = \frac{1}{m_j} \left(\mathbf{P}_j^{n+1/2} - \frac{q_j}{c} \mathbf{A}^{n+1/2} \right) \quad (4.13)$$

where the superscript denotes time-steps.

To obtain \mathbf{A}^n at the full time-step, the particle momentum $\mathbf{p}_j^{n-1/2}$ is first projected ahead by a half time-step to $\tilde{\mathbf{p}}_j^n$ by using the same rate of change that was used in obtaining $\mathbf{p}_j^{n-1/2}$. The equation for computing $\tilde{\mathbf{p}}_j^n$ is given by

$$\frac{\tilde{\mathbf{p}}_j^n - \mathbf{P}_j^{n-1/2}}{\Delta t/2} = \frac{q_j}{m_j c} (\nabla \mathbf{A}^{n-1}) \cdot \left(\frac{\mathbf{P}_j^{n-1/2} + \mathbf{P}_j^{n-3/2}}{2} - \frac{q_j}{c} \mathbf{A}^{n-1} \right) - q_j \nabla \phi^{n-1}$$

However, it is easy to verify that

$$\frac{\tilde{\mathbf{p}}_j^n - \mathbf{P}_j^{n-1/2}}{\Delta t/2} = \frac{q_j}{m_j c} (\nabla \mathbf{A}^{n-1}) \cdot \left(\frac{\tilde{\mathbf{p}}_j^n + \mathbf{P}_j^{n-1/2}}{2} - \frac{q_j}{c} \mathbf{A}^{n-1} \right) - q_j \nabla \phi^{n-1} + O(\Delta t) \quad (4.14)$$

where $O(\Delta t)$ represents terms of the order of Δt , which is smaller than the other terms on the right hand side of (4.14) and hence can be neglected. Therefore, the projected $\tilde{\mathbf{p}}_j^n$ can be approximately calculated from (4.14). Then, the potentials \mathbf{A}^n and ϕ^n are solved based on the sources computed from $\{\mathbf{x}_j^n\}$ and $\{\tilde{\mathbf{p}}_j^n\}$. After that, the momenta of particles are advanced by a full-time step according to (4.12). The vector potential at the half-time step, which is needed for particle position advancing, is obtained from extrapolation

$$\mathbf{A}^{n+1/2} = \frac{3}{2} \mathbf{A}^n - \frac{1}{2} \mathbf{A}^{n-1} \quad (4.15)$$

Finally, the positions of particles are moved by a full-time step according to (4.13). The above algorithm is very stable for the Hamiltonian formulation, although an analogous procedure in the Lagrangian formulation may be violently unstable [Nielson and Lewis, 1976].

A similar second-order, leap-frog time differencing scheme was later proposed by Swift [1986] in his simulation study of the collisionless tearing mode. In Swift's scheme, the basic algorithm is the same as that of Nielson and Lewis [1976], except that the momenta of particles are a half time-step ahead of the positions of particles and the particle positions, instead of the particle momenta, are first projected ahead by a half time-step from $\{\mathbf{x}_j^n\}$ to $\{\tilde{\mathbf{x}}_j^{n+1/2}\}$ by using the same rate of change used to obtain $\{\mathbf{x}_j^n\}$. The equation for projecting particle positions is given by

$$\frac{\tilde{\mathbf{x}}_j^{n+1/2} - \mathbf{x}_j^n}{\Delta t/2} = \frac{1}{m_j} \left(\mathbf{p}_j^{n-1/2} - \frac{q_j}{c} \mathbf{A}^{n-1/2} \right)$$

It is also easy to verify that

$$\frac{\tilde{\mathbf{x}}_j^{n+1/2} - \mathbf{x}_j^n}{\Delta t/2} = \frac{1}{m_j} \left(\mathbf{p}_j^{n+1/2} - \frac{q_j}{c} \mathbf{A}^{n-1/2} \right) + O(\Delta t) \quad (4.16)$$

where $O(\Delta t)$ represents terms of the order of Δt , which is smaller than the other terms on the right hand side of (4.16) and hence can be neglected. Thus, the projection of particle positions can be approximately computed from (4.16). Then, the vector potential $\mathbf{A}^{n+1/2}$ is solved based on the sources calculated from $\{\tilde{\mathbf{x}}_j^{n+1/2}\}$ and $\{\mathbf{p}_j^{n+1/2}\}$, and the vector potential at the full time-step is obtained by extrapolation from

$$\mathbf{A}^{n+1} = \frac{3}{2} \mathbf{A}^{n+1/2} - \frac{1}{2} \mathbf{A}^{n-1/2} \quad (4.17)$$

After the particle positions are moved from $\{\mathbf{x}_j^n\}$ to $\{\mathbf{x}_j^{n+1}\}$ with $\{\mathbf{p}_j^{n+1/2}\}$ and $\mathbf{A}^{n+1/2}$, the electrostatic potential ϕ^{n+1} is computed. Finally, the particle momenta are advanced from $\{\mathbf{p}_j^{n+1/2}\}$ to $\{\mathbf{p}_j^{n+3/2}\}$ based on \mathbf{A}^{n+1} and ϕ^{n+1} .

Two simulation codes have been developed and tested, one based on Nielson and Lewis's algorithm and the other based on Swift's scheme. It is found that for the same plasma parameters, the results obtained from these two codes do not show any significant differences, except that the first code consumes more CPU time than the second one, because (4.14) is much more complicated than (4.16). A more detailed investigation shows that $T_{\mathbf{x}_j}/T_{\mathbf{p}_j} \simeq 1 : 2$, where $T_{\mathbf{x}_j}$ is the CPU time needed for completing the particle position projection for all particles at once and $T_{\mathbf{p}_j}$ is the corresponding CPU time for particle momentum projection. Since both algorithms are stable in the Hamiltonian formulation and Swift's algorithm is more efficient than that of Nielson and Lewis, Swift's algorithm is adopted in the present simulation model for the driven collisionless magnetic reconnection.

4.3 A $2\frac{1}{2}$ -D Particle Simulation Model for Magnetic Reconnection

The basic equations for the present simulation model are (4.9)–(4.13) and (4.16)–(4.17). Notice that the simulation model described by the basic equations is general and multi-dimensional. However, in the following only the two-dimensional (2-D) case, with $-L_x \leq x \leq L_x$ and $-L_z \leq z \leq L_z$, is considered, and the variations of all physical quantities in the y -direction are assumed to be zero, e.g., $\partial/\partial y = 0$. Since the model is two-dimensional (2-D) in the configuration space (x, z) and three-dimensional (3-D) in the momentum space (p_x, p_y, p_z) , it is also referred to as a two-and-one-half-dimensional ($2\frac{1}{2}$ -D) model. The above basic equations are in dimensional form, i.e., each physical quantity is expressed in its dimensional unit. To transform them into a dimensionless form that can be used conveniently in the simulation, a normalization procedure is needed. The normalization of physical

quantities in an MHD fluid simulation model is straightforward. But the normalization of physical quantities in the particle simulation model is not so trivial and is somewhat confusing.

The first step is to determine the charge and mass of the macro particles used in the simulation. If q_α , m_α , and \tilde{n}_α are, respectively, the charge, mass, and number density for species α in dimensional units, the macro charge (Q_α) and macro mass (M_α) of species α in the simulation are given respectively by

$$Q_\alpha = q_\alpha \tilde{n}_\alpha \left(\frac{N_x N_z}{N_\alpha} \right) \Delta_x \Delta_z \quad (4.18)$$

and

$$M_\alpha = m_\alpha \tilde{n}_\alpha \left(\frac{N_x N_z}{N_\alpha} \right) \Delta_x \Delta_z \quad (4.19)$$

where N_x and Δ_x respectively are the number of grid (mesh) cells and grid spacing in the x -direction, N_z and Δ_z respectively are the number of grid cells and grid spacing in the z -direction, and N_α is the number of macro particles used in the simulation for species α . In the simulation, the macro charge is needed for calculating the charge density and the current density, and the macro mass is needed for computing the kinetic energy of particles.

Then, a normalization unit must be specified for the normalization of each physical quantity used in the simulation. In the present model, $t_0 = \Omega_e^{-1} = (eB_0/m_e c)^{-1}$, $x_0 = \rho_e$, $v_0 = x_0/t_0 = v_{the}$, B_0 , $A_0 = B_0 x_0 = B_0 \rho_e$, $\phi_0 = 2T_e/e$, $E_0 = \phi_0/x_0 = 2T_e/e\rho_e$, and $p_0 = m_e v_0 = m_e v_{the}$ are chosen as the normalization units for the time, space, speed, magnetic field, vector potential, electrostatic potential, electric field, and particle momentum, respectively. In above, Ω_e , ρ_e , $v_{the} = \Omega_e \rho_e$, and $T_e = m_e v_{the}^2/2$, are respectively the gyrofrequency, the Larmor radius, the thermal speed, and the thermal energy of an electron. After dividing

each physical quantity with its corresponding normalization unit, the dimensionless physical quantities are obtained. These dimensionless quantities are $t^* = t/t_0$, $\mathbf{x}^* = \mathbf{x}/x_0$, $\mathbf{v}^* = \mathbf{v}/v_0$, $\mathbf{p}^* = \mathbf{p}/p_0$, $\mathbf{A}^* = \mathbf{A}/A_0$, $\mathbf{B}^* = \mathbf{B}/B_0$, $\phi^* = \phi/\phi_0$, $\chi^* = \chi/\chi_0$, and $\mathbf{E}^* = \mathbf{E}/E_0$, where $\chi = \partial\phi/\partial t$ and $\chi_0 = \phi_0/t_0$ has been used.

Inserting the dimensionless variables specified above into the basic equations (4.9)-(4.13), the dimensionless equations used in the simulation are found to be

$$\nabla^2 \phi = -\alpha_e \rho \quad (4.20)$$

$$\nabla^2 \mathbf{A} = -\alpha_m \mathbf{J} + \frac{\alpha_m}{\alpha_e} \nabla \chi \quad (4.21)$$

$$\nabla^2 \chi = \alpha_e \nabla \cdot \mathbf{J} \quad (4.22)$$

$$\frac{d\mathbf{p}_i}{dt} = \frac{1}{\gamma} (\nabla \mathbf{A}) \cdot (\mathbf{p}_i - \mathbf{A}) - \nabla \phi \quad (4.23)$$

$$\frac{d\mathbf{x}_i}{dt} = \frac{1}{\gamma} (\mathbf{p}_i - \mathbf{A}) = \mathbf{v}_i \quad (4.24)$$

$$\frac{d\mathbf{p}_e}{dt} = -(\nabla \mathbf{A}) \cdot (\mathbf{p}_e + \mathbf{A}) + \nabla \phi \quad (4.25)$$

$$\frac{d\mathbf{x}_e}{dt} = (\mathbf{p}_e + \mathbf{A}) = \mathbf{v}_e \quad (4.26)$$

where

$$\alpha_e = (4\pi\bar{n}_e e^2/m_e)(\rho_e^2/v_{the}^2)(N_x N_z/N_e)$$

$$\alpha_m = (4\pi\bar{n}_e e^2/m_e)(\rho_e^2/c^2)(N_x N_z/N_e)$$

and $\gamma = m_i/m_e$ respectively are the electrostatic coupling constraint, the magnetic coupling constraint, and the mass ratio of ion to electron used in the simulation. In (4.20)-(4.26), the * sign, denoting the dimensionless variables, has been dropped from all of the normalized quantities for the sake of convenience. Notice that Swift's time-integration algorithm, which has been described earlier, is used for the equations of particle motion (4.23)-(4.26) in the present simulation.

In the simulation, the charge density ρ and the current density \mathbf{J} in the field equations respectively are computed from

$$\rho = (n_i - n_e) \quad (4.27)$$

$$\mathbf{J} = [(n\mathbf{u})_i - (n\mathbf{u})_e] \quad (4.28)$$

where

$$n = \sum_k S[\mathbf{x} - \mathbf{x}_k(t)] \quad (4.29)$$

$$(n\mathbf{u})_i = \sum_k \frac{1}{\gamma} [\mathbf{p}_k - \mathbf{A}(\mathbf{x}_k)] S[\mathbf{x} - \mathbf{x}_k(t)] \quad (4.30)$$

$$(n\mathbf{u})_e = \sum_k [\mathbf{p}_k + \mathbf{A}(\mathbf{x}_k)] S[\mathbf{x} - \mathbf{x}_k(t)] \quad (4.31)$$

and $S[\mathbf{x} - \mathbf{x}_k(t)]$ is the weighting factor based on the first-order PIC bilinear interpolation method as discussed in Birdsall and Langdon [1985]. Notice that the fields are evaluated at the positions of particles in the equation of motion, which is given by

$$\mathbf{A}(\mathbf{x}_k) = \int S[\mathbf{x} - \mathbf{x}_k(t)] \mathbf{A}(\mathbf{x}) d^2\mathbf{x}.$$

After some straightforward algebraic manipulations, (4.21) and (4.22) can be rewritten as

$$(\nabla^2 - \alpha_m \eta) \mathbf{A} = -\alpha_m \left(\frac{1}{\gamma} \mathbf{\Pi}_i - \mathbf{\Pi}_e \right) + \frac{\alpha_m}{\alpha_e} \nabla \chi \quad (4.32)$$

$$\nabla^2 \chi = \alpha_e [\nabla \cdot (\mathbf{\Pi}_i - \mathbf{\Pi}_e) - \nabla \cdot (\eta \mathbf{A})] \quad (4.33)$$

where

$$\mathbf{\Pi} = \sum_k \mathbf{p}_k S[\mathbf{x} - \mathbf{x}_k(t)]$$

and

$$\eta = \frac{1}{\gamma} n_i + n_e$$

Here an assumption has been made that

$$\sum_k \mathbf{A}(\mathbf{x}_k) S[\mathbf{x} - \mathbf{x}_k(t)] \simeq \mathbf{A}(\mathbf{x}) \sum_k S[\mathbf{x} - \mathbf{x}_k(t)]$$

As mentioned earlier, due to the coupling between \mathbf{A} and χ , equations (4.32) and (4.33) must be solved through iterations, and at each iteration a supplementary operation is necessary to ensure that solution \mathbf{A} satisfies $\nabla \cdot \mathbf{A} = 0$. The iteration scheme used in the present simulation can be written as

$$\nabla^2 \chi^{l+1} = \alpha_e [\nabla \cdot (\mathbf{\Pi}_i - \mathbf{\Pi}_e) - \nabla \cdot (\eta \mathbf{A}^l)] \quad (4.34)$$

$$(\nabla^2 - \alpha_m \bar{\eta}) \tilde{\mathbf{A}}^{l+1} = -\alpha_m (\bar{\eta} - \eta) \mathbf{A}^l - \alpha_m \left(\frac{1}{\gamma} \mathbf{\Pi}_i - \mathbf{\Pi}_e \right) + \frac{\alpha_m}{\alpha_e} \nabla \chi^{l+1} \quad (4.35)$$

$$\nabla^2 \Psi^{l+1} = \nabla \cdot \tilde{\mathbf{A}}^{l+1} \quad (4.36)$$

$$\mathbf{A}^{l+1} = \tilde{\mathbf{A}}^{l+1} - \nabla \Psi^{l+1} \quad (4.37)$$

where l is the iteration level, $\tilde{\mathbf{A}}$ is the intermediate value of the vector potential, and

$$\bar{\eta} = \frac{1}{2} (\eta_{max} + \eta_{min})$$

in which η_{max} and η_{min} respectively are the maximum and minimum values of $\eta(\mathbf{x}, z)$ in the $\mathbf{x} - z$ plane.

The total number of iterations can be either fixed in advance or determined by the convergence of the process. For example, for a given convergence parameter ε , the iteration stops when $|\mathbf{A}^{l+1} - \mathbf{A}^l|/|\mathbf{A}^l| \leq \varepsilon$ is reached. It is found in the simulation that for $\varepsilon = 0.001$, the total number of iterations is usually less than five and that for $\varepsilon = 0.0001$, the total number of iterations generally is smaller than ten. In the present simulation, the convergence parameter is chosen to be

either $\varepsilon = 0.005$ or $\varepsilon = 0.0001$. The partial differential equation solver FISHPAK, developed by NCAR, is used to solve the field equations.

In the Hamiltonian formulation, the electric field and the magnetic field can be obtained for the purpose of diagnostics from

$$\mathbf{E} = -\nabla\phi - \frac{\partial\mathbf{A}}{\partial t} \quad (4.38)$$

and

$$\mathbf{B} = \nabla \times \mathbf{A} \quad (4.39)$$

where the electric field includes both the electrostatic and induction fields. It is easy to verify that in the present simulation model the total magnetic energy (E_M^*), the total electric energy (E_E^*), the total kinetic energy of ions (E_i^*), and the total kinetic energy of electrons (E_e^*) respectively are given by

$$E_M^* = \frac{E_M}{E_{0e}} = \frac{1}{\alpha_m} \sum_{i,j} B_{i,j}^2 \quad (4.40)$$

$$E_E^* = \frac{E_E}{E_{0e}} = \frac{1}{\alpha_e} \sum_{i,j} E_{i,j}^2 \quad (4.41)$$

$$E_i^* = \frac{E_i}{E_{0e}} = \gamma \sum_k v_{ik}^2 \quad (4.42)$$

and

$$E_e^* = \frac{E_e}{E_{0e}} = \sum_k v_{ek}^2 \quad (4.43)$$

where $E_{0e} = M_e v_0^2 / 2$ is the kinetic energy of a single macro electron, $B_{i,j}$ and $E_{i,j}$ respectively are the magnetic field and electric field at the grid point $\{i, j\}$, v_{ik} is the speed of the k -th macro ion, and v_{ek} is the speed of the k -th macro electron.

Thus, the normalized total energy in the simulation system ($E_{tot}^* = E_{tot}/E_{0e}$) can be written as

$$E_{tot}^* = \sum_k v_{ek}^2 + \gamma \sum_k v_{ik}^2 + \sum_{i,j} \left(\frac{1}{\alpha_m} B_{i,j}^2 + \frac{1}{\alpha_e} E_{i,j}^2 \right) \quad (4.44)$$

In this section, a $2\frac{1}{2}$ -dimensional particle simulation model using the Darwin approximation was developed in the Hamiltonian formulation for the study of the driven collisionless magnetic reconnection process. The normalization of the simulation model was discussed. In the following sections, the initial and boundary conditions used in simulating the driven collisionless magnetic reconnection process are presented. The initialization of the simulation will also be discussed.

4.4 Initial Conditions

The initial magnetic field configuration in the present simulation is assumed to be a one-dimensional current sheet located at $x = x_0$ and surrounded by background plasma. The magnetic field has only an antiparallel B_z component and the current is in the y -direction. The current sheet can be either symmetric or asymmetric. The general form of the initial magnetic field can be written as

$$B_z(x, z) = \frac{B_{zm} - B_{zs}}{2} - \frac{B_{zm} + B_{zs}}{2} \tanh\left(\frac{x - x_0}{L}\right) \quad (4.45)$$

where $B_{zm} = B_z(-\infty, z)$ and $B_{zs} = -B_z(\infty, z)$ respectively are the magnetic fields outside the current sheet; x_0 is the current sheet location, determined by $\tanh(x_0/L) = -(B_{zm} - B_{zs})/(B_{zm} + B_{zs})$; and L is the the current sheet thickness. The corresponding initial vector potential is found to be

$$A_x(x, z) = 0 \quad (4.46)$$

$$A_y(x, z) = \frac{B_{zm} - B_{zs}}{2}(x - x_0) - L \frac{B_{zm} + B_{zs}}{2} \ln\left[\cosh\left(\frac{x - x_0}{L}\right)\right] \quad (4.47)$$

$$A_z(x, z) = 0 \quad (4.48)$$

Under the assumption that the initial zero order electric field is zero, initial electrostatic potential is found to be zero

$$\phi(x, z) = 0 \quad (4.49)$$

The initial time derivative of the electrostatic potential is also assumed to be zero

$$\chi(x, z) = 0 \quad (4.50)$$

The particle temperature profile, in general, can be written as

$$T_\alpha(x, z) = \frac{T_{\alpha m} + T_{\alpha s}}{2} - \frac{T_{\alpha m} - T_{\alpha s}}{2} \tanh\left(\frac{x - x_0}{L}\right) \quad (4.51)$$

where $T_{\alpha m} = T_\alpha(-\infty, z)$ and $T_{\alpha s} = T_\alpha(\infty, z)$ respectively are the particle temperatures outside the current sheet for species α . Due to the elimination of the zero order electric field, ions and electrons must have the same particle number density profile, i.e., $n_i(x, z) = n_e(x, z) = n(x, z)$. In the initial equilibrium configuration, the pressure gradient is balanced by the $\mathbf{J} \times \mathbf{B}$ force. Thus, the particle number density can be obtained from the pressure balance condition

$$n(x, z)[T_i(x, z) + T_e(x, z)] + \frac{B_z^2(x, z)}{8\pi} = \frac{B_{zm}^2}{8\pi}(1 + \beta_m) = \frac{B_{zs}^2}{8\pi}(1 + \beta_s) \quad (4.52)$$

where β_m and β_s are the ratios of plasma pressure to magnetic pressure at $x = -\infty$ and $x = +\infty$, respectively.

The initial particle velocity distribution is assumed to be a drift Maxwellian distribution, with ions drifting in the y -direction and electrons drifting in the opposite direction. The local total drift speed of particles is determined from

$$U_i - U_e = -\frac{\frac{dB_x}{dz}}{\frac{4\pi}{c}en} \quad (4.53)$$

where U_i and U_e respectively are the drift speeds for ions and electrons. The drift speed of ions is related to the drift speed of electrons by

$$\frac{U_i}{T_i} = -\frac{U_e}{T_e} \quad (4.54)$$

where $T_i = \frac{1}{2}m_i v_{thi}^2$ is the ion thermal energy and $T_e = \frac{1}{2}m_e v_{the}^2$ is the electron thermal energy. Notice that as a special case, when the current sheet is symmetric ($B_{zm} = B_{ze}$), the temperature profile is a constant ($T_{\alpha m} = T_{\alpha s}$), and the ratio of plasma pressure to magnetic pressure outside the current sheet is zero ($\beta_m = \beta_s = 0$), the well-known Harris [1962] current model is obtained.

In the simulation, ions are loaded on the top of electrons so that the initial electrostatic field is eliminated. The drift speed for ions is calculated from

$$U_i = \frac{|\nabla \times \mathbf{B}|}{\alpha_m n_i (1 + T_e/T_i)} \quad (4.55)$$

Then, the electron drift speed is obtained from (4.54). After the velocities are assigned to the particles, the self-consistent vector potential is computed and particle momenta are initialized for ions and electrons according to (4.24) and (4.26) respectively.

Before the driven boundary conditions are imposed for study of the driven collisionless magnetic reconnection process, the simulation model developed above is checked for energy conservation. A test run is carried out to simulate the collisionless tearing mode instability, in which the Harris [1962] current sheet model

is used as the initial magnetic field and plasma configurations. In the test run, a periodic boundary condition is imposed in the z -direction while a Dirichlet or Neumann boundary condition is used in the x -direction. The test is run from $t = 0$ to $t = 600\Omega_e^{-1}$. During the test run, it is observed that the total energy is conserved within 0.1%. Therefore, it is believed that numerical heating or cooling is insignificant in the present simulation model.

4.5 Boundary Conditions Necessary for Driven Reconnection

One of the applications of particle simulation in fusion and space plasma research is the study of the collisionless tearing mode instabilities and magnetic field line reconnection processes observed in fusion devices, in the earth's magnetosphere, and in other space and astrophysical plasma environments [e.g., Dickman et al., 1969; Katanuma and Kamimura, 1980; Terasawa, 1981; Brunel et al., 1982; Leboeuf et al., 1982; Ambrosiano et al., 1983, 1986; Swift, 1982, 1983, 1986; Price and Swift, 1986; Ding et al., 1986; Hoshino, 1987; Swift and Allen, 1987; Lee and Ding, 1987; Hewett et al., 1988; Francis et al., 1989; Allen and Swift, 1989; Pritchett et al., 1989; Ding and Lee, 1990]. However, in most of the previous simulations, either a one-component plasma model or periodic boundary conditions for particles and fields was used. In some 2-D simulations, the periodic condition is imposed in one direction, while a fixed value boundary or a fixed gradient boundary is applied in the other direction.

The one-component plasma model is the simplest particle simulation model, in which only the ion dynamics is included, while the electron dynamics and electrostatic interaction are neglected. The periodic conditions, on the other hand, represent the simplest and most convenient method for handling the particles and

fields at the boundaries of simulation domain, where the simulated plasma process takes place. In the present simulation, the simulation domain is a rectangular box in the $x - z$ plane, with $-L_x \leq x \leq L_x$ and $-L_z \leq z \leq L_z$. With the periodic boundary conditions, particles leaving the simulation domain through one of its boundaries are reintroduced into the simulation domain at the opposite boundary and field equations are solved by taking advantage of the fast Fourier transform (FFT) method. However, it has been found that the periodic boundary conditions imposed on the simulation domain significantly affect the nonlinear development of the tearing instabilities and hence the nonlinear evolution of magnetic reconnection processes due to the presence of nonphysical forces in the periodic system [e.g., Price and Swift, 1986]. Therefore, to investigate the nonlinear development of the collisionless tearing mode instabilities and magnetic reconnection processes in a more realistic manner, periodic boundary conditions become inadequate.

It has also been observed that with the periodic conditions imposed at the simulation boundary, the simulation of tearing mode instabilities and magnetic reconnection usually ends in a more or less steady and saturated state. But in reality, a magnetic reconnection process, such as FTEs at the dayside magnetopause [Russell and Elphic, 1978, 1979], is intrinsically a sporadic and intermittent process driven by the solar wind when the interplanetary magnetic field has a southward B_z component. To simulate the driven magnetic field reconnection process, in which both incoming and outgoing plasma flows are present, the periodic boundary conditions become improper.

To introduce the incoming plasma flow, a driven boundary condition is needed, through which the incoming plasma and magnetic field are pumped into the simulation domain. To allow the outgoing plasma flow, on the other hand, a non-periodic open boundary condition is required, across which the outgoing plasma

can escape freely from the simulation domain. In the simulation, the driven and nonperiodic open boundary conditions are necessary for advancing particles and for solving fields. The first particle simulation of the magnetic reconnection process with driven and nonperiodic open boundaries was reported by Ding et al. [1986]. In their one-component particle simulation, magnetic reconnection is observed to take place intermittently, leading to the repeated formation and convection of magnetic islands and the generation of superthermal particles. Later on, the driven and nonperiodic open boundary conditions are generalized and applied to the two-component full particle simulation [e.g., Ding and Lee, 1990]. In the following, the particle boundary conditions are presented before the boundary conditions for fields are discussed.

The concept and application of a particle buffer zone are closely related to the new particle boundary conditions. The particle buffer zone is a special region set up adjacent to the simulation domain. Its purpose is to prevent the boundary from interrupting particle orbits and generating spurious boundary currents [Naitou et al., 1979]. Another benefit of using a particle buffer zone in the present study to handle particles which cross the boundaries of the simulation domain is to facilitate the incoming and outgoing plasma flows at the simulation boundaries.

In the present simulation, the particle buffer zone is technically divided into two parts: an inner buffer zone and an outer buffer zone. The inner buffer zone, located outside the simulation domain but inside the outer buffer zone, has a typical width of 6Δ , where Δ is the grid size. The outer buffer zone, located outside the inner buffer zone, has a typical width of 2Δ . Initially, both particle buffer zones and the simulation domain are loaded with particles according to initial particle distributions and field potentials. Thus, plasma quantities experience a continuous variation across the simulation boundary. Particles in the simulation

are technically divided into three parts: the simulation particles that are located inside the simulation domain, the buffer zone particles that are located in the inner buffer zone, and the reservoir particles that are located in the outer buffer zone. During the simulation, only the simulation particles contribute to the sources for computing field potentials (\mathbf{A} and ϕ). The buffer zone and reservoir particles, whose motion is calculated based on the extrapolated fields, provide a reservoir of particles.

A simulation particle becomes a buffer zone particle when it moves from the simulation domain across the simulation boundary into the inner buffer zone; whereas a buffer zone particle becomes a simulation particle when it moves from the inner buffer zone across the simulation boundary into the simulation domain. A buffer zone particle in the inner buffer zone keeps its identity until it moves into the outer buffer zone, becoming a reservoir particle. A reservoir particle becomes a buffer particle when it moves into the inner buffer zone, whereas a reservoir particle is eliminated from the simulation when it moves out of the outer buffer zone. At the end of each time step, the reservoir particles in the outer buffer zone are replaced with new thermal particles. A schematic diagram of simulation domain and particle buffer zones is shown in Figure 4.1. The blank area in the center represents the simulation domain while the shaded area adjacent to the simulation domain represents the particle buffer zones. The inner buffer zone and the outer buffer zone are separated by the dashed line. Small arrows in Figure 4.1 indicate the imposed incoming plasma flow as well as the outgoing plasma flow generated during the simulated magnetic reconnection process.

The imposed incoming plasma flow is formed by new particles injected into the upper and lower parts of the inner buffer zone at every time step. The average density flux of the incoming plasma flow is $N_b \mathbf{V}_1$, where N_b and $\mathbf{V}_1 = \mp V_1 \mathbf{e}_z$ are,

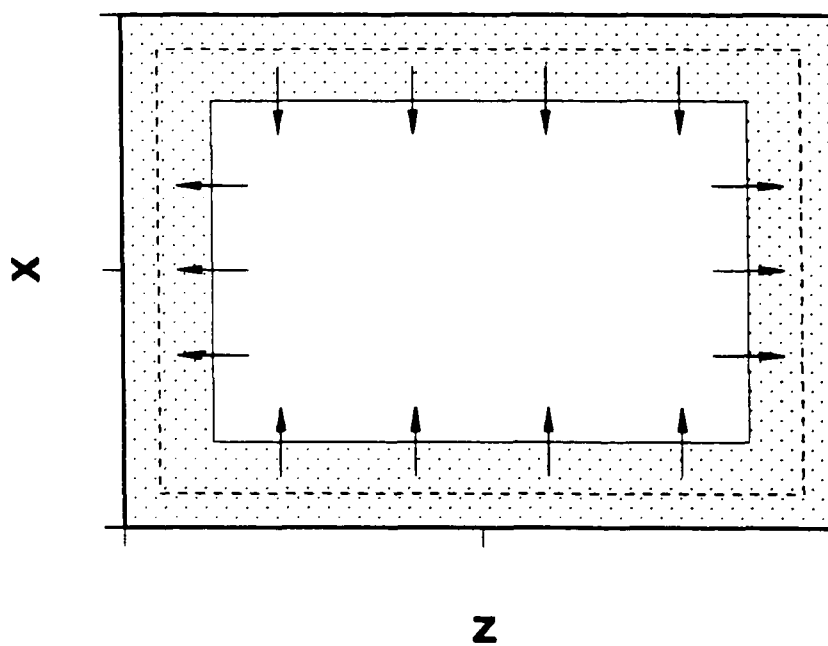


Figure 4.1 A schematic diagram of simulation domain (blank area) and particle buffer zones (shaded area). Dashed line separates the inner buffer zone from the outer buffer zone. Arrows indicate the imposed incoming plasma flow as well as the outgoing plasma flow generated during the simulated magnetic reconnection process.

respectively, the average particle number density and average velocity of the incoming plasma at $x = \pm L_x$. Due to the $\mathbf{E} \times \mathbf{B}$ drift motion, these buffer zone particles are convected into the simulation domain, becoming simulation particles. On the other hand, the outgoing plasma flow is formed during the magnetic reconnection process. Along with the outgoing plasma flow, simulation particles convect out of the left and right boundaries of the simulation domain and move into the left and right parts of the inner buffer zone, becoming buffer zone particles. Thus, with the new driven and nonperiodic open particle boundary conditions, it is possible to maintain an imposed incoming plasma flow at the top and bottom boundaries of the simulation domain, while allowing outgoing plasma flow to escape freely from the simulation domain through the left and right boundaries. Notice that the present particle boundary is different from the traditional periodic boundary, in which particles leaving the left (right) boundary of the simulation domain are reintroduced into the simulation domain at the right (left) boundary.

The driven boundary condition at $x = \pm L_x$ and the nonperiodic open boundary condition at $z = \pm L_z$ for particles were discussed above. The driven and nonperiodic open boundary conditions for potential fields are presented below. Compared to the boundary conditions for the electrostatic potential (ϕ) and its time derivative (χ), the boundary conditions for the vector potential (\mathbf{A}) are relatively simple. To maintain the constant influx ($N_b \mathbf{V}_1$) of the incoming plasma at the driven boundary ($x = \pm L_x$), a constant electric field \mathbf{E}_1 is imposed. The electric field is determined from $\mathbf{E}_1 = -\mathbf{V}_1 \times \mathbf{B}_0 / c$ so that the average incoming plasma flow velocity \mathbf{V}_1 is consistent with the $\mathbf{E}_1 \times \mathbf{B}_0$ drift velocity at the boundary, where \mathbf{B}_0 is the initial magnetic field at the boundary. Since \mathbf{B}_0 has only the z -component and \mathbf{V}_1 has only the x -component, \mathbf{E}_1 is found to only have the y -component, i.e., $\mathbf{E}_1 = E_{1y} \mathbf{e}_y$. Through the driven boundary condition described above, the

incoming plasma and magnetic field are pumped continuously into the simulation domain. At the nonperiodic open outflow boundary ($z = \pm L_z$), on the other hand, the Neumann boundary condition is used, in which the normal derivative of \mathbf{A} is set to zero. However, as an additional constraint, the vector potential is required to satisfy the Coulomb gauge $\nabla \cdot \mathbf{A} = 0$ at the boundary. Therefore, boundary conditions for the vector potential \mathbf{A} at the driven boundary $x = \pm L_x$ are given by

$$\frac{\partial A_x}{\partial x} = 0 \quad (4.56)$$

$$A_y(\pm L_x, z, t) = A_y(\pm L_x, z, 0) - V_1 B_{0z}(\pm L_x, z, 0)t \quad (4.57)$$

$$A_z(\pm L_x, z, t) = A_z(\pm L_x, z, 0) \quad (4.58)$$

At the nonperiodic open outflow boundary $z = \pm L_z$, the boundary conditions for the vector potential \mathbf{A} are given by

$$A_x(x, \pm L_z, t) = A_x(x, \pm L_z, 0) \quad (4.59)$$

$$\frac{\partial A_y}{\partial z} = 0 \quad (4.60)$$

$$\frac{\partial A_z}{\partial z} = 0 \quad (4.61)$$

Notice that the boundary condition (4.60) for A_y at the nonperiodic open outflow boundary $z = \pm L_z$ precludes the existence of magnetic field component B_x at the boundary. However, the existence of a normal magnetic field component, B_x in the present coordinate system, at the outflow boundary may be important for the magnetic reconnection process [e.g., Petschek, 1964]. To allow the presence of B_x at the outflow boundary, an alternate boundary condition may be used for A_y at $z = \pm L_z$, i.e.,

$$\frac{\partial^2 A_y}{\partial z^2} = 0 \quad (4.60')$$

In the present simulation, either (4.60) or (4.60') is used as the boundary condition for A_y at the nonperiodic open outflow boundary. An example of magnetic field lines, represented by the contours of A_y , observed in the simulation is shown in Figure 4.2. In Figure 4.2a, boundary condition (4.60) is used at the outflow boundary while in Figure 4.2b, boundary condition (4.60') is applied. It can be seen clearly that with the boundary condition (4.60') magnetic field lines may have a significant B_x component at the outflow boundary $z = \pm L_z$.

Compared to the boundary conditions for the vector potential \mathbf{A} , the boundary conditions for the electrostatic potential ϕ , as well as its time derivative χ , are very complicated and tricky. At the driven boundary $x = \pm L_x$, magnetic field lines are straight lines parallel to the boundary of the simulation domain. It is reasonable to assume that the magnetic field lines are equal potential lines at the boundary $x = \pm L_x$, since low frequency perturbations such as the tearing mode will not support a parallel electric field. Thus, the electrostatic potential and its time derivative are assumed to be constant along the driven boundary, i.e., at $x = \pm L_x$,

$$\phi(\pm L_x, z, t) = \phi(\pm L_x, z, 0) = 0 \quad (4.62)$$

$$\chi(\pm L_x, z, t) = \chi(\pm L_x, z, 0) = 0 \quad (4.63)$$

At the nonperiodic open outflow boundary $z = \pm L_z$, where magnetic field lines are either oblique or perpendicular to the simulation domain boundary depending on the boundary conditions of \mathbf{A} , a constant potential is no longer a good assumption. As an attempt to solve for ϕ and χ , the Neumann boundary condition is used, in which the normal derivatives of ϕ and χ are assumed to be zero at the outflow boundary $z = \pm L_z$. However, it is observed that with the boundary conditions for ϕ and χ described above, a large electrostatic potential is generated in the simulation.

MAGNETIC FIELD LINES

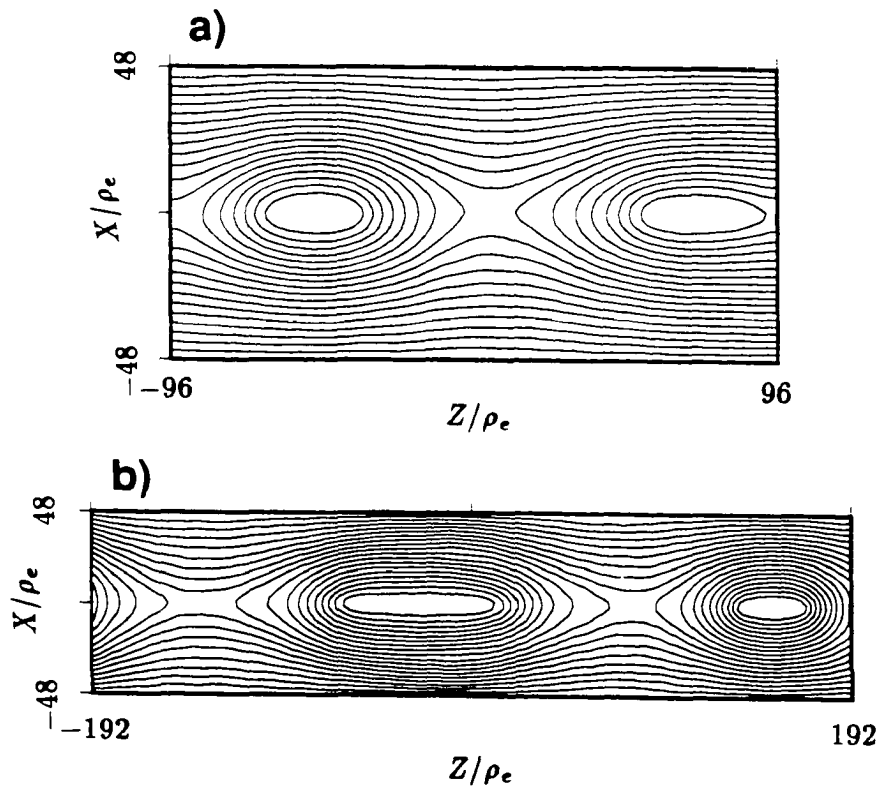


Figure 4.2 Magnetic field lines, represented by the contours of A_y , observed in the simulation with different boundary conditions at the nonperiodic open outflow boundary, (a) $\partial A_y / \partial z = 0$ at $z = \pm L_z$ and (b) $\partial^2 A_y / \partial z^2 = 0$ at $z = \pm L_z$.

Such large electrostatic potential is found to be caused by the Neumann boundary conditions applied to ϕ at the outflow boundary $z = \pm L_z$.

The generation of large electrostatic potential can be explained as follows. If a charge Q is located at $z = z_0$ near the outflow boundary $z = L_z$ and the distance from the charge Q to the boundary $z = L_z$ is $L_z - z_0$, an image charge $Q' = Q$ is induced outside the outflow boundary at $z = 2L_z - z_0$ with the boundary condition $\partial\phi/\partial z = 0$ imposed at $z = L_z$. If the charge Q is a net charge caused by the charge separation, $Q > 0$ means more ions and fewer electrons are located at $z = z_0$. Due to the presence of the image charge $Q' > 0$ at $z = 2L_z - z_0$, electrons are attracted towards the boundary $z = L_z$ while ions are expelled from the boundary. Because of its smaller mass, an electron may move easily across the boundary under the attraction of the image charge, leading to an even larger net positive charge and larger charge separation at $z = z_0$. This is a positive feedback process, in which a small charge separation causes a larger charge separation. Thus, a large electrostatic potential is generated in the simulation, leading to the presence of a large electrostatic field. The above scenario can also be applied to the outflow boundary at $z = -L_z$. However, if $Q < 0$, more electrons and fewer ions are located at $z = z_0$; a negative image charge is induced outside the boundary; and electrons are expelled from the boundary, while ions are attracted toward the boundary. But an ion is slower than an electron to cross the boundary due to its larger mass. On the other hand, an electron may be expelled away from $z = z_0$ even before the ions move away, resulting in a decrease of the negative net charge at $z = z_0$. Thus, a negative net charge $Q < 0$ at $z = z_0$ tends to be neutralized rather than amplified. An overreaction of electrons may lead to the presence of a positive charge $Q > 0$ at $z = z_0$. Therefore, it is clear that the Neumann boundary condition ($\partial\phi/\partial z = 0$) is not a proper choice for handling the electrostatic potential for a nonperiodic

open boundary. Notice that the Neumann boundary condition $\partial\phi/\partial z = 0$ may also result in numerical instabilities in the particle simulation, if particle fluxes across the boundary are improperly correlated with the variations of the electrostatic potential [Swift and Ambrosiano, 1981].

To avoid the influence of the induced image charges on the particles in the simulation domain, a force free boundary condition is chosen for ϕ as well as χ at the nonperiodic open outflow boundary, i.e., at $z = \pm L_z$,

$$\phi(\mathbf{x}, \pm L_z, t) = \text{force free} \quad (4.64)$$

$$\chi(\mathbf{x}, \pm L_z, t) = \text{force free} \quad (4.65)$$

With the force free boundary condition imposed at the outflow boundary, no image charges are induced outside the boundary and the plasma inside the simulation domain sees a charge neutral or charge vacuum plasma environment outside the boundary, even though buffer zone and reservoir particles are present in the particle buffer zones. Thus, the Poisson equation is solved inside the simulation domain while the Laplace equation is solved outside the simulation domain. By matching the solution of the Poisson equation to the appropriate decaying solution of the Laplace equation at the boundary of the simulation domain, the desired potential, which satisfies the force free boundary condition, is obtained. Notice that the force free boundary condition used in the present simulation is similar to the vacuum boundary condition discussed in Birdsall and Langdon [1985]. The detailed procedure of solving the potential ϕ with the force free boundary condition is described below.

Since the potential $\phi(\pm L_x, z) = 0$ at the driven boundary $x = \pm L_x$, a discrete sine transform can be made on the charge density and the potential in the x -direction, i.e.,

$$\hat{\phi}_{k,j} = \sum_{i=1}^{N'_x} \phi_{i,j} \sin \left[\frac{\pi}{N'_x - 1} (k-1)(i-1) \right] \quad (4.66)$$

$$\hat{\rho}_{k,j} = \sum_{i=1}^{N'_x} \rho_{i,j} \sin \left[\frac{\pi}{N'_x - 1} (k-1)(i-1) \right] \quad (4.67)$$

where i is the grid point index in the x -direction, j is the grid point index in the z -direction, k is the mode number index in the sine transform, $\phi_{i,j}$ and $\rho_{i,j}$ are respectively the electrostatic potential and the charge density at the grid point $\{i, j\}$ in the $x - z$ space, $\hat{\phi}_{k,j}$ and $\hat{\rho}_{k,j}$ are respectively the k -component of the electrostatic potential and the charge density in the $k - z$ phase space, and N'_x is the number of grid points in the x -direction. The inverse sine transforms of ϕ and ρ are given by

$$\phi_{i,j} = \frac{1}{N'_x - 1} \sum_{k=1}^{N'_x} \hat{\phi}_{k,j} \sin \left[\frac{\pi}{N'_x - 1} (k-1)(i-1) \right] \quad (4.68)$$

$$\rho_{i,j} = \frac{1}{N'_x - 1} \sum_{k=1}^{N'_x} \hat{\rho}_{k,j} \sin \left[\frac{\pi}{N'_x - 1} (k-1)(i-1) \right] \quad (4.69)$$

With the standard 2-D five-point central differencing scheme, the Poisson equation for the electrostatic potential (4.20) can be written as

$$\frac{\phi_{i+1,j} + \phi_{i-1,j} - 2\phi_{i,j}}{(\Delta x)^2} + \frac{\phi_{i,j+1} + \phi_{i,j-1} - 2\phi_{i,j}}{(\Delta z)^2} = -\alpha_e \rho_{i,j} \quad (4.70)$$

After substituting (4.68) and (4.69) into (4.70),

$$\hat{\phi}_{k,j+1} - 2\beta(k)\hat{\phi}_{k,j} + \hat{\phi}_{k,j-1} = -\hat{s}_{k,j} \quad (4.71)$$

is obtained for $k = 1, 2, 3, \dots, N'_z$ where

$$\hat{s}_{k,j} = \alpha_e (\Delta z)^2 \hat{\rho}_{k,j}$$

and

$$\beta(k) = 1 + 2 \left[\frac{\Delta z}{\Delta x} \sin \left(\frac{\pi}{N'_z - 1} \frac{k-1}{2} \right) \right]^2$$

Since $\hat{\rho}_{k,j}$ can be computed directly from (4.67), (4.71) is solvable for a specified k . In the following, (4.71) is solved by using the Thomas tridiagonal algorithm [Hockney and Eastwood, 1981] and the force free boundary condition is implemented at $j = 1$ and $j = N'_z$, where N'_z is the number of the grid points in the z -direction.

Because net charge is assumed to be zero, the potential $\hat{\phi}_{k,j}$ satisfies the Laplace equation outside the simulation domain, i.e.,

$$\hat{\phi}_{k,j+1} - 2\beta(k)\hat{\phi}_{k,j} + \hat{\phi}_{k,j-1} = 0 \quad (4.72)$$

and the solution of the Laplace's equation can be written as

$$\hat{\phi}_{k,j} \propto \begin{cases} \gamma^{N'_z-j}, & \text{if } j > N'_z; \\ \gamma^{j-1}, & \text{if } j < 1. \end{cases} \quad (4.73)$$

After substituting the above solution into the Laplace equation, it is found that for $k = 1, 2, 3, \dots, N'_z$

$$\gamma^2 - 2\beta(k)\gamma + 1 = 0 \quad (4.74)$$

and that the roots can be written as

$$\gamma = \beta(k) \pm \sqrt{\beta^2(k) - 1} \quad (4.75)$$

For the larger root $\gamma = \beta(k) + \sqrt{\beta^2(k) - 1}$, it is obtained

$$\gamma - \gamma^{-1} = 2\sqrt{\beta^2(k) - 1} \quad (4.76)$$

On the other hand, if $\hat{\phi}_{k,j}$, the solution of the Poisson equation (4.71) inside the simulation domain, and $\hat{\phi}_{k,j}^{\text{ext}}$, the solution of the Laplace equation outside the simulation domain, can be written as

$$\hat{\phi}_{k,j+1} = \eta_j \hat{\phi}_{k,j} + \xi_j \quad (4.77)$$

$$\hat{\phi}_{k,j}^{\text{ext}} = \begin{cases} \gamma^{N'_z-j} \hat{\phi}_{k,N'_z}, & \text{if } j > N'_z; \\ \gamma^{j-1} \hat{\phi}_{k,1}, & \text{if } j < 1. \end{cases} \quad (4.78)$$

then, it is found from (4.71) and (4.77) that

$$\eta_{j-1} = -\frac{1}{\eta_j - 2\beta(k)} \quad (4.79)$$

and

$$\xi_{j-1} = -\frac{\xi_j + \hat{s}_{k,j}}{\eta_j - 2\beta(k)} = (\xi_j + \hat{s}_{k,j})\eta_{j-1} \quad (4.80)$$

Notice that (4.77), (4.79), and (4.80) constitute the Thomas tridiagonal algorithm. The solution of (4.71) can be obtained by a backward elimination using (4.79) and (4.80) and then a forward substitution using (4.77) [Hockney and Eastwood, 1981].

By calculating the derivative of ϕ with respect to z at $j = N'_z$, two equations, one from (4.71) and another from (4.78), are obtained. Then, by matching these two derivatives at $j = N'_z$, it is obtained

$$\hat{\phi}_{k,N'_z} = \eta_{N'_z-1} \hat{\phi}_{k,N'_z-1} + \xi_{N'_z-1} \quad (4.81)$$

where

$$\eta_{N'_z-1} = \frac{2}{2\beta(k) + (\gamma - \gamma^{-1})} \quad (4.82)$$

$$\xi_{N'_z-1} = \frac{\hat{s}_{k,N'_z}}{2\beta(k) + (\gamma - \gamma^{-1})} \quad (4.83)$$

With (4.82) and (4.83), η_{j-1} and ξ_{j-1} can be computed for $j = N'_z - 1, N'_z - 2, \dots, 2$, respectively, from the backward elimination using (4.79) and (4.80).

Similarly, by computing the derivatives of ϕ with respect to z at $j = 1$, one from (4.71) and another from (4.78), and matching them at $j = 1$, it is obtained

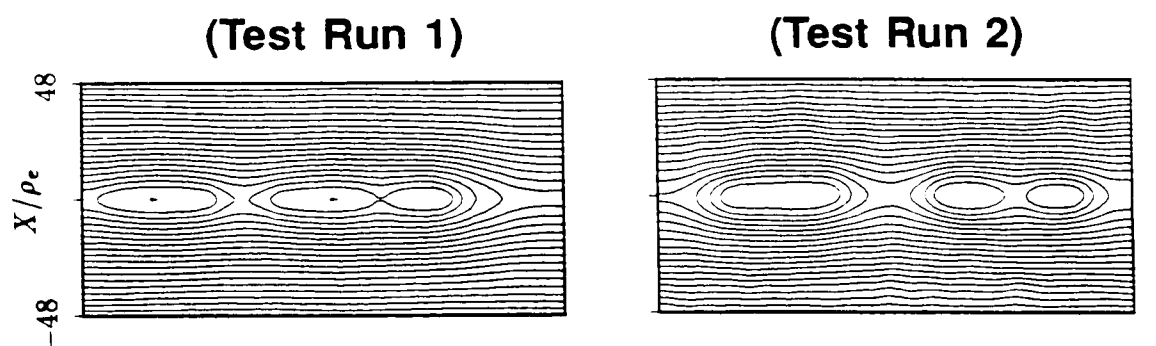
$$\hat{\phi}_{k,1} = \frac{\xi_1 + \hat{s}_{k,1}/2}{\beta(k) - \eta_1 + (\gamma - \gamma^{-1})/2} \quad (4.84)$$

Then, with $\hat{\phi}_{k,1}$ and η_j and ξ_j , which are computed above, $\hat{\phi}_{k,j+1}$ can be found for $j = 1, 2, \dots, N'_z - 1$, respectively, from the forward substitution using (4.77). Finally, with the inverse sine transform (4.68), the electrostatic potential $\phi_{i,j}$, which satisfies the force free boundary condition, is obtained. Notice that the computation of the time derivative of the electrostatic potential (χ) can also be based on the same method discussed above.

For comparison, two simulation cases are tested with exactly same plasma parameters and boundary conditions, except that in the first case the Neumann boundary condition ($\partial\phi/\partial z = 0$) is imposed, while in the second case the force free boundary condition is used. Part of the results observed in the two simulation test runs are shown in Figure 4.3. Figure 4.3a shows the magnetic field lines, represented by the contours of A_y , at the simulation time $t = 120\Omega_e^{-1}$. In both cases, three magnetic islands are present and the coalescence of the two smaller magnetic islands can also be seen. In spite of the slight differences in the locations of magnetic islands, magnetic field lines in both cases exhibit similar configurations, indicating that in the early stage the different boundary conditions used in solving the electrostatic potential do not significantly affect the development of the tearing mode and magnetic reconnection process. However, in the later stage, the magnetic field pattern (not shown) can be significantly affected by the Neumann boundary condition used in the first test run due to the buildup of a large electrostatic potential.

Figure 4.3b shows the contours of the electrostatic potential at $t = 120\Omega_e^{-1}$. In the first test run, the maximum of the potential is located in the central current

a) MAGNETIC FIELD LINES



b) ELECTROSTATIC POTENTIAL

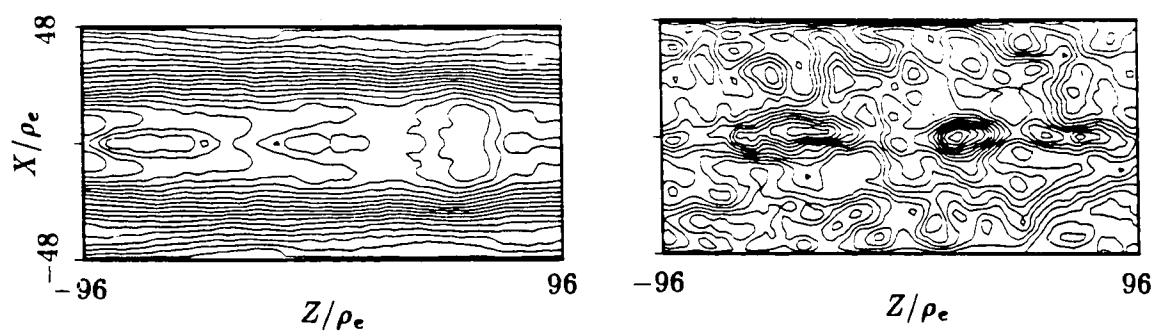


Figure 4.3 Simulation results with different boundary conditions imposed for the electrostatic potential, $\partial\phi/\partial z = 0$ in the first test run and force free in the second test run. (a) Magnetic field lines, represented by the contours of A_y , and (b) contours of electrostatic potential ϕ at simulation time $t = 120\Omega_e^{-1}$.

sheet near the left boundary with $\phi_{max} = 31.41$, while the minimum of the potential is at the driven boundary with $\phi_{min} = 0.0$. The presence of a large positive potential near the left boundary is due to the Neumann boundary condition $\partial\phi/\partial z = 0$ imposed at the boundary, as discussed earlier in the image charge scenario. In the second test run, the maximum of the potential is located at the lower right driven boundary with $\phi_{max} = 1.13$, while the minimum of the potential is located at the central current sheet near the middle of the simulation domain with $\phi_{min} = -7.96$. The large negative potential near the middle of the simulation domain is due to the concentration of electrons trapped by the magnetic island. Contrary to the first test run, where only large scale simple structures are present in the ϕ contours, many small complicated structures in the ϕ contours are exhibited in the second test run.

The time history of the maximum and minimum of electrostatic potential, ϕ_{max} and ϕ_{min} , observed in both of the test runs is plotted in Figure 4.4. Figure 4.4a shows that when the Neumann boundary condition $\partial\phi/\partial z = 0$ is used, the maximum of the potential ϕ_{max} increases with time almost monotonously, while the minimum of the potential ϕ_{min} remains almost exclusively zero. The large positive ϕ_{max} and nonnegative ϕ_{min} indicate the presence of a large net positive charge in the simulation domain due to electron escaping through the open boundary. This results seems consistent with the speculation based on the image charge scenario. Figure 4.4b shows that when the force free boundary condition is imposed, the electrostatic potential generated in the simulation is much smaller than when the Neumann boundary condition is used. While ϕ_{max} slowly increases with time, the average ϕ_{min} remains nearly a constant. The presence of a positive ϕ_{max} and a negative ϕ_{min} represents the high density regions of ions and electrons, respectively, which is more reasonable than the previous one shown in Figure 4.4a. The above

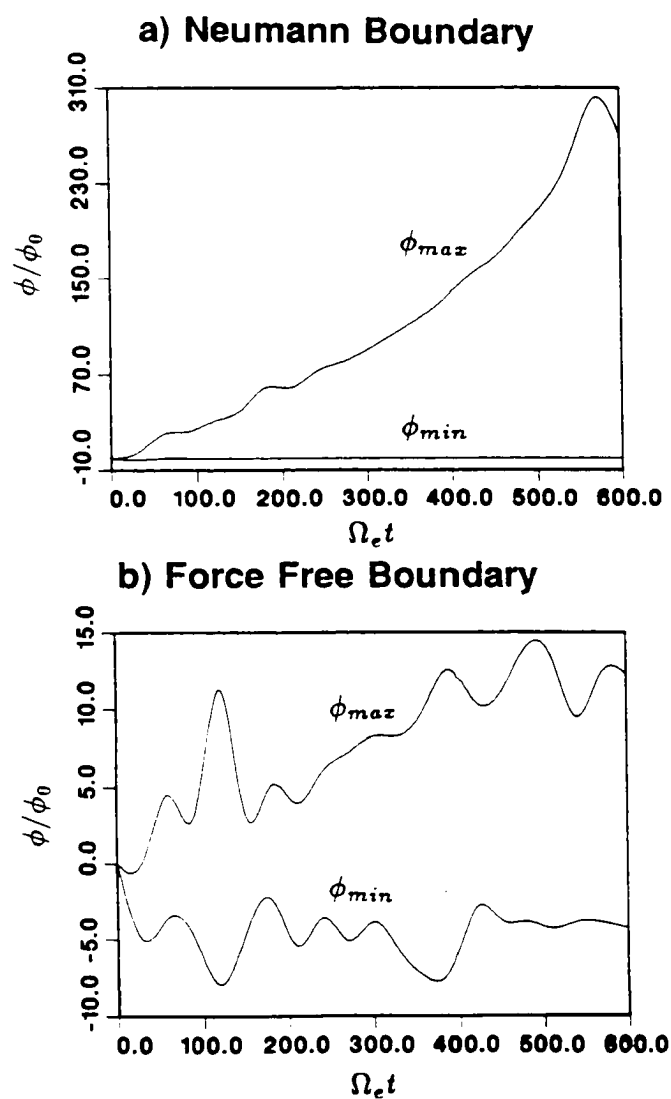


Figure 4.4 The time history of the maximum and minimum of electrostatic potential, ϕ_{max} and ϕ_{min} , observed in the simulation, (a) the first test run with the Neumann boundary condition $\partial\phi/\partial z = 0$ and (b) the second test run with the force free boundary condition.

results indicate that the force free boundary condition is a much better choice for the electrostatic potential when a nonperiodic open outflow boundary is required in the simulation. Therefore, in the following simulations, the force free boundary condition is imposed for both the electrostatic potential ϕ and its time derivative χ at the outflow boundary $z = \pm L_z$.

4.6 Summary

In this chapter, a brief introduction to particle simulation methods used in fusion and space plasma research was presented. A $2\frac{1}{2}$ -dimensional particle simulation model under the Darwin approximation was developed using the Hamiltonian formulation. The initial conditions used in the present simulation and the driven and nonperiodic open boundary conditions necessary for the simulation study of the driven magnetic reconnection process were discussed. Particle buffer zones, driven boundary for vector potential, and force free boundary for electrostatic potential were identified as the three most important parts of the driven and nonperiodic open boundary conditions. In the present model, the zero order magnetic field component B_{0y} is assumed to be zero. When a nonzero B_{0y} is included, the driven and nonperiodic open outflow boundary conditions become even more complicated and will be discussed later. In the next chapter, results are presented from a series of particle simulations that investigate the driven magnetic reconnection process in the collisionless plasma. These simulation results are used to develop an explanation for the observed features of FTEs at the earth's dayside magnetopause.

Chapter 5 One-Component Simulation of Driven Collisionless Magnetic Reconnection

In the previous chapter, a particle simulation model for the driven collisionless magnetic reconnection process was formulated. In the simulation model, the dynamics of both ions and electrons, the electrostatic interaction between ions and electrons, and the self-consistent generated magnetic field B_y component are included. In the present chapter, however, as a first step to study the driven collisionless magnetic reconnection process, the above model is simplified to a one-component particle simulation. In the one-component simulation of the driven collisionless magnetic reconnection, only ion dynamics is included. Although the electron dynamics is neglected, the charge neutrality is assumed to be maintained by the absent electrons and, hence, the electrostatic interaction between particles is ignored. The above assumption is based on the fact that, at least in the linear stage, the effects of the perturbed electrostatic potential do not significantly affect the development of the collisionless tearing mode and the magnetic reconnection process [see review in Chapter 3]. The electron dynamics and the electrostatic interaction will be included in the full particle simulations presented in Chapter 6.

In the present one-component particle simulation of the driven collisionless magnetic reconnection, the magnetic field component B_y , which is perpendicular to the simulation plane, is arbitrarily suppressed. Thus, the magnetic field has two components only, i.e., B_x and B_z , which are confined in the simulation plane, and the vector potential only has the y -component, i.e., $\mathbf{A} = A_y \mathbf{e}_y$. Similar one-component particle simulation models have been used in previous studies of

the collisionless tearing mode instabilities and magnetic reconnection process [e.g., Terasawa, 1981; Swift, 1983; Ambrosiano et al., 1983, 1986; Price and Swift, 1986]. In these simulations, either periodic boundary or nondriven boundary conditions are imposed, but in the present simulation, the driven and nonperiodic open boundary conditions discussed in the previous chapter are used. Notice that due to the absence of electrons in the simulation, the ion Larmor radius (ρ_i), the ion gyrofrequency (Ω_i), and the ion thermal speed (v_{thi}) are used as the normalization units for length, time, and velocity, respectively. Since a symmetric boundary condition is imposed at $x = 0$, the one-component particle simulation is performed in the half plane only with $x \geq 0$ and $-L_z < z < L_z$.

In the one-component simulation of the driven collisionless magnetic reconnection, both the time-dependent multiple X line reconnection (MXR) and the quasi-steady single X line reconnection (SXR) are observed, depending on the size of the simulation domain. For a given width of the simulation domain (L_x), the multiple X line reconnection tends to occur when the length of the simulation domain (L_z) is large ($> L_x$), whereas the quasi steady single X line reconnection takes place when the length of the simulation domain (L_z) is small ($\sim L_x$). Similar phenomena were observed in the MHD simulations [e.g., Lee and Fu, 1986]. The simulation results of the MXR process, characterized by the repeated formation and convection of magnetic islands and the generation of superthermal particles, are presented in the Section 5.1. The simulated MXR process and the flux transfer events (FTEs) observed at the dayside magnetopause are compared in Section 5.2. Simulation results of the quasi-steady SXR process, characterized by the current sheet acceleration of particles, is reported in the Section 5.3. A summary and discussion of the one-component of driven collisionless magnetic reconnection are included in the Section 5.4.

5.1 A Particle Simulation of MXR Process

The one-component particle simulation of the multiple X line reconnection process is carried out in a larger simulation domain with $L_x = 32\Delta$ and $L_z = 64\Delta$, where $\Delta = 1\rho_i$ is the grid size used in the simulation. A symmetric current sheet model located at $x = 0$ is used as the initial condition. The initial magnetic field configuration is given by

$$\mathbf{B}_0 = B_0 \tanh\left(\frac{x}{L}\right) \mathbf{e}_z \quad (5.1)$$

where the current sheet thickness is chosen to be $L = 4\Delta$. Outside the current sheet, the ratio of plasma pressure to magnetic pressure is specified as $\beta = 8\pi N_b T_i / B_0^2 = 1$, where N_b is the particle number density at the driven boundary. It is easy to verify that the Alfvén speed $v_A = B_0 / \sqrt{4\pi N_b m_i}$ can be related to the ion thermal speed by $v_A = \beta^{-1/2} v_{thi}$. The drift speed of ions in the y -direction is given by $U_i / v_{thi} = \rho_i / L = 0.25$. The time step used in the simulation is chosen to be $\Delta t = 0.05\Omega_i^{-1}$. Initially, the number of macro ion particles is 25,000. During the simulation, the number of ions varies between 20,000 and 40,000.

At the driven boundary $x = \pm L_x$, a parameter $R_0 = V_1 / v_A$ is defined, where V_1 is the incoming plasma flow speed. Physically, the parameter R_0 can be considered as an imposed magnetic reconnection rate at the driven boundary. Then, at the driven boundary, the imposed convection electric field is given by $\mathbf{E}_1 = R_0 v_A B_0 \mathbf{e}_y$. At the outflow open boundary $z = \pm L_z$, the boundary condition (4.60), i.e., $\partial A_y / \partial z = 0$, is used. Notice that in the one-component simulation, only one field equation,

$$\nabla^2 A_y = -\alpha_m J_y \quad (5.2)$$

must be solved. Since $\partial/\partial y = 0$ is assumed in the present model and $\mathbf{A} = A_y \mathbf{e}_y$, the Coulomb gauge $\nabla \cdot \mathbf{A} = 0$ is automatically satisfied. The equations of motion for ions are given by

$$\frac{d\mathbf{p}_j}{dt} = (\nabla \mathbf{A}) \cdot (\mathbf{p}_j - \mathbf{A}) \quad (5.3)$$

$$\frac{d\mathbf{x}_j}{dt} = (\mathbf{p}_j - \mathbf{A}) = \mathbf{v}_j \quad (5.4)$$

where \mathbf{x}_j , \mathbf{v}_j , and \mathbf{p}_j are respectively the position, velocity, and canonical momentum of the j -th ion particle. The computation of current density J_y at the grid points and the calculation of forces at the particle positions, as well as the time-integration scheme for the equations of particle motion, are the same as that discussed in Chapter 4.

To study the MXR process in the collisionless plasma, several cases with different incoming plasma flow speeds at the driven boundary ($x = \pm L_x$) are simulated, with imposed magnetic reconnection rates (R_0) chosen to be 0.14, 0.28, 0.42, and 0.56, respectively. As an example, the simulation results of the MXR process with $R_0 = 0.42$ are presented below. In Figure 5.1, magnetic field lines, positions of ion particles, and plasma flow patterns at different simulation times are plotted.

Figure 5.1a shows that magnetic islands (flux tubes) with various sizes are repeatedly formed and convected out of the simulation domain through the open boundaries at $z = \pm L_z$. The coalescence of small magnetic islands that leads to the formation of a larger magnetic island, e.g., the magnetic island A , is also observed in the simulation. Magnetic islands can grow to a large size before they are convected out of the simulation domain. Following the formation and convection of a large magnetic island, several small magnetic islands tend to be formed. In Figure 5.1a several small magnetic islands are observed to be formed at $t = 180\Omega_i^{-1}$ after the convection of the magnetic island B . The average length (l_z) and width (l_x) of

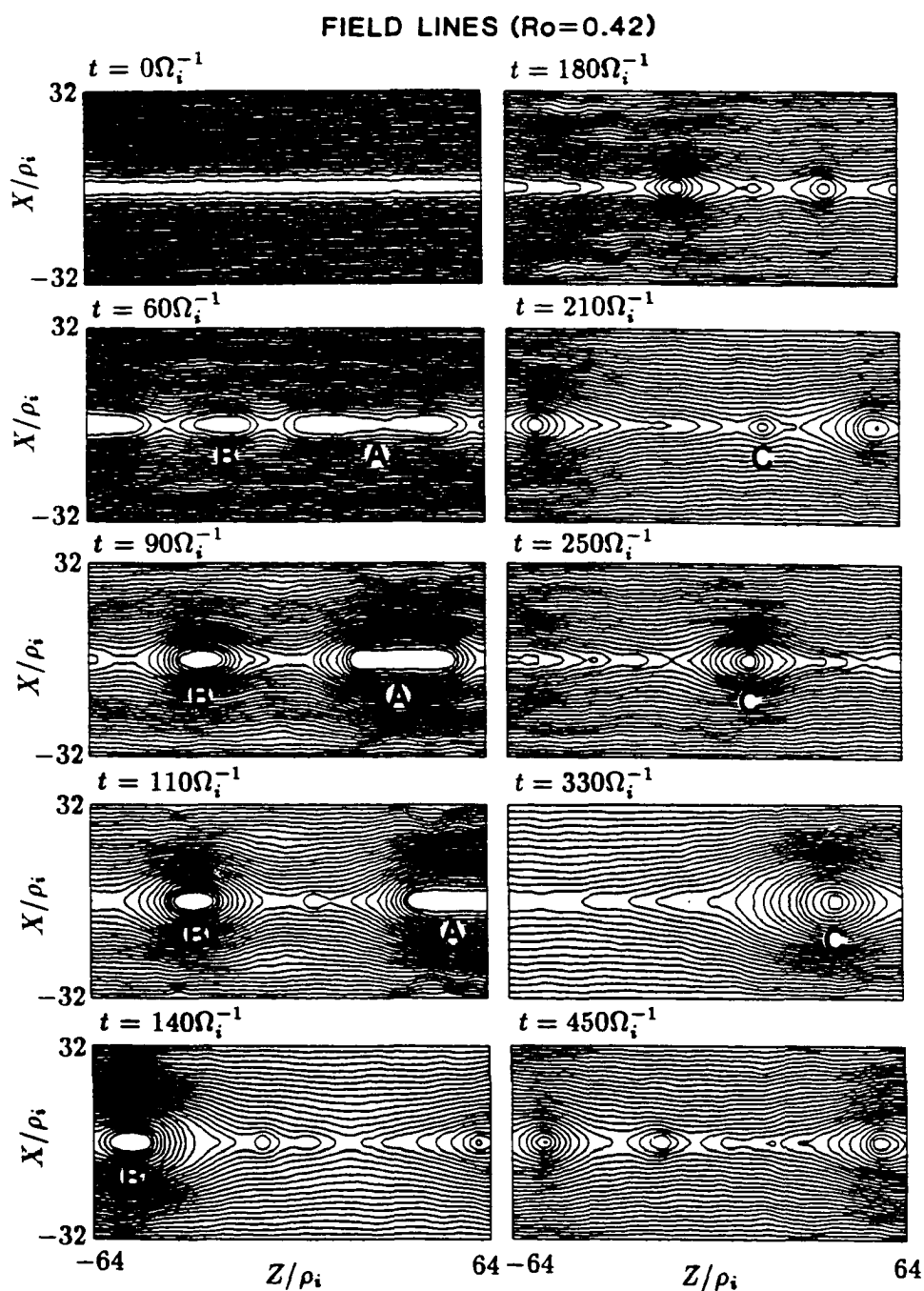


Figure 5.1a Magnetic field lines at various simulation times. $R_0 = 0.42$ is the imposed reconnection rate at $x = \pm L_x$.

large magnetic islands are, respectively, $l_z = 60\rho_i$ and $l_x = 30\rho_i$. The recurrence time (τ) of large magnetic islands on each side of the simulation domain is found to be $\tau \simeq 200\Omega_i^{-1}$.

Figure 5.1b shows the distributions of particles and the plasma flow patterns in the $x - z$ plane at various simulation times. The particle number density is high inside the magnetic islands because particles tend to be convected toward the magnetic field O line region under the influence of the induction electric field. The total particle number is found to increase during the growth phase of large magnetic islands. It is also found that the ejection of a large magnetic island from the simulation domain usually results in a drastic decrease of the total number of particles. The unit vectors in Figure 5.1b correspond to the ion thermal speed v_{thi} , which is equal to the Alfvén speed v_A when β , the ratio of plasma pressure to magnetic pressure, is equal to 1. From the flow patterns, it is found that high-speed plasma flows with flow speed $\geq v_A$ are associated with the ejection of large magnetic islands. But, during the formation stage, the convection velocities of the magnetic islands are usually small. For example, at $t = 90 \sim 110\Omega_i^{-1}$ the convection velocity of magnetic island B is small, whereas at $t = 140\Omega_i^{-1}$ the velocity is equal to or larger than the Alfvén speed (v_A).

It is found during the simulation that the particle thermal energy increases from T_i at the driven boundary $x = \pm L_x$ to $2 \sim 5T_i$ at the center of the current sheet or the magnetic islands. For example, at $t = 110\Omega_i^{-1}$ the thermal temperature is $3.6T_i$ at the center of the magnetic island A and $4.1T_i$ at the center of the magnetic island B . The peak values of the thermal energy at $t = 110\Omega_i^{-1}$ also occur at the regions near the X lines. Notice that the energization of particles during the collisionless reconnection process may be caused either by slow shocks or by the current sheet

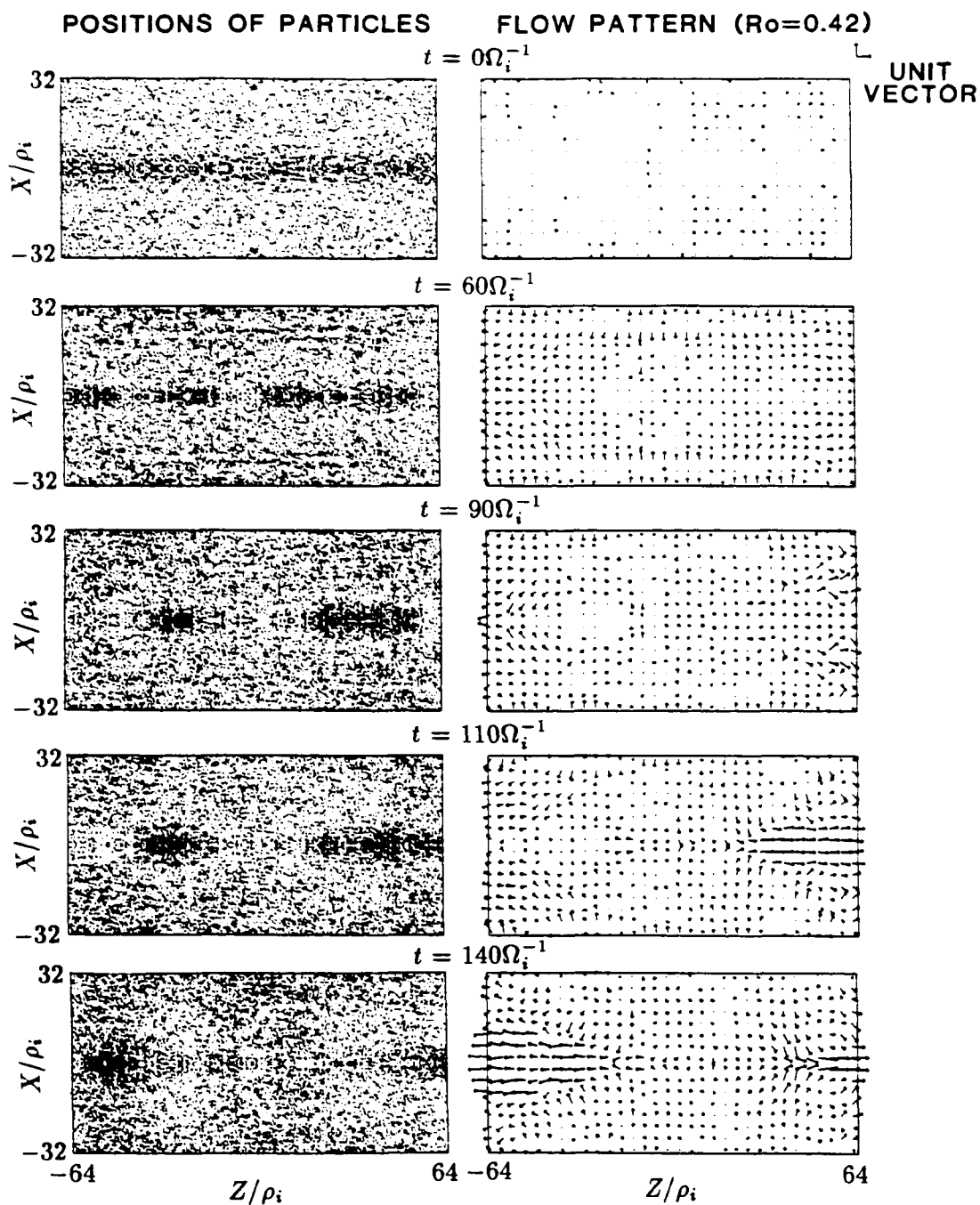


Figure 5.1b The corresponding positions of particles and plasma flow patterns at various simulation times. The unit vectors correspond to the ion thermal speed v_{thi} .

[e.g., Hill, 1975]. A study of the particle acceleration during the driven collisionless reconnection process will be presented in the Section 5.4.

As discussed in Chapter 3, the magnetic reconnection process is closely related to the development of tearing mode instabilities. However, the magnetic islands formed at $t = 60\Omega_i^{-1}$ in Figure 5.1a are not due to the development of the ion tearing mode instability in the initial current sheet. The growth rate of the ion tearing mode instability [e.g., Galeev and Zelenyi, 1976; Terasawa, 1981; Ambrosiano et al., 1983; Swift, 1986] can be written as

$$\gamma \simeq 0.12 \left(\frac{U_i}{v_{thi}} \right)^{5/2} \Omega_i \quad (5.5)$$

Without the driving force applied at the driven boundary $x = \pm L_x$, the growth rate of the ion tearing mode instability in the initial current sheet with $U_i/v_{thi} = 0.25$ is found to be $\gamma \simeq 0.004\Omega_i$, which corresponds to an e-folding time of $250\Omega_i^{-1}$. But, in the simulation, due to the driving force imposed at the driven boundary, both the magnetic field and the particle drift speed in the current sheet are increasing with time after the simulation is started.

At $t = 60\Omega_i^{-1}$, it is found that both the magnetic field and the particle drift speed are increased to twice as much as the initial values, i.e., $B = 2B_0$ and $U_i = 0.5v_{thi}$. Thus, from (5.5), the growth rate is found to be $\gamma \simeq 0.04\Omega_i$, where Ω_i is based on the initial magnetic field B_0 , i.e., $\Omega_i = eB_0/m_i c$. Now the corresponding e-folding time is found to be $25\Omega_i^{-1}$, which is comparable to the growth time of the magnetic islands developed in the simulation shown in Figure 5.1a. Therefore, a scenario for the development of the multiple X line reconnection process in the collisionless plasma can be described as follows. At first, the driving force applied at the driven boundary leads to an enhancement of magnetic field and current density in the current sheet, which in turn leads to an enhanced growth rate of the

ion tearing mode instability developed in the current sheet. Then, the formation of magnetic islands in the current sheet due to the enhanced ion tearing mode instability results in the multiple X line reconnection process. Finally, the magnetic islands are ejected from the open outflow boundaries along with the convection of high-speed plasma flow generated by the reconnection process. If the driving force is continuously applied at the driven inflow boundary, the multiple X line reconnection process, characterized by the repeated formation and convection of magnetic islands, should take place intermittently.

Figure 5.2 shows the maximum reconnection rate R which equals the maximum induction electric field $E_y = -\partial A_y / \partial t$ in the simulation domain as a function of time. The solid line indicates the imposed reconnection rate $R_0 = 0.42$ at the driven boundary $x = \pm L_x$. As shown in Figure 5.2, the reconnection rate R has many impulsive peaks, although the imposed reconnection rate R_0 is a constant, indicating the highly nonlinear nature of the MXR process. It is found that the impulsive peaks of R are associated not only with the formation of large magnetic islands, such as the magnetic islands A , B , and C in Figure 5.1a, but also with the formation of some small magnetic islands. Notice that during the MXR process, the reconnection takes place simultaneously at several sites and only the maximum reconnection rate is plotted in Figure 5.2. During the later stage of the ejection of magnetic islands from the simulation domain, the maximum reconnection rate cannot be exactly determined, which is indicated by the dashed lines in Figure 5.2.

Figure 5.3 shows the position of the centers of three large magnetic islands A , B , and C as a function of simulation time. As mentioned earlier, the convection speed of a magnetic island is small at the earlier formation stage and may increase to Alfvén speed at the later ejection stage. For example, the convection speed of the magnetic island A , which can be obtained from the derivative of its trajectory

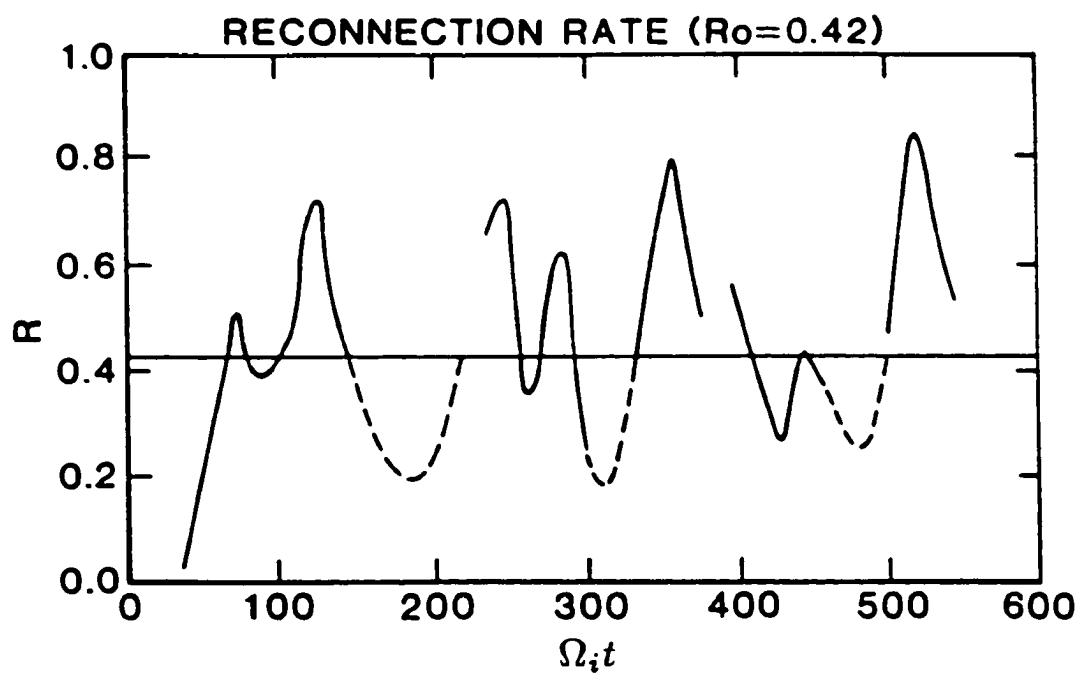


Figure 5.2 The maximum reconnection rate in the simulation domain as a function of time. The solid line indicates the imposed reconnection rate $R_0 = 0.42$ at the driven boundary $x = \pm L_x$.

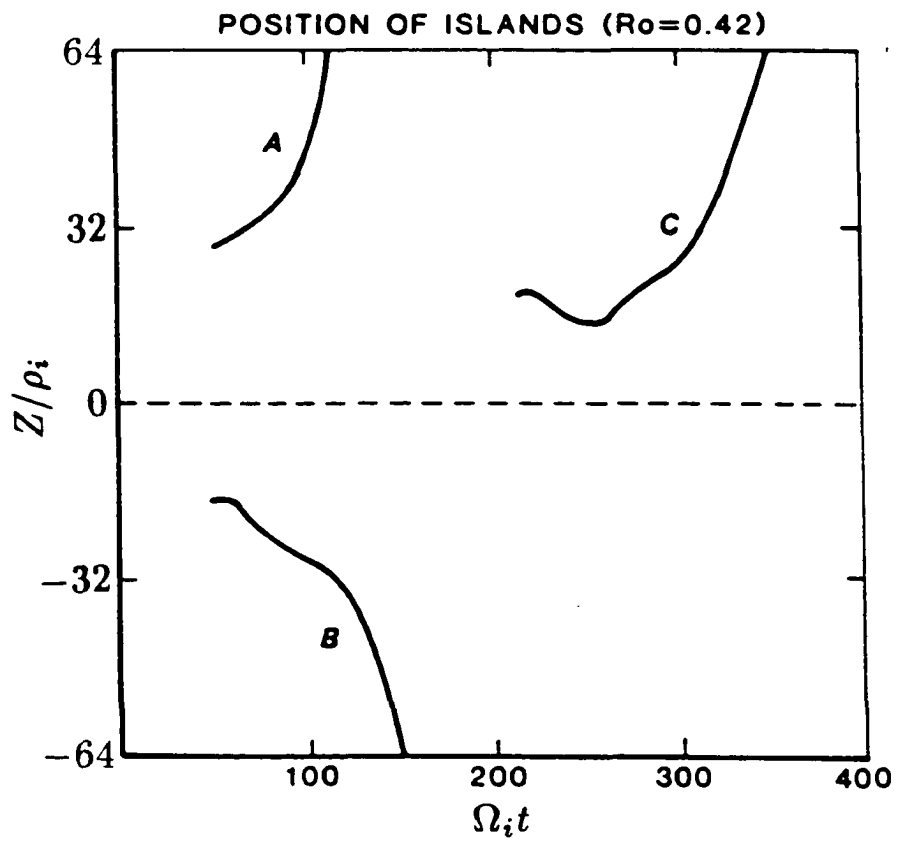


Figure 5.3 Position of the centers of three large magnetic islands *A*, *B*, and *C* as a function of simulation time.

with respect to t , is found to be $\sim 0.3v_A$ at $t = 70\Omega_i^{-1}$ and $\sim 1.2v_A$ at $t = 110\Omega_i^{-1}$, respectively. Notice that the convection speed of the center of magnetic islands is generally different from the plasma flow velocity shown in Figure 5.1b due to the presence of field-aligned flows.

Figure 5.4 shows the averaged power spectrum of the vector potential A_y , $P_A(k) = \langle \tilde{A}_y^2(x = 0, k, t) \rangle$, where $\tilde{A}_y(x = 0, k, t)$ is the Fourier component of $A_y(x = 0, z, t)$, k is the wave number in the z -direction, and the average is over all simulation time steps. It is found in Figure 5.4 that $P_A(k) \sim k^{-2.6}$. The corresponding power spectrum of the normal magnetic field component B_z near the current sheet $x = 0$, $P_B(k)$ can be related to $P_A(k)$ by

$$P_B(k) = k^2 P_A(k) \sim k^{-0.6} \quad (5.6)$$

Since the phase velocity of the magnetic field perturbations associated with FTEs is generally smaller than the average convection speed of FTEs in the magnetosheath plasma flow, the frequency of the magnetic field perturbations of FTEs observed by satellites can be approximately expressed as $f' \simeq kV_c/2\pi$, where V_c is the average convection speed of FTEs. If the average convection speed V_c can be assumed to be a constant, the spectrum of FTEs observed by satellites in the frequency space would be similar to the power spectrum obtained above in the wave number space. Notice that the averaged power spectrum of the normal magnetic field given by (5.6) is for the source region of FTEs only; the power spectrum may change when the magnetic islands are moving away from the source region.

Figure 5.5 shows particle kinetic energy, magnetic energy, and total energy, which is the sum of particle kinetic energy and magnetic energy, in the simulation domain as a function of time. It is shown that the particle kinetic energy and the magnetic energy vary together in time. From Figure 5.1a and Figure 5.5, it

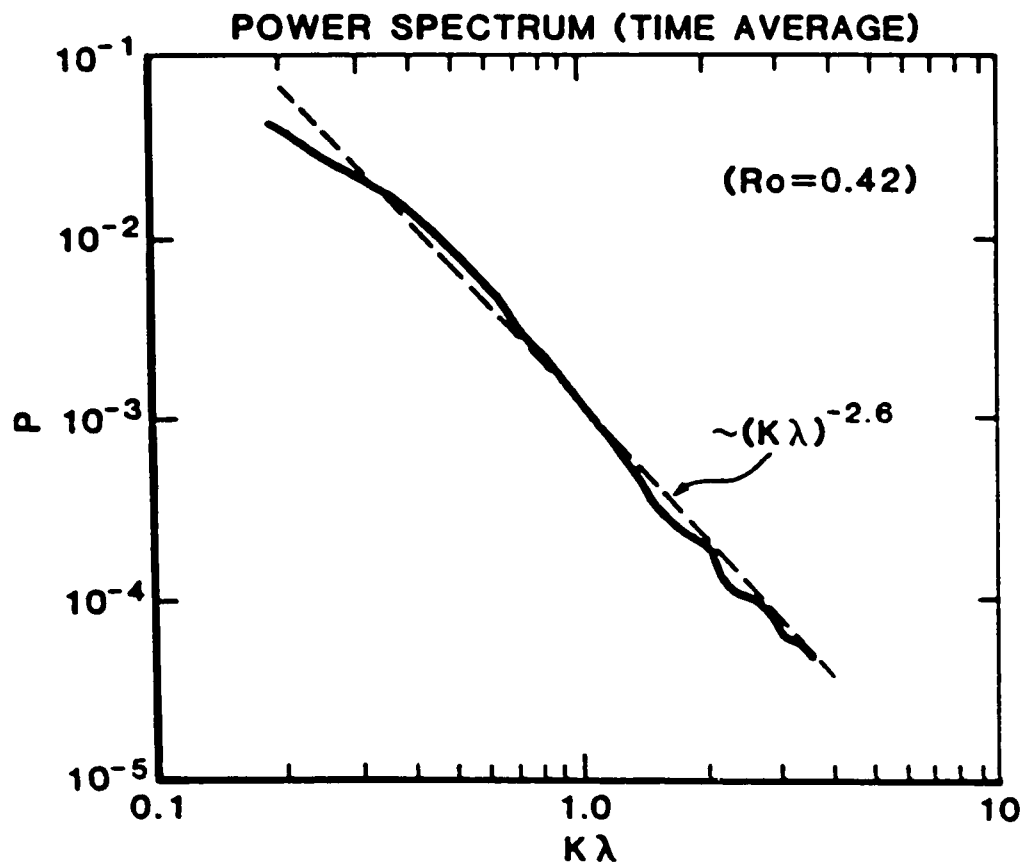


Figure 5.4 The averaged power spectrum $P_A(k)$ of the vector potential A_y measured near the current sheet $x = 0$.

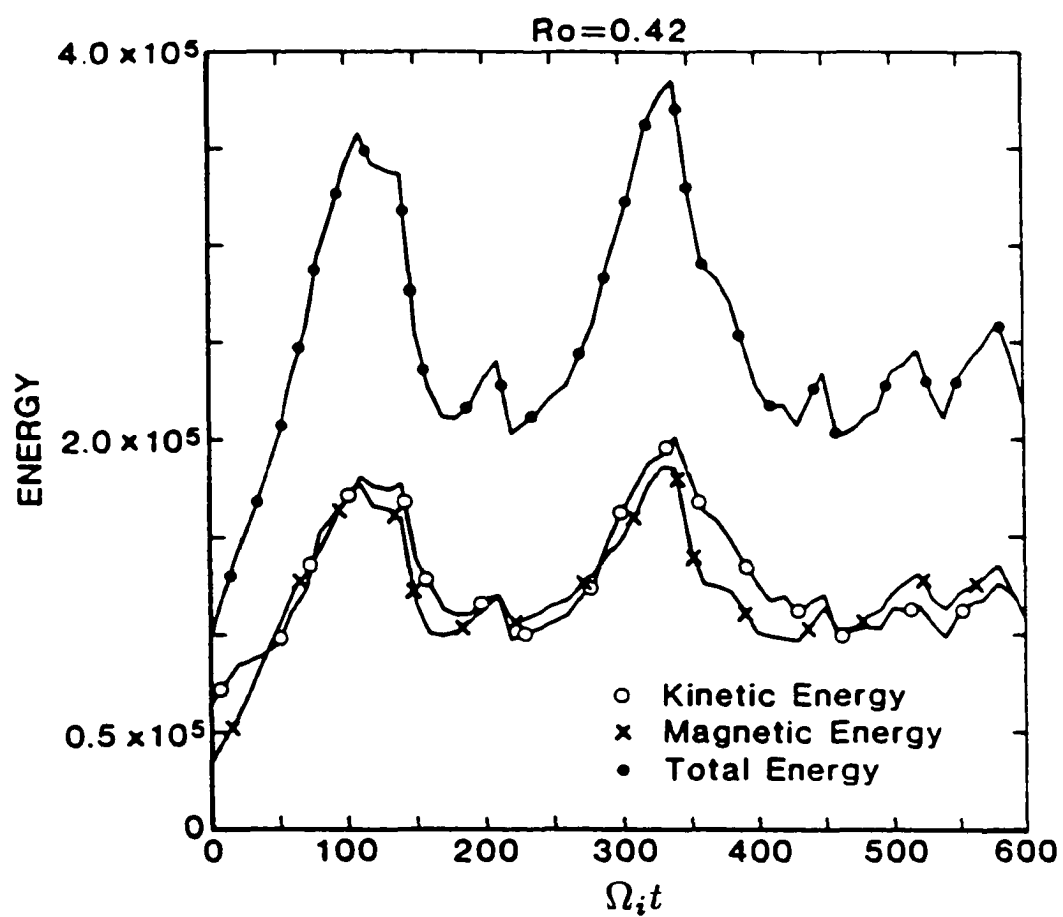


Figure 5.5 Particle kinetic energy, magnetic energy, and total energy in the simulation domain as a function of time. The unit for energy is $T_i/2$.

can be seen that the increase (decrease) of kinetic energy and magnetic energy is associated with the formation (ejection) of magnetic islands. The large energy peak at $t = 110\Omega_i^{-1}$ is associated with the formation of the magnetic islands A and B , whereas the large energy peak at $t = 340\Omega_i^{-1}$ is associated with the magnetic island C . The smaller peaks in the Figure 5.5 are associated with the formation and convection of smaller magnetic islands in the simulation.

That the kinetic energy and magnetic energy observed in the simulation vary together in time, as shown in Figure 5.5, at first glance seems contradictory to the usual understanding of magnetic reconnection process, in which magnetic energy is converted into plasma kinetic energy. However, a more careful examination of energetics of the simulation system reveals that at the driven boundary $x = \pm L_x$, the influx of magnetic energy is $\mathbf{S}_m \sim (B_0^2/4\pi)\mathbf{V}_1$, the influx of kinetic energy is $\mathbf{S}_k \sim (m_i N_b v_{thi}^2/2)\mathbf{V}_1$, and the ratio of magnetic energy influx to kinetic energy influx is $|\mathbf{S}_m/\mathbf{S}_k| \sim 2v_A^2/v_{thi}^2 = 2\beta^{-1}$, so that the influx of magnetic energy is almost twice as much as the corresponding influx of kinetic energy when $\beta = 1$. On the other hand, at the open outflow boundary $z = \pm L_z$, the energy outflux is found to be completely dominated by the kinetic energy flux. The comparison of the energy influxes at the driven inflow boundary with the energy outfluxes at the open outflow boundary indicates that in the simulation, magnetic energy is continuously converted into plasma kinetic energy. Due to the complicated driven and nonperiodic open particle and field boundary conditions used in the simulation, the energy influxes and outfluxes at the boundaries of the simulation domain are not calculated continuously.

Akasofu [1980] found that the magnetic energy density in the high-latitude lobe of the earth's magnetotail increases after the onset of the substorms. The feature of Figure 5.5 that kinetic energy and magnetic energy vary together in time is

consistent with the observation of the magnetotail lobe field during the substorms, which are believed to be associated with the multiple X line reconnection process in the magnetotail [Lee et al., 1985].

Figure 5.6 shows particle kinetic energy averaged over the simulation domain as a function of simulation time. At $t = 0$, the initial average particle kinetic energy is $\sim 1.5T_i$. In the simulation, particle heating is found to occur mainly during the formation of large magnetic islands. For example, during the period from $t = 70\Omega_i^{-1}$ to $t = 150\Omega_i^{-1}$, which corresponds to the formation of the large magnetic islands *A* and *B*, the average particle kinetic energy is increased to $\sim 3.3T_i$, whereas during the period from $t = 270\Omega_i^{-1}$ to $t = 350\Omega_i^{-1}$, which corresponds to the formation of the large magnetic island *C*, the average particle kinetic energy is increased to $\sim 3.7T_i$. The increase in the average particle kinetic energy is mainly due to the presence of superthermal particles generated during the reconnection process, whereas the average particle kinetic energy decreases rapidly after the ejection of large magnetic islands from the simulation domain.

Figure 5.7 shows the particle energy distribution functions $f(E)$ at $t = 0$ and $t = 150\Omega_i^{-1}$. The solid line in Figure 5.7 is a theoretical fit for the initial energy distribution and is given by a Maxwellian energy distribution

$$f_0(E) = \frac{2}{\pi^{1/2}T_i^{3/2}} E^{1/2} \exp\left(-\frac{E}{T_i}\right) \quad (5.7)$$

For $E/T_i < 6$, $f_0(E)$ fits the initial distribution very well, while for $E/T_i > 6$, the deviation of the initial distribution $f(E)$ from the Maxwellian distribution $f_0(E)$ may be due to the small number of particles with $E > 6T_i$ in the simulation. Notice that the distribution (5.7) includes particle thermal energy only, the streaming energy of particles is not included. At $t = 150\Omega_i^{-1}$, superthermal particles with energy ranging from $5T_i$ to $50T_i$ are generated during the reconnection process,

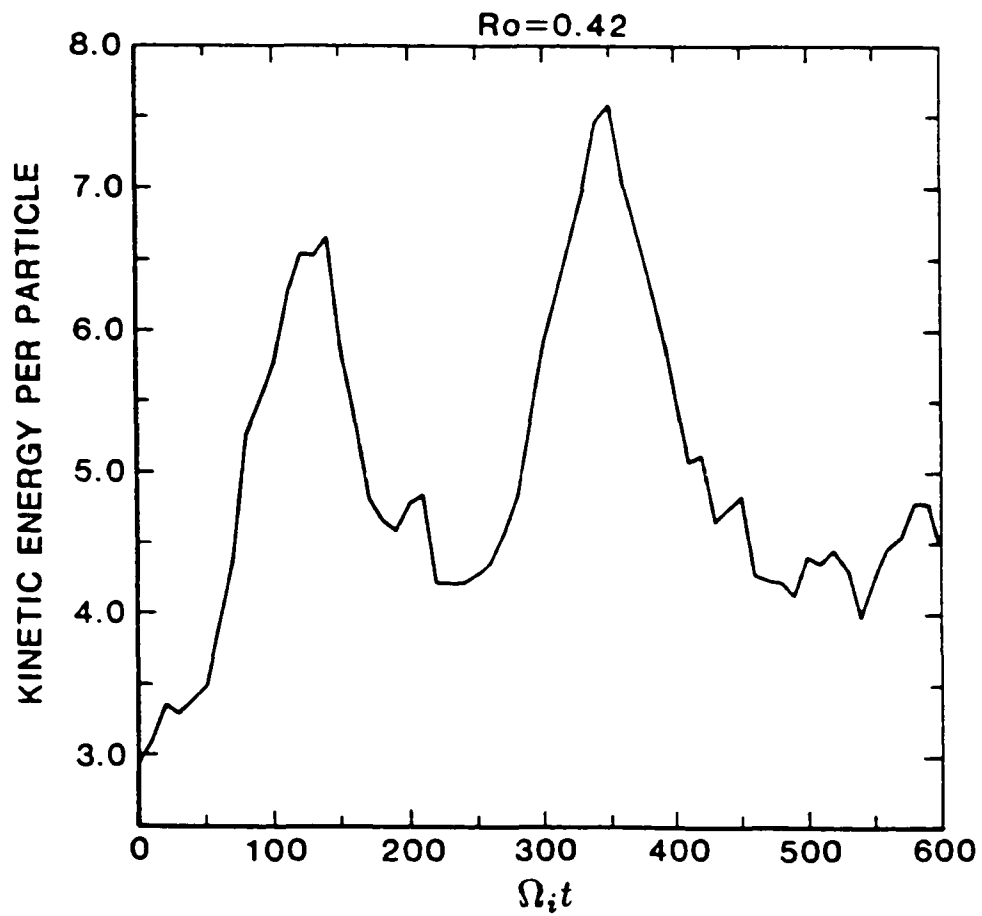


Figure 5.6 The average kinetic energy per particle as a function of simulation time. The unit for energy is $T_i/2$.

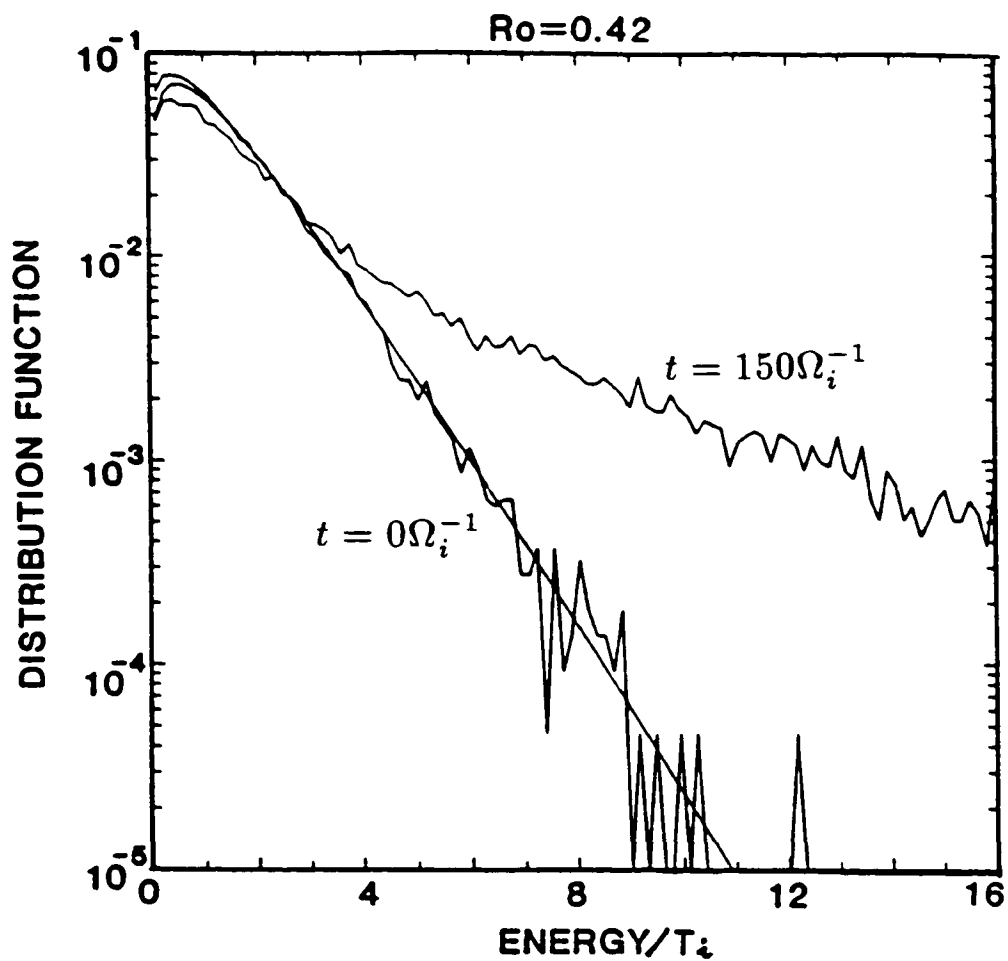


Figure 5.7 The particle energy distribution functions $f(E)$ at $t = 0$ and $t = 150\Omega_i^{-1}$. The solid line which represents a Maxwellian energy distribution is a theoretical fit for $f(E)$ at $t = 0$.

leading to the presence of a high energy component in the particle distribution. At $t = 150\Omega_i^{-1}$, the thermal energy of Maxwellian particles with $E < 5T_i$ is found to be increased only to $\sim 1.2T_i$. The high energy component of the particle distribution with $E > 5T_i$ at $t = 150\Omega_i^{-1}$ can be approximated by a power law function as

$$f(E) \sim E^{-\alpha} \quad (5.8)$$

where $\alpha = 1.9$. Although the value of α may vary during a simulation run, the energy distribution curve at $t = 150\Omega_i^{-1}$ represents the typical energy distribution function observed in the simulation, in which both a low energy Maxwellian component and a high energy component are present. Notice that the particle energy distribution function, as well as the presence of superthermal particles, cannot be obtained from the MHD simulation. Matthaeus et al. [1984] also reported that the reconnection electric fields may accelerate particles to high energies.

In the above, the simulation results with imposed reconnection rate $R_0 = 0.42$ at the driven boundary $x = \pm L_x$ were presented. As mentioned earlier, several cases with different R_0 have been simulated. The results are similar to those described above. Repeated formation and convection of magnetic islands and the presence of superthermal particles are the common features observed in the simulations. However, it is found that the recurrence time τ of large magnetic islands is approximately inversely proportional to R_0 [Lee et al., 1985]. For example, the recurrence time is found to be $\tau \simeq 400 - 600\Omega_i^{-1}$ for the case with $R_0 = 0.14$. The size of large magnetic islands with $R_0 = 0.14$ is found to be $l_x = 40\rho_i$ and $l_z = 90\rho_i$, which is slightly larger than that in the case with $R_0 = 0.42$. Based on the above simulation, the recurrence time is approximately given by

$$\tau \simeq \frac{100}{R_0}\Omega_i^{-1} \quad (5.9)$$

5.2 A Comparison of Particle Simulation of MXR and Flux Transfer Events

Before simulation results are compared with observations of flux transfer events at the dayside magnetopause, it should be pointed out that the present simulation domain may only represent the region at the magnetopause where FTEs are formed. As the magnetic flux tubes (magnetic islands) are convected away from the source region of FTEs, the physical parameters associated with the flux tubes may evolve and become different from those in the source region. Although the present simulation is only two-dimensional (2-D), in the real three-dimensional (3-D) environment, the superthermal particles observed in the simulation may propagate away from the source region of FTEs.

Futhermore, the highly twisted magnetic fields formed at the magnetopause due to the multiple X line reconnection may propagate as Alfvén waves along the open field lines to the magnetosheath and to the magnetosphere and ionosphere [Lee and Fu, 1985]. As a consequence, the helical magnetic fields associated with FTEs may become less twisted. Open magnetic flux tubes with helical fields may also appear in the magnetosheath and the magnetosphere, which are outside the reconnection region. Most of the observed FTEs in the magnetosheath may be located outside the reconnection region. In fact, observations of electron heat flux associated with FTEs [Scudder et al., 1986] indicate that most observed FTEs are outside the source region. However, FTEs inside the source region have also been observed [e.g., Lühr and Klöcker, 1987].

At the dayside magnetosheath, the typical plasma and field parameters observed are $B_0 = 20 - 30\text{nT}$, $n = 10 - 20\text{cm}^{-3}$, and $T_i = 0.5 - 1\text{keV}$. The thickness of the magnetopause is $L = 500 - 1500\text{km}$, and the ratio of plasma pressure to

magnetic pressure is $\beta = 0.5 - 2$ [e.g., Berchem and Russell, 1982; Paschmann et al., 1982]. Based on the above parameters, it is found that $\Omega_i \simeq 2 - 3\text{s}^{-1}$, $v_A \simeq 200 - 300\text{km/s}$, $v_{thi} \simeq 200 - 400\text{km/s}$, $\rho_i \simeq 70 - 150\text{km}$, and $\rho_i/L \simeq 0.14 - 0.4$. The size of large magnetic flux tubes (magnetic islands) in the simulation are $l_x \simeq 30 - 40\rho_i \simeq 0.35 - 0.5R_E$ and $l_z \simeq 60 - 90\rho_i \simeq 0.7 - 2.0R_E$, where R_E is the earth's radius. The above results are consistent with the observations of FTEs [e.g., Russell and Elphic, 1979; Saunders et al., 1984].

In the MXR model, FTE signatures are generated by the convection of magnetic flux tubes in the magnetosheath plasma flow. Observations at the dayside magnetopause show that FTEs have a recurrence time of 5 – 15min, indicating the intermittent nature of the dayside reconnection process. In the simulation of the MXR process with $R_0 = 0.42$, it is found the recurrence time of FTEs is $\tau \simeq 200 - 300\Omega_i^{-1} \simeq 2 - 3\text{min}$. However, (5.9) shows that the recurrence time is approximately inversely proportional to R_0 . Thus, if $R_0 = 0.1$ at the dayside magnetopause, the recurrence time obtained from (5.9) is $\tau \simeq 8 - 12\text{min}$, which is consistent with FTE observations.

The convection speed of flux tubes deduced from ISEE observations of FTEs is on the order of 50 – 300km/s [e.g., Daly and Keppler, 1983; Daly et al., 1984; Berchem and Russell., 1984; Rijnbeek et al., 1984; Saunders et al., 1984]. In the simulation, as shown in Figure 5.3, the convection speed of flux tubes is small ($0.3v_A \simeq 60 - 90\text{km/s}$) at the early stage and can reach the Alfvén speed ($v_A \simeq 200 - 300\text{km/s}$) at the later stage, which is comparable to the FTE observations. Energetic ions and electrons with energy of 5 – 40keV are observed to be associated with FTEs [e.g., Daly et al., 1981; Sonnerup et al., 1981; Saunders et al., 1984; Thomsen et al., 1987; Klumpar et al., 1989]. The present simulation of the MXR process also shows that the formation of flux tubes leads to the presence of

superthermal ions with energy of $5 - 50T_i$, which corresponds to the energetic ions with energy of $5 - 50\text{keV}$. Energetic ions leaked along the reconnected open magnetic field lines from the magnetosphere may also be responsible for the observed energetic particles associated with FTEs [e.g., Scholer et al., 1981; Sibeck et al., 1987].

It has been shown above that the simulation results of the MXR process are generally consistent with the observations of FTEs at the dayside magnetopause. However, in the present simulation, a symmetry in the magnetic fields is assumed about the plane $x = 0$. At the dayside magnetopause, the magnetic fields are not symmetrical. The magnetosheath field is usually smaller than the field in the magnetosphere. The asymmetry in the magnetic fields may lead to the presence of a wavy structure of the magnetopause current sheet as demonstrated by Fu and Lee [1986] in their MHD simulations of the MXR process. On the other hand, as discussed in Chapter 3, an asymmetry in the magnetic fields results in the presence of a high β plasma on one side of the current sheet and a low β plasma on the other side, which in turn may slow down the development of the tearing mode instabilities and hence the MXR process, leading to a longer recurrence time of FTEs.

5.3 A Particle Simulation of Quasi Steady SXR Process

As discussed in Chapter 2, magnetic reconnection has been extensively studied on the basis of fluid equations. The reconnection configuration in the two-dimensional (2-D) steady-state MHD model [Petschek, 1964; Sonnerup, 1970] consists of two parts: the inner diffusion region and the external convection region. The main feature of the convection region is the presence of four slow shocks that are attached to the diffusion region. The incoming plasma is accelerated to the Alfvén speed by

the slow shocks. However, in the 2-D steady-state collisionless reconnection model [Hill, 1975], the magnetic field reversal takes place mainly along the central current sheet. There is only a small amount of field line bending across the slow shocks. The magnetic tension force associated with the central current sheet may provide most of the particle energization.

Since for a given width of the simulation domain (L_x), the steady-state magnetic reconnection tends to occur when the length of the simulation domain (L_z) is small [Lee and Fu, 1986], a simulation domain with $L_x = L_z = 32\Delta$ is used to simulate the quasi-steady collisionless magnetic reconnection process, where $\Delta = 0.5\rho_i$ is the grid size. The simulation domain is a square box in the $x - z$ plane, with $-16 < x/\rho_i < 16$ and $-16 < z/\rho_i < 16$. Notice that the present length of the simulation domain ($L_z = 16\rho_i$) is much smaller than the previous one ($L_z = 64\rho_i$) used in Section 5.2, which leads to the quasi-steady single X line reconnection observed in the simulation. In the present simulation of the quasi-steady single X line reconnection (SXR) process, the basic equations and the time-integration scheme are identical with those used in the previous simulation of the MXR process. The initial conditions are the same as those used previously, except that the current sheet thickness is $L = 8\Delta$. The boundary conditions are also the same as those used in the simulation of the MXR process, except that (4.60'), i.e., $\partial^2 A_y / \partial z^2 = 0$, is applied at $z = \pm L_z$. The boundary condition (4.60') allows the presence of a nonzero normal magnetic field component B_x at the outflow boundary, which is required for the steady-state reconnection in the Petschek model. At the driven boundary $x = \pm L_x$, the imposed reconnection rate $R_0 = V_1/v_A = 0.3$ is assumed. The simulation of the quasi-steady SXR process is carried out in the $x > 0$ region only because the symmetric boundary is also imposed at the $x = 0$ plane.

As pointed out by Hill [1975], the particle energization in the steady-state collisionless magnetic reconnection can be caused either by the slow shock acceleration or by the current sheet acceleration, depending on the value of plasma β , the ratio of plasma pressure to magnetic pressure. To study the steady-state collisionless magnetic reconnection, several cases with different values of plasma β at the driven boundary are simulated. The simulations are run from $t = 0$ to $t = 350\Omega_i^{-1}$ with a time step of $\Delta t = 0.05\Omega_i^{-1}$. In the simulation, a reconnection line (X line) is observed during most of the simulation period. However, the reconnection process is only quasi-steady, because small magnetic islands are occasionally formed and convected out of the simulation domain. The present results differ from the previous simulation of the MXR process, in which magnetic islands are observed to grow to a very large size before being convected out of the simulation domain. As an example, simulation results of the quasi-steady SXR process with $\beta = 1$ are presented below.

Figure 5.8 shows the magnetic field configuration, the plasma flow pattern, the current density contours, and the magnetic tension force ($\mathbf{T} = (\mathbf{B} \cdot \nabla)\mathbf{B}/4\pi$) observed in the simulation at $t = 200\Omega_i^{-1}$. As shown in Figure 5.8a, the reconnection site is located near $z \simeq 0$ in the $x = 0$ plane. The reconnection rate at $t = 200\Omega_i^{-1}$ is found to be $M_A \simeq 0.32$, which is very close to $R_0 = 0.3$, the imposed reconnection rate at the driven boundary. It can be seen clearly in Figure 5.8a that the magnetic field reversal occurs mainly near the central plane $x = 0$. Slow shocks cannot be identified from the magnetic field pattern of Figure 5.8a. The flow pattern in Figure 5.8b shows that plasmas are convected from the driven boundary ($x = \pm L_x$) towards the midplane ($x = 0$) and are accelerated to Alfvén speed v_A before being convected out of the simulation domain through the open boundary at $z = \pm L_z$. The generation of the high-speed plasma flow is associated with the

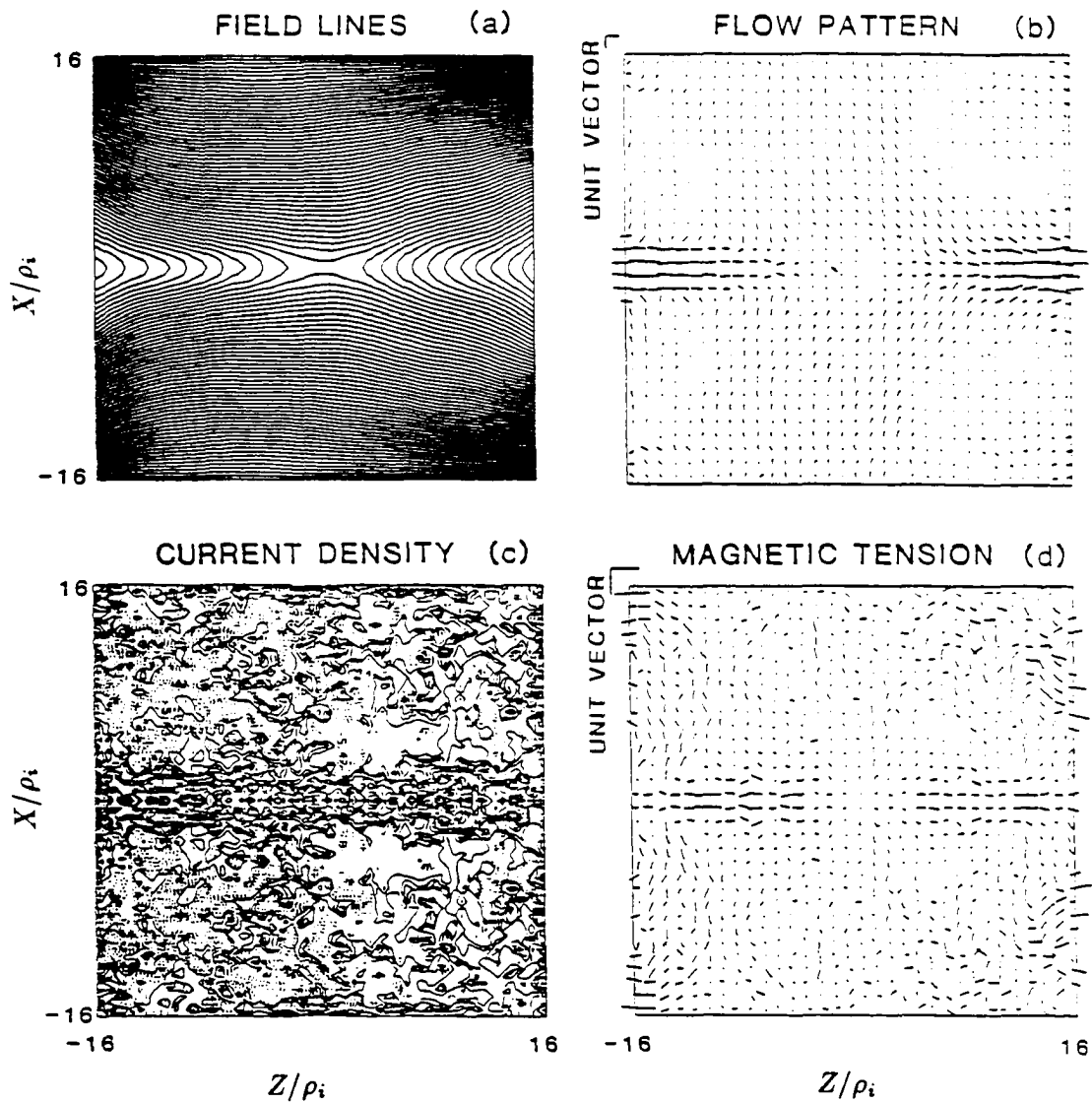


Figure 5.8 (a) The magnetic field lines, (b) the plasma flow pattern, (c) the current density contours, and (d) the magnetic tension force observed at $t = 200\Omega_i^{-1}$ in the simulation of the quasi-steady SXR process.

particle energization caused by the current sheet acceleration. The existence of a current sheet in the outflow region can be clearly identified from the current density contours shown in Figure 5.8c. The high current density region is found to be located in the layer $|x| \leq 3\rho_i$. Figure 5.8d shows that the magnetic tension force is large inside the central current sheet and small at the edge of the current sheet. This is consistent with the presence of the magnetic field reversal in that region.

As discussed in Chapter 2, the reconnection rate M_A in the Hill's collisionless magnetic reconnection model is related to the angle χ between the separatrix line and the z -axis by the relation $M_A = \sin\chi\cos\chi$. The separation angle in Figure 5.8a is found to be $\chi \sim 19^\circ$ and hence, the predicted reconnection rate is found to be $M_A \simeq 0.31$, remarkably close to the observed value ($\simeq 0.32$). Therefore, the present simulation results are consistent in many respects with Hill's collisionless reconnection model.

Two possible models of the diffusion region in the Petschek reconnection model were discussed by Priest and Cowley [1975]. However, the current sheet in the outflow region observed in the present simulation cannot be considered as the diffusion region in the Petschek model because both of the two possible models of Priest and Cowley completely fail to fit the field and flow patterns of current sheet in the outflow region shown in Figure 5.8.

Figure 5.9 shows the particle distribution in the $x - V_z$ phase space plane. Energetic particles with an energy of $2 - 10T_i$ can be seen in the figure and most of them are located in the current sheet within $|x| \leq 3\rho_i$. To study particle acceleration, 250 particles are arbitrarily chosen and their trajectories are followed. It is found that particle accelerations occur mainly within the region $|x| \leq 3\rho_i$ of the central current sheet. This suggests that the acceleration by shocks is insignificant.

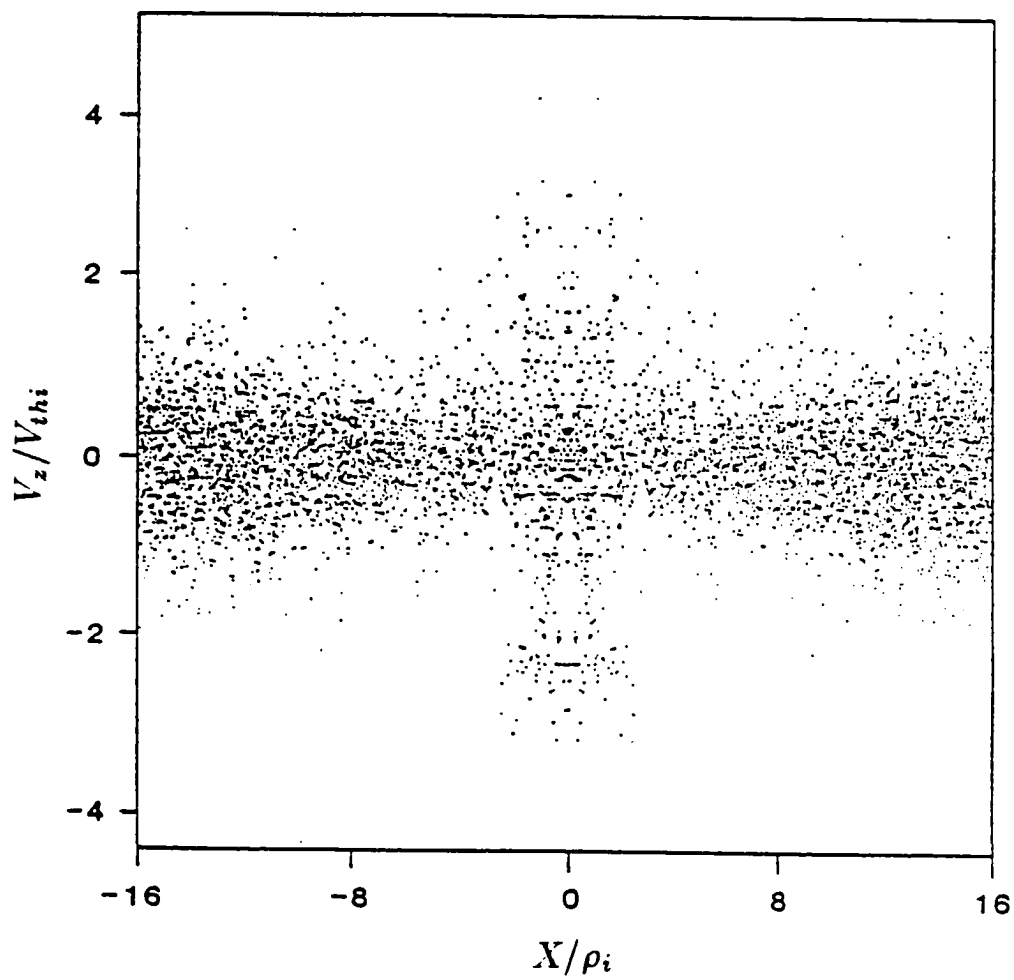


Figure 5.9 The particle distribution in the $x - V_z$ phase space.

A typical trajectory of the selected particles is shown in Figure 5.10, in which the three components (V_x, V_y, V_z) of the particle velocity, the speed V , and the x coordinate are plotted as a function of the z coordinate of the particle. Since a symmetric boundary condition is imposed at the $x = 0$ plane, the trajectory of the conjugate particle in the $x - z$ plane is also plotted in the Figure 5.10. It is shown that the two particles drift towards the current sheet, reach the midplane at $x \simeq 2.5\rho_i$, and are trapped in the current sheet. From the V profile, it is found that energization occurs in the region with $z > 2.5\rho_i$ and $|x| \leq 1.2\rho_i$. From the V_y profile, it is found that $V_y > 0$ in the current sheet and hence, the particles drift in the y -direction, which is the direction of the reconnection electric field. In this case, no evidence of shock acceleration is observed and the particle energization occurs in the central current sheet.

According to Hill [1975], slow shock acceleration may play an important role in a high β plasma, whereas current sheet acceleration is more important in a low β plasma. To examine the relative importance of slow shock acceleration and current acceleration, the quasi-steady SXR process with a high β plasma is also simulated, in which $\beta = 5$ is assumed and all other parameters are the same as those in the case with $\beta = 1$. However, the simulation results show that even in the high β plasma, current sheet acceleration is still the dominant process.

5.4 Summary and Discussion

One-component particle simulations are carried out to study the driven magnetic reconnection in the collisionless plasma. The simulation study emphasizes multiple X line reconnection and quasi-steady single X line reconnection processes. It is

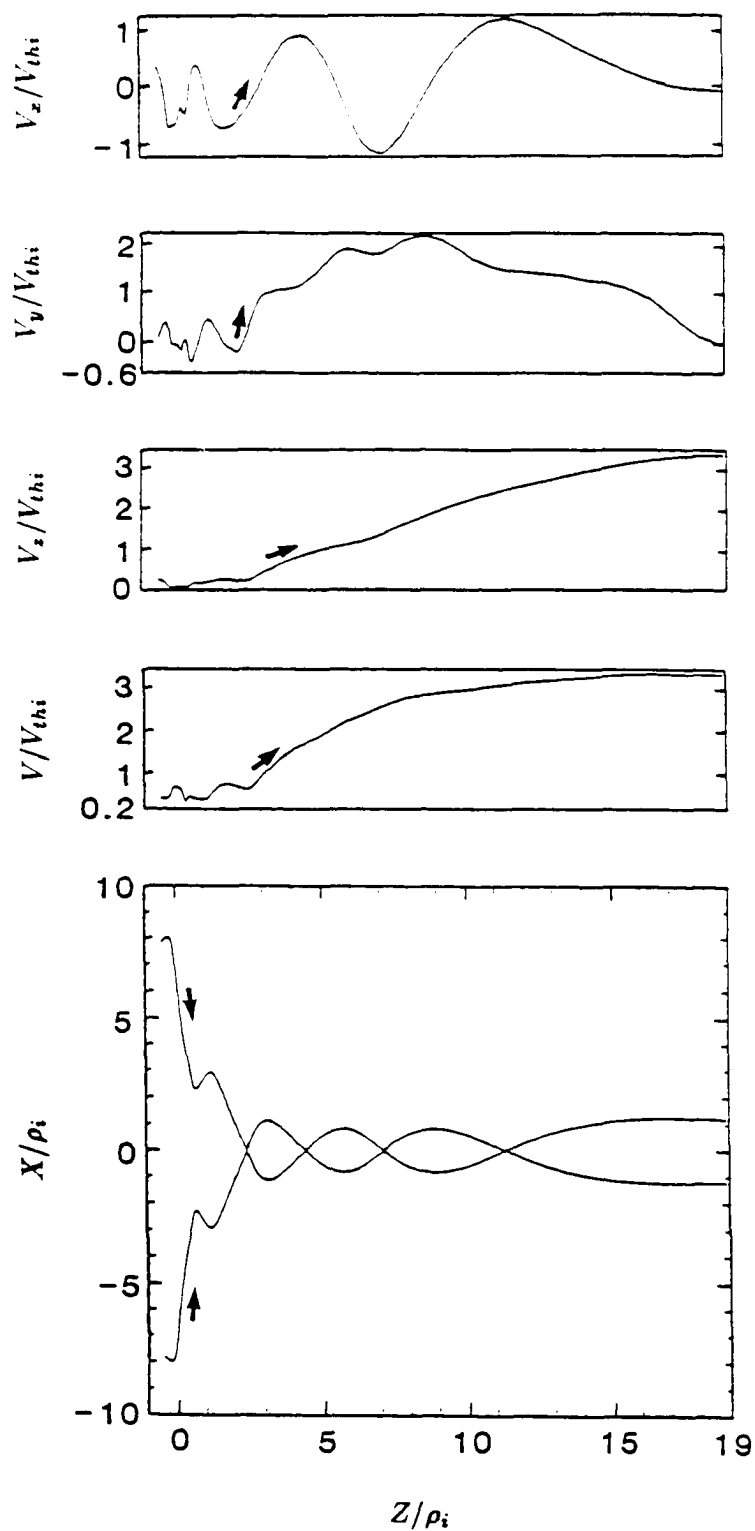


Figure 5.10 A typical particle trajectory indicating the current sheet acceleration.

found that the MXR process, characterized by the repeated formation and convection of magnetic flux tubes (magnetic islands) and the generation of superthermal particles, tends to occur when the length of simulation domain (L_z) is long; the quasi-steady SXR process, characterized by the current sheet acceleration of particles, takes place when the length of simulation domain is short. Although particle simulation of the MXR process reproduces results of MHD simulation, the presence of superthermal particles can only be seen in the particle simulation. The simulation results of the MXR process are generally consistent with satellite observations of the flux transfer events at the dayside magnetopause.

Specifically, the simulation results of the MXR process can be summarized as follows. (1) Repeated formation and convection of magnetic flux tubes are observed with a recurrence time $\tau \simeq 8\text{min}$ for $R_0 = 0.1$ and $\Omega_i \simeq 2\text{s}^{-1}$. (2) The diameter of large magnetic flux tubes is typically $40 - 90\rho_i \simeq 0.7 - 1.5R_E$, where ρ_i ($\simeq 100\text{km}$) is the ion gyroradius. Smaller flux tubes are also observed. (3) The power spectrum of magnetic field in the FTE source region is found to be $P_B(k) \sim k^{-0.6}$, where k is the wave number. (4) Superthermal ions with energy $5 - 50\text{keV}$ are present during the formation of magnetic flux tubes. The energy spectrum of these ions is found to be $f(E) \sim E^{-1.9}$ for $E > 5\text{keV}$.

On the other hand, particle simulation of the quasi-steady SXR process reveals that (1) magnetic field reversal and particle energization takes place mainly in the midplane of the outflow region; (2) particle acceleration by the slow shocks is not important; and (3) particle energization in the collisionless magnetic reconnection process is dominated by current sheet acceleration. The simulation results are consistent with the only collisionless reconnection model proposed by Hill [1975]. Notice that the present results differ from those obtained from the MHD simulations by Sato [1979] and Lee and Fu [1986]. In the MHD simulations, the current layer

associated with the four slow shocks can be clearly identified from the current density contours, and the current density near the $x = 0$ plane of the outflow region was found to be very small. Possible causes for the presence of a current sheet and the lack of slow shocks in the outflow region of the reconnection configuration in the collisionless plasma are suggested below.

First, the width of a slow shock in a collisionless plasma is found to be many ion gyroradii (ρ_i) [e.g., Swift, 1983], which is comparable to or larger than the width of the outflow region in the present simulation. This may prevent the formation of slow shocks in the simulation domain. Second, the presence of trapped particles in the outflow region may re-distribute the currents to the central plane, as discussed by Stern and Palmadesso [1975], which may lead to the formation of a current sheet near the central plane. Third, as discussed by Vasyliunas [1975], a nonuniform magnetic field outside the field reversal region may also lead to the bending of field lines within the field reversal region.

Finally, it should be pointed out that in the present simulation study, the effects of electron dynamics on the reconnection process, which may be important [e.g., Lembege and Pellat, 1982; Swift, 1986], have been neglected. To investigate the driven collisionless magnetic reconnection process in a more realistic manner, full particle code simulation should be carried out. The next chapter will report on the results of full particle simulation of the driven collisionless magnetic reconnection, in which the electron dynamics, the electrostatic interaction, and the self-consistently generated magnetic field B_y component are included.

Chapter 6 Simulations of Driven Reconnection Based on a Full Particle Code

In the previous chapter, the driven collisionless magnetic reconnection processes were studied based on a one-component particle simulation model. Both intermittent multiple X line reconnection (MXR) and quasi-steady single X line reconnection (SXR) processes were obtained. During the MXR process, repeated formation and convection of magnetic islands are observed. Associated with the formation of magnetic islands, energetic particles are generated. The simulation results of the MXR process are in many respects consistent with observations of FTEs at the dayside magnetopause. On the other hand, during the SXR process, a single X line is present in most of the simulation time, with only occasional formation and rapid convection of small magnetic bubbles. Magnetic field line bending and particle acceleration are found to occur mainly in the midplane of the current sheet. Particle acceleration is dominated by the current sheet acceleration, whereas the particle acceleration by slow shocks is found to be insignificant.

However, the dynamics of electrons and the electrostatic interaction between particles, which under certain circumstances may be important to the magnetic reconnection process [Lembege and Pellat, 1982; Swift, 1986; Hoshino, 1987], are not included in the one-component particle simulations. To examine the effects of electron dynamics and electrostatic interactions on the driven collisionless magnetic reconnection processes, full particle simulations with both ions and electrons are needed. In this chapter, the driven collisionless magnetic reconnection processes

are further studied based on the full particle simulation model developed in the Chapter Four.

To save computational resources, a small mass ratio assumption in which the mass ratio of ion to electron is arbitrarily chosen as $m_i/m_e = 1 \sim 100$ has been commonly used in the explicit full particle simulations [e.g., Katanuma and Kamimura, 1980; Leboeuf et al., 1982; Swift, 1986; Hoshino, 1987; Ding and Lee, 1990]. Recently, based on implicit full particle simulations of collisionless magnetic reconnection in which large ion-to-electron mass ratio ($m_i/m_e = 200 \sim 2000$) was used, Hewett et al. [1988] and Francis et al. [1989] found that the artificially small mass ratio of ion to electron may have some effects on the nonlinear growth of the reconnection process. However, the effect of large ion-to-electron mass ratio on the driven collisionless magnetic reconnection process will not be considered in this study. In the present full particle simulation of the driven collisionless magnetic reconnection, a mass ratio of $m_i/m_e = 25$ is assumed and used in all simulation runs.

In the simulations, different simulation domain sizes, initial configurations, and plasma parameters are used. Various features associated with the driven collisionless magnetic reconnection are examined. The simulation results of the driven collisionless magnetic reconnection in a symmetric current sheet are presented in Section 6.1. The simulation results of the driven collisionless magnetic reconnection in an asymmetric current sheet are presented in Section 6.2. The simulation results are applied to the dayside magnetopause to explain observations of flux transfer events. Since the driven collisionless magnetic reconnection is a highly nonlinear dynamic system with both energy input and dissipation, the driven collisionless magnetic reconnection may also exhibit features associated with the self-organization process

[e.g., Nicolis and Prigogine, 1977; Hasegawa, 1985]. A discussion on the simulation results of the driven collisionless magnetic reconnection from the perspective of self-organization process is presented in Section 6.3. At the end of this chapter, a brief summary is included in Section 6.4.

6.1 Driven Collisionless Reconnection in a Symmetric Current Sheet

As the first attempt in the particle simulation study of driven collisionless magnetic reconnection, the one-component particle simulation model has been used in Chapter Five. As the second step of the continued simulation study of driven collisionless magnetic reconnection, full particle simulations with both ions and electrons have been carried out. In this section, three typical cases of the full particle simulation of driven collisionless magnetic reconnection in a symmetric current sheet are presented. The simulation results are compared with observations of FTEs at the dayside magnetopause.

In the first simulation case, Case A, both ion dynamics and electron dynamics and electrostatic interaction are included. However, the self-generated magnetic field B_y component, which is perpendicular to the simulation plane, has been artificially suppressed and the vector potential is assumed to have the y -component only, *i.e.* $\mathbf{A} = A\mathbf{e}_y$. This assumption is justified since the self-generated B_y component has only negligible effect on the tearing mode instability and hence the reconnection process [Swift, 1986]. The effect of the self-generated B_y component will be included and examined in the later cases. Furthermore, in Case A, a symmetric boundary condition is imposed at $x = 0$ plane so that the simulation is only performed in the region with $x > 0$ and $-L_z < z < L_z$. In Case A, the grid size is chosen to be $\Delta = 1.5\rho_e$ and the size of simulation domain is chosen to be $L_x = 48\rho_e$

and $L_z = 192\rho_e$, respectively. The initial magnetic field configuration for Case A is a symmetric current sheet, i.e., $B_s = B_m - B_0$ and $\mathbf{B} = B_0 \tanh(x/L)\mathbf{e}_z$, where $L = 5.0\rho_e$ is the initial current sheet thickness. The initial temperature profile is assumed to be uniform, i.e., $T_{s\alpha} = T_{m\alpha} = T_\alpha$ for both ions ($\alpha = i$) and electrons ($\alpha = e$).

Case A is run from $t = 0$ to $t = 600\Omega_e^{-1}$ with a time step of $0.2\Omega_e^{-1}$, where $\Omega_e = (eB_0/m_e c)$ is the electron gyrofrequency on the basis of the magnetic field outside the current sheet. Other parameters used in the simulation are: $\rho_i/\rho_e = 12.5$, $\Omega_i/\Omega_e = 0.04$, $T_i/T_e = 6.25$, $v_{thi}/v_{the} = 0.5$, $u_e/v_{the} = 0.2$, $u_i/v_{the} = 1.25$, $\omega_{pe}/\Omega_e = 1.0$, and $\omega_{pi}/\Omega_e = 0.2$, where ρ_α , Ω_α , T_α , $v_{th\alpha}$, u_α , and $\omega_{p\alpha}$ are, respectively, the Larmor radius, the gyrofrequency, the thermal energy, the thermal speed, the drift speed, and the plasma frequency for the particles of α species. At the driven inflow boundary ($x = \pm L_x$), the ratio of plasma pressure to magnetic pressure is chosen to be $\beta = 8\pi N_b(T_i + T_e)/B_0^2 = 1.0$, where N_b is the particle number density at the inflow boundary. The Alfvén speed is found to be $v_A = B_0/\sqrt{4\pi N_b m_i} = 1.52v_{thi}$ and the imposed driving rate is chosen to be $R_0 = V_1/v_A = 0.3$. Initially, the simulation is started with 40,000 ions and electrons. In Case A, $\partial^2 A_y/\partial z^2 = 0$ is used as the boundary condition for the vector potential A_y at the outflow boundary ($z = \pm L_z$).

Figure 6.1a shows the magnetic field lines which are contours of the vector potential A_y at different simulation times. At $t = 0$, the simulation is started with a symmetric and uniform current sheet located at the $x = 0$ plane. The magnetic fields on two sides of the current sheet are anti-parallel and equal in magnitude. Due to the driving force applied at the driven boundary ($x = \pm L_x$), the current sheet is pinched, and at $t = 60\Omega_e^{-1}$ the development of tearing mode instability can be clearly observed. As the tearing instability grows, at $t = 120\Omega_e^{-1}$ the magnetic

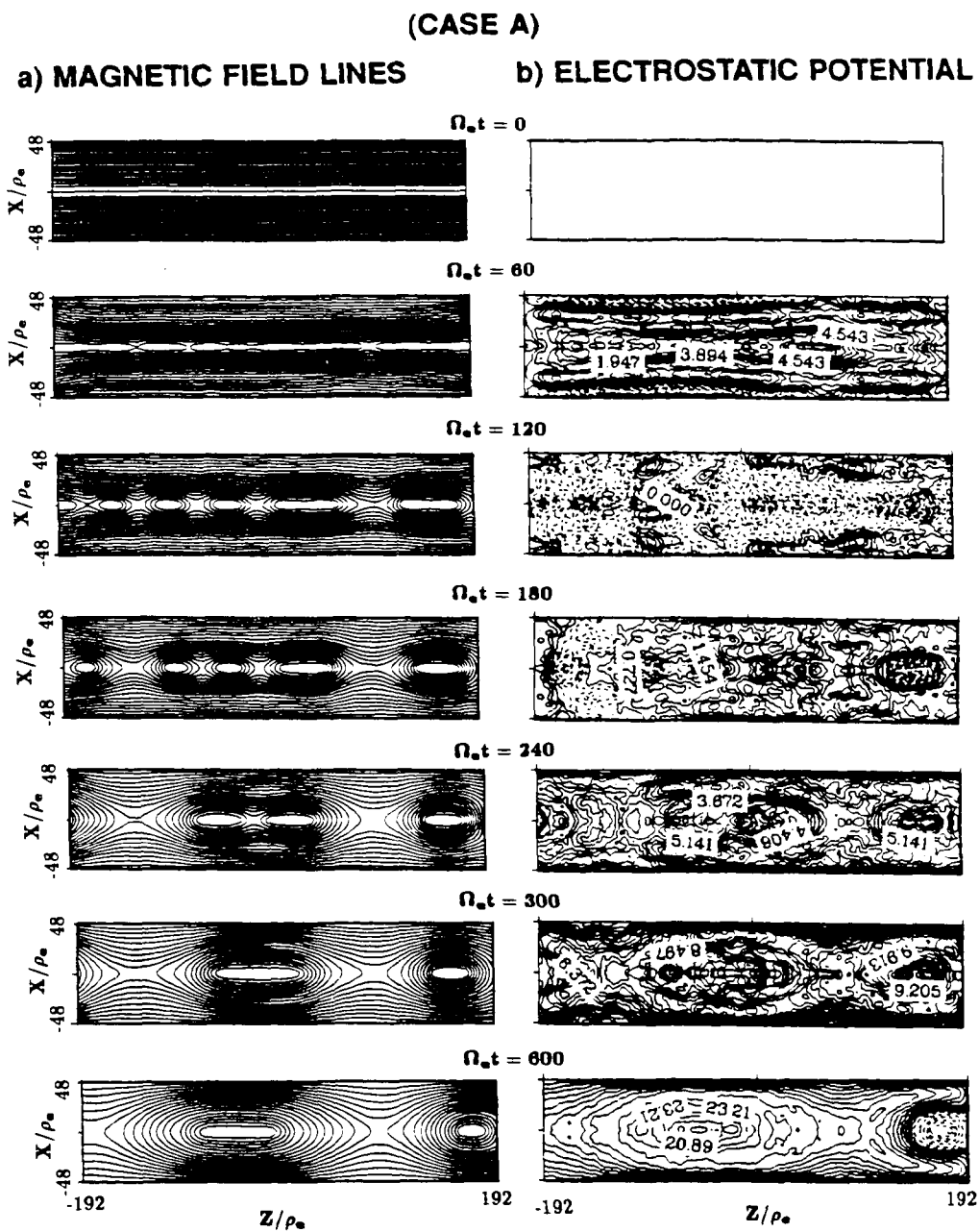


Figure 6.1 (a) Magnetic field lines and (b) contours of electrostatic potential observed at various simulation times in Case A.

field line reconnection takes place at multiple sites and the current sheet breaks into filaments, leading to the formation of several small magnetic islands in the current sheet. As magnetic reconnection continues, the sizes of magnetic islands increase, and in the nonlinear stage, some of the small magnetic islands coalesce to form a larger magnetic island. For example, at $t = 180\Omega_e^{-1}$, five small magnetic islands are formed. At $t = 240\Omega_e^{-1}$, two of the small magnetic islands near the center of the simulation domain coalesce, forming a medium size magnetic island. The formed medium size magnetic island in turn coalesces with another medium size magnetic island nearby, leading to formation of a large magnetic island at the center of the simulation domain at $t = 300\Omega_e^{-1}$. In the meantime, the convection of magnetic islands formed near the outflow boundary ($z = \pm L_x$) can also be seen in the simulation. While a giant magnetic island is formed in the simulation at $t = 600\Omega_e^{-1}$, the magnetic island formed near the left outflow boundary ($z = -L_x$) has moved completely out of the simulation domain and a part of the magnetic island formed near the right outflow boundary ($z = L_x$) has also moved out along with the plasma flows generated during the reconnection process.

Figure 6.1b shows the contours of the electrostatic potential ϕ at the corresponding simulation times. In Figure 6b, the numbers represent the values of the electrostatic potential ϕ , the dashed lines indicate the regions with $\phi < 0$, and the solid lines indicate the regions with $\phi \geq 0$. The initial electrostatic potential at $t = 0$ is zero everywhere in the simulation domain, because the initial macroscopic electric field is set to be zero in the simulation. As the simulation is started, charge separation is developed and small scale turbulent electrostatic fields are formed. The rapidly changing patterns and values of the electrostatic potential shown in Figure 6.1b indicate the highly fluctuating electrostatic field generated by the driven collisionless magnetic reconnection. It can be seen from Figure 6.1b that no large

scale pattern of the electrostatic potential can be formed unless large magnetic islands are present. The contours of electrostatic potential at $t = 600\Omega_e^{-1}$ show that when large magnetic islands are present, magnetic field lines outside the current sheet are more or less equipotential lines. The formation of equipotential field line structures can be easily understood. Because tearing mode instability and magnetic reconnection are low-frequency plasma processes and electrons are strongly magnetized outside the current sheet, any field-aligned electrostatic field caused by the charge separation will be quickly eliminated by the fast electron motions along the magnetic field lines and only cross-field-line electrostatic field can be maintained. Figure 6.1b also shows that due to trapping of particles by the magnetic islands, the center of a magnetic island can be either a positive maximum or a negative minimum of the electrostatic potential, indicating the excessive accumulation of ions or electrons inside magnetic islands. The simulations show that particle trapping by magnetic islands is closely associated with particle acceleration during the driven collisionless magnetic reconnection. A detailed study of particle trapping and acceleration will be presented in the next chapter.

The full particle simulation of driven collisionless magnetic reconnection illustrated in Figure 6.1 looks very similar to that shown in Figure 5.1, even though the electron dynamics and electrostatic interaction are included in the present simulation. However, in the one-component simulations, ions are magnetized outside the current sheet and their motions are controlled by the drift motions in the magnetic field, whereas in the present full particle simulations, ions are unmagnetized in the neighbourhood of the current sheet due to their large Larmor radius; their motions are mainly determined by induction and electrostatic electric fields. On the other hand, in the one-component simulations, electrons are assumed to provide an instantaneous charge neutral plasma environment so that no charge separation is

allowed, whereas in the full particle simulations, charge separation is present due to the different motions of electrons and ions.

Similar to one-component simulations, if the present simulations were run for longer time, repeated formation and convection of magnetic islands leading to FTE signatures at the dayside magnetopause would have been observed. However, computing resources were not available to simulate the repeated formation and convection of magnetic islands and to examine other features associated with the driven collisionless reconnection process in a long simulation system with $L_z = 192\rho_e$. On the other hand, although the sizes and recurrence times of large magnetic islands may be affected by the size of the simulation domain, basic features associated with the driven collisionless reconnection process are not changed when a shorter simulation domain is used. Therefore, in order to effectively and economically investigate various features associated with the driven collisionless magnetic reconnection process and FTEs at the dayside magnetopause, a shorter simulation domain with $L_z = 96\rho_e$ is chosen for the full particle simulation cases presented below.

Case B is run from $t = 0$ up to $t = 1500\Omega_e^{-1}$ with the same assumptions, parameters, and boundary conditions as those used in case A, except that the length of the simulation domain is shorter, i.e., $L_z/\rho_e = 96$, and the boundary condition $\partial A_y/\partial z = 0$ is used for the vector potential A_y at the outflow boundary ($z = \pm L_z$). Figure 6.2 shows the magnetic field lines at different simulation times observed in Case B. In the simulation of driven collisionless magnetic reconnection, the intermittent multiple X line reconnection is observed to take place, leading to the repeated formation and convection of magnetic islands with various sizes. For example, at $t = 240\Omega_e^{-1}$ and $t = 1140\Omega_e^{-1}$, magnetic islands of medium size are convected out of the right outflow boundary of the simulation domain, whereas at $t = 420\Omega_e^{-1}$ and $t = 1500\Omega_e^{-1}$, large magnetic islands are ejected from the right and

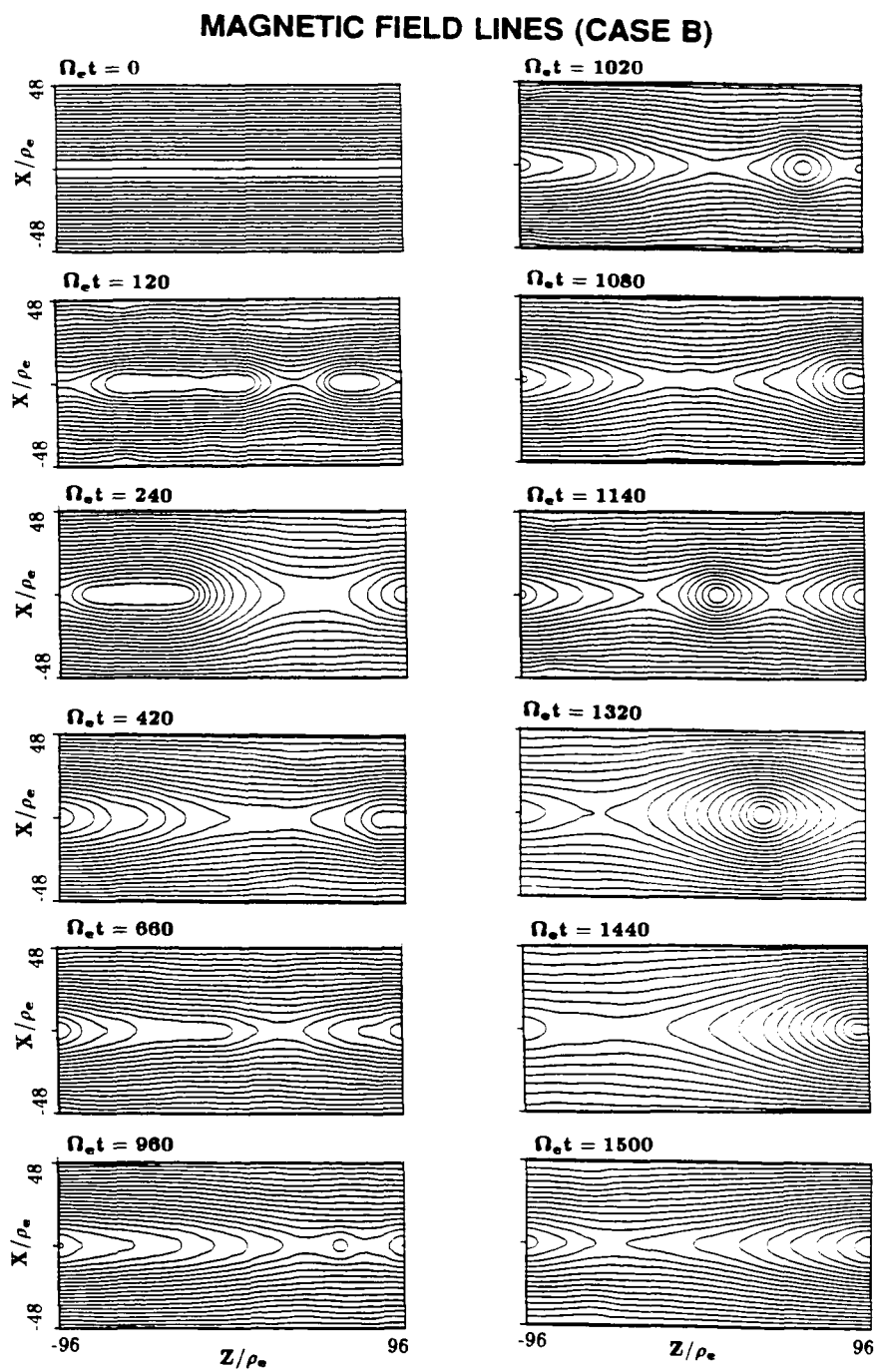


Figure 6.2 Magnetic field lines observed at various simulation times in Case B.

left outflow boundaries of the simulation domain, respectively. As suggested by Lee and Fu [1985], the repeated formation and convection of magnetic islands caused by the intermittent multiple X line reconnection at the magnetopause current sheet would produce the observed features of FTEs at the dayside magnetopause.

Apart from the intermittent multiple X line reconnection process, which is characterized by the repeated formation and convection of magnetic islands, a quasi-steady single X line reconnection period can also be identified during the simulation shown in Figure 6.2. For example, between $t = 420\Omega_e^{-1}$ and $t = 1080\Omega_e^{-1}$, a single X line persists in the simulation domain with only occasional formation and convection of small magnetic bubbles. Notice that when a small magnetic bubble is moving along with the plasma flow generated during the reconnection process towards the outflow boundary of the simulation domain, the size of the magnetic bubble is still growing. This indicates a continued magnetic reconnection at the X line region. It can also be seen in Figure 6.2 that during the quasi-steady single X line reconnection, the bending of magnetic field lines takes place mainly in the midplane of the current sheet. In the meantime, it is observed that high-speed plasma flows are also mainly confined in the central current sheet, providing further evidence for current sheet particle acceleration during the collisionless magnetic reconnection process. The above results are consistent with the theoretical collisionless magnetic reconnection model [Hill, 1975] and the results of previous particle simulations [Lee and Ding, 1987].

Figure 6.3 shows the time series of the magnetic energy contained at various wave modes near the current sheet region ($x \simeq 0$) from $t = 0$ to $t = 240\Omega_e^{-1}$. The curves with squares, solid dots, and circles are for the mode numbers of $m = 1, 2,$ and $3,$ respectively. It can be seen in Figure 6.3 that the mode of $m = 3$ is dominant at the early stage. However, according to the linear theory of tearing mode

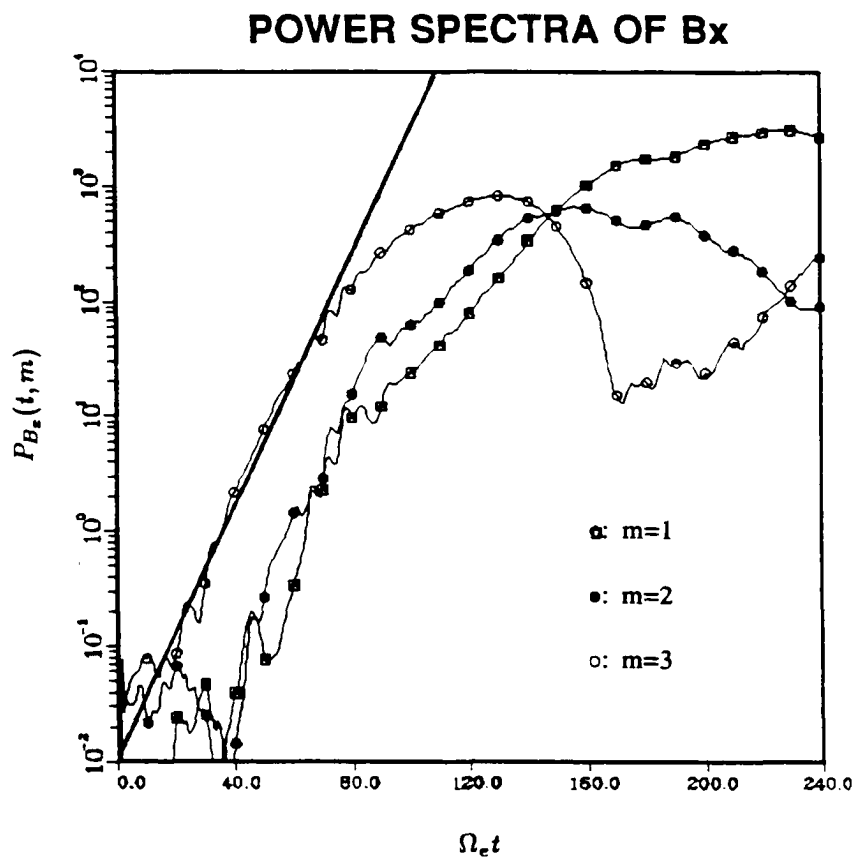


Figure 6.3 Time series of the magnetic energy contained at various wave modes near the current sheet region ($x \simeq 0$). Curves with squares, solid dots, and circles are for mode number $m = 1, 2,$ and $3,$ respectively.

instability discussed in Chapter Three, the mode of $m = 2$ is found to be the most unstable mode which satisfies $k_z L \simeq 0.3$, where $k_z = m\pi/L_z$ is the wavenumber and L is the current sheet thickness. The apparent difference mentioned above can be explained as follows. At the early stage, particle acceleration and heating are negligible. Due to the driving force applied at the driven inflow boundary, the current sheet is pinched and the magnetic field is piled up outside the current sheet, leading to enhanced current and particle drift speed in the current sheet, which in turn results in an effectively thinner current sheet thickness L' ($L' < L$). Thus, a shift of the previous most unstable mode toward larger wavenumbers is required in order to satisfy the most unstable tearing mode condition $k_z L' \simeq 0.3$.

Previous studies show that linear growth rates for ion and electron tearing modes can be written as $\gamma_i \simeq 0.12(u_i/v_{thi})^{5/2}\Omega_i$ and $\gamma_e \simeq 0.5(u_e/v_{the})^{5/2}\Omega_e$, respectively [e.g., Terasawa, 1981; Quest and Coroniti, 1981a, 1981b; Swift, 1986; Ding et al., 1986]. With plasma parameters used in the present simulation, an ion tearing mode would have a linear growth rate of $\gamma_i = 0.047\Omega_e$ and an electron tearing mode would have a linear growth rate of $\gamma_e = 0.009\Omega_e$, if no driving force is imposed at the driven inflow boundary. To compare the tearing mode instability developed in the present simulation with the ion and electron tearing modes, the linear growth rate of the tearing mode observed in the simulation is calculated. The linear growth rate (γ) of the tearing mode observed in the simulation can be easily obtained by taking the slope of $m = 3$ curve and then dividing by 2, since the power spectrum P_{B_x} is proportional to $e^{2\gamma t}$. The growth rate is found to be $\gamma \simeq 0.027\Omega_e$. This result indicates that an enhanced electron tearing mode is developed in the simulation due to the imposed driving force at the driven inflow boundary. Similar results were obtained earlier with the one-component particle

simulations, in which an enhanced ions tearing mode is observed. Notice that although the current is mainly carried by ions in the present full particle simulations, electrons are the particles that interact with the tearing waves, leading to the development of enhanced electron tearing mode in the simulation. The simulation results of Swift [1986] also indicated that an ion tearing mode having a larger linear growth rate is developed in the one-component particle simulations, whereas an electron tearing mode having a smaller linear growth rate is developed in the full particle simulations.

Figure 6.3 also shows that after $t \simeq 40\Omega_e^{-1}$, the perturbations of $m = 1$ and $m = 2$ modes also grow with linear growth rates comparable to that of $m = 3$ mode, and that after $t \simeq 150\Omega_e^{-1}$, the perturbation of $m = 1$ becomes dominant while the perturbations of $m = 2$ and $m = 3$ decrease, due to the coalescence of small magnetic islands and the formation of a larger magnetic island. However, the nonlinear growth rate of the $m = 1$ mode is much smaller ($\gamma \simeq 0.003\Omega_e$) than that in the earlier linear stage ($\gamma \simeq 0.032\Omega_e$, for $40 \leq \Omega_e t < 80$ and $\gamma \simeq 0.014\Omega_e$, for $80 \leq \Omega_e t < 150$). As large magnetic islands move out of the simulation domain, perturbations with smaller mode numbers start to grow again, leading to the formation of small magnetic islands, which later coalesce to form larger magnetic islands. These results indicate that as long as the simulations are continued, the formation and convection of magnetic islands by the driven collisionless magnetic reconnection process repeat quasi-periodically, producing signatures similar to FTEs observed at the dayside magnetopause. Besides the formation and convection of magnetic islands and bubbles, high-speed plasma flows, particle energization and acceleration,

intense electromagnetic waves, and particle heat fluxes are also observed associated with the driven collisionless reconnection process.

Driven magnetic reconnection is intrinsically a time-dependent and highly nonlinear process. The nonlinear nature of the driven reconnection process is reflected by the intermittent and sporadic formation of magnetic islands caused by the multiple X line reconnection observed in the simulation. If the driven reconnection process is considered as a dynamic system, the imposed constant reconnection electric field at the inflow boundary as an input that drives the system, and the reconnection electric field in the current sheet region as a response to the input driving force and an output of the driven system, then the nonlinear nature of the driven reconnection process is clearly displayed by the temporal variations of the average reconnection electric field in the current sheet region, as plotted in Figure 6.4. As discussed in Chapter One, the reconnection electric field can also be considered as the reconnection rate for the magnetic reconnection process. Besides the high-frequency fluctuations, the temporal variation of the reconnection electric field in the current sheet region shown in Figure 6.4 has several spiky structures, e.g., $E_y = 0.47(v_{the}B_0/c)$ at $t = 60\Omega_e^{-1}$ and $E_y \geq 0.75(v_{the}B_0/c)$ at $t = 1440\Omega_e^{-1}$, although the imposed reconnection electric field at the driven inflow boundary is only a constant ($E_y = 0.23(v_{the}B_0/c)$), indicated by the straight line in Figure 6.4. These spiky structures indicate the enhanced reconnection periods and the bursty nature of the driven magnetic reconnection process, which is usually characterized by the formation of magnetic islands and bursts of energetic particles.

Another striking feature of Figure 6.4 is that during the quasi-steady single X line reconnection period (identified approximately between $t = 640\Omega_e^{-1}$ to $t = 1040\Omega_e^{-1}$) the average reconnection electric field in the current sheet region

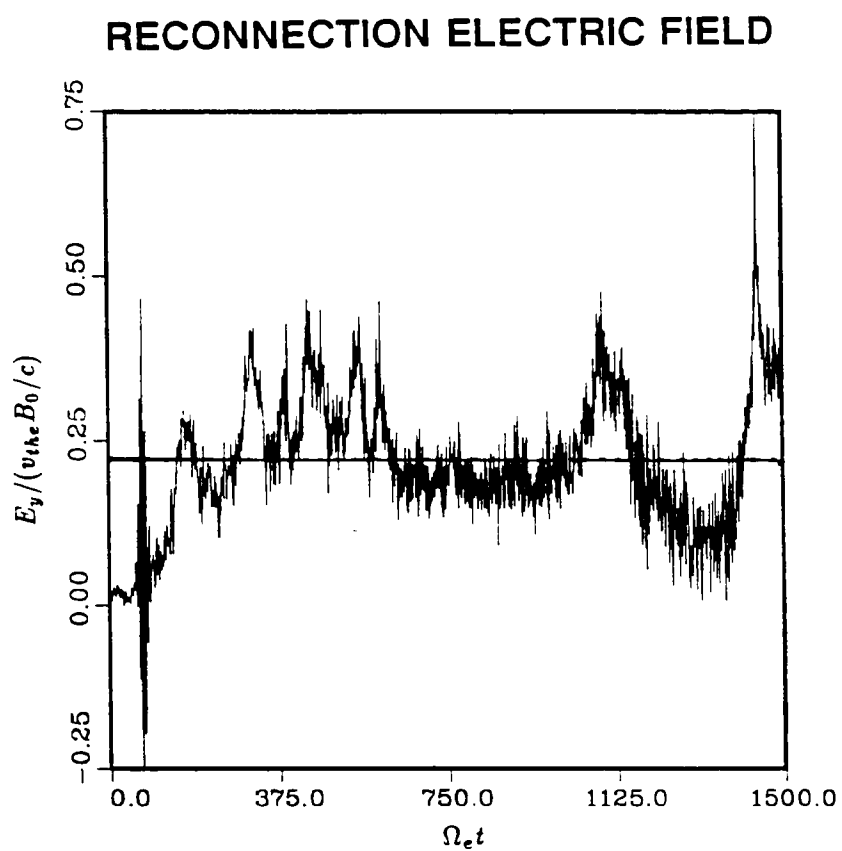


Figure 6.4 Average reconnection electric field as a function of time measured in the current sheet region ($x \simeq 0$) in the simulation Case B. The straight line indicates the imposed reconnection electric field at the driven inflow boundary ($x = \pm L_x$).

can be estimated as a constant that is only slightly smaller than the imposed reconnection electric field at the driven inflow boundary. A similar feature has also been demonstrated by Lee and Ding [1987] in their one-component particle simulation of the collisionless magnetic reconnection. In Lee and Ding [1987], it was shown that during the quasi-steady single X line reconnection, the reconnection rate ($M_A = 0.32$) in the current sheet region is very close to the imposed reconnection rate ($R_0 = 0.3$) at the driven inflow boundary. From the above observations, it is conceived that for the driven magnetic reconnection, a linear response to the constant driving force leads to the quasi-steady single X line reconnection, whereas a nonlinear response to the constant driving force results in the multiple X line reconnection; this in turn leads to the repeated formation and convection of magnetic islands. Therefore, the quasi-steady single X line reconnection can be considered as a special case in the nonlinear time-dependent driven magnetic reconnection processes. The criterion for the transition from single X line reconnection to multiple X line reconnection has been examined by Lee and Fu [1986] based on MHD simulations.

One of the features associated with FTEs at the dayside magnetopause is the detection of energetic particles [e.g., Daly et al., 1981; Scholer et al., 1982]. It is found in the simulation that coincident with the magnetic reconnection enhancements, which are indicated by the peaks in the reconnection electric field, ions and electrons are accelerated by the magnetic reconnection. A detailed study of particle acceleration during collisionless magnetic reconnection will be reported in the next chapter. Shown in Figure 6.5 are the electron energy distributions at $t = 0$ and $t = 1020\Omega_e^{-1}$. At $t = 0$, the initial distribution is a Maxwellian distribution. At $t = 1202\Omega_e^{-1}$, energetic electrons with energies up to $300T_e$ are generated during the driven collisionless magnetic reconnection and the electron distribution shows

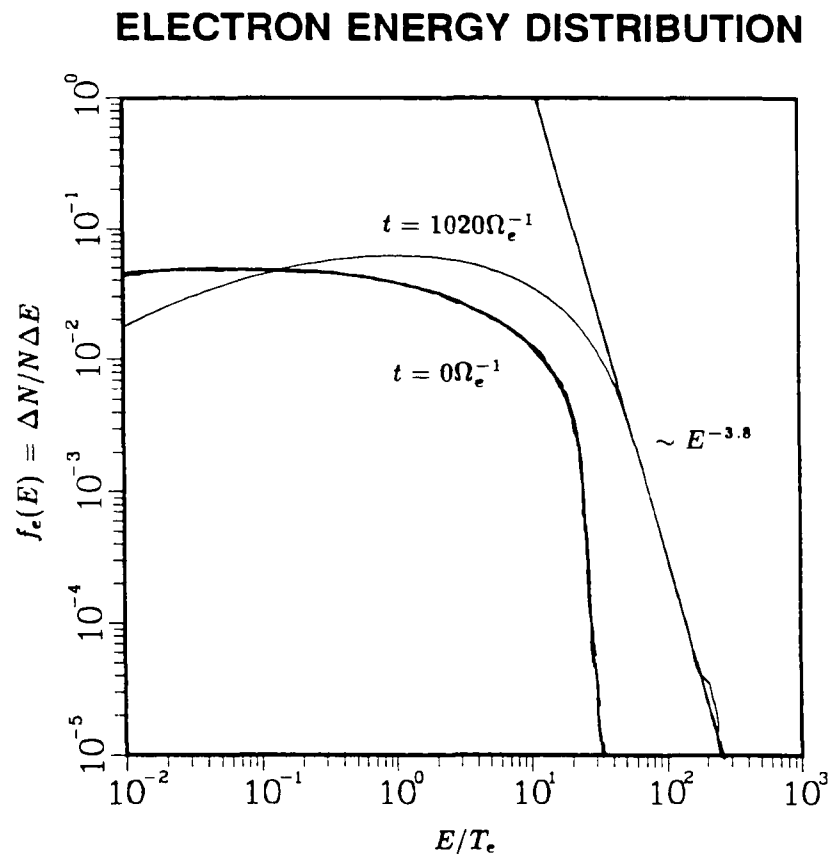


Figure 6.5 Electron energy distributions at $t = 0$ and $t = 1020 \Omega_e^{-1}$ in Case B. At $t = 1020 \Omega_e^{-1}$ energetic electrons with an energy spectrum of $f_e(E) \sim E^{-3.8}$ is generated by the reconnection process.

a high-energy tail, which fits approximately a power law of $f_e(E) \sim E^{-3.8}$ for $E > 50T_e$. At $t = 1020\Omega_e^{-1}$, the ion energy distribution (not shown) also has a high-energy tail, which is approximately given by a power law of $f_i(E) \sim E^{-4.4}$ for $E > 40T_i$.

Similar to the results of the one-component simulations presented in Chapter Five, the numbers of energetic ions and electrons in the present simulations are found to increase during the formation of magnetic islands and decrease with the ejection of magnetic islands. Therefore, the number of energetic particles and the high-energy parts of ion and electron distribution functions vary from time to time as the time-dependent driven collisionless magnetic reconnection process continues. On the basis of an examination of particle energy distribution functions at various simulation times, it is found that the energy spectra for energetic ions and electrons can be respectively written as

$$f_i(E) \sim E^{-4.2 \pm 0.7} \quad (6.1)$$

and

$$f_e(E) \sim E^{-3.9 \pm 0.5} \quad (6.2)$$

High-speed plasma flows associated with FTEs are often observed at the day-side magnetopause. An example of the high-speed plasma flow data associated with FTEs observed by AMPTE/UKS satellite [Smith et al., 1986] is reproduced in Figure 6.6. Several FTEs were detected from 17:45 to 17:57 on August 26, 1984, while the satellite was moving from the magnetosphere into the magnetosheath. It is shown in Figure 6.6 that in the absence of FTEs, the plasma flow velocity is generally less than $50 \sim 100\text{km/s}$, whereas during FTEs, the plasma flow velocity can reach as high as $200 \sim 300\text{km/s}$, which is comparable to the Alfvén speed at

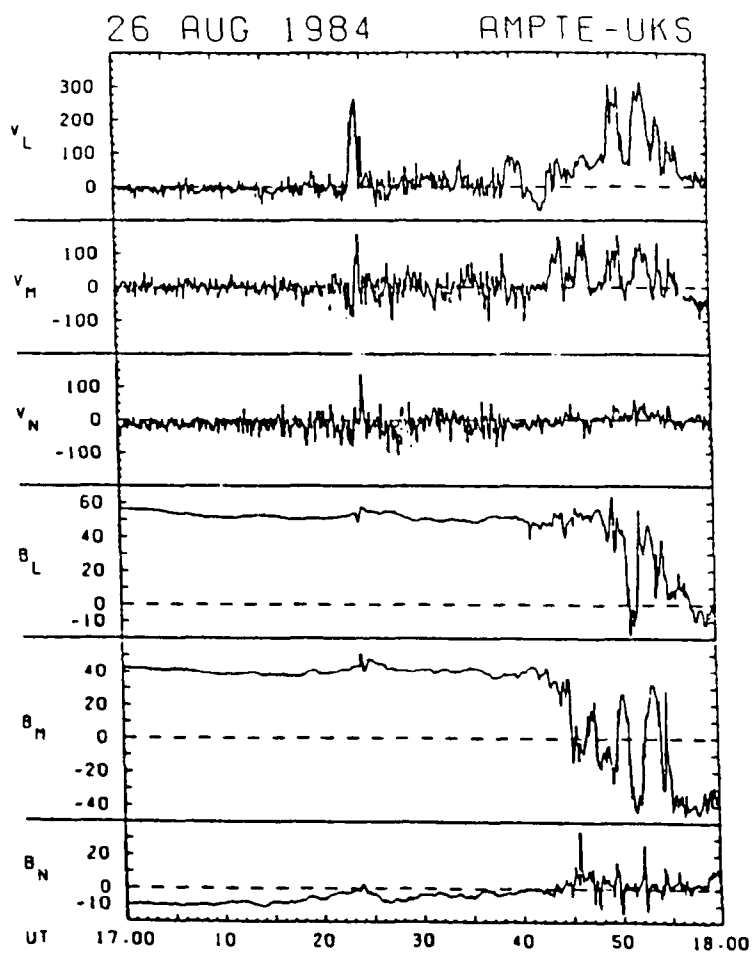


Figure 6.6 Satellite observation of high-speed plasma flows associated with FTEs at the dayside magnetopause [Smith et al., 1986]. The components of plasma flow velocity and magnetic field in the boundary normal coordinate system [Russell and Elphic, 1979] are plotted as functions of time.

the dayside magnetopause. Notice that the high-speed plasma flows are mainly in the L - and M -directions tangential to the magnetopause, whereas the flow speed normal to the magnetopause remains more or less the same as when FTEs are absent. Besides high-speed plasma flows, particle heat fluxes formed by energetic particles streaming along magnetic field lines are also observed during FTEs at the dayside magnetopause [Scudder et al., 1984; Thomsen et al., 1987; Klumpar et al., 1989]. The high-speed plasma flows associated with FTEs are believed to be caused by the magnetic reconnection process at the dayside magnetopause. However, the field-aligned particle heat fluxes associated with FTEs may be caused by particle acceleration during magnetic reconnection and/or by the leakage of hot magnetospheric particles along the reconnected open magnetic field lines [Daly et al., 1981; Scholer et al., 1981; Sonnerup et al., 1981; Sibeck et al., 1987].

To compare the simulation results with FTE observations, plasma flow patterns and particle heat fluxes at various simulation times are computed. It is found that high-speed plasma flows with a speed comparable to the Alfvén speed are generated by the driven collisionless magnetic reconnection process, especially during the convection of large magnetic islands, which is similar to what is observed in the one-component particle simulations. In the meantime, field-aligned particle heat fluxes are also generated by the reconnection process. An example of the high-speed plasma flows and particle heat fluxes associated with the driven collisionless magnetic reconnection observed in Case B are presented in Figure 6.7.

Figure 6.7a shows the magnetic field line at $t = 1020\Omega_e^{-1}$. Two X lines are present, one near the center of the simulation domain and the other close to the right outflow boundary. A small magnetic island is formed in the current sheet region with $z > 0$, while a significant amount of magnetic field bending is present in the current sheet with $z < 0$. Figure 6.7b shows the contours of electrostatic potential

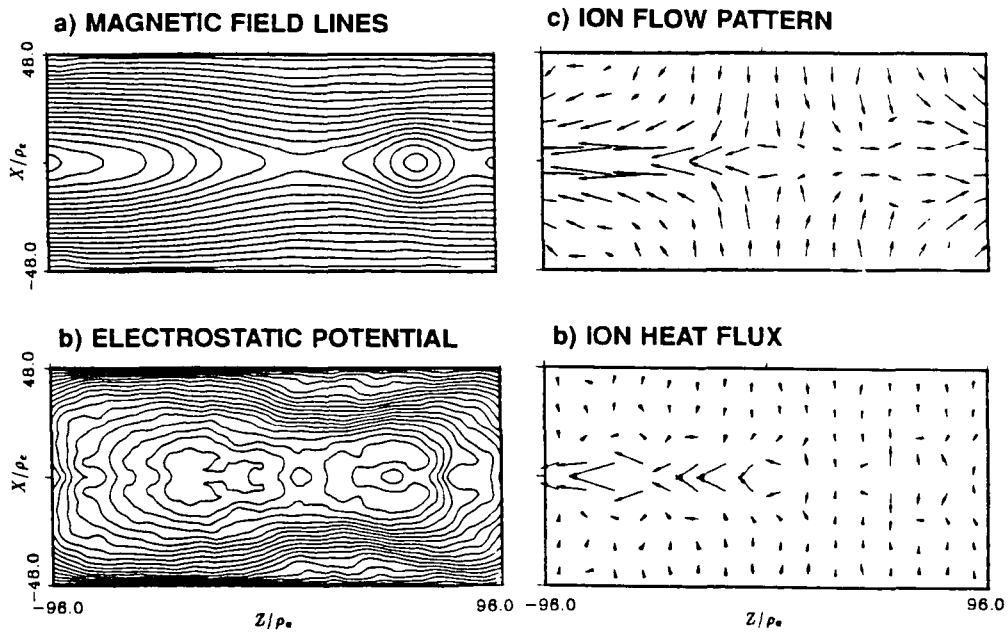


Figure 6.7 High-speed plasma flow and particle heat flux generated by the driven collisionless magnetic reconnection. (a) Magnetic field lines, (b) contours of electrostatic potential, (c) ion flow pattern, and (d) ion heat flux obtained at $t = 1020\Omega_e^{-1}$ in Case B. The maximum flow speed corresponds to $\sim 1.3v_A$, where v_A is the Alfvén speed.

at the corresponding simulation time, which are similar to the feature discussed earlier in Figure 6.1b. The ion flow pattern at $t = 1020\Omega_e^{-1}$ is shown in Figure 6.7c. Incoming plasma is found to flow from the driven boundary at $x = \pm L_x$ towards the central current sheet ($x = 0$), due to the $\mathbf{E} \times \mathbf{B}$ drift motion of particles. Plasma is accelerated at the reconnection sites (X line regions), leading to the formation of high-speed plasma flow. The maximum flow speed at $t = 1020\Omega_e^{-1}$ is found to be $\sim 1.3v_A$, where v_A is the Alfvén speed. Associated with ejection of magnetic islands, high-speed plasma flows are formed and near the growing magnetic island, the flow speed is small. Notice that the high-speed plasma flows are mainly confined in the central current sheet region with $|x| < 7.5\rho_e$. This result and the bending of magnetic field shown in Figure 6.7a indicate that the high-speed plasma flows are mainly caused by current sheet acceleration.

Apart from particle acceleration, particle heating is also observed in the simulation. Both ion and electron heat fluxes are generated during the reconnection process. The heat flux is computed from

$$\mathbf{q}_\alpha = \sum_k \frac{1}{2} m_\alpha (\mathbf{v}_{\alpha k} - \mathbf{u})^2 (\mathbf{v}_{\alpha k} - \mathbf{u}) S[\mathbf{x}_\alpha - \mathbf{x}_{\alpha k}(t)] \quad (6.3)$$

where \mathbf{u} is the average plasma flow velocity and α indicates species of particles. Shown in Figure 6.7d is the vector plot of ion heat flux at $t = 1020\Omega_e^{-1}$. It is clear that the heat flux is originated from the X line region and confined in the current sheet. The direction of particle heat flux is basically field-aligned. A large heat flux is generated by the bending magnetic field in the $z < 0$ region, providing further evidence for the current sheet acceleration.

To further demonstrate the superthermal particles and particle heat fluxes generated during the driven collisionless reconnection process, the ion distribution at $t = 1020\Omega_e^{-1}$ is plotted in Figure 6.8 as a function of V_{\parallel} , the velocity component

parallel to the magnetic field. The distribution function has a high-energy component in the region with $-2.4 \leq V_{\parallel}/v_{the} \leq -1.5$, indicating the presence of particle heat flux. The number of energetic particles is estimated to be 3% of the number of total particles. It is clear that the particle heat flux is carried by the superthermal particles streaming along the magnetic field lines. A similar feature has been found in electron distribution functions.

The observed ion and electron velocity distributions during FTEs have been reported by Thomsen et al. [1987] with ISEE data and by Klumpar et al. [1989] with AMPTE/CCE data. Both ion and electron distributions show the presence of heat flux along magnetic field lines. To show the similarity between simulation results and the observational data at the dayside magnetopause, proton distribution functions associated with FTEs obtained by ISEE 1 on November 6, 1977 [Thomsen et al., 1987] are reproduced in Figure 6.9. The top panel shows a two-dimensional proton velocity distribution and the bottom panel shows an one-dimensional velocity distribution that is obtained by cutting the two-dimensional distribution function along the direction of magnetic field (\mathbf{B}). Therefore, the one-dimensional distribution is actually a distribution function of V_{\parallel} . The shaded area shows the presence of field-aligned proton heat flux associated with FTEs that is very similar to the simulation result shown in Figure 6.8. The particle heat fluxes observed in simulations are mainly generated by the particle acceleration during the collisionless magnetic reconnection process. At the dayside magnetopause, however, particle heat fluxes associated with FTEs may also be contributed by the leakage of hot magnetospheric particles along the connected open magnetic field lines, as well as by the particle acceleration during magnetic reconnection.

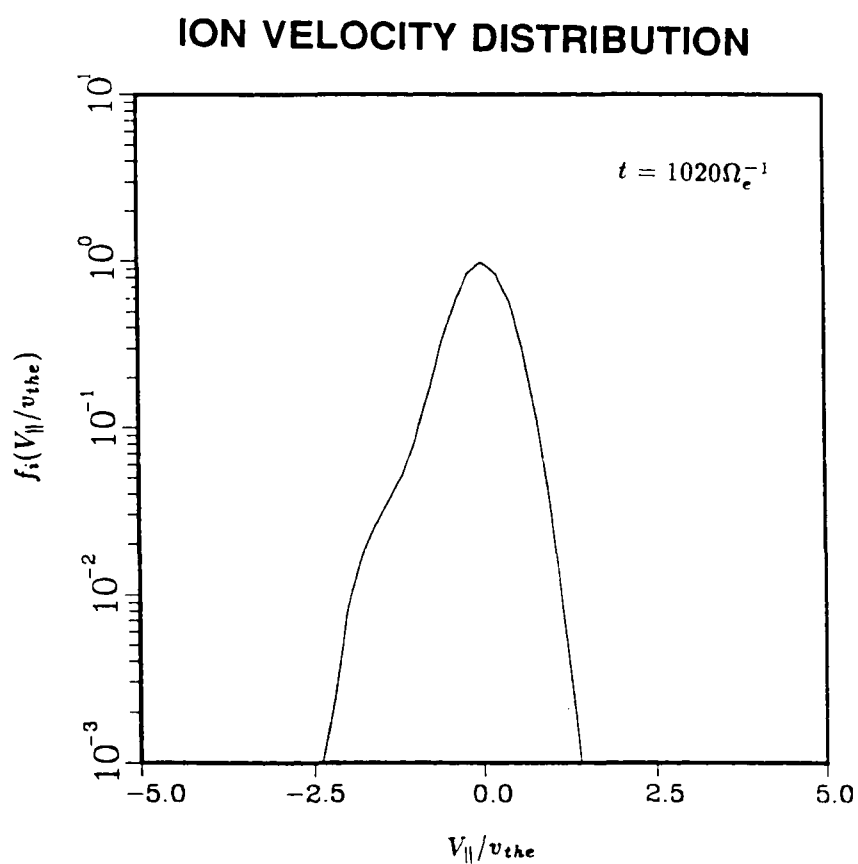


Figure 6.8 Ion distribution as a function of V_{\parallel} , the velocity component parallel to the magnetic field, obtained at $t = 1020\Omega_e^{-1}$ in Case B. The distribution shows the presence of a high-energy component in the region with $-2.4 \leq V_{\parallel}/v_{the} \leq -1.5$, corresponding to the presence of a particle heat flux.

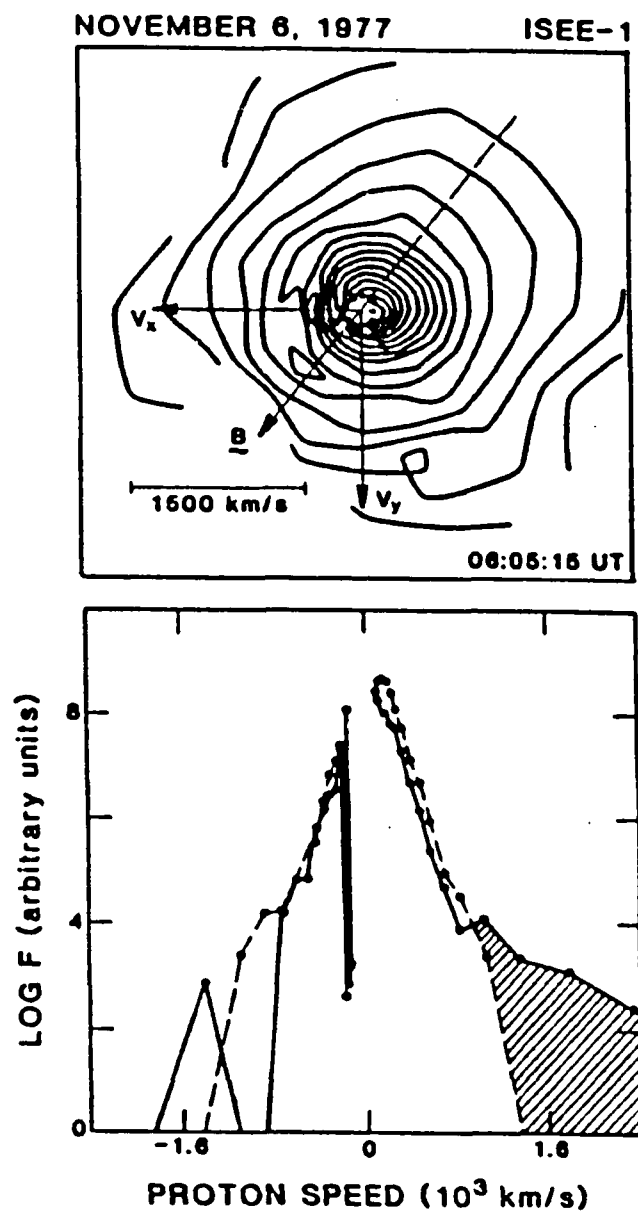


Figure 6.9 Proton distribution functions associated with FTEs at the day-side magnetopause. The top panel shows a two-dimensional proton velocity distribution and the bottom panel shows an one-dimensional velocity distribution, which is obtained by cutting the two-dimensional distribution function along the direction of magnetic field (B) [Thomsen et al., 1987].

Various plasma waves have been observed at the dayside magnetopause. The fluctuating electric field has a typical magnitude of a few mV/m and the fluctuating magnetic field has a typical magnitude of 10nT. The power spectrum for the fluctuating magnetic field, ranging from 10 to 1000Hz, can be approximated by a power law of $P_B \sim f^{-\alpha}$ with $\alpha = 3.3 \sim 4.7$. The power spectrum for the fluctuating electric field, ranging from 10Hz to 100kHz, can also be fitted by a power law of $P_E \sim f^{-\alpha}$ with $\alpha = 2.0 \sim 2.8$ [Gurnett et al., 1979; Anderson et al., 1982; LaBelle and Treumann, 1988]. The observation that wave intensities at the dayside magnetopause increase with an increase of the negative IMF B_z component indicates a possible correlation between the waves and magnetic reconnection process [Tsurutani et al., 1989]. Intense plasma waves associated with FTEs have also been reported by LaBelle et al. [1987].

Intense fluctuations in both electric and magnetic fields are observed in the particle simulation of the driven collisionless magnetic reconnection. To examine the electric and magnetic waves associated with the driven collisionless magnetic reconnection process, the electric field \mathbf{E} and magnetic field \mathbf{B} are recorded at a time interval of $1\Omega_e^{-1}$ at selected points in the simulation domain. The magnetic field data show that, associated with the convection of magnetic islands, the magnetic field component B_x displays the bipolar signatures similar to the observations of FTEs. The temporal variations of the power spectrum of the magnetic field component B_x show a distinct feature, which will be discussed on the basis of the self-organization theory in the later section. Notice that in the simulation, the electrostatic field is two-dimensional, confined in $x - z$ plane, whereas the induction electric field is one-dimensional, with an E_y component only. As discussed earlier, the magnetic field lines outside the current sheet are more or less equipotential lines, because the fast electron motion tends to short out the parallel electrostatic

field along the field lines. Therefore, the electrostatic fluctuation in the electrostatic field component E_z is usually smaller than that in the cross-field line component E_x . However, in the current sheet region, the electric field is more irregular and turbulent than outside the current sheet so that the fluctuation in the electric field component E_z is comparable to that in E_x . The power spectra of magnetic field \mathbf{B} and electric field \mathbf{E} are computed. An example of the typical power spectra of the electromagnetic waves associated with the driven collisionless magnetic reconnection is shown in Figure 6.10.

Figure 6.10a shows the typical power spectrum of the magnetic field component B_x recorded at $(x/\rho_e = 12, z/\rho_e = 72)$, which is outside the current sheet and near the right boundary of the simulation domain. The power spectrum can be approximated by a power law of $P_B \sim f^{-3.8}$, which is comparable to the power spectrum of $P_B \sim f^{-4}$ observed in FTEs [Elphic, 1988], where f is frequency. Figure 6.10b shows the typical power spectrum of the electrostatic field $E = \sqrt{E_x^2 + E_z^2}$ recorded at $(x/\rho_e = 24, z/\rho_e = 0)$. The power spectrum can be approximately fitted by a power law of $P_E \sim f^{-1.8}$, which is close to the observed spectrum of $P_E \sim f^{-2}$ [Anderson et al., 1982]. Notice that the small peak in both the magnetic field spectrum and the electric field spectrum at the frequency range $f = 0.1(\Omega_e/2\pi)$, which corresponds to the ions gyrofrequency in the simulation. Therefore, these peaks in the power spectra may be related to the ion cyclotron waves in the simulation. The power spectra in the high-frequency region, e.g., $f > 0.2(\Omega_e/2\pi)$, are believed to be caused by the thermal noise in the simulation.

Although the power spectra shown in Figure 6.10 represent the typical power spectra of the electric and magnetic fluctuations observed in the simulation, the power spectra at different locations do show a little variation. In general, the power spectra in the current region are higher than outside the current sheet. An

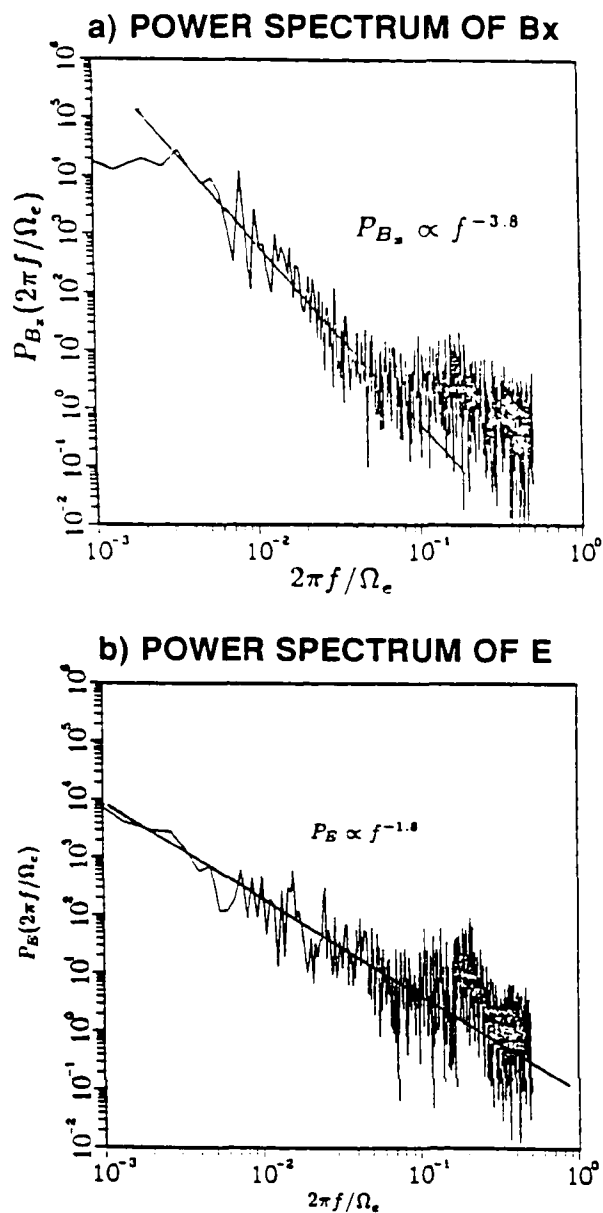


Figure 6.10 Typical power spectra of electromagnetic waves associated with the driven collisionless magnetic reconnection observed in simulation Case B. (a) Power spectrum of magnetic field component B_x obtained at $(x/\rho_e = 12, z/\rho_e = 72)$ and (b) power spectrum of electrostatic field $E = \sqrt{E_x^2 + E_z^2}$ obtained at $(x/\rho_e = 24, z/\rho_e = 0)$.

examination of power spectra at 49 different locations, both inside and outside the current sheet, shows that the spectrum for the fluctuating magnetic field can be approximated as

$$P_B \sim f^{-3.5 \pm 0.5} \quad (6.4)$$

and the spectrum for the fluctuating electric field can be approximately written as

$$P_E \sim f^{-1.6 \pm 0.4} \quad (6.5)$$

Due to the limited number of particles in each grid cell used in particle simulations, the thermal noise, which may also contribute to the fluctuating electric and magnetic fields, is unavoidable. To examine the effects of thermal noise in the simulation code on the spectra of fluctuating electric and magnetic fields, several simulation cases were run with a uniform or nonuniform parallel magnetic field and plasma configurations, corresponding to the cases when IMF has a northward B_z . The simulation results show that in the absence of magnetic reconnection, the power spectra of the fluctuating electric and magnetic fields, mainly caused by the thermal noise, are much lower and less steep than when the reconnection process is present. For example, in a uniform magnetic field and plasma configuration, the average power spectra of the fluctuating magnetic and electric fields are found to be

$$P_B \sim f^{-1.5 \pm 0.3} \quad (6.6)$$

and

$$P_E \sim f^{-1.1 \pm 0.2} \quad (6.7)$$

respectively, which are quite different from (6.4) and (6.5) obtained when the driven collisionless magnetic reconnection takes place.

In the above simulations, Case A and Case B, both quasi-steady single X line reconnection (SXR) and intermittent multiple X line reconnection (MXR) can be obtained during the driven collisionless magnetic reconnection. Various features associated with the driven collisionless reconnection process have been examined and the results are compared with FTE observations at the dayside magnetopause. However, in Case A and Case B, the effects of the magnetic field component B_y , which is perpendicular to the simulation $x - z$ plane and self-generated by the currents J_x and J_z in the simulation plane, have been artificially suppressed for the sake of simplicity. In the following simulations, the self-generated magnetic field B_y component is included and the symmetric boundary condition is no longer imposed at $x = 0$. Now the vector potential has three components, $\mathbf{A} = A_x \mathbf{e}_x + A_y \mathbf{e}_y + A_z \mathbf{e}_z$ and simulations are carried out in the full plane with $-L_x \leq x \leq L_x$ and $-L_z \leq z \leq L_z$.

The self-generated magnetic field B_y component included in the following simulations is different from the so-called guiding field B_{y0} , which is a zero-order magnetic component parallel to the current sheet. If the initial magnetic field configuration is strictly antiparallel, there is no guiding field B_{y0} in the current sheet direction; whereas if the rotation of initial magnetic field across the current sheet is less than 180° , the magnetic field will have an antiparallel component and a guiding field B_{y0} along the current sheet. The guiding field B_{y0} has been found to have an important influence on the tearing mode instability and magnetic reconnection process. It has been shown by both theoretical analyses and numerical simulations that the growth rate of tearing mode instability is significantly reduced due to magnetization of electrons by the guiding field B_{y0} [e.g. Katanuma and Kamimura, 1980; Quest and Coroniti, 1981a, 1981b; Hoshino, 1987; Allen and Swift, 1989]. However, in the present simulations, the initial field configuration is

strictly antiparallel and the guiding field B_{y0} is set at zero. During simulations, a magnetic field component B_y will be generated self-consistently by the currents J_x and J_z in the simulation $x - z$ plane. This self-generated B_y component is now included in the simulation study of the driven collisionless magnetic reconnection process. Although it is not difficult to implement a nonzero guiding field B_{y0} in the particle simulations of magnetic reconnections with nondriven and periodic boundary conditions, as demonstrated in Allen and Swift [1989], the inclusion of the nonzero guiding field B_{y0} into the particle simulations of driven collisionless magnetic reconnection, to be discussed in later chapter, is not as trivial as first thought.

Several cases of the driven collisionless magnetic reconnection with the self-generated magnetic field B_y component are simulated. A typical example of such simulations, Case C, is presented below. Parameters and initial conditions for Case C are the same as those used in Case B. The simulation is run from $t = 0$ to $t = 600\Omega_e^{-1}$. Magnetic field lines, which are contours of A_y , and contours of the self-generated magnetic field B_y component at different simulation times in Case C are shown in Figure 6.11. The magnetic field lines plotted in Figure 6.11a display the similar features of driven collisionless magnetic reconnection shown by Case B in Figure 6.2a. The development of the reconnection process is altered a little due to the inclusion of the B_y component. It is also found in the simulation that the basic features associated with driven collisionless magnetic reconnection, such as intermittent formation and convection of magnetic islands, generation of energetic particles and particle heat fluxes, generation of high-speed plasma flows, and generation of intense plasma waves, are not affected significantly.

Figure 6.11b shows the contours of the self-generated magnetic field B_y component at different simulation times. In Figure 6.11b, solid lines indicate the regions

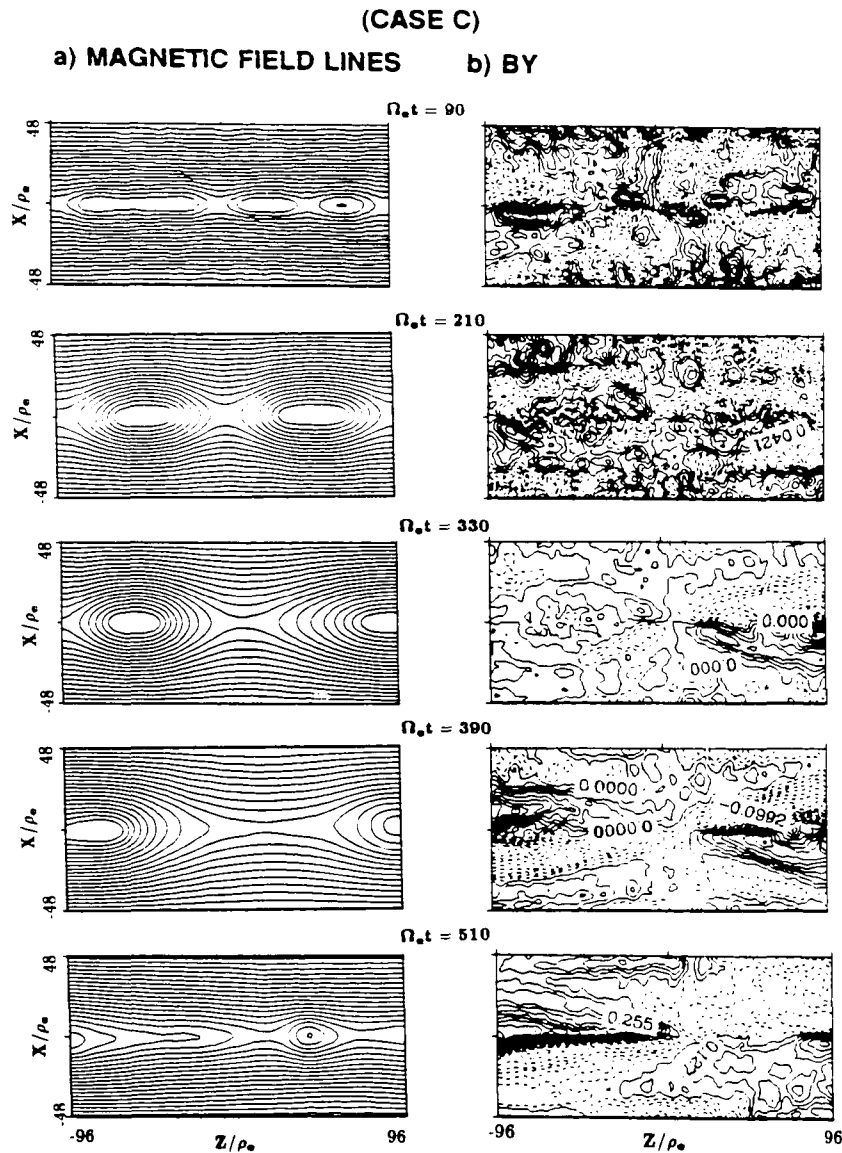


Figure 6.11 (a) Magnetic field lines and (b) contours of the self-generated magnetic field B_y component at different simulation times in Case C. In B_y contours, solid lines indicate the regions with $B_y \geq 0$ while dash lines represent the regions with $B_y < 0$.

with $B_y \geq 0$ while dashed lines represent the regions with $B_y < 0$. It can be seen in Figure 6.11b that at the early stage, the values of B_y are small and its patterns are irregular; at the later stage, a large B_y component can be generated and a macroscopic pattern of B_y can be formed associated with the ejection of magnetic islands. For example, at $t = 90\Omega_e^{-1}$, the maximum value of $|B_y|$ is found to be $\sim 0.4B_0$, about 0.25% of the value of the magnetic field outside the current sheet. Notice that due to the driving force applied at the driven boundary ($x = \pm L_x$), magnetic field lines are piled up outside the current, leading to an increase of magnetic field strength. At $t = 510\Omega_e^{-1}$, the maximum value of $|B_y|$ is found to be as high as $\sim 1.2B_0$, which is about 50% of the value of the magnetic field outside the current. The large magnetic field component B_y and its macroscopic pattern are found to be caused mainly by the large x -component of electron current associated with the ejection of magnetic islands. As indicated by the B_y contours, in the $z > 0$ region the total current J_x is negative, which leads to a negative B_y in the $x > 0$ region above the current sheet and a positive B_y in the $x < 0$ region below the current sheet. The directions of total current J_x and the self-generated magnetic field B_y component are reversed in the $z < 0$ region. The presence of a positive magnetic field B_y component causes magnetic field lines to loop into the simulation plane, while a negative magnetic field B_y component caused magnetic field lines to loop out of the simulations plane, as also observed in Swift and Allen [1987].

Swift [1986] showed that the self-generated B_y has little effect on the development of tearing mode. But, in the presence of a convection electric field E_y , electrons lose potential energy and gain kinetic energy while streaming along the looped magnetic field lines; the self-generated B_y tends to confine electrons close to the current sheet, which in turn results in large electrostatic potential differences across magnetic field lines [Swift and Allen, 1987]. However, both electron

energization along looped magnetic field lines and large potential difference across magnetic field lines are not clearly observed in the present simulations. This may be due to the fact that in Swift and Allen [1987], a uniform convection electric field E_y is externally imposed, while in the present simulations the reconnection induction electric field E_y is self-generated and nonuniform, larger near the X line regions in the current sheet and smaller outside the current sheet. Therefore, electron acceleration by the electric field E_y is significant only in the small region near X lines, instead of in the whole simulation domain as in the simulations of Swift and Allen [1987]. Furthermore, in the present simulations both electrons and ions are unmagnetized near the current sheet, whereas in Swift and Allen [1987], electrons but not ions were magnetized in the current sheet region due to the presence of a nonzero magnetic field component (B_{10}) normal to the current sheet. Notice that in Swift and Allen [1987], no tearing instability was observed.

6.2 Driven Collisionless Reconnection in an Asymmetric Current Sheet

In the above simulations, a simplified symmetric current sheet model is used as the initial magnetic field and plasma configurations. Various features associated with the driven collisionless magnetic reconnection process have been examined and compared with FTE observations. However, the magnetic field configuration is generally asymmetric at the dayside magnetopause, where the magnetosheath field is usually smaller than the magnetospheric field. Furthermore, the magnetosheath plasma has a higher density and lower temperature, whereas the magnetospheric plasma has lower density and higher temperature. The asymmetric nature of the

dayside magnetopause current sheet can also be seen in the observations of magnetosheath and magnetospheric FTEs.

FTEs have been observed both in the magnetosheath and in the magnetosphere. Although magnetosheath FTEs and magnetospheric FTEs have similar recurrence times and similar scale sizes, the magnitude of magnetospheric FTE B_n signatures is generally smaller than those of magnetosheath FTEs, and more magnetosheath FTEs than magnetospheric FTEs tend to be observed [Rijnbeek et al., 1984]. Sometimes, two-regime FTEs are observed, characterized by a simultaneous FTE signature both in the magnetosheath and in the magnetosphere at the dayside magnetopause (Figure 6.12) [Farrugia et al., 1987]. Sometimes FTEs are only observed in the magnetosheath [Rijnbeek et al., 1984]. Recently, AMPTE/UKS satellite data reveal that the magnetospheric FTEs have a multilayered structure (Figure 6.13) in which plasma and fields show a systematic behavior [Farrugia et al., 1988]. The crater-like FTEs that feature a decrease in the magnetic field strength and an increase in the plasma density have been observed inside the magnetosphere [Rijnbeek et al., 1984; LaBelle et al., 1987; Farrugia et al., 1988]. Similar magnetic field and plasma signatures have also been identified in AMPTE/IRM data by Lühr and Klöcker [1987] as magnetic cavities or magnetic holes at the dayside magnetopause. It is suggested that the signatures of the crater-like FTEs and the magnetic cavities might indicate an early evolutionary state of an FTE, because they are often observed in the low-latitude region of the dayside magnetopause [Rijnbeek et al., 1984; Lühr and Klöcker, 1987].

To examine features of FTEs associated with the asymmetric dayside magnetopause, simulations of driven collisionless magnetic reconnection in an asymmetric current sheet have also been carried out. The asymmetric current sheet has a strong magnetic field on one side and a weak magnetic field on the other side. A

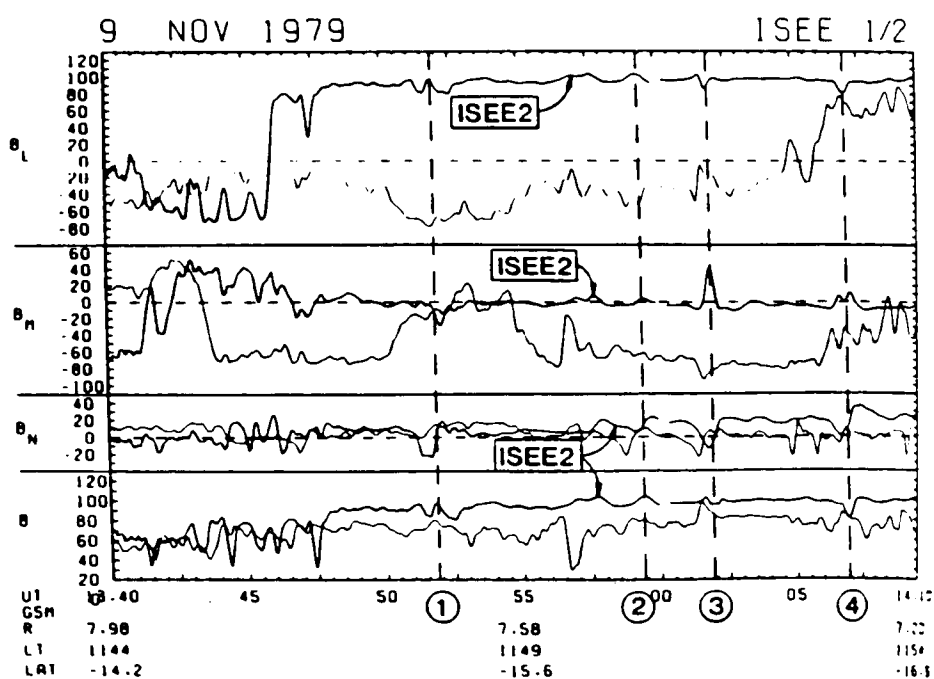


Figure 6.12 Magnetic field data for the inbound pass on November 9, 1979, which show detections of two-regime FTEs. The heavier trace refers to measurements on ISEE 2 while the lighter trace refers to ISEE1, which is about 3817km behind ISEE 2. The main two-regime FTEs are indicated by vertical lines [Farrugia et al., 1987].

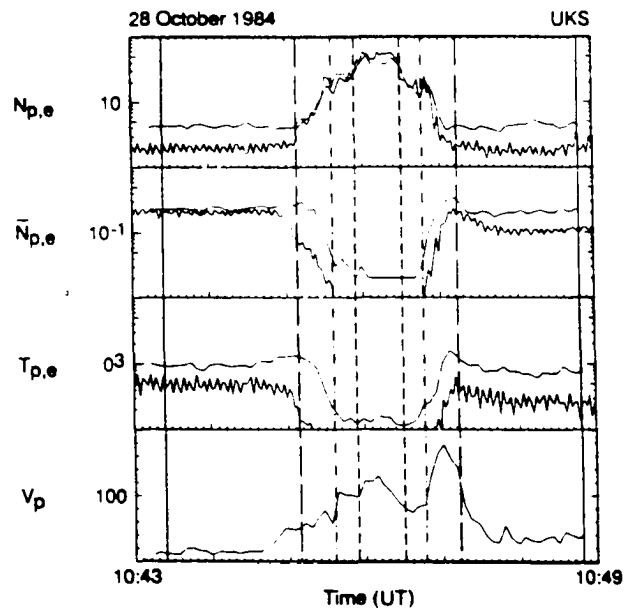
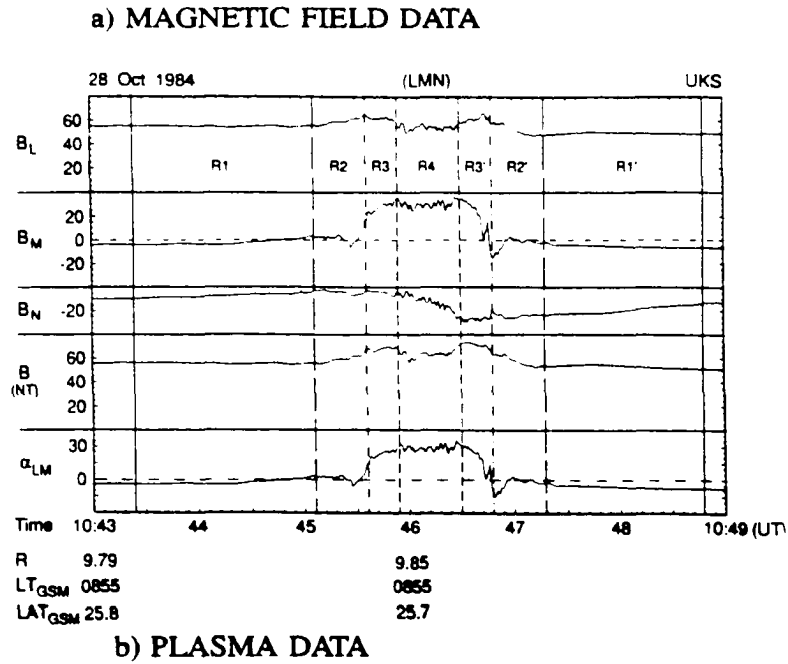


Figure 6.13 The multilayered structure observed in a magnetospheric FTE by AMPTE/UKS satellite on October 28, 1984. (a) Magnetic field data, and (b) plasma data, where more jagged trace refers to electrons, and the second panel shows number density of energetic particles [Farrugia et al., 1988].

dense and cool plasma population is present in the weak field region to represent magnetosheath plasma, while a hot and dilute plasma population is present in the strong field region to represent magnetospheric plasma. Several cases of the driven collisionless magnetic reconnection in the asymmetric current sheet configuration have been simulated. An example of simulations with the asymmetric current sheet, Case D, is presented below.

For the asymmetric current sheet, the magnetic field and temperature profiles can be written as

$$\mathbf{B}(\mathbf{x}) = -B_0 \left[\left(\frac{1 + R_B}{2} \right) + \left(\frac{1 - R_B}{2} \right) \tanh\left(\frac{x}{L}\right) \right] \mathbf{e}_z \quad (6.8)$$

$$T(\mathbf{x}) = T_0 \left[\left(\frac{1 + R_T}{2} \right) + \left(\frac{1 - R_T}{2} \right) \tanh\left(\frac{x}{L}\right) \right] \quad (6.9)$$

where $B_0 = -B_z(x = \infty)$, $T_0 = T(x = \infty)$, $R_B = -B_z(x = -\infty)/B_z(x = \infty)$, and $R_T = T(x = -\infty)/T(x = \infty)$ respectively are the magnetosheath field strength, the magnetosheath plasma temperature, the ratio of magnetospheric field to magnetosheath field, and the temperature ratio of magnetospheric plasma to magnetosheath plasma. The initial plasma density profile is determined by balancing the magnetic pressure with the plasma pressure. In the simulation, the ratio of magnetic fields is chosen to be $R_B = 2.0$ and the temperature ratio is chosen to be $R_T = 4.0$. Other parameters used in Case D are the same as those in the symmetric case, Case C, except that the temperature ratio of ions to electrons is chosen to be $T_i/T_e = 4.0$. It is also assumed that the imposed reconnection electric fields at the driven inflow boundary ($x = \pm L_x$) are equal. Case D is run from $t = 0$ to $t = 1500\Omega_e^{-1}$.

Figure 6.14a shows the magnetic field lines at various simulation times observed in Case D. At $t = 0$, an asymmetric current sheet is present. The dense magnetic

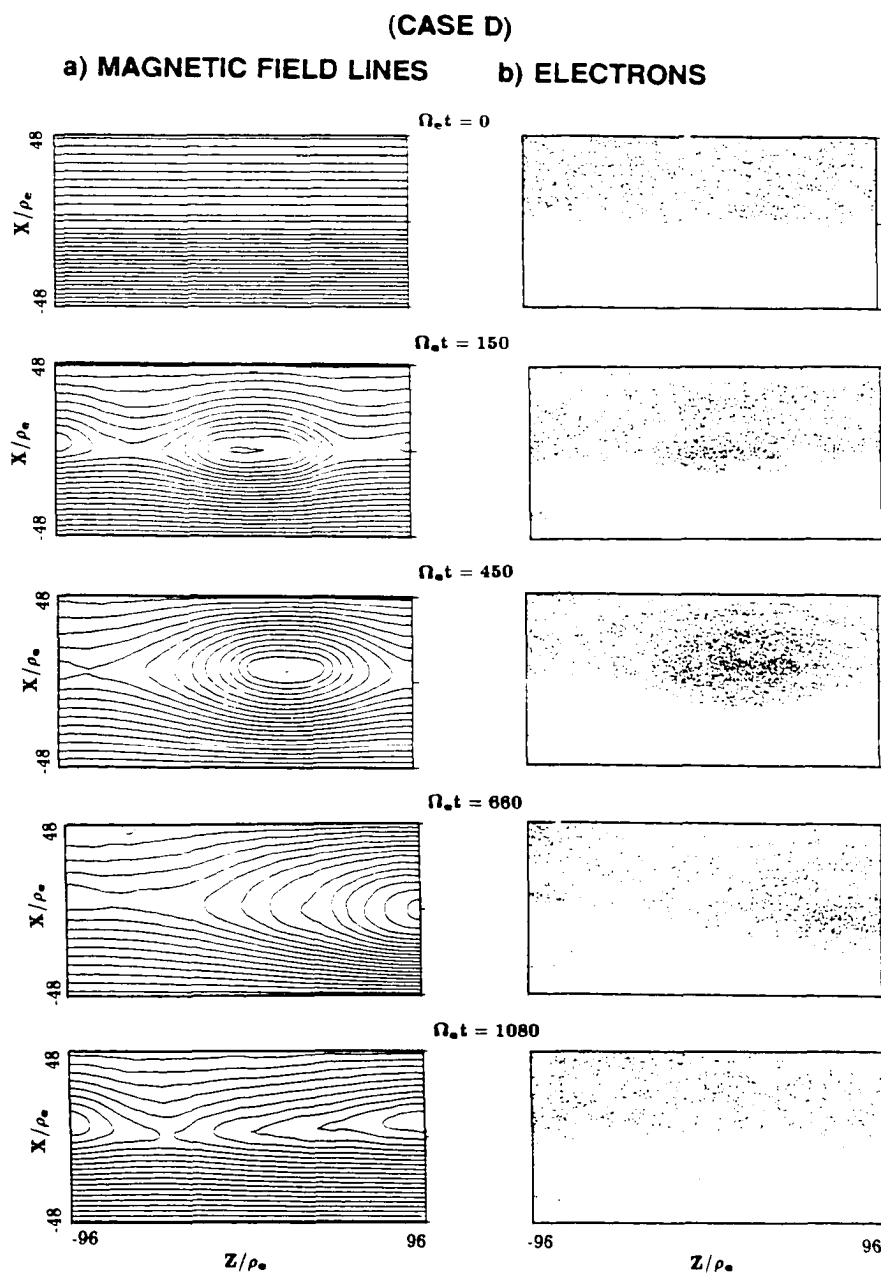


Figure 6.14 Driven collisionless magnetic reconnection is an asymmetric current sheet. (a) Magnetic field lines and (b) scatter plot of electron positions at various simulation times observed in Case D.

field lines in the $x < 0$ region represent the strong magnetospheric field, while the less dense magnetic field lines in the $x > 0$ region indicate the weak magnetosheath field. Similar to the cases shown previously, the driving force at the driven boundary ($x = \pm L_x$) results in the development of an enhanced tearing instability in the current sheet, which in turn leads to the development of the intermittent multiple X line reconnection. At $t = 150\Omega_e^{-1}$, two X lines and one magnetic island are present in the simulation domain. Notice that a magnetic island causes a simultaneous magnetic field perturbations in both the weak field region with $x > 0$ and the strong field region with $x < 0$, similar to the observations of two-regime FTEs (Figure 6.12); the magnetic field perturbations caused by the magnetic island are much larger in the weak field region than that in the strong field region. At $t = 450\Omega_e^{-1}$, the magnetic island grows to a larger size and at the same time, the convection of the island toward the right outflow boundary of the simulation domain is already started. Along with the plasma flows generated by the reconnection process, half of the large magnetic island formed earlier has moved out of the simulation domain at $t = 660\Omega_e^{-1}$. At $t = 1080\Omega_e^{-1}$, a single X line configuration is present in the simulation domain. A striking feature of this single X line configuration is that in the strong field region ($x < 0$), magnetic field lines are almost flat, indicating very limited magnetic field perturbations, whereas in the weak field region ($x > 0$), two magnetic bulges are formed and a significant amount of magnetic field perturbations is present. Although the earlier simulation results of Case A, B, and C show that both MXR and SXR processes can generate large magnetic perturbations on both sides of a symmetric current sheet, the results of Case D shown in Figure 6.14a indicate that in an asymmetric current sheet, only MXR process can generate a simultaneous magnetic field perturbation on both sides of the asymmetric current

sheet, and the magnetic field perturbations caused by SXR process are mainly in the weak field side of the current sheet.

Figure 6.14b shows the scatter plots of electron positions at the corresponding simulation times in Case D. At $t = 0$, a dense and cool plasma population representing magnetosheath plasma is located in the $x > 0$ region; a dilute and hot plasma population representing magnetospheric plasma is located in the $x < 0$ region. At $t = 150\Omega_e^{-1}$, during the multiple X line reconnection, a part of the dense and cool plasma becomes trapped by the magnetic island, forming a bulge of dense and cool plasma population intruded into the strong magnetic field region with $x < 0$. The intrusion of dense and cool plasma into the strong magnetic field region becomes further evident when the magnetic island grows to a larger size at $t = 450\Omega_e^{-1}$. With the convection of the magnetic island, part of the bulge of dense and cool plasma population moves out of the simulation domain at $t = 660\Omega_e^{-1}$. The intrusion of dense and cool plasma bulge into the strong field region disappears after the magnetic island moves out of the simulation domain and a single X line is formed at $t = 1080\Omega_e^{-1}$.

The intrusion of magnetosheath plasma bulge into the magnetosphere during the MXR process shown in Figure 6.14b can be important to the magnetospheric FTEs. If a satellite is in the magnetosphere and passing through a magnetic island formed by the MXR process, it will detect magnetic field perturbations similar to that of FTEs [Lee and Fu, 1985]. In the meantime, the satellite detects (1) hot and dilute magnetospheric plasma before encountering the magnetosheath plasma bulge, (2) a transition region with decreasing plasma temperature and increasing plasma density when encountering the magnetosheath bulge, (3) dense and cool magnetosheath plasma inside the magnetosheath plasma bulge, (4) a transition region again, but with increasing plasma temperature and decreasing plasma density,

when leaving the magnetosheath plasma bulge, and (5) hot and dilute magnetospheric plasma again, after leaving the magnetosheath plasma bulge. The magnetic field in the transition region may be stronger than that inside the magnetic island due to magnetic field compression. Thus, when encountering a magnetosheath plasma bulge in the magnetosphere, the satellite may observe a multilayered structure with systematic magnetic field and plasma variations as it detects a magnetospheric FTE. Such systematic changes in field and plasma have indeed been observed in the magnetosphere recently by AMPTE/UKS satellite (Figure 6.13) [Farrugia et al., 1988].

To further illustrate the different magnetic signatures generated by the MXR and SXR processes, the magnetic field lines and profiles of magnetic field B_x component obtained in both the weak field region ($x = 12\rho_e$) and strong field region ($x = -12\rho_e$) at time $t = 150\Omega_e^{-1}$ and $t = 1080\Omega_e^{-1}$ are shown in Figure 6.15. Since the present simulation box represents a small domain at the subsolar region of the dayside magnetopause, the magnetic field B_x component in the simulations is equivalent to the magnetic field B_n component in the boundary normal coordinate system [Russell and Elphic, 1979]. In the following, both B_x and B_n are used without distinction. Figure 6.15a is a reproduction of the second and the last panels of Figure 6.14a, which shows the MXR configuration at $t = 150\Omega_e^{-1}$ and the SXR configuration at $t = 1080\Omega_e^{-1}$. Figure 6.15b shows the profiles of FTEs B_n signatures generated by the MXR and SXR processes. The left two panels show that a magnetic island formed by the MXR process tends to produce simultaneous FTE B_n signatures on both sides of the asymmetric current sheet, even though the B_n signature in the strong field region ($x = -12\rho_e$) is smaller than that in the weak field region ($x = 12\rho_e$). On the other hand, the right two panels show that FTE B_n signatures generated by a magnetic bulge formed during the SXR process

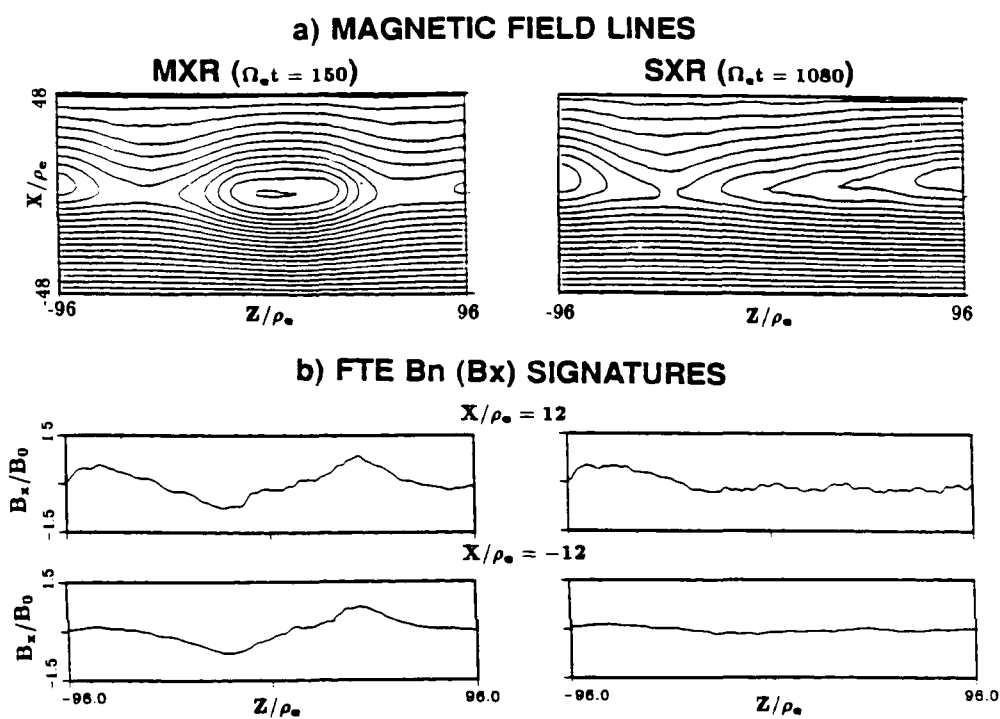


Figure 6.15 Different FTE B_n (B_z) signatures generated by the MXR and SXR processes observed in Case D. (a) Magnetic field lines and (b) FTE B_n signatures at $t = 150\Omega_e^{-1}$ and $t = 1080\Omega_e^{-1}$.

are mainly on the weak field side of the asymmetric current sheet and the B_n perturbations in the strong field region are insignificant. The above results indicate that the MXR and SXR processes tend to generate different FTE B_n signatures at the dayside magnetopause. The asymmetric B_n signatures on the two sides of an asymmetric current sheet were also observed in MHD simulations [Scholer, 1989b]. Recently, a systematic study of the different FTE signatures generated the MXR and SXR processes has been completed by Ding et al. [1990] on the basis of 2-D MHD simulations. Although Figure 6.15b shows the spatial profiles of the B_x signatures generated by the MXR and SXR processes, the temporal variations of B_x signatures associated with the MXR and SXR processes exhibit features similar to Figure 6.15b, as demonstrated in the simulations of Fu and Lee [1986] and Ding et al. [1990].

Figure 6.16 shows the magnetic field strength as a function of z at different locations relative to the current sheet ($x \simeq 0$) when an FTE signature is generated due to the formation of magnetic island by the MXR process at $t = 150\Omega_e^{-1}$. The top panel (1) and the bottom panel (6) show that far away from the current sheet, the magnetic field strength is enhanced when an FTE signature is detected. Panel 2 shows that near the current sheet, the magnetic field strength in an FTE may decrease due to the depletion of magnetic field in the X line region and at the center of the magnetic island, and increase at the edges of the magnetic island due to the compression of magnetic field lines. Close to the current sheet, the magnetic field strength may also remain almost unchanged during an FTE (panel 5). Inside the current, the magnetic field strength may become very small (panel 3) and at several locations the magnetic field strength may drop to near zero (panel 4), which is similar to the observations of magnetic cavities or magnetic holes reported by Lühr and Klöcker [1987]. Panel 4 also shows that magnetic field strength is

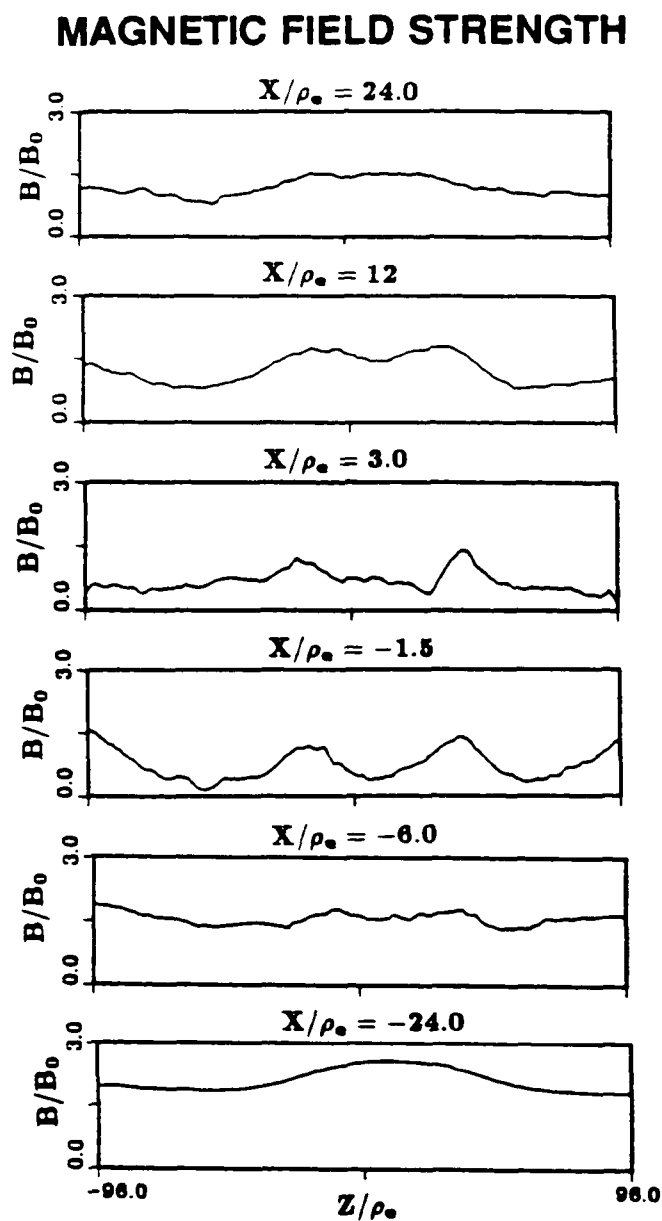


Figure 6.16 Magnetic field strength as a function of z observed at different locations relative to the current sheet ($x \simeq 0$) when an FTE signature is generated due to the formation of magnetic island by the MXR process at $t = 150\Omega_e^{-1}$.

enhanced at the edges of an FTE and reduced in the center of the FTE. This feature resembles the observed characteristics of the crater-like FTEs inside the magnetopause [Rijnbeek et al., 1984; LaBelle et al., 1987; Farrugia et al., 1988]. Our simulation results show that variations of magnetic field strength during an FTE are complicated and are closely related to the penetration of a satellite into the magnetic islands (flux tubes) at the dayside magnetopause.

FTEs have been observed both in the magnetosheath region and inside the magnetosphere at the dayside magnetopause. FTE signatures have been simultaneously observed by ISEE 1 and ISEE 2 spacecraft while they were separated by a few thousand kilometers, with ISEE 1 in the magnetosheath region and ISEE 2 inside the magnetosphere [Farrugia et al., 1987]. In the simulation, we have shown that the signatures of the two-regime FTEs can be generated by the formation of a magnetic island (a magnetic flux tubes in the three-dimensional environment) during the MXR process. Our simulation and recent simulations of Scholer [1989b] and Ding et al. [1990] have also shown that during the SXR process, magnetic bulges can be formed in the magnetosheath region, leading to the signatures of magnetosheath FTEs. Magnetic field perturbations inside the magnetosphere caused by the SXR at the dayside magnetopause are very weak. Therefore, observation of two-regime FTEs would indicate an MXR process at the dayside magnetopause, whereas observation of magnetosheath-only FTEs would indicate an SXR process. Since both the MXR and the SXR processes can produce the signatures of the magnetosheath FTEs and only the MXR process can generate the signatures of the magnetospheric FTEs, more FTEs at the dayside magnetopause would be detected in the magnetosheath region than inside the magnetosphere. This result is consistent with the ISEE 1 and 2 observations of FTEs [Rijnbeek et al., 1984].

A multilayered structure of magnetospheric FTEs was reported by Farrugia et al. [1988]. Within the layered FTE structure, the magnetic field and the plasma population show distinct properties. Inside the magnetospheric FTEs, cool and dense magnetosheath plasma is observed; outside the magnetospheric FTEs, hot and dilute magnetospheric plasma is observed; in between a transition region with a mixture of magnetosheath and magnetospheric plasma is observed. Within the layered FTE structure, the magnetic pressure and plasma pressure show an out-of-phase variation. In the simulation, we have shown that an intrusion of magnetosheath plasma bulge into the magnetosphere, due to the formation of a magnetic island (a magnetic flux tube) during the MXR process, may lead to the presence of the layered magnetospheric FTE structure. The variations of plasma and magnetic field observed in the simulation show qualitative agreement with the AMPTE observations [Rijnbeek et al., 1987; Farrugia et al., 1988].

The early observations show that the magnetic field strength in FTEs is typically enhanced [Russell and Elphic, 1979]. Then, Rijnbeek et al. [1984] found that the magnetic strength in FTEs may decrease as well as increase. Later on, crater-like FTEs were identified that featured a magnetic field strength enhancement at the edges of the FTEs and a magnetic field strength reduction in the center of the FTEs [LaBelle et al., 1987; Farrugia et al., 1988]. The crater-like FTEs appear to be a regular feature of magnetospheric FTEs. Observations of magnetic cavities or magnetic holes at the dayside magnetopause [Lühr and Klöcker, 1987] show magnetic field and plasma features similar to that of the crater-like FTEs. In the simulation, we have shown that the magnetic field strength in FTEs is typically increased during the MXR process when a satellite is far way from the current sheet region, whether it is located exterior or interior to the dayside magnetopause. Close to the current sheet, the magnetic field strength in FTEs may remain unchanged or

decrease. In the current sheet, detection of magnetic islands (magnetic flux tubes) inside the magnetosphere may produce magnetic field and plasma features resembling the crater-like FTEs. The signatures of magnetic cavities or magnetic holes may be detected when a satellite penetrates deep into a magnetic island (magnetic flux tube). The simulation results confirm the previous speculation that the presence or absence of the reduced magnetic field strength of an FTE indicates how deeply the satellite penetrates the FTE [LaBelle et al., 1987].

6.3 Self-organization in Driven Collisionless Magnetic Reconnection

In the previous two sections, the driven collisionless magnetic reconnection in both symmetric and asymmetric current sheets are studied on the basis of full particle simulations. Various particle properties and field features associated with the driven collisionless magnetic reconnection are examined and the results are compared with observations of FTEs at the dayside magnetopause. In this section, the driven collisionless magnetic reconnection process is examined from another perspective, on the basis of the self-organization theory.

The concept of self-organization has been developed in the studies of hydrodynamic and magnetohydrodynamic (MHD) turbulence since 1970s [Taylor, 1974; Rhines, 1975; Bretherton and Haidvogel, 1976; Montgomery et al., 1978; Matthaeus and Montgomery, 1980; Hasegawa, 1983]. The self-organization process has also been named as selective decay, selective dissipation, dynamic alignment, or relaxation processes and has been studied extensively [Matthaeus and Montgomery, 1984; Horiuchi and Sato, 1986; Taylor, 1986; Ting et al., 1986]. It is now well known that self-organization is a process in which an ordered structure can be formed from

a disordered structure in a nonlinear and dissipative system [Nicolis and Prigogine, 1977; Hasegawa, 1985].

It is well known in thermodynamics that if the energy of a system is the only conserved quantity, entropy is defined as a measure of the disorder nature in the quality of the system energy. If the system is allowed to evolve, the entropy of the system tends to increase. In other words, the system evolves toward greater disorder. However, in the presence of a local energy source and nonlinear interactions, a quasi-stationary and stable state having an ordered structure can be formed in a dissipative system [Nicolis and Prigogine, 1977; Nicolis, 1986 and references therein]. Here, the local decrease of entropy is compensated by an increase of entropy in the environment and the ordered structure is formed without violating the global entropy increase law [Hasegawa, 1985].

On the other hand, as pointed out by Hasegawa [1985], if more than one physical quantity is conserved in a physical system, the system can in principle form an ordered structure in one physical quantity, while letting other quantities take care of the increase of entropy through the self-organization process. For example, in a two-dimensional incompressible MHD turbulence, the total energy $E = \frac{1}{2} \int (\rho v^2 + B^2 / 4\pi) d^2 x$, the total cross helicity $H_c = \frac{1}{2} \int \mathbf{v} \cdot \mathbf{B} d^2 x$, and the squared vector potential $H_A = \frac{1}{2} \int \mathbf{A} \cdot \mathbf{A} d^2 x$ are conserved. In such a system with $H_c \simeq 0$, an ordered structure can be formed in \mathbf{A} due to an inverse cascade of the squared vector potential H_A to small wavenumber and a direct cascade of magnetic energy to large wavenumbers through self-organization [Pouquet, 1978]. The example shows that in a system, an ordered structure can be formed in one physical quantity at the expenses of an increased disorder in other quantities. Thus, whether you see an ordered structure totally depends on which quantity you look at. In some other cases, such as two- and three-dimensional (2- and 3-D) MHD turbulence with

$H_c \neq 0$, no ordered macroscopic structure is formed; instead, the self-organization appears in the alignment of the velocity and magnetic field vectors. Therefore, as Hasegawa [1985] perceived, the ordered structure in a self-organization process is subjective. Furthermore, the direct and inverse cascades of the conserved quantities in a system may have specific modal spectra in the wavenumber space during the self-organization process [e.g., Kraichnan and Montgomery, 1980; Hasegawa, 1985; Montgomery, 1989, and references therein].

During magnetic reconnection, ordered structures such as magnetic islands are often formed from the turbulent reconnection magnetic field. Therefore, magnetic reconnection can also be considered as a self-organization process. Previous examinations of magnetic reconnection as a self-organization process are mainly based on MHD turbulence theories [e.g., Taylor, 1986; Matthaeus and Lamkin, 1986; Horiuchi and Sato, 1986; Song and Lysak, 1989]. In the following, the driven collisionless magnetic reconnection is considered as a self-organization process. An explanation of some of the results obtained in the particle simulations of driven collisionless magnetic reconnection is attempted on the basis of the self-organization concept. It is not the purpose of the present study to vigorously verify that the driven collisionless magnetic reconnection is a self-organization process based on the first principle. Several concepts of the self-organization theory are only borrowed without verification to describe the driven collisionless magnetic reconnection from a different perspective. Some preliminary results are presented.

Since the self-organization process is subjective, as pointed out by Hasegawa [1985], whether an ordered structure can be observed depends on physical quantities examined. The simulation results presented above demonstrate that ordered magnetic island structures can be repeatedly formed by the driven collisionless reconnection process. Below, the repeated formation of ordered magnetic island

structures observed in the driven collisionless magnetic reconnection are explained by a hypothesis of generation and inverse cascade of the modal spectrum of the magnetic field component B_x in a self-organization process.

In the driven collisionless magnetic reconnection, the driving force applied at the driven boundary leads to an enhanced tearing mode instability, as shown in the simulations. The growth of the most unstable mode of the enhanced tearing instability produces an energy source at a specific wavenumber range with $k_x L \sim 0.3$, which can generate normal magnetic field component B_x . An inverse cascade of the modal spectrum of B_x results in an energy condensation at the smaller wavenumbers, leading to the formation of large ordered magnetic island structures; in the meantime, a direct cascade of magnetic energy results in plasma heating. Although part of the magnetic energy dissipates into plasma kinetic energy, the magnetic energy in the system may also increase, if the driving force at the driven boundary pumps more magnetic energy into the system than is dissipated, which is just the case shown in Figure 5.5. As the enhanced tearing instability slows down in the nonlinear stage when magnetic islands grow to large sizes, the rate of energy input at the most unstable wavenumber decreases and so does the rate of energy condensation at the smaller wavenumbers. Associated with the ejection of large magnetic islands, the energy condensation at the smaller wavenumbers in the modal spectrum of B_x can be drastically reduced. Since the system is driven continuously by the driving force imposed at the driven boundary, the whole cycle of process described above will resume, leading to the repeated formation and convection of magnetic islands and other features associated with the driven collisionless magnetic reconnection.

To check the scenario described above, that the generation and inverse cascade of the modal spectrum of B_x leads to the repeated formation of ordered magnetic

island structures, the power spectra of B_x as a function of the normalized wavenumber $k_z L$ at different simulation times in Case B are plotted in Figure 6.17. The corresponding magnetic field lines are shown in Figure 6.2. Since at $t = 0$ the initial magnetic field lines are strictly antiparallel, no magnetic field component B_x is present. At $t = 120\Omega_e^{-1}$, the enhanced tearing instability caused by the driving force applied at the driven boundary is already in progress, leading to the significant amount of energy input at the most unstable tearing mode with a wavenumber of $k_z L \sim 0.3$, indicated by the peak in the spectrum. Due to the inverse cascade of the modal spectrum of B_x , a condensation of energy in smaller wavenumbers can be seen at $t = 240\Omega_e^{-1}$, leading to the formation of ordered magnetic island structures as shown in Figure 6.2. In the meantime, the energy input level at the wavenumber of $k_z L \sim 0.3$ is reduced due to a slowdown of the enhanced tearing instability. Associated with the ejection of magnetic islands, the energy condensation in the smaller wavenumbers is significantly decreased as indicated by power spectra of B_x at $t = 420\Omega_e^{-1}$ and $t = 660\Omega_e^{-1}$. At $t = 960\Omega_e^{-1}$, as the enhanced tearing instability resumes, the generation and inverse cascade of the modal spectrum of B_x are started again. As time goes on, the cycle of the process described above is repeated, as shown by the power spectra of B_x between $t = 1020\Omega_e^{-1}$ and $t = 1500\Omega_e^{-1}$.

Since the driven collisionless reconnection is a highly nonlinear process, the repeated generation and inverse cascade of the modal spectrum of B_x is only a qualitative observation. The result of Figure 6.17 provides the first evidence that the driven collisionless magnetic reconnection is a self-organization process, in which the generation and inverse cascade of the modal spectrum of the magnetic field component B_x leads to the repeated formation of the ordered magnetic island structures from the turbulent magnetic field. If the driven collisionless magnetic reconnection

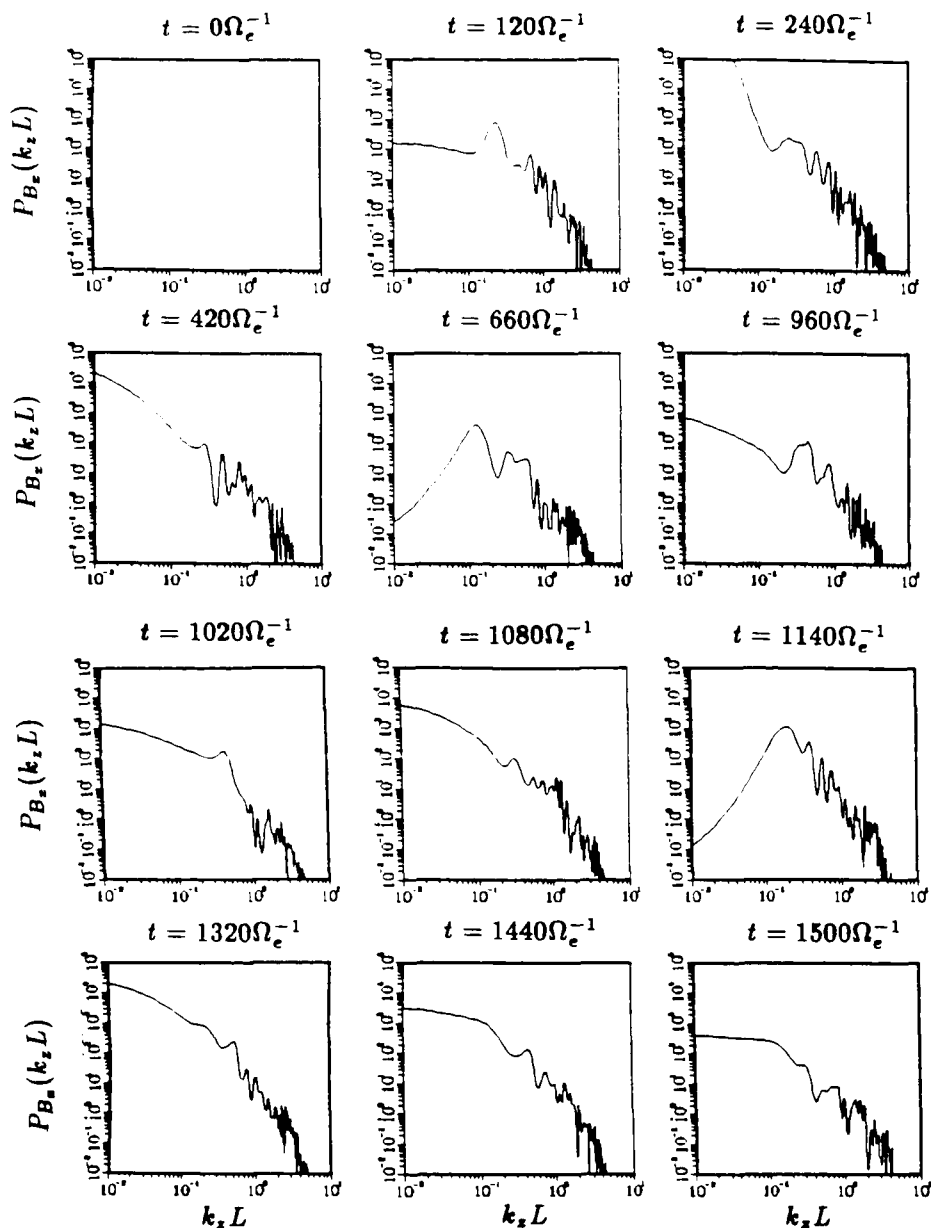


Figure 6.17 The power spectra of magnetic field component B_z as a function of the normalized wavenumber $k_z L$ at different simulation times observed in Case B. The peak at $k_z L \sim 0.3$ corresponds to the energy input caused by the enhanced tearing instability. The corresponding magnetic field lines are shown in Figure 6.2.

can be considered as an ergodic system, and if the simulations are run long enough, then a time-averaged quantity would be very close to its ensemble-averaged counterpart. The time-averaged power spectrum of B_x in Case B has been calculated. It is found the time-averaged spectrum can be approximately written as

$$P_{B_x} \sim \begin{cases} k_z^{-1.1}, & k_z L < 0.3; \\ k_z^{-4.0}, & k_z L > 0.3. \end{cases} \quad (6.10)$$

6.4 Summary

In this chapter, the driven collisionless magnetic reconnection process is studied on the basis of full particle simulations. Both symmetric and asymmetric current sheet models are used as the initial configurations for the simulations. The results of four different simulation cases are presented. The results of the full particle simulation of driven collisionless magnetic reconnection are applied to the magnetic reconnection and FTEs at the dayside magnetopause. A summary of the main results are listed below.

(1) Although ions tearing mode instability is developed in the current sheet in the one-component simulations, electron tearing mode instability is developed in the full particle simulations. The driving force applied at the driven boundary leads to an enhanced tearing growth rate.

(2) Both quasi-steady single X line reconnection (SXR) and intermittent multiple X line reconnection (MXR) configurations are observed in the simulations. The MXR process is found to be characterized by the repeated formation and convection of magnetic islands (flux tubes in 3-D environment) and magnetic reconnection enhancements, which are indicated by the peaks in the reconnection electric field.

(3) Coincident with the magnetic reconnection enhancements, bursts of energetic particles, electrons with an energy spectrum of $f_e(E) \sim E^{-3.9 \pm 0.5}$ and ions with an energy spectrum of $f_i(E) \sim E^{-4.2 \pm 0.7}$, are generated. High-speed plasma flows and field-aligned particle heat fluxes are also observed.

(4) It is also found that magnetic reconnection processes generate intense plasma waves and that the fluctuating magnetic field has a power spectrum of $P_B \sim f^{-3.5 \pm 0.5}$ and the fluctuating electric field has a power spectrum of $P_E \sim f^{-1.6 \pm 0.4}$.

(5) In a symmetric current sheet, both MXR and SXR processes generate large FTE signatures on the two sides of the current sheet. In an asymmetric current sheet, the signatures of the magnetosheath FTEs can be produced by both the MXR and SXR processes, while the signatures of the magnetospheric FTEs are mainly generated by the MXR process. Therefore, more FTEs are expected to be observed in the magnetosheath than in the magnetosphere. Furthermore, the magnetospheric FTEs usually have a smaller B_n signature than that of the magnetosheath FTEs.

(6) The presence of a magnetic island (a flux tube in 3-D space) tends to generate simultaneous FTE signatures on both sides of the current sheet, which resembles two-regime FTEs observed at the dayside magnetopause. An intrusion of magnetosheath plasma bulge into the magnetosphere is often observed when a magnetic island is formed. A detection of the magnetosheath bulge intruded in the magnetosphere may lead to the layered FTE structures observed in the magnetospheric FTEs.

(7) During FTEs, the magnetic field strength is usually increased when a satellite is away from the current sheet and decreased when it is near the current sheet. The signatures of crater-like FTEs and magnetic cavity structures can be observed

when a satellite penetrates deep inside magnetic islands (flux tubes) formed in the current sheet region.

(8) If the driven collisionless magnetic reconnection is considered as a self-organization process, the enhanced tearing mode instability in the current sheet caused by the driving force applied at the driven inflow boundary creates an energy source at a specific wavenumber range, with $k_z L \sim 0.3$ in the modal spectrum of the magnetic field component B_x . An inverse cascade of the modal spectrum of B_x leads to the formation of ordered magnetic island structures. During the self-organization process, the continuous generation and inverse cascade of the modal spectrum of B_x results in the repeated formation of magnetic islands observed in the driven collisionless magnetic reconnection process.

Chapter 7 Particle Acceleration in Driven Collisionless Magnetic Reconnection

It is commonly observed in such plasma processes as solar flares, flux transfer events (FTEs), and magnetospheric substorms that a small fraction of particles is accelerated to high energy. For example, during magnetospheric substorms, energetic protons with an energy range of several hundreds of keV up to an MeV are often detected in the earth's magnetotail [e.g., Baker and Belian, 1986]. Explaining the generation of such energetic particles has been a major challenge for space plasma physicists. Magnetic reconnection was proposed as one of many attempts to account for accelerating particles to high energy [see review and cited references in Chapter Two]. In this chapter, an investigation of particle acceleration in collisionless magnetic reconnection is based on the simulation results of the driven collisionless magnetic reconnection presented in the previous chapters.

These simulation results will show that besides the current sheet acceleration, particles can be accelerated after they become trapped by magnetic islands during the time-dependent collisionless magnetic reconnection processes. Particularly, those particles that stochastically bounce within magnetic islands can be accelerated to high energy by the reconnection electric field, due to rapid random crossing of the central current sheet in a very short period of time. This may provide an important mechanism for the generation of energetic particles during the time-dependent collisionless magnetic reconnection processes. This chapter is organized as follows. In Section 7.1, particle acceleration processes in magnetic reconnection are introduced. In Section 7.2, various different types of particle orbits observed

in the driven collisionless magnetic reconnection are presented. In Section 7.3, the discussion of particle acceleration processes in collisionless magnetic reconnection is based on the results obtained in the particle simulation of driven collisionless magnetic reconnection.

7.1 An Introduction to Particle Acceleration in Magnetic Reconnection

Single particle motions in reconnection magnetic and electric fields are very important to the particle acceleration processes in magnetic reconnection. Below, single particle motions in a neutral plasma sheet configuration are described before particle acceleration in magnetic reconnection is discussed. Figure 7.1 shows particle trajectories in a plasma neutral sheet with and without electric field.

When an electric field is absent, Figure 7.1a shows that ion trajectories can be divided into three categories: (1) outside the current sheet, magnetized ions in the strong field region simply gyrate around magnetic field lines; (2) inside the current sheet, less magnetized ions in the region with strong magnetic field gradient experience ∇B drift while they are gyrating around magnetic field lines; and (3) inside the current sheet, unmagnetized ions near the center of the neutral sheet meander around the neutral sheet while being trapped in the current sheet due to the strong ∇B force. The trajectories of electrons in a neutral sheet without an electric field are similar to that of ions shown in Figure 7.1a, except that the directions of electron gyration and ∇B drift are opposite to that of ions. Figure 7.1b shows the trajectories of ions and electrons in a neutral sheet with an electric field $\mathbf{E} = E_y \mathbf{e}_y$ in the direction of current. The trajectories show that outside the current sheet, both ions and electrons move toward the neutral sheet under the influence of $\mathbf{E} \times \mathbf{B}$ drift and that inside the neutral sheet, ions and electrons

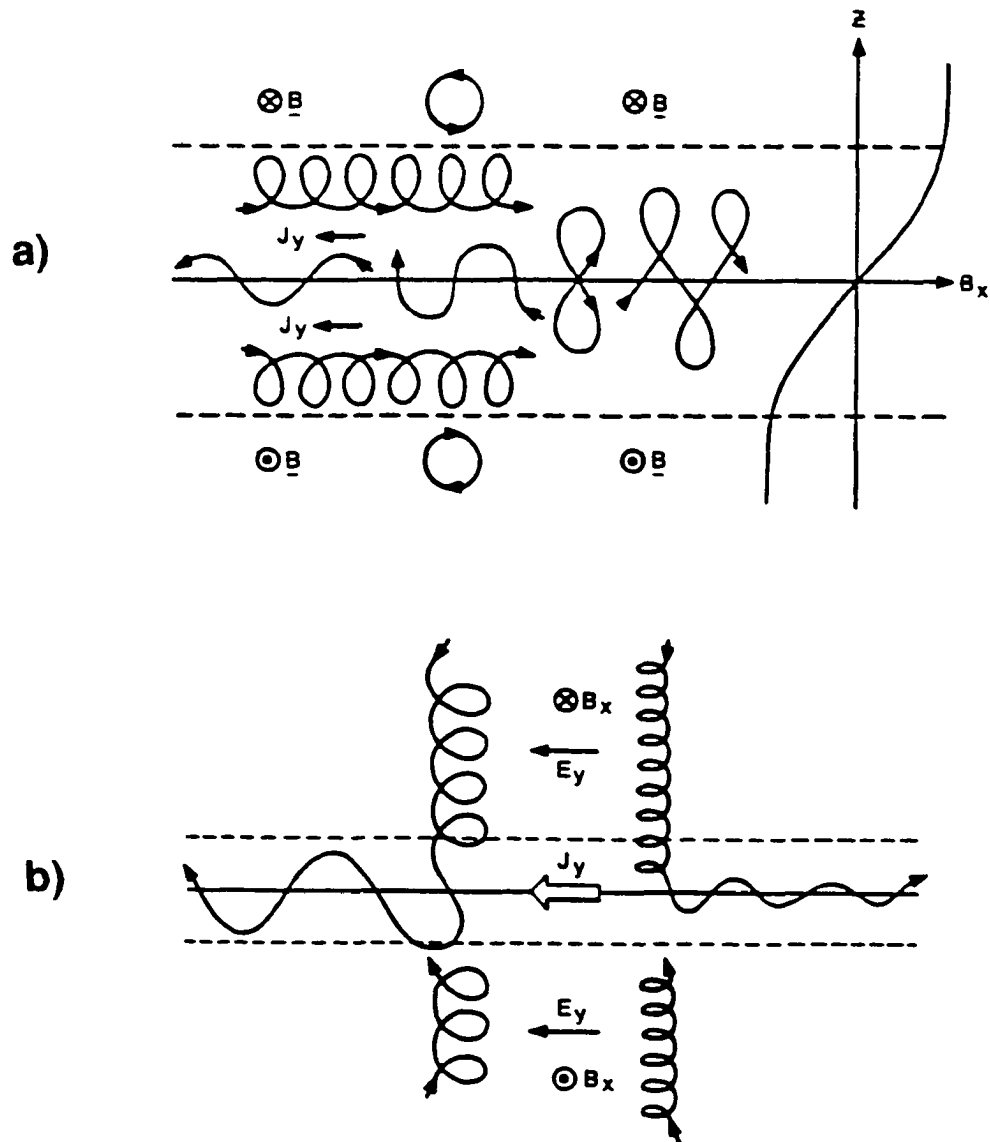


Figure 7.1 Particle trajectories in plasma neutral sheets. (a) Ion trajectories in a neutral sheet without electric field ($\mathbf{E} = 0$) and (b) ion and electron trajectories in a neutral sheet with electric field ($\mathbf{E} = E_y \mathbf{e}_y \neq 0$).

are trapped and accelerated by the electric field in the opposite directions. Notice that Figure 7.1b shows exactly the same picture of Alfvén's collisionless magnetic merging model [Alfvén, 1968], in which particles are accelerated during magnetic merging process by the induction electric field.

Since the induction electric field can accelerate particles during the reconnection process, it was suggested in early studies of magnetic reconnection that particles may be accelerated to high energy by strong reconnection electric fields near the X-type magnetic neutral lines (X lines) [Giovanelli, 1947; Dungey, 1958; Sweet, 1958; Parker, 1963]. Subsequently, substantial effort was devoted to investigating particle acceleration and energization during magnetic reconnection by examining test particle trajectories in various modeled steady reconnection magnetic and electric fields [Speiser, 1965, 1967; Rusbridge, 1971, 1977; Sonnerup, 1971; Eastwood, 1972; Stern and Palmadesso, 1975; Stern, 1978, 1979; Wagner et al., 1979, 1981; Lyons and Speiser, 1982; Lyons, 1984; Kim and Cary, 1983; Speiser and Lyons, 1984]. In the modeled steady reconnection magnetic and electric fields, it is usually assumed that the normal magnetic field component, which is much smaller than the tangential magnetic field component that changes signs across the current sheet, is uniform so that the constant electric field can be transformed away by a special Lorentz transformation [Speiser, 1965, 1967; Sonnerup, 1971].

Figure 7.2 shows the trajectories of non-adiabatic ion motion in a current sheet with a magnetic field B_z component caused by magnetic reconnection. Such particle trajectories are called the Speiser trajectories or Speiser orbits, due to pioneering work by Speiser [1965, 1967]. Figure 7.2a shows an example of Speiser orbits in the neutral line rest frame in which a reconnection electric field is present ($E_y \neq 0$). The particle moves toward the current sheet, due to the $\mathbf{E} \times \mathbf{B}$ drift. In the current sheet, the particle gyrates a half circle in the magnetic field B_z , while

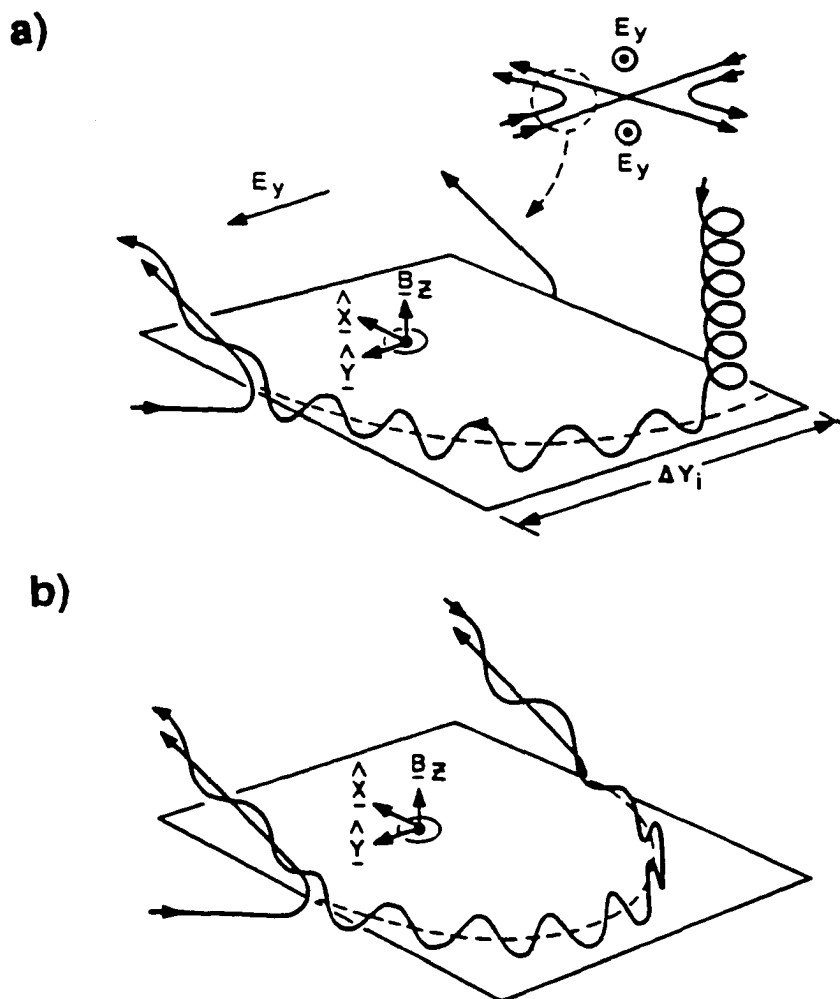


Figure 7.2 Non-adiabatic ion trajectories in a current sheet with a magnetic field B_z component, which is present due to magnetic reconnection, (a) in the neutral sheet rest frame in which $E_y \neq 0$ and (b) in the field line rest frame in which $E_y = 0$ [Speiser, 1965]. The field line rest frame moves with a speed of $V_F = cE_y/B_z e_x$ away from the X line region.

being accelerated by the reconnection electric field. Figure 7.2b shows the Speiser orbit in the field line rest frame which moves with a speed of $\mathbf{V}_F = cE_y/B_z\mathbf{e}_x$ away from the neutral line. Since the reconnection electric field is transformed away, $E_y = 0$ in the field line rest frame. The particle streams along magnetic field line into the current sheet, oscillates around the current sheet while gyrating in the B_z field, and ejects from the current sheet after a half of gyration. In the field line rest frame, the particle simply changes the sign of its velocity in the x -direction from $-V_F$ to V_F . In the neutral line rest frame, the total energy gain in the current sheet for a particle is $\Delta E \sim 2eR_zE_y$, where $R_z = V_x/\Omega_z \simeq V_F/\Omega_z$ is the particle gyroradius in the magnetic field B_z , and Ω_z is the corresponding gyrofrequency. It is easy to verify that the energy gain in the neutral line rest frame can be written as

$$\Delta E \simeq 2eR_zE_y = \frac{1}{2}m(2V_F)^2 \quad (7.1)$$

which is exactly the same as the energy change that occurred in the field line rest frame. For the typical values in the earth's magnetotail, $E_y \sim 0.5\text{mV/m}$, $B_z \sim 1\text{nT}$, $V_F \sim 500\text{km/s}$, and $R_z \sim 2500\text{km}$, it is found that the energy gain is $\Delta E_i \sim 5\text{keV}$ for a proton and $\Delta E_e \sim 3\text{eV}$ for an electron.

The test particle trajectories calculated in the modeled steady reconnection magnetic and electric fields shown above indicate that test particles generally do not spend much time near the X-type magnetic neutral lines. The relatively short residence time of particles in the X line region imposes a limitation on the efficiency of the X line acceleration mechanism. However, the test particle trajectories calculated in the modeled steady reconnection fields with an O-type magnetic neutral line (magnetic island) show that a particle can easily become trapped by the magnetic island and test particles may experience a runaway acceleration near the O

line region [Stern, 1979; Wagner et al., 1981]. Recent studies also suggested that under certain circumstances, particle motions in the reconnection magnetic and electric fields may become nonadiabatic and chaotic [Kim and Cary, 1983; Chen and Palmadesso, 1986; Martin, 1986; Büchner and Zelenyi, 1986, 1989]. The nonlinear dynamics and stochastic motions of particles in the reconnection magnetic and electric fields, in turn, may lead to particle pitch angle diffusion [Gray and Lee, 1982] and particle chaotic scattering and acceleration [Ashour-Abdalla et al., 1990].

Moreover, test particle trajectories were also calculated in the nonsteady magnetic and electric fields obtained from MHD simulations of magnetic reconnection [Sato et al., 1982; Matthaeus et al., 1984; Goldstein et al., 1986; Scholer and Jamitzky, 1987]. In the simulated nonsteady reconnection magnetic and electric fields, Sato et al. [1982] showed that particles may gain significant energy when they encounter a slow shock layer and/or when they approach the X line region. Scholer and Jamitzky [1987] found that during the plasmoid development, particles can drift large distances along the neutral lines and gain high energy before they become trapped on the close field lines in the plasmoids.

Finite-amplitude fluctuations are often observed in the reconnection magnetic and electric fields and the turbulent reconnection magnetic and electric fields may have important effects on the magnetic reconnection processes, e.g., the enhancement of reconnection electric field near the X line region [Matthaeus and Montgomery, 1981; Matthaeus, 1982; Matthaeus and Lamkin, 1985, 1986] and the formation of magnetic flux tubes [Song and Lysak, 1989]. It was demonstrated by Matthaeus et al. [1984] that test particles can be trapped by turbulent fluctuations in the small magnetic bubbles formed near X line regions during the turbulent magnetic reconnection. The trapped particles can be accelerated by the turbulently enhanced reconnection electric fields for a longer time, on the order of an

Alfvén transit time, to become energetic. Based on the analytic formula derived by Matthaeus et al. [1984] and their simulation results, Goldstein et al. [1986] found that magnetic reconnection is capable of accelerating particles to several GeV in solar flares and up to an MeV in magnetospheric substorms.

Magnetic reconnection processes in a collisionless plasma have been investigated by many authors based on theoretical analyses and particle simulations. In the theoretical study of collisionless magnetic reconnection, Hill [1975] found that particle acceleration during collisionless magnetic reconnection may be provided either by slow shock acceleration and/or current sheet acceleration. In the previous simulation studies of collisionless tearing mode instability and collisionless magnetic reconnection, trapping of particles by magnetic islands are commonly observed and particle acceleration and heating during collisionless magnetic reconnection also have been examined [Katanuma and Kamimura, 1980; Terasawa, 1981; Leboeuf et al., 1982]. It was observed in the simulations of Terasawa [1981] that particles are accelerated in the X line region and decelerated in the O line region; that particles ejected from the X line region are injected into O line region; and that particles confined inside magnetic islands are heated due to adiabatical compression. Leboeuf et al. [1982] reported that particle acceleration and heating, and generation of energetic particles can be caused by coalescence of magnetic islands. Ding et al. [1986] used a driven inflow and open outflow boundary conditions to simulate the driven collisionless magnetic reconnection process and FTEs. Repeated formation and convection of magnetic islands and generation of energetic particles were observed in their simulations. It was reported that particle acceleration and heating mainly occur during the formation of large magnetic islands. Lee and Ding [1987] used similar driven and open boundary conditions to simulate the driven collisionless magnetic reconnection and obtained the first computational evidence

for the current sheet particle acceleration during the collisionless magnetic reconnection. However, in the previous simulations, either one-component plasma model or periodic boundary conditions were used.

In the present thesis research, the driven collisionless magnetic reconnection processes are studied on the basis of full particle simulations with the driven inflow and open outflow boundaries. Many properties associated with the driven collisionless magnetic reconnection have been presented in Chapter Six. In the following sections, various types of particle trajectories observed in the simulation of driven collisionless magnetic reconnection are presented and particle acceleration processes in collisionless magnetic reconnection are discussed.

7.2 Particle Trajectories in Driven Collisionless Magnetic Reconnection

Several cases of the full particle simulation of driven collisionless magnetic reconnection were presented in Chapter Six. Various features associated with the driven collisionless magnetic reconnection processes were also examined. To investigate the particle acceleration processes in the driven collisionless magnetic reconnection, trajectories of particles, both ions and electrons, are followed. Some typical particle orbit examples are presented below. These particle trajectories are computed in the simulation Case C.

Figure 7.3 shows the magnetic field lines at different simulation times in Case C. The left column shows the magnetic field lines from $t = 210\Omega_e^{-1}$ to $t = 330\Omega_e^{-1}$; the right column shows the magnetic field lines from $t = 480\Omega_e^{-1}$ to $t = 600\Omega_e^{-1}$. As shown in the left column, during most of the simulation time between $t = 210\Omega_e^{-1}$ and $t = 330\Omega_e^{-1}$, two magnetic islands are present. Although the motion of the magnetic island in the region with $z < 0$ is very slow, the convection of the magnetic

MAGNETIC FIELD LINES

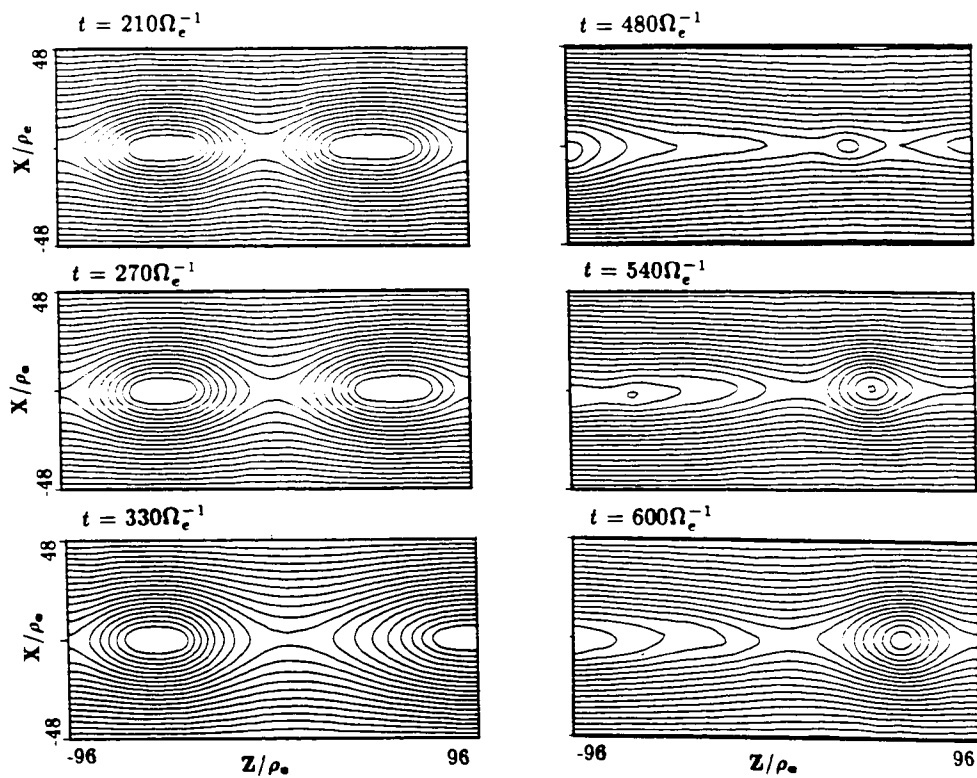


Figure 7.3 Magnetic field lines at different simulation times in Case C. The left column shows the magnetic field lines from $t = 210\Omega_e^{-1}$ to $t = 330\Omega_e^{-1}$ while the right column shows the magnetic field lines from $t = 480\Omega_e^{-1}$ to $t = 600\Omega_e^{-1}$. During these two periods particle trajectories were calculated.

island in the region with $z > 0$ is much more rapid and half of the magnetic island has moved out of the simulation domain at $t = 330\Omega_e^{-1}$. The magnetic field lines in the right column show that between $t = 480\Omega_e^{-1}$ to $t = 600\Omega_e^{-1}$, a magnetic island is formed in the $z > 0$ region, while a current sheet structure is present in the $z < 0$ region. During the two periods shown in Figure 7.3, 200 sample ions and electron were arbitrarily chosen and their trajectories were followed. Several different types of particle trajectories with distinct features were observed in the simulation. Some examples of typical particle trajectories are presented below. All particle trajectories are started at $y = 0$.

Figure 7.4 shows the typical trajectory of an electron outside the current sheet obtained between $t = 210\Omega_e^{-1}$ and $t = 330\Omega_e^{-1}$. The left column shows particle trajectories projected on the $x - y$, $y - z$, and $x - z$ planes; the right column shows particle trajectories projected on the $x - v_x$, $y - v_y$, and $z - v_z$ phase spaces, and particle energy as a function of z . The trajectories shown in the left column indicate that the particle moves toward the current sheet due to $\mathbf{E} \times \mathbf{B}$ drift and that the particle is reflected between the strong magnetic field regions formed above the magnetic islands due to magnetic field compression. At the driven inflow boundary ($x = \pm L_x$), a typical electron has an energy of $v^2/v_{the}^2 \simeq 1.5$. The bottom panel in the right column shows that the electron gains some energy while drifting toward the current sheet, due to the presence of a weak induction electric field outside the current sheet.

Inside the current sheet, the induction electric field is much stronger than outside the current sheet, especially during the magnetic reconnection enhancements, as indicated by the spiky structures shown in Figure 6.4. Particles inside the current sheet can be accelerated to high energy by the strong induction electric field.

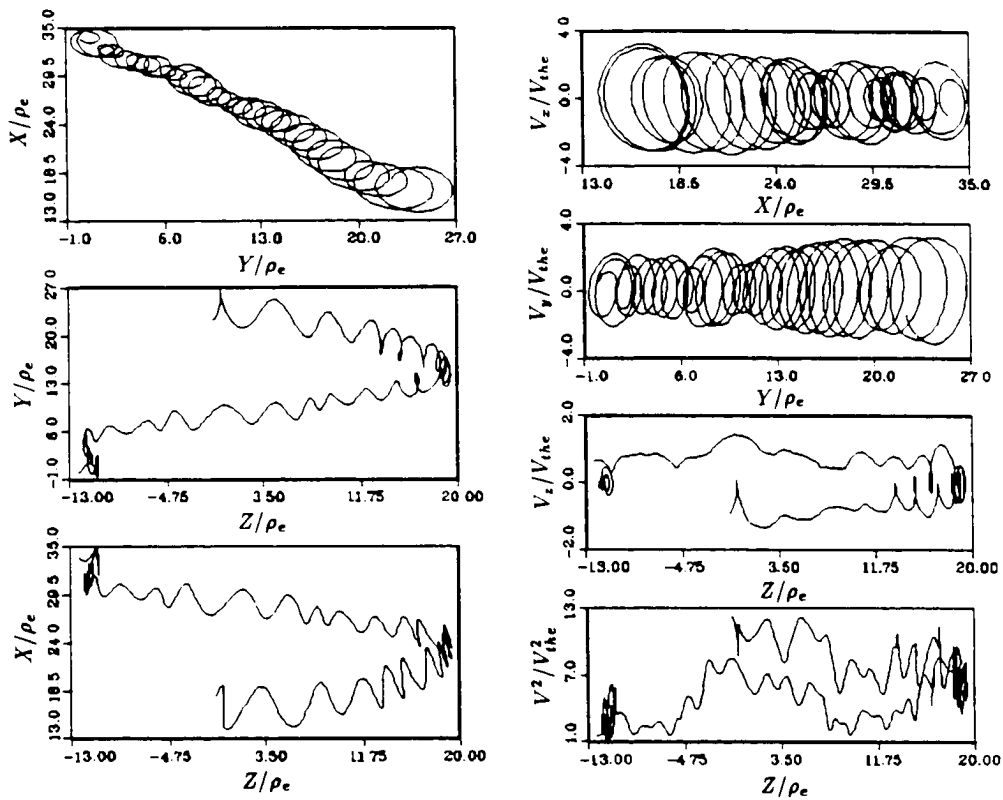


Figure 7.4 The typical trajectory of an electron outside the current sheet obtained between $t = 210\Omega_e^{-1}$ and $t = 330\Omega_e^{-1}$. The left column shows particle trajectories projected on the $x - y$, $y - z$, and $x - z$ planes while the right column shows particle trajectories projected on the $x - v_x$, $y - v_y$, and $z - v_z$ phase spaces, and particle energy as a function of z .

Particle acceleration by the current sheet was observed in the one-component simulations of driven collisionless magnetic reconnection [Lee and Ding, 1987] and an example of current sheet particle acceleration has been shown in Chapter 5. Particle acceleration by the current sheet was also observed in the full particle simulation of the driven collisionless magnetic reconnection. For example, particle trajectories similar to that shown in Figure 5.10 are observed between $t = 480\Omega_e^{-1}$ and $t = 600\Omega_e^{-1}$ when a current sheet structure is present in the region with $z < 0$. Besides current sheet particle acceleration, particle acceleration also occurs after particles become trapped by the magnetic islands.

Figure 7.5 shows the typical trajectory of an electron that becomes trapped by the magnetic island during its formation between $t = 480\Omega_e^{-1}$ and $t = 600\Omega_e^{-1}$. The bottom panel in the left column shows that the particle comes from the lower left region of the simulation domain with $x < 0$ and $z < 0$ and then becomes trapped by the magnetic island formed in the region with $z > 0$. The trajectories in the other panels of the left column indicate that the particle drifts in the $-y$ -direction, which is consistent with the electron acceleration by the induction electric field E_y . The bottom panel in the right column shows that a significant energy increase takes place after the particle becomes trapped by the magnetic island. The other three panels of the right column shows that after the particle becomes trapped, all of the three particle velocity components are increased and a closed trajectory is formed in the $x - v_x$ phase space. The particle trajectories shown in Figure 7.5 indicate that a particle is accelerated by the induction electric field during its multiple crossing of the current sheet after it is trapped by the magnetic island.

Figure 7.5 shows that a particle can become trapped by the magnetic island when the island is formed during magnetic reconnection. In the following, several different types of trapped particle trajectories are presented. Figure 7.6 shows the

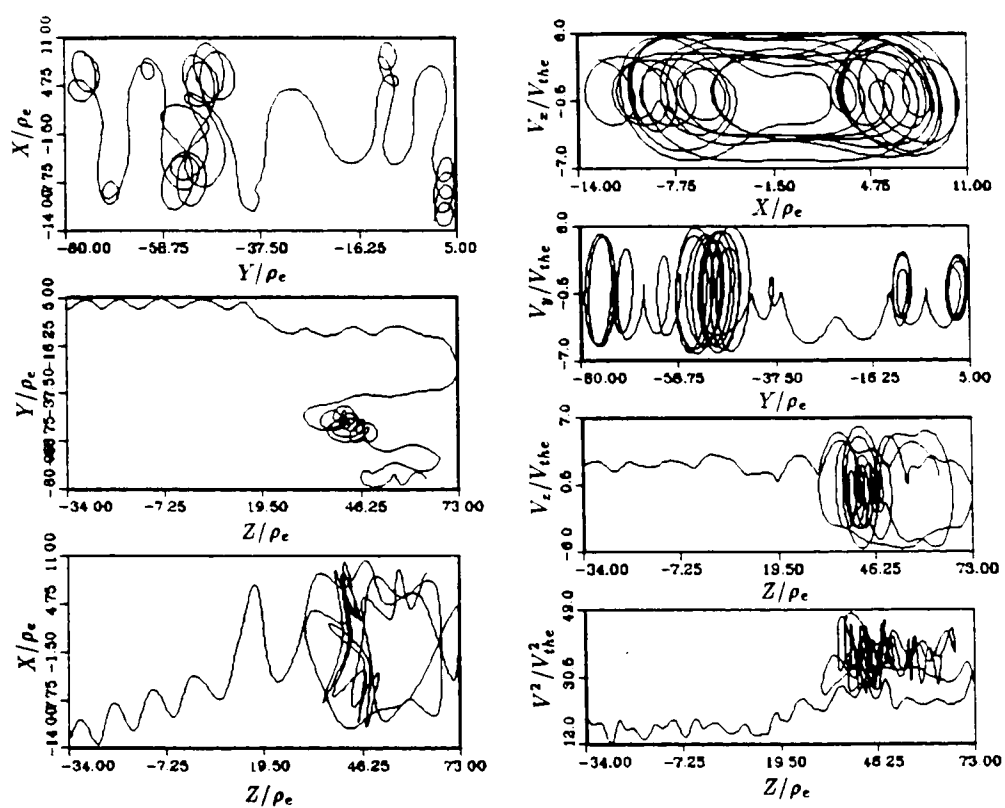


Figure 7.5 The trajectory of a typical electron that becomes trapped by the magnetic island during its formation between $t = 480\Omega_e^{-1}$ and $t = 600\Omega_e^{-1}$. The format of the present figure is the same as that in Figure 7.4.

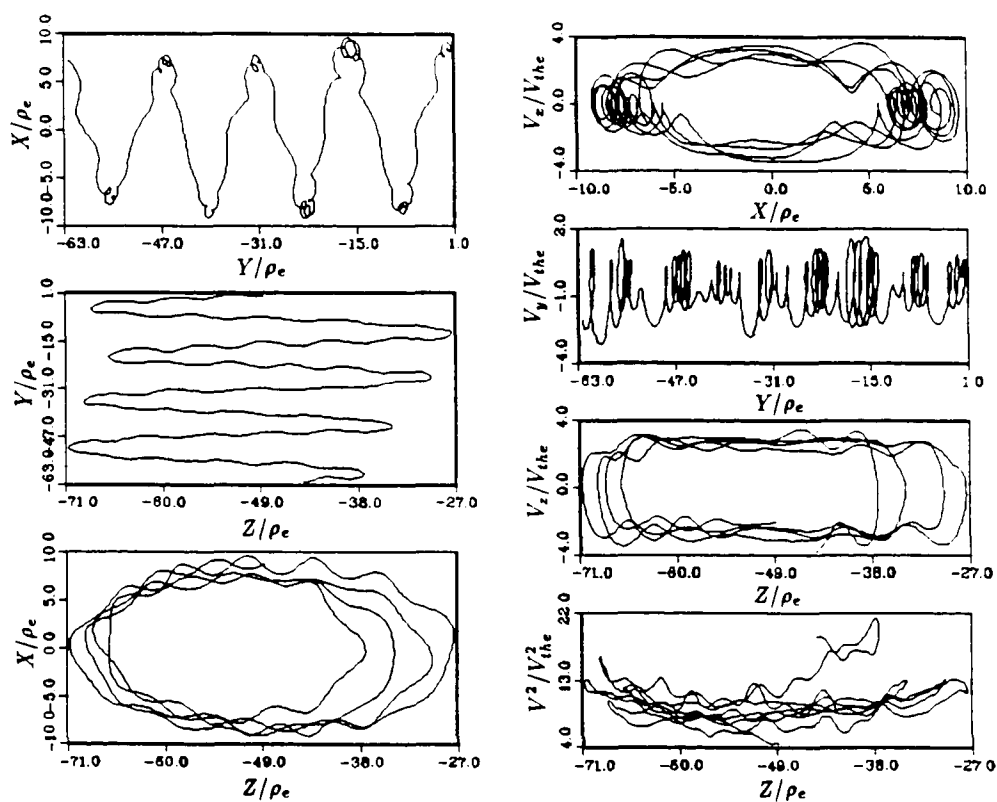


Figure 7.6 The typical trajectory of a trapped electron which streams along the closed magnetic field lines around the magnetic island in the region with $z < 0$ during the period from $t = 210\Omega_e^{-1}$ to $t = 330\Omega_e^{-1}$. The format of the present figure is the same as that in Figure 7.4.

trajectory of a trapped electron streaming along the closed magnetic field lines around the magnetic island in the $z < 0$ region during the period from $t = 210\Omega_e^{-1}$ to $t = 330\Omega_e^{-1}$. The bottom panel in the left column clearly shows the streaming electron orbits. Due to the convection of the magnetic island, the streaming electron orbits drift toward the left outflow boundary at $z = -L_z$. The other two panels of the left column show that the particle crosses the central current sheet ($x \sim 0$) eight times while streaming around the magnetic island. The average particle drift speed in the $-y$ -direction is found to be $\sim 0.53v_{the}$. The bottom panel in the right column shows that the particle energy is increased more than five times during the period from $t = 210\Omega_e^{-1}$ to $t = 330\Omega_e^{-1}$. The particle gains most of energy while passing through the central current sheet ($x \sim 0$) where the induction electric field is strong. The rest of the panels in the right column show that for a particle streaming along the magnetic island, a closed trajectory can be formed in both the $x - v_x$ and $z - v_z$ phase spaces. The drift of the closed trajectory toward the left outflow boundary ($z = -L_z$) in the $z - v_z$ phase space is due to the convection of the magnetic island.

Figure 7.7 shows the trajectory of a trapped electron which bounces rapidly inside the magnetic island formed in the region with $z < 0$ during the period between $t = 210\Omega_e^{-1}$ and $t = 330\Omega_e^{-1}$. The trajectory projected on the $x - z$ plane shown in the bottom panel of the left column is very irregular. The other two panels in the left column show that during the rapid and stochastic bouncing inside the magnetic island, the particle crosses the central current sheet ($x \sim 0$) about thirty times and the distance it drifts in the $-y$ -direction is more than twice as much as that shown in Figure 7.6. The average particle drift speed in the $-y$ -direction is found to be $\sim 1.2v_{the}$. The panels of the right column show a feature similar to that shown in Figure 7.6, but the maximum absolute value of the particle velocity is

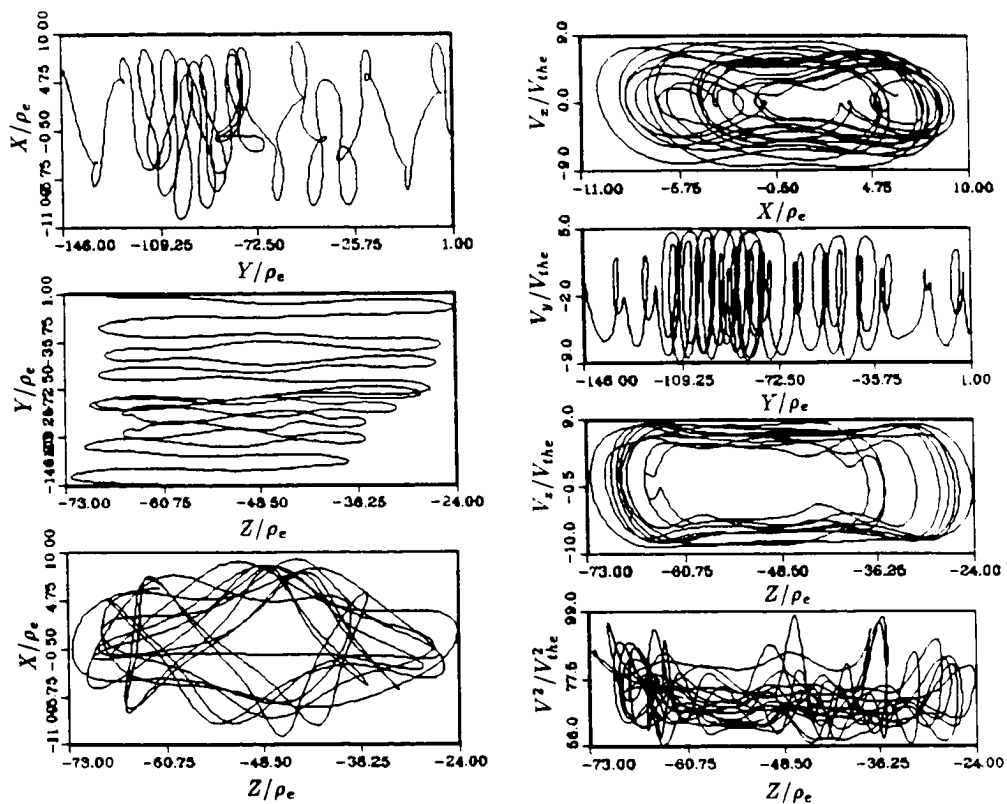


Figure 7.7 The typical trajectory of a trapped electron which bounces rapidly inside the magnetic island formed in the $z < 0$ region between $t = 210\Omega_e^{-1}$ and $t = 330\Omega_e^{-1}$. The format of the present figure is the same as that in Figure 7.4.

more than twice as much as in Figure 7.6. The maximum particle energy shown in Figure 7.7 is $v^2/v_{the}^2 \sim 99$, which is about 66 times particle energy ($v^2/v_{the}^2 \sim 1.5$) at the driven inflow boundary ($x = \pm L_x$). Although the particle trajectory shown in Figure 7.7 was only traced to $t = 330\Omega_e^{-1}$, the particle could gain much higher energy while rapidly and stochastically bouncing inside the magnetic island before it moves out of the simulation domain.

Two different types of trajectories of particles trapped by magnetic island are shown in Figures 7.6 and 7.7. A third type of trapped particle trajectory has also been observed in the simulations. These particles are trapped between magnetic mirrors formed by magnetic field compression above and below a magnetic island. An example of such a trapped particle trajectory is shown in Figure 7.8. The bottom panel of the left column shows that an electron is trapped between the magnetic mirrors formed around the magnetic island in the $z < 0$ region while it is $\mathbf{E} \times \mathbf{B}$ drifting in the $-z$ -direction. The other two panels show that the particle passes through the X line region in central current sheet ($x \sim 0$ and $-39 < z/\rho_e < -19$) nine times while bouncing between the magnetic mirrors. The average drift speed in the $-y$ -direction is found to be $\sim 0.28v_{the}$. The bottom panel of the right column indicates that the particle accelerated by the induction electric field while bouncing between the magnetic mirrors gains a maximum energy of $v^2/v_{the}^2 \sim 30$, which is about 20 times the particle energy at the driven inflow boundary. The phase spaces trajectories plotted in the remaining panels of the right column show that for the particle trapped between magnetic mirrors, the closed trajectory is only present in the $x - v_x$ plane.

Various types of electron trajectories observed in the simulation are presented above. Because of its larger mass, an ion moves much slowly than an electron. Thus, the ion trajectories obtained in a period of $120\Omega_e^{-1}$, which is equal to $6\Omega_i^{-1}$

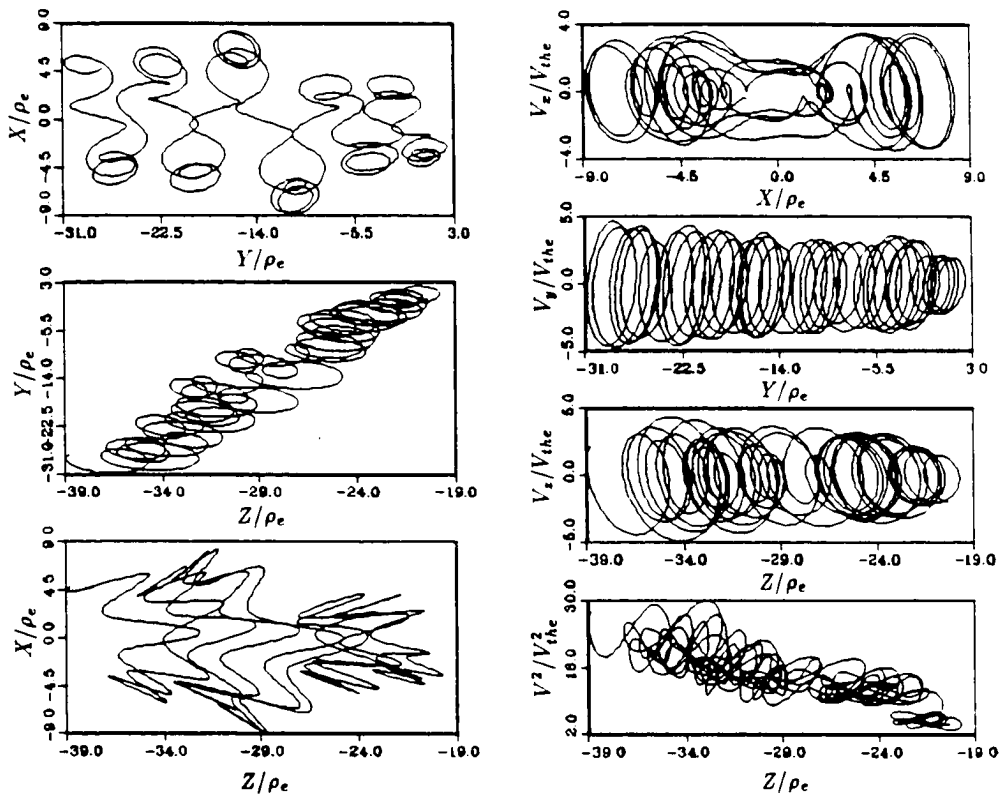


Figure 7.8 The typical trajectory of a trapped electron which bounces between magnetic mirrors formed by magnetic field compression above and below the magnetic island formed in the $z < 0$ region during the period from $t = 210\Omega_e^{-1}$ to $t = 330\Omega_e^{-1}$. The format of the present figure is the same as that in Figure 7.4.

for the mass ratio $m_i/m_e = 25$ used in the simulation, do not provide much information about the trajectories of ions. To follow ion trajectories for a longer period, however, requires much more computational resources than are available for this study. Therefore, in order to investigate the ion trajectories in the collisionless magnetic reconnection process, a test particle method is used, in which trajectories of ions are computed in a model of reconnection magnetic and electric fields with proper scaling.

For example, to compute the ion trajectories near the X line region, model reconnection magnetic and electric fields

$$\mathbf{B} = B_{x0} \left(\frac{z}{\lambda_z} \right) \mathbf{e}_x + B_{z0} \left(\frac{x}{\lambda_x} \right) \mathbf{e}_z \quad (7.2)$$

$$\mathbf{E} = E_{y0} \mathbf{e}_y \quad (7.3)$$

were used, where B_{x0} , λ_z , B_{z0} , λ_x , and E_{y0} are constants. For $B_{z0} = 1.0$, $B_{x0}/B_{z0} = 0.6$, $\lambda_x/\rho_i = 7.0$, $\lambda_z/\lambda_x = 2.0$, an example of the magnetic field configuration described by (7.2) is plotted in Figure 7.9. Notice that the model steady magnetic field configuration plotted in Figure 7.9 is very similar to the central X line regions shown in the left column of Figure 7.3. An example of ion trajectories computed in the model steady reconnection magnetic and electric fields given by (7.2) and (7.3) is shown in Figure 7.10, where $E_{y0} = 0.25$ is assumed. The ion trajectory of Figure 7.10 shows similar features to the trajectory of the electron trapped between magnetic mirrors plotted in Figure 7.8. Therefore, it is reasonable to believe that with proper scaling, ions would have similar trajectories to that of electrons shown in Figures 7.4-7.8. The ion trajectories near a reconnection O line were examined by Stern [1979] and Wagner et al. [1981]. They showed that an ion can experience a runaway acceleration after being trapped by the magnetic O line.

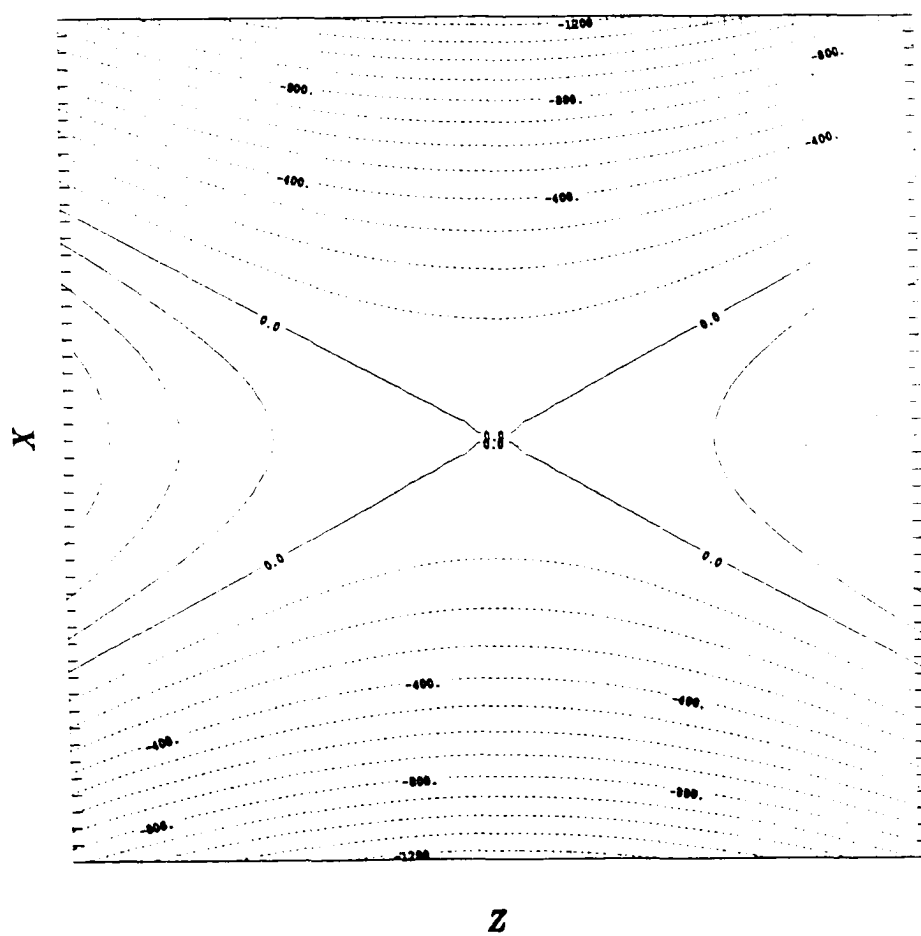


Figure 7.9 A model steady reconnection magnetic field configuration given by (7.2), with $B_{x0}/B_{z0} = 0.6$, $\lambda_x/\rho_i = 7.0$, $\lambda_z/\lambda_x = 2.0$.

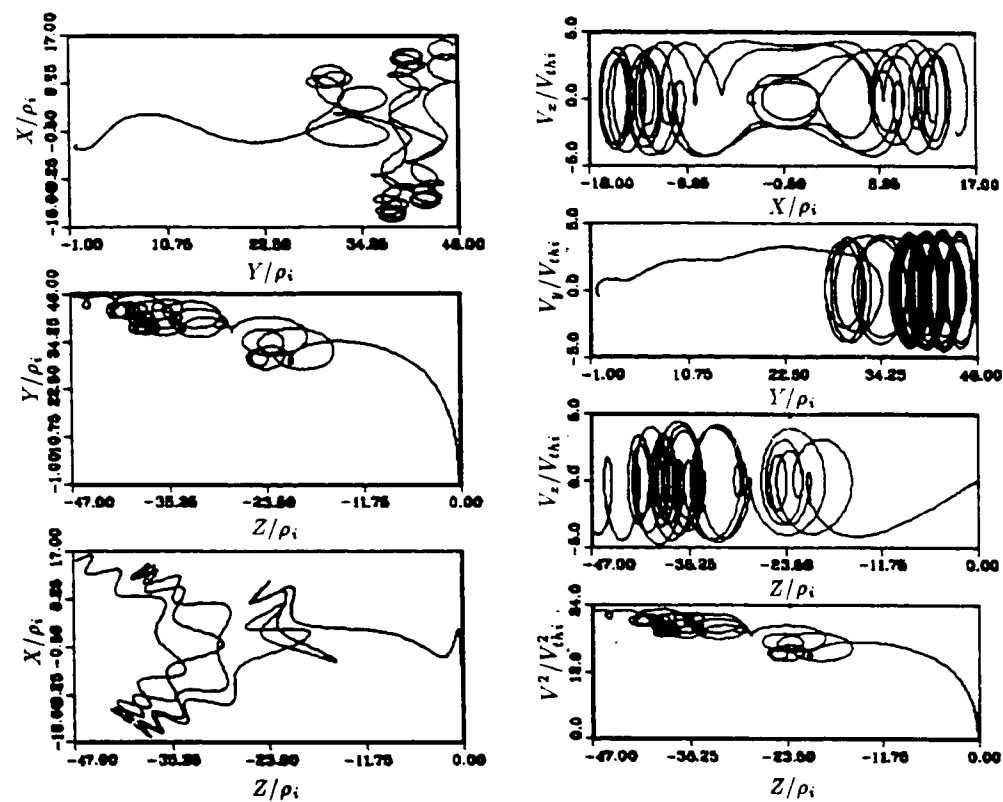


Figure 7.10 A test particle calculation of ion trajectory in the model steady reconnection magnetic and electric fields given by (7.2) and (7.3). Parameters used are $B_{z0} = 1.0$, $B_{x0}/B_{z0} = 0.6$, $\lambda_x/\rho_i = 7.0$, $\lambda_z/\lambda_x = 2.0$, and $E_{y0} = 0.25$.

7.3 Summary and Discussion

Magnetic reconnection is believed to play an important role in such processes as solar flare, flux transfer events, and magnetospheric substorms, in which the presence of energetic particles is often observed. Particle acceleration and generation of energetic particles have been important issues in the study of magnetic reconnection processes. In MHD models, plasma is accelerated to the Alfvén speed by slow shocks; whereas in collisionless magnetic reconnection, particle acceleration is mainly provided by the current sheet acceleration [see review and cited references in Chapter Two].

The generation of energetic particles during magnetic reconnection was first suggested to be caused by the strong reconnection electric field near the X line regions [Giovanelli, 1947; Dungey, 1958; Sweet, 1958; Parker, 1963]. However, the test particle calculations in the steady reconnection magnetic and electric fields indicate that particles may not be able to gain much energy in the reconnection X line region, due to a shorter residence time [e.g., Speiser, 1965, 1967]. On the other hand, test particle calculations also indicate that particles may be accelerated to high energy due to a much longer residence time near reconnection O line region [Stern, 1979; Wagner et al., 1981]. It is also found in the test particle calculation that particle nonlinear dynamics in the reconnection magnetic and electric fields may also lead to particle chaotic scattering and acceleration [Ashour-Abdalla et al., 1990].

In collisionless magnetic reconnection, previous particle simulation results indicate that energetic particles can be generated during coalescence of small magnetic islands and formation of large magnetic islands [Leboeuf et al., 1982; Ding et al.,

1986] or by current sheet acceleration [Lee and Ding, 1987]. In the present simulations of driven collisionless magnetic reconnection, it is found that particles can become trapped on the closed field lines during the formation of magnetic islands and that, besides the current sheet acceleration, energetic particles can also be produced due to trapping of particles by magnetic islands during the time-dependent collisionless magnetic reconnection. Various types of particle trajectories observed in the present simulations are presented in the previous section. Three different types of trapped particles with distinct features can be identified among the trajectories: 1) particles streaming along the closed magnetic field lines around magnetic islands, 2) particles rapidly and stochastically bouncing inside magnetic islands, and 3) particles reflecting between magnetic mirrors formed due to magnetic field compression near magnetic islands.

It is found that due to the particle acceleration by the induction electric field, all of the three different types of trapped particles gain energy. However, the energy gain of the first type of trapped particles, which stream along the closed field lines around magnetic islands, is less than the other two types of trapped particles. Those trapped particles which reflect between magnetic mirrors near magnetic islands and stochastically bounce within magnetic islands can gain much more energy, due to multiple particle crossings of the central current sheet region in a short period of time. Particularly, the second type of trapped particles shown in Figure 7.7 are found to be capable of becoming energetic particles due to the multiple rapid and chaotic particle accelerations by the reconnection electric field. It is suggested that the stochastical particle bouncing inside magnetic islands may be an important mechanism for the generation of energetic particles during the collisionless magnetic reconnection.

The acceleration of trapped particles, especially those particles with the second type of trapped trajectory (Figure 7.7) observed in the present simulations, are similar to that reported by Matthaeus et al. [1984], in which particles trapped by magnetic bubbles near reconnection X line region are accelerated to high energy by the strong reconnection electric field. However, the present results differ from those obtained by Scholer and Jamitzky [1987], in which particles are accelerated to high energy by the reconnection electric field before they become trapped in the closed magnetic field lines of magnetic islands. Furthermore, trapped electron distributions have been observed in FTEs at the dayside magnetopause, which was explained by the reflection of electrons between magnetic mirrors formed on the open magnetic field lines [Daly and Fritz, 1982]. The presence of trapped electrons with a third type of trapped trajectory (Figure 7.8) in the present simulations, which reflect between magnetic mirrors formed by magnetic field compression near the magnetic islands, indicates that trapped electron distribution observed in FTEs at the dayside magnetopause may also be caused by the reflection of electrons between magnetic mirrors while they are trapped on the closed magnetic field lines.

Chapter 8 Summary and Discussion

Magnetic field reconnection plays a crucial role in many important plasma processes, ranging from solar flares and magnetospheric substorms to tokamak disruptions. Magnetic field reconnection in the earth's magnetosphere, which may occur both at the dayside magnetopause and in the nightside magnetotail, has been a prevailing hypothesis for transferring energy, mass, and momentum from the solar wind into the magnetosphere. The discovery of flux transfer events (FTEs) has provided evidence for magnetic reconnection at the dayside magnetopause. In this thesis research, the basic plasma processes associated with the driven collisionless magnetic reconnection at the earth's dayside magnetopause were studied using particle simulations. The simulation results were applied to FTEs observed at the dayside magnetopause. The main results of the present thesis research are summarized below.

1. Observations of FTEs at the dayside magnetopause indicate that magnetic reconnection process may occur preferentially when the ratio of plasma pressure to magnetic pressure in the magnetosheath has a small value ($\beta_s < 2$) [Paschmann et al., 1986]. A possible explanation for the above observation is that development of tearing mode instabilities triggering the onset of dayside magnetic reconnection may have a dependence on the plasma β values. A larger plasma β value may lead to a smaller tearing growth rate. A theoretical study of the β -dependence of tearing mode instabilities was carried out in Chapter Three. It is found that in the collisionless magnetospheric plasmas, the collisionless tearing mode has a strong β -dependence when the neutral sheet is symmetric and a much weaker β -dependence

when the neutral sheet is asymmetric. At the dayside magnetopause, the magnetopause current sheet is, in general, asymmetric, with a strong magnetic field and low β plasma on the magnetospheric side and a weak magnetic field and high β plasma on the magnetosheath side. According to the results of the present theoretical study, the development of tearing mode and hence, the occurrence of magnetic reconnection at the dayside magnetopause, should not exhibit a strong dependence on the magnetosheath β_s values. Although the present results do not support the data analyses reported by Paschmann et al. [1986], they are not inconsistent with recent observations at the dayside magnetopause reported by Gosling et al. [1990], which showed that the detection of FTEs did not have the strong β -dependence as claimed by Paschmann et al. [1986]. Furthermore, the effects of sheared magnetic field, which were not included in the present study, need to be considered in the future study of the β -dependence of the tearing mode instabilities at the dayside magnetopause.

2. A two-and-one-half dimensional ($2\frac{1}{2}$ -D) magnetoinductive particle simulation model with a driven inflow boundary and an open outflow boundary was developed in Chapter Four for the present study of the driven collisionless magnetic reconnection processes. New features associated with the present simulation model include: (a) the driven boundary condition for vector potential at the inflow boundary, (b) the vacuum force free boundary condition for electrostatic field at the outflow boundary, and (c) particle buffer zones for handling particles crossing the simulation boundaries. In the present simulation model, the initial zero-order guiding magnetic field component (B_{y0}) has not been included. A self-consistent inclusion of the initial guiding field component B_{y0} leads to the presence of an electric field component $E_{1z} = \pm V_1 B_{y0}/c$ at the driven inflow boundary ($x = \pm L_x$),

which in turn pumps the magnetic flux associated with B_y into the simulation domain. The boundary conditions for vector potential components A_x and A_z given in Chapter Four have to be modified to deal with the change of magnetic field B_y in the simulation domain. An improper boundary condition for A_x and A_z at the outflow boundary ($z = \pm L_z$) results in nonphysical variations of B_y in the simulation. Many attempts have been made to incorporate the initial guiding field B_{y0} into the present particle simulation study of the driven collisionless magnetic reconnection. However, no satisfactory boundary condition for A_x and A_z at the outflow boundary has been found. Nonphysical heating and cooling of particles are commonly observed in the attempted simulations with $B_{y0} \neq 0$. Therefore, particle simulation of driven collisionless magnetic reconnection with B_{y0} remains a challenge for the future study.

3. The driven collisionless magnetic reconnection process was first studied with one-component particle simulations. The results were presented in Chapter Five. It is found in the simulation that the multiple X line reconnection (MXR) process, which is characterized by the repeated formation and convection of magnetic islands (flux tubes in 3-D space) and the generation of superthermal particles, tends to occur when the length of simulation domain (L_z) is long; the quasi-steady single X line reconnection (SXR) process, which is characterized by the current sheet acceleration of particles, takes place when the length of simulation domain is short. The simulation results of the MXR process are, in general, consistent with satellite observations of FTEs at the dayside magnetopause. The particle simulation of the quasi-steady SXR process, on the other hand, provides the first computational evidence for current sheet particle acceleration in collisionless plasmas. The simulation results are, in many respects, consistent with the only collisionless reconnection model proposed by Hill [1975].

4. The driven collisionless magnetic reconnection process was studied on the basis of full particle simulations in Chapter Six, and the simulation results were compared with FTE observations. Similar to the one-component simulations, both quasi-steady SXR and intermittent MXR configurations are observed in the simulation. The MXR process is found to be characterized not only by the repeated formation and convection of magnetic islands but also by magnetic reconnection enhancements, which are indicated by peaks in the reconnection electric field. Coincident with the magnetic reconnection enhancements, bursts of energetic particles, electrons with an energy spectrum of $f_e(E) \sim E^{-3.9 \pm 0.5}$, and ions with an energy spectrum of $f_i(E) \sim E^{-4.2 \pm 0.7}$ are generated. High-speed plasma flows and field-aligned particle heat fluxes are also observed. It is found that magnetic reconnection processes generate intense plasma waves, that the fluctuating magnetic field has a power spectrum of $P_B \sim f^{-3.5 \pm 0.5}$, and that the fluctuating electric field has a power spectrum of $P_E \sim f^{-1.6 \pm 0.4}$. The presence of a magnetic island (flux tube in 3-D space) tends to generate a simultaneous FTE signatures on both sides of the current sheet, which resembles two-regime FTEs observed at the dayside magnetopause. The detection of a magnetosheath plasma bulge intruded in the magnetosphere due to the formation of magnetic island may lead to the layered structures observed in the magnetospheric FTEs.

5. If the driven collisionless magnetic reconnection is considered as a self-organization process, the enhanced tearing mode instability in the current sheet caused by the driving force applied at the driven inflow boundary creates an energy source at a specific wavenumber range with $k_z L \sim 0.3$ in the modal spectrum of the magnetic field component B_x . An inverse cascade of the modal spectrum of B_x leads to the formation of ordered magnetic island structures. During the self-organization process, the continuous generation and inverse cascade of the modal

spectrum of B_x results in the repeated formation of magnetic islands observed in the driven collisionless magnetic reconnection process.

6. Particle acceleration in collisionless magnetic reconnection was investigated in Chapter Seven based on the particle simulations of driven collisionless magnetic reconnection. It is found in the simulations that, besides current sheet particle acceleration, particles may also be accelerated by the reconnection electric field after they become trapped by magnetic islands. Three different types of trapped particles with distinct features can be identified among various particle trajectories observed in the simulations. They include 1) particles streaming along the closed magnetic field lines around magnetic islands, 2) particles rapidly and stochastically bouncing inside magnetic islands, and 3) particles reflecting between magnetic mirrors formed due to magnetic field compression near magnetic islands.

It is found that due to the particle acceleration by the induction electric field, all of the three different types of trapped particles gain energy. However, the energy gain of the first type of trapped particles, which stream along the closed field lines around magnetic islands, is less than the other two types. Trapped particles that reflect between magnetic mirrors near magnetic islands and stochastically bounce within magnetic islands can gain much more energy due to multiple particle crossings of the central current sheet region in a short period of time. Particularly, the second type is found to be capable of becoming energetic particles due to the multiple rapid and chaotic particle accelerations by the reconnection electric field. It is suggested that the stochastic particle bouncing inside magnetic islands may be an important mechanism for the generation of energetic particles during the collisionless magnetic reconnection.

Although many interesting results have been obtained from the present simulation study of the driven collisionless magnetic reconnection, artificially small

ion-to-electron mass ratio ($m_i/m_e = 25$) is still the major limitation of present simulations. The present simulation model, which uses an explicit time integration scheme, becomes inadequate to simulate the driven collisionless magnetic reconnection with a large ion-to-electron mass ratio. Both hybrid particle models and implicit full particle models are capable of handling particle simulations with large ion-to-electron mass ratio. However, since electron kinetic effects are important in the collisionless magnetic reconnection, an implicit full particle model seems more suitable for the future simulation study of the driven collisionless magnetic reconnection process. Of course, an implicit full particle code is much more complicated than the present explicit simulation code. More information on the implicit particle simulation models can be found in Mason [1981], Denavit [1981], Brackbill and Forslund [1982], Barnes et al. [1983], Birdsall and Langdon [1985], Hewett and Langdon, [1987], Tanaka [1988], Cohen et al. [1989], and references therein.

References

- Akasofu, S-I., The solar wind-magnetosphere energy coupling and magnetosphere disturbances, *Planet. Space Sci.*, **28**, 495, 1980.
- Alder, B., S. Fernback, and M. Rotenburg, *Methods in Computational Physics*, Vol. 9, Academic, New York, 1970.
- Alder, B., S. Fernback, and M. Rotenburg, *Methods in Computational Physics*, Vol. 16, Academic, New York, 1976.
- Alfvén, H., and C-G. Fälthammar, *Cosmical Electrodynamics*, 2nd ed., Clarendon Press, Oxford, 1963.
- Alfvén, H., Some properties of magnetospheric neutral surfaces, *J. Geophys. Res.*, **73**, 4379, 1968.
- Allen, C., and D. W. Swift, A particle simulation of the tearing mode instability at the dayside magnetopause, *J. Geophys. Res.*, **94**, 6925, 1989.
- Ambrosiano, J. J., L. C. Lee, and D. W. Swift, Simulation of the ion tearing instability in the presence of a background plasma, *J. Geophys. Res.*, **88**, 7860, 1983.
- Ambrosiano, J., L. C. Lee, and Z. F. Fu, Simulation of the collisionless tearing instability in an anisotropic neutral sheet, *J. Geophys. Res.*, **91**, 113, 1986.
- Anderson, R. R., C. C. Harvey, M. M. Hoppe, B. T. Tsurutani, T. E. Eastman, and J. Etcheto, Plasma waves near the magnetopause, *J. Geophys. Res.*, **87**, 2087, 1982.
- Ashour-Abdalla, M., J. Berchem, J. Büchner, and L. M. Zelenyi, Chaotic scattering and acceleration of ions in the Earth's magnetotail, to be submitted to *J. Geophys. Res.*, 1990.
- Auer, P. L., H. Hurwitz, and R. W. Kilb, Low Mach number magnetic compression waves in a collision-free plasma, *Phys. Fluids*, **4**, 1105, 1961.
- Axford, W. I., Magnetic field reconnection, in *Magnetic Reconnection in Space and Laboratory Plasmas*, ed. by E. W. Hones, Jr., p. 1, Geophysical Monograph 30, AGU, Washington, D.C., 1984.

- Baker, D. A., The role of magnetic reconnection phenomena in the reversed-field pinch, in *Magnetic Reconnection in Space and Laboratory Plasmas*, ed. by E. W. Hones, Jr., p. 332, Geophysical Monograph 30, AGU, Washington, D.C., 1984.
- Baker, D. N., and R. D. Belian, Impulsive ion acceleration in Earth outer magnetosphere, in *Ion Acceleration in the Magnetosphere and Ionosphere*, ed. by T. Chang, p. 375, Geophysical Monograph 38, AGU, Washington, D.C., 1986.
- Barnes, D. C., T. Kamimura, J. N. Leboeuf, and T. Tajima, Implicit particle simulation of magnetized plasmas, *J. Comput. Phys.*, **52**, 480, 1983.
- Bauer, F., O. Betancourt, and P. Garabedian, *A Computational Method in Plasma Physics*, Springer Series in Computational Physics, Springer-Verlag, New York, 1978.
- Baum, P. J., and A. Bratenahl, Magnetic reconnection experiments, *Adv. Electronics and Electron Phys.*, **54**, 1, 1980.
- Berchem, J., and C. T. Russell, The thickness of the magnetopause current layer, ISEE 1 and 2 observations, *J. Geophys. Res.*, **87**, 2108, 1982.
- Berchem, J., and C. T. Russell, Flux transfer events on the magnetopause: Spatial distribution and controlling factors, *J. Geophys. Res.*, **89**, 6689, 1984.
- Birdsall, C. K., and A. B. Langdon, *Plasma Physics via Computer Simulation*, McGraw-Hill, New York, 1985.
- Biskamp, D., R. Z. Sagdeev, and K. Schindler, Nonlinear evolution of the tearing instability in the geomagnetic tail, *Cosmic Electrodyn.*, **1**, 297, 1970.
- Brackbill, J. U., and D. W. Forslund, An implicit method for electromagnetic plasma simulation in two dimensions, *J. Comput. Phys.*, **46**, 271, 1982.
- Bretherton, F. P., and D. B. Haidvogel, Two-dimensional turbulence above topography, *J. Fluid Mech.*, **78**, 129, 1976.
- Brunel, F., T. Tajima, and J. M. Dawson, Fast magnetic reconnection processes, *Phys. Rev. Lett.*, **49**, 323, 1982.
- Büchner, J., and L. M. Zelenyi, Deterministic chaos in the dynamics of charged particles near a magnetic field reversal, *Phys. Lett. A.*, **118**, 395, 1986.

- Büchner, J., and L. M. Zelenyi, Adiabatic and chaotic charged particle motion in two-dimensional magnetic field reversals: 1. Basic theory of trapped motion, *J. Geophys. Res.*, **94**, 11821, 1989.
- Buneman, O., Dissipation of currents in ionized media, *Phys. Rev.*, **115**, 503, 1959.
- Burkhart, G. R., and J. Chen, Linear, collisionless, bi-Maxwellian neutral sheet tearing instability, *Phys. Rev. Lett.*, **63**, 159, 1989a.
- Burkhart, G. R., and J. Chen, Collisionless tearing instability of a bi-Maxwellian neutral sheet: An integrodifferential treatment with exact particle orbits, *Phys. Fluids*, **B1**, 1578, 1989b.
- Chaloner, C. P., D. S. Hall, R. P. Rijnbeek, and D. J. Southwood, Electrons at the dayside magnetopause: Recent observations by AMPTE/UKS, in *Solar Wind-Magnetosphere Coupling*, ed. by Y. Kamide and J. A. Slavin, p. 331, Terra Scientific, Tokyo, 1986.
- Chen, J., and R. C. Davidson, Tearing-mode stability properties of a diffuse anisotropic field-reversed layer at marginal stability, *Phys. Fluids*, **24**, 2208, 1981.
- Chen, J., and P. J. Palmadesso, Tearing instability properties of an anisotropic neutral sheet, *Phys. Fluids*, **27**, 1198, 1984.
- Chen, J., and Y. C. Lee, Collisionless tearing instability in a non-Maxwellian neutral sheet: An integro-differential formulation, *Phys. Fluids*, **28**, 2137, 1985.
- Chen, J., and P. J. Palmadesso, Chaos and nonlinear dynamics of single particle orbits in a magnetotail-like magnetic field, *J. Geophys. Res.*, **91**, 1499, 1986.
- Chen, J., and Y. C. Lee, A quadratic-form analysis of the collisionless tearing mode, *Phys. Fluids*, **31**, 2944, 1988.
- Cohen, B. I., A. B. Langdon, D. W. Hewett, and R. J. Procassini, Performance and optimization of direct implicit particle simulation, *J. Comput. Phys.*, **81**, 151, 1989.
- Coppi, B., G. Laval., and R. Pellat, Dynamics of the geomagnetic tail, *Phys. Rev. Lett.*, **16**, 1207, 1966.
- Coppi, B., J. W.-K. Mark, L. Sugiyama, and G. Bertin, Reconnecting modes in collisionless plasmas, *Phys. Rev. Lett.*, **42**, 1058, 1979.

- Coroniti, F. V., and K. B. Quest, Nonlinear evolution of magnetopause tearing modes, *J. Geophys. Res.*, **89**, 137, 1984.
- Cowley, S. W. H., A self-consistent model of a simple magnetic neutral sheet system surrounded by a cold, collisionless plasma, *Cosmic Electrodyn.*, **3**, 448, 1973.
- Cowley, S. W. H., Comments on the merging of non antiparallel fields, *J. Geophys. Res.*, **81**, 3455, 1976.
- Cowley, S. W. H., The causes of convection in the Earth's magnetosphere: A review of developments during the IMS, *Rev. Geophys.*, **20**, 531, 1982.
- Cowley, S. W. H., Evidence for the occurrence and importance of reconnection between the Earth's magnetic field and the interplanetary field, in *Magnetic Reconnection in Space and Laboratory Plasmas*, ed. by E. W. Hones, Jr., p. 375, Geophysical Monograph 30, AGU, Washington, D.C., 1984.
- Cowley, S. W. H., Magnetic reconnection, in *Solar System Magnetic Field*, ed. by E. R. Priest, p. 121, D. Reidel Publ. Co., Dordrecht, Holland, 1985.
- Crooker, N. U., A split separator line merging model of the dayside magnetopause, *J. Geophys. Res.*, **90**, 12104, 1985.
- Daily, R., C. A. Cattell, F. S. Mozer, and J. Berchem, Electric fields and convection velocities associated with flux transfer events, *Geophys. Res. Lett.*, **12**, 843, 1985.
- Daly, P. W., and E. Keppler, Observation of a flux transfer event on the earthward side of the magnetopause, *Planet. Space Sci.*, **30**, 331, 1982.
- Daly, P. W., and T. A. Fritz, Trapped electron distributions on open magnetic field lines, *J. Geophys. Res.*, **87**, 6081, 1982.
- Daly, P. W., and E. Keppler, Remote sensing of a flux transfer events with energetic particles, *J. Geophys. Res.*, **88**, 3971, 1983.
- Daly, P. W., D. J. Williams, C. T. Russell, and E. Keppler, Particle signature of magnetic flux transfer events at the magnetopause, *J. Geophys. Res.*, **86**, 1628, 1981.
- Daly, P. W., M. A. Saunders, R. P. Rijnbeek, N. Sckopke, and C. T. Russell, The distribution of reconnection geometry in flux transfer events using energetic ions, plasma, and magnetic data, *J. Geophys. Res.*, **89**, 3843, 1984.

- Darwin, C. G., Dynamical motions of charged particles, *Phil. Mag.*, **39**, 537, 1920.
- Dawson, J. M., One-dimensional plasma model, *Phys. Fluids*, **5**, 445, 1962.
- Dawson, J. M., Particle simulation of plasmas, *Rev. Mod. Phys.*, **55**, 403, 1983.
- Denavit, J., Time-filtering particle simulations with $\omega_{pe}\Delta t \gg 1$, *J. Comput. Phys.*, **42**, 337, 1981.
- Denstrovskii, Y. N., and D. P. Kostomarov, *Numerical Simulations of Plasmas*, Springer Series in Computational Physics, Springer-Verlag, New York, 1986.
- Dessler, A. J., Magnetic merging in the magnetospheric tail, *J. Geophys. Res.*, **73**, 209, 1968.
- Dickman, D. O., R. L. Morse, and C. W. Nielson, Numerical simulation of axisymmetric, collisionless, finite- β plasma, *Phys. Fluids*, **12**, 1708, 1969,
- Ding, D. Q., and L. C. Lee, A simulation study of particle heat flux and plasma waves associated with magnetic reconnections at the dayside magnetopause, in *Physics of Magnetic Flux Ropes*, ed. by C. T. Russell, E. R. Priest, and L. C. Lee, p. 507, Geophysical Monograph 58, AGU, Washington, D.C., 1990.
- Ding, D. Q., L. C. Lee, and Z. F. Fu, Multiple X line reconnection, 3: A particle simulation of flux transfer events, *J. Geophys. Res.*, **91**, 13384, 1986.
- Ding, D. Q., L. C. Lee, and Z. W. Ma, Different FTE signatures generated by the bursty single X line reconnection and the multiple X line reconnection at the dayside magnetopause, in press *J. Geophys. Res.*, **95**, 1990.
- Dobrowolny, M., Instability of a neutral sheet, *Nuovo Cimento*, **B55**, 427, 1968.
- Drake, J. F., and Y. C. Lee, Kinetic theory of tearing instabilities, *Phys. Fluids*, **20**, 1341, 1977.
- Dubinin, E. M., I. M. Podgornyi, and Yu. N. Potanin, Structure of the magnetic field at the boundary of the magnetosphere: Analysis of a simulation experiment, *Kosmicheskie Issledovaniya*, **18**, 99, 1980.
- Dungey, J. W., *Cosmic Electrodynamics*, Cambridge University Press, Cambridge, 1958.
- Dungey, J. W., Interplanetary magnetic field and the auroral zones, *Phys. Rev. Lett.*, **6**, 47, 1961.

- Eastwood, J. W., Consistency of fields and particle motion in the 'Speiser' model of the current sheet, *Planet. Space Sci.*, **20**, 1555, 1972.
- Elphic, R. C., *private communication*, 1988.
- Elphic, R. C., Observations of flux transfer events: Are FTEs flux ropes, islands, or surface waves?, in *Physics of Magnetic Flux Ropes*, ed. by C. T. Russell, E. R. Priest, and L. C. Lee, p. 455, Geophysical Monograph 58, AGU, Washington, D.C., 1990.
- Elphic, R. C., and D. J. Southwood, Simultaneous measurements of the magnetopause and flux transfer events at widely separated sites by AMPTE/UKS and ISEE 1 and 2, *J. Geophys. Res.*, **92**, 13666, 1987.
- Farrugia, C. J., D. J. Southwood, S. W. H. Cowley, R. P. Rijnbeek, and P. W. Daly, Two-regime flux transfer events, *Planet. Space Sci.*, **35**, 737, 1987.
- Farrugia, C. J., R. P. Rijnbeek, M. A. Sauer, D. J. Southwood, D. J. Rodgers, M. F. Smith, C. P. Chaloner, D. S. Hall, P. J. Christiansen, and L. J. C. Woolliscroft, A multi-instrument study of flux transfer event structure, *J. Geophys. Res.*, **93**, 14465, 1988.
- Forslund, D. W., *Ph.D. Thesis*, Princeton University, 1968.
- Francis, G. E., D. W. Hewett, and C. E. Max, Kinetic simulation of magnetic reconnection in the presence of shear, in *Reconnection in Space Plasma*, ed. by T. D. Guyenne and J. J. Hunt, p. 61, ESA SP-285, Vol. II, Netherland, 1989.
- Freeman, M. P., and D. J. Southwood, The effect of magnetospheric erosion on mid- and high-latitude ionospheric flows, *Planet. Space Sci.*, **36**, 509, 1988.
- Fu, Z. F., 2-D and 3-D simulation study of multiple X line reconnection, in *Magnetic Reconnection in Space Plasma*, ed. by T. D. Guyenne and J. J. Hunt, p. 275, ESA SP-285, Vol. II, Netherland, 1989.
- Fu, Z. F., and L. C. Lee, Simulation of multiple X line reconnection at the dayside magnetopause, *Geophys. Res. Lett.*, **12**, 291, 1985.
- Fu, Z. F., and L. C. Lee, Multiple X line reconnection, 2. The dynamics, *J. Geophys. Res.*, **91**, 13373, 1986.
- Fu, Z. F., L. C. Lee, and Y. Shi, A three-dimensional MHD simulation of the multiple X line reconnection process, in *Physics of Magnetic Flux Ropes*, ed. by C. T. Russell, E. R. Priest, and L. C. Lee, p. 515, Geophysical Monograph 58, AGU, Washington, D.C., 1990.

- Furth, H. P., The mirror instability for finite particle gyroradius, *Nucl. Fusion Suppl. Pt. 1*, 169, 1962.
- Furth, H. P., J. Killeen, and M. N. Rosenbluth, Finite-resistivity instabilities of a sheet pinch, *Phys. Fluids*, **6**, 459, 1963.
- Galeev, A. A., Spontaneous reconnection of magnetic field lines in a collisionless plasma, in *Handbook of Plasma Physics Vol II: Basic Plasma Physics*, ed. by A. A. Galeev and R. N. Sudan, p. 305, North-Holland, Amsterdam, 1984.
- Galeev, A. A., and L. M. Zelenyi, Nonlinear instability theory for a diffusive neutral layer, *Sov. Phys. JEPT*, **42**, 450, 1975a.
- Galeev, A. A., and L. M. Zelenyi, Metastable states of diffusive neutral sheet and the substorm explosive phase, *JETP Lett.*, **22**, 170, 1975b.
- Galeev, A. A., and L. M. Zelenyi, Tearing instability in plasma configurations, *Sov. Phys. JETP*, **43**, 1113, 1976.
- Galeev, A. A., and L. M. Zelenyi, Model of magnetic-field reconnection in a plane layer of collisionless plasma, *JETP Lett.*, **25**, 380, 1977.
- Galeev, A. A., and L. M. Zelenyi, Magnetic reconnection in a space plasma, in *Theoretical and Computational Plasma Physics*, p. 93, IAEA-SMR-31/100, IAEA, Vienna, 1978.
- Galeev, A. A., L. M. Zelenyi, and M. M. Kuznetsova, Nonlinear drift tearing mode: Hard onset and stabilization mechanisms, *JETP Lett.*, **41**, 387, 1985.
- Galeev, A. A., M. M. Kuznetsova, and L. M. Zelenyi, Magnetopause stability threshold for patchy reconnection, *Space Sci. Rev.*, **44**, 1, 1986.
- Gekelman, W., R. L. Stenzel, and N. Wild, Magnetic field line reconnection experiments, *Physica Scripta*, **T2/2**, 277, 1982.
- Gillis, E. J., R. Rijnbeek, R. Kling, T. W. Speiser, and T. A. Fritz, Do flux transfer events cause long-period micropulsations in the dayside magnetopause?, *J. Geophys. Res.*, **92**, 5820, 1987.
- Giovanelli, R. G., A theory of chromospheric flares, *Nature*, **158**, 81, 1946.
- Giovanelli, R. G., Magnetic and electric phenomena in the Sun's atmosphere associated with sunspots, *Mon. Not. Roy. Ast. Soc.*, **107**, 338, 1947.
- Gladd, N. T., Collisionless drift-tearing modes in the magnetopause, submitted to *J. Geophys. Res.*, **95**, 1990.

- Goertz, C. K., E. Neilsen, A. Korth, K.-H. Glassmeier, C. Haldoupis, P. Hoeg, and D. Hayward, Observations of a possible ground signature of flux transfer events, *J. Geophys. Res.*, **90**, 4069, 1985.
- Goldstein, H., *Classical Mechanics*, 2nd ed., Addison-Wesley Pub. Co., Reading, Mass., 1980.
- Goldstein, M. L., W. H. Matthaeus, and J. J. Ambrosiano, Acceleration of charged particles in magnetic reconnection: Solar flares, the magnetosphere, and solar wind, *Geophys. Res. Lett.*, **13**, 205, 1986.
- Gosling, J. T., M. F. Thomsen, S. J. Bame, R. C. Elphic, and C. T. Russell, Plasma flow reversals at the dayside magnetopause and the origin of asymmetric polar cap convection, *J. Geophys. Res.*, **95**, 8073, 1990.
- Gray, P. C., and L. C. Lee, Particle pitch angle diffusion due to nonadiabatic effects in the plasma sheet, *J. Geophys. Res.*, **87**, 7445, 1982.
- Greene, J. M., Geometrical properties of three-dimensional magnetic fields with nulls, *J. Geophys. Res.*, **93**, 8583, 1988.
- Greengard, L., and V. Rokhlin, A fast algorithm for particle simulations, *J. Comput. Phys.*, **73**, 325, 1987.
- Greenly, J. B., and B. U. Ö. Sonnerup, Tearing modes at the magnetopause, *J. Geophys. Res.*, **86**, 1305, 1981.
- Gruber, R., and J. Rappaz, *Finite Element Methods in Linear Ideal Magnetohydrodynamics*, Springer Series in Computational Physics, Springer-Verlag, New York, 1985.
- Gurnett, D. A., R. R. Anderson, B. T. Tsurutani, E. J. Smith, G. Paschmann, G. Haerendel, S. J. Bame, and C. T. Russell, Plasma wave turbulence at the magnetopause: Observations from ISEE 1 and 2, *J. Geophys. Res.*, **84**, 7043, 1979.
- Haber, I., R. Lee, H. H. Klein, and J. R. Boris, Advances in electromagnetic plasma simulation techniques, *Proc. Sixth Conf. Num. Sim. Plasmas*, p. 46, Lawrence Livermore Lab., 1973.
- Haerendel, G., and G. Paschmann, Interaction of the solar wind with the dayside magnetopause, in *Magnetospheric Plasma Physics*, ed. by A. Nishida, p. 49, D. Reidel Publ. Co., Dordrecht, Holland, 1982.

- Haerendel, G., G. Paschmann, N. Sckopke, H. Rosenbauer, and P. C. Hedgecock, The frontside boundary layer of the magnetosphere and the problem of reconnection, *J. Geophys. Res.*, **83**, 3195, 1978.
- Harris, E. G., On a plasma sheath separating regions of oppositely directed magnetic field, *Nuovo Cimento*, **23**, 15, 1962.
- Hasegawa, A., A test of self-organization hypothesis in Jovian and Saturnian wind systems, *J. Phys. Soc. Japan*, **52**, 1930, 1983.
- Hasegawa, A., Self-organization processes in continuous media, *Adv. Phys.*, **34**, 1, 1985.
- Hasegawa, A., and C. K. Birdsall, Sheet-current plasma model for ion cyclotron waves, *Phys. Fluids*, **7**, 1590, 1964.
- Heikkila, W. J., Transport of plasma across the magnetopause, in *Solar Wind-Magnetosphere Coupling*, ed. by Y. Kamide and J. A. Slavin, p. 337, Terra Scientific, Tokyo, 1986.
- Heikkila, W. J., Magnetic reconnection, merging, and viscous interaction in the magnetosphere, *Space Sci. Rev.*, **53**, 1, 1990.
- Hesse, M., and K. Schindler, A theoretical foundation of general magnetic reconnection, *J. Geophys. Res.*, **93**, 5559, 1988.
- Hesse, M., J. Birn, and K. Schindler, Flux transfer events: Reconnection without separators? in *Reconnection in Space Plasma*, ed. by T. D. Guyenne and J. J. Hunt, p. 263, ESA SP-285, Vol. II, Netherland, 1989.
- Hewett, D. W., and A. B. Langdon, Electromagnetic direct implicit plasma simulation, *J. Comput. Phys.*, **72**, 121, 1987.
- Hewett, D. W., G. E. Francis, and C. E. Max, New regimes of magnetic reconnection in collisionless plasmas, *Phys. Rev. Lett.*, **61**, 893, 1988.
- Hill, T. W., Magnetic merging in a collisionless plasma, *J. Geophys. Res.*, **80**, 4689, 1975.
- Hockney, R. W., and J. W. Eastwood, *Computer Simulation Using Particles*, McGraw-Hill, New York, 1981.
- Hoh, F. C., Stability of sheet pinch, *Phys. Fluids*, **9**, 227, 1966.
- Hones, E. W., Jr., Editor, *Magnetic Reconnection in Space and Laboratory Plasmas*, Geophysical Monograph 30, AGU, Washington, D.C., 1984.

- Horiuchi, R., and T. Sato, Self-organization process in three-dimensional compressible magnetohydrodynamics, *Phys. Fluids*, **29**, 4174, 1986.
- Hoshino, M., The electrostatic effect for the collisionless tearing mode, *J. Geophys. Res.*, **92**, 7368, 1987.
- Hoyle, F., Magnetic storms and aurorae, in *Some Recent Researches in Solar Physics*, p. 102, Cambridge University Press, London, 1949.
- Kan, J. R., A theory of patchy and intermittent reconnection for magnetospheric flux transfer events, *J. Geophys. Res.*, **93**, 5613, 1988.
- Katanuma, I, and T. Kamimura, Simulation studies of the collisionless tearing instabilities, *Phys. Fluid.*, **23**, 2500, 1980.
- Killeen, J., G. D. Kerbel, M. G. McCoy, and A. A. Mirin, *Computational Methods for Kinetic Models of Magnetically Confined Plasmas*, Springer Series in Computational Physics, Springer-Verlag, New York, 1986.
- Kim, J-S., and J. R. Cary, Charged particle motion near a linear magnetic null, *Phys. Fluids*, **26**, 2167, 1983.
- Klumpar, D. M., S. A. Fuselier, T. A. Potemra, and K. Takahashi, AMPTE/CCE observations of electron distributions in flux transfer events, *EOS Trans. AGU*, **70**, 437, 1989.
- Kraichnan, R. H., and D. Montgomery, Two-dimensional turbulence, *Rep. Prog. Phys.*, **43**, 547, 1980.
- Kuznetsova, M. M., and L. M. Zelenyi, Stability and structure of the perturbations of the magnetic surfaces in the magnetic transitional layers, *Plasma Phys. Contr. Fusion*, **27**, 363, 1985.
- LaBelle, J., and R. A. Treumann, Plasma waves at the dayside magnetopause, *Space Sci. Rev.*, **47**, 175, 1988.
- LaBelle, J., R. A. Treumann, G. Haerendel, O. H. Bauer, G. Paschmann, W. Baumjohann, H. Lühr, R. R. Anderson, H. C. Koons, and R. H. Holzworth, AMPTE IRM observations of waves associated with flux transfer events in the magnetopause, *J. Geophys. Res.*, **92**, 5827, 1987.
- Lanzerotti, L. J., and C. G. MacLennan, Hydromagnetic waves associated with possible flux transfer events, *Astrophys. Space Sci.*, **44**, 279, 1988.

- Lanzerotti, L. J., L. C. Lee, C. G. MacLennan, A. Wolfe, and L. V. Medford, Possible evidence of flux transfer events in the polar ionosphere, *Geophys. Res. Lett.*, **13**, 1089, 1986.
- Laval, G., and R. Pellat, Méthode d'étude de la stabilité de certaines solutions de l'équation de Vlasov, *C. R. Acad. Sc. Paris*, **259**, 1706, 1964.
- Laval, G., and R. Pellat, Stability of the plane neutral sheet for oblique propagation and anisotropic temperature, in *The Stability of Plane Plasmas*, p. 5, ESPO SP-36, 1968.
- Laval G., R. Pellat, and M. Vuillemin, Instabilités électromagnétiques des plasma sans collisions, in *Plasma Physics and Controlled Nuclear Fusion Research*, vol. 2, p. 259, International Atomic Energy Agency, Vienna, 1966.
- Leboeuf, J. N., T. Tajima, and J. M. Dawson, Dynamic magnetic X points, *Phys. Fluids*, **25**, 784, 1982.
- Lee, L. C., Magnetic flux transfer events at the earth's magnetopause, in *Solar Wind-Magnetosphere Coupling*, ed. by Y. Kamide and J. Slavin, p. 297, Terra Scientific, Tokyo, 1986.
- Lee, L. C., Toward a time-dependent magnetic reconnection model, *EOS Trans. AGU*, **69**, 1617, 1988.
- Lee, L. C., and Z. F. Fu, A theory of magnetic flux transfer at the Earth's magnetopause, *Geophys. Res. Lett.*, **12**, 105, 1985.
- Lee, L. C., and Z. F. Fu, Multiple X line reconnection, 1. A criterion for the transition from a single X line to a multiple X line reconnection, *J. Geophys. Res.*, **91**, 6807, 1986.
- Lee, L. C., and D. Q. Ding, Magnetic reconnection in a collisionless plasma: Evidence for the current sheet acceleration, *Geophys. Res. Lett.*, **14**, 1003, 1987.
- Lee, L. C., Z. F. Fu, and S.-I. Akasofu, A simulation study of forced reconnection processes and magnetospheric storms and substorms, *J. Geophys. Res.*, **90**, 10896, 1985.
- Lee, L. C., Y. Shi, and L. J. Lanzerotti, A mechanism for the generation of cusp region hydromagnetic waves, *J. Geophys. Res.*, **93**, 7578, 1988.
- Lembege, B., and R. Pellat, Stability of a thick two-dimensional quasi-neutral sheet, *Phys. Fluids*, **22**, 1995, 1982.

- Levy, R. H., H. E. Petschek, and G. L. Siscoe, Aerodynamic aspects of the magnetospheric flow, *AIAA J.*, **2**, 2065, 1964.
- Liu, Z. X., and Y. D. Hu, Local magnetic reconnection caused by vortices in the flow field, *Geophys. Res. Lett.*, **15**, 752, 1988.
- Lockwood, M., P. E. Sandholt, and S. W. H. Cowley, Dayside auroral activity and magnetic flux transfer from the solar wind, *Geophys. Res. Lett.*, **16**, 33, 1989.
- Lühr, H., and N. Klöcker, AMPTE/IRM observations of magnetic cavities near the magnetopause, *Geophys. Res. Lett.*, **14**, 186, 1987.
- Lundin, R., On the magnetospheric boundary layer and solar wind energy transfer into the magnetosphere, *Space Sci. Rev.*, **48**, 263, 1988.
- Lyons, L. R., Electron energization in the geomagnetic tail current sheet, *J. Geophys. Res.*, **89**, 5479, 1984.
- Lyons, L. R., and T. W. Speiser, Evidence for current sheet acceleration in the geomagnetic tail, *J. Geophys. Res.*, **87**, 2276, 1982.
- Lyons, L. R., and T. W. Speiser, Ohm's law for a current sheet, *J. Geophys. Res.*, **90**, 8543, 1985.
- Martin, R. F., Jr., Chaotic particle dynamics near a two-dimensional magnetic neutral point with application to the geomagnetic tail, *J. Geophys. Res.*, **91**, 11985, 1986.
- Mason, R. J., Implicit moment particle simulation of plasmas, *J. Comput. Phys.*, **41**, 233, 1981.
- Matsumoto, H., and T. Sato, Editors, *Computer Simulation of Space Plasmas*, Terra Scientific Publishing Company, Tokyo, Japan, 1985.
- Matthaeus, W. H., Reconnection in two dimensions: Localization of vorticity and current near magnetic X points, *Geophys. Res. Lett.*, **9**, 660, 1982.
- Matthaeus, W. H., and D. Montgomery, Selective decay hypothesis at high mechanical and magnetic Reynolds number, *Ann. N. Y. Acad. Sci.*, **357**, 203, 1980.
- Matthaeus, W. H., and D. Montgomery, Nonlinear evolution of the sheet pinch, *J. Plasma Phys.*, **25**, 11, 1981.

- Matthaeus, W. H., and D. Montgomery, Dynamic alignment and selective decay in MHD, in *Statistical Physics and Chaos in Fusion Plasmas*, ed. by C. W. Horton, Jr., and L. E. Reichl, p. 285, John Wiley and Sons, New York, 1984.
- Matthaeus, W. H., and S. L. Lamkin, Rapid magnetic reconnection caused by finite amplitude fluctuations, *Phys. Fluids*, **28**, 303, 1985.
- Matthaeus, W. H., and S. L. Lamkin, Turbulent magnetic reconnection, *Phys. Fluids*, **29**, 2513, 1986.
- Matthaeus, W. H., J. J. Ambrosiano, and M. L. Goldstein, Particle acceleration by turbulent magnetohydrodynamic reconnection, *Phys. Rev. Lett.*, **53**, 1449, 1984.
- McHenry, M. A., and C. R. Clauer, Modeled ground signatures of flux transfer events, *J. Geophys. Res.*, **92**, 11231, 1987.
- Miura A., Anomalous transport by magnetohydrodynamic Kelvin-Helmholtz instabilities in the solar wind-magnetosphere interaction, *J. Geophys. Res.*, **89**, 801, 1984.
- Montgomery, D., Introduction to the theory of fluid and magnetic turbulence, in *Nagoya Lectures in Plasma Physics and Controlled Fusion*, ed. by Y. H. Ichikawa and T. Kamimura, Tokai University Press, Tokyo, Japan, 1989.
- Montgomery, D., L. Turner, and G. Vahala, Three-dimensional magnetohydrodynamic turbulence in cylindrical geometry, *Phys. Fluids*, **21**, 757, 1978.
- Naitou, H., S. Tokuda, and T. Kamimura, On boundary conditions for a simulation plasma in a magnetic field, *J. Comput. Phys.*, **33**, 86, 1979.
- Nicolis, G., Dissipative system, *Rep. Prog. Phys.*, **49**, 873, 1986.
- Nicolis, G., and I. Prigogine, *Self-organization in Nonequilibrium Systems*, John Wiley and Sons, New York, 1977.
- Niedner, M. B., Jr., Magnetic reconnection in comets, in *Magnetic Reconnection in Space and Laboratory Plasmas*, ed. by E. W. Hones, Jr., p. 79, Geophysical Monograph 30, AGU, Washington, D.C., 1984.
- Nielson, C. W., and H. R. Lewis, Particle code models in the nonradiative limit, in *Methods of Computational Physics*, vol. 16, ed. by J. Killeen, p. 367, Academic, Orlando, Fla., 1976.

- Nishida, A., Reconnection in the Jovian magnetosphere, in *Magnetic Reconnection in Space and Laboratory Plasmas*, ed. by E. W. Hones, Jr., p. 90, Geophysical Monograph 30, AGU, Washington, D.C., 1984.
- Ogino, T., R. J. Walker, and M. Ashour-Abdalla, A magnetohydrodynamic simulation of the formation of magnetic flux tubes at the earth's dayside magnetopause, *Geophys. Res. Lett.*, **16**, 155, 1989.
- Papamastorakis, I., G. Paschmann, W. Baumjohann, B. U. Ö. Sonnerup, and H. Lühr, Orientation, motion, and other properties of flux transfer event structures on September 4, 1984, *J. Geophys. Res.*, **94**, 8852, 1989.
- Paré, V. K., Reconnection in Tokamaks, in *Magnetic Reconnection in Space and Laboratory Plasmas*, ed. by E. W. Hones, Jr., p. 341, Geophysical Monograph 30, AGU, Washington, D.C., 1984.
- Parker, E. N., Sweet's mechanism for merging magnetic fields in conducting fluids, *J. Geophys. Res.*, **62**, 509, 1957.
- Parker, E. N., The solar flare phenomenon and the theory of reconnection and annihilation of magnetic fields, *Astrophys. J. Suppl. Ser.*, **8**, 117, 1963.
- Paschmann, G., B. U. Ö. Sonnerup, I. Papamastorakis, N. Sckopke, G. Haerendel, S. J. Bame, J. R. Asbridge, J. T. Gosling, C. T. Russell, and R. C. Elphic, Plasma acceleration at the earth's magnetopause: Evidence for reconnection, *Nature*, **282**, 243, 1979.
- Paschmann, G., G. Haerendel, I. Papamastorakis, N. Sckopke, S. J. Bame, J. T. Gosling, and C. T. Russell, Plasma and magnetic characteristics of magnetic flux transfer events, *J. Geophys. Res.*, **87**, 2159, 1982.
- Paschmann, G., I. Papamasrtorakis, W. Baumjohann, N. Sckopke, C. W. Carlson, B. U. Ö. Sonnerup, and H. Lühr, The magnetopause for larger magnetic shear: AMPTE/IRM observations, *J. Geophys. Res.*, **91**, 11099, 1986.
- Petschek, H. G. Magnetic Annihilation, in *AAS-NASA Symposium on the Physics of Solar Flares*, ed. by W. N. Hess, p. 425, NASA Spec. Publ. SP-50, 1964.
- Pfirsch, D., Electrostatic stability of a non-Maxwellian homogeneous plasma, *Z. Naturforsch. 17a*, **315**, 1962.
- Podgorny, I. M., E. M. Dubinin, and Yu. N. Potanin, On magnetic curl in front of the magnetosphere boundary, *Geophys. Res. Lett.*, **7**, 247, 1980.
- Potter, D., *Computational Physics*, Wiley, New York, 1973.

- Pouquet, A., On two-dimensional magnetohydrodynamic turbulence, *J. Fluid Mech.*, **88**, 1, 1978.
- Price, C. P., and D. W. Swift, Ion tearing mode simulations with open boundary conditions, *J. Geophys. Res.*, **91**, 11993, 1986.
- Priest, E. R., Editor, *Solar System Magnetic Fields*, D. Reidel Publishing Co., Dordrecht, Holland, 1985.
- Priest, E. R., and S. W. H. Cowley, Some comments on magnetic field reconnection, *J. Plasma Phys.*, **14**, 271, 1975.
- Priest, E. R., and T. G. Forbes, New models for fast steady state magnetic reconnection, *J. Geophys. Res.*, **91**, 5579, 1986.
- Priest, E. R., and L. C. Lee, Nonlinear magnetic reconnection models with separatrix jets, submitted to *J. Geophys. Res.*, **95**, 1990.
- Pritchett, P. L., F. V. Coroniti, R. Pellat, and H. Karimabadi, Collisionless reconnection in a quasi-neutral sheet near marginal stability, *Geophys. Res. Lett.*, **16**, 1269, 1989.
- Pudovkin, M. I., and V. S. Semenov, Magnetic field reconnection theory and the solar wind-magnetosphere interaction: A review, *Space Sci. Rev.*, **41**, 1, 1985.
- Quest, K. B. and F. V. Coroniti, Tearing at the dayside magnetopause, *J. Geophys. Res.*, **86**, 3289, 1981a.
- Quest, K. B. and F. V. Coroniti, Linear theory of tearing in a high- β plasma, *J. Geophys. Res.*, **86**, 3299, 1981b.
- Quest, B., and F. C. Coroniti, Collisionless tearing in a field-reversed sheet pinch assuming nonparallel propagation, *J. Geophys. Res.*, **90**, 1458, 1985.
- Rhines, P. B., Waves and turbulence on a beta-plane, *J. Fluid Mech.*, **69**, 417, 1975.
- Rijnbeek, R. P., and S. W. H. Cowley, Magnetopause flux erosion events are flux transfer events, *Nature*, **309**, 135, 1984.
- Rijnbeek, R. P., S. W. H. Cowley, D. J. Southwood, and C. T. Russell, Observations of reverse polarity flux transfer events at the Earth's magnetopause, *Nature*, **300**, 23, 1982.

- Rijnbeek, R. P., S. W. H. Cowley, D. J. Southwood, and C. T. Russell, A survey of dayside flux transfer events observed by ISEE 1 and 2 magnetometers, *J. Geophys. Res.*, **89**, 786, 1984.
- Rijnbeek, R. P., C. J. Farrugia, D. J. Southwood, M. W. Dunlop, W. A. C. Mier-Jedrzejowicz, C. P. Chaloner, D. S. Hall, and M. F. Smith, A magnetic boundary signature within flux transfer events, *Planet. Space Sci.*, **35**, 871, 1987.
- Rusbridge, M., Non-adiabatic charged particle motion near a magnetic field zero line, *Plasma Phys.*, **13**, 977, 1971.
- Rusbridge, M., Non-adiabatic effects in charged particle motion near a neutral line, *Plasma Phys.*, **19**, 1087, 1977.
- Russell, C. T., The magnetopause, in *Physics of Magnetic Flux Ropes*, ed. by C. T. Russell, E. R. Priest, and L. C. Lee, p. 439, Geophysical Monograph 58, AGU, Washington, D.C., 1990.
- Russell, C. T., and R. C. Elphic, Initial ISEE magnetometer results: Magnetopause observations, *Space Sci. Rev.*, **22**, 681, 1978.
- Russell, C. T., and R. C. Elphic, ISEE observations of flux transfer events at the dayside magnetopause, *Geophys. Res. Lett.*, **6**, 33, 1979.
- Russell, C. T., E. R. Priest, and L. C. Lee, Editors, *Physics of Magnetic Flux Ropes*, Geophysical Monograph 58, AGU, Washington, D.C., 1990.
- Sandholt, P. E., C. S. Deehr, A. Egeland, B. Lybekk, R. Viereck, and G. J. Romick, Signatures in the dayside aurora of plasma transfer from the magnetosheath, *J. Geophys. Res.*, **91**, 10063, 1986.
- Sato, T., Strong plasma acceleration by slow shocks resulting from magnetic reconnection, *J. Geophys. Res.*, **84**, 7177, 1979.
- Sato, T., H. Matsumoto, and K. Nagai, Particle acceleration in time-developing magnetic reconnection process, *J. Geophys. Res.*, **87**, 6089, 1982.
- Sato, T., T. Shimada, M. Tanaka, T. Hayashi, and K. Watanabe, Formation of field-twisting flux tubes on the magnetopause and solar wind particle entry into the magnetosphere, *Geophys. Res. Lett.*, **13**, 801, 1986.
- Saunders, M. A., C. T. Russell, and N. Sckopke, Flux transfer events: Scale and interior structure, *Geophys. Res. Lett.*, **11**, 131, 1984.

- Schindler, K., A variational principle for one-dimensional plasmas, in *Proceedings of the Seventh International Conference on Phenomena in Ionized Gases: Vol. II Space Physics*, ed. by B. Perovic and D. Tomic, p. 736, Gradevinska Knjiga Publishing House, Beograd, Yugoslavia, 1966.
- Schindler, K., and M. Soop, Stability of plasma sheaths, *Phys. Fluids*, **11**, 1192, 1968.
- Schindler, K., M. Hesse, and J. Birn, General Magnetic Reconnection, parallel electric field, and helicity, *J. Geophys. Res.*, **93**, 5547, 1988.
- Scholer, M., Magnetic flux transfer at the magnetopause based on single X line bursty reconnection, *Geophys. Res. Lett.*, **15**, 291, 1988.
- Scholer, M., Undriven magnetic reconnection in an isolated current sheet, *J. Geophys. Res.*, **94**, 8805, 1989a.
- Scholer, M., Asymmetric time-dependent and stationary magnetic reconnection at the dayside magnetopause, *J. Geophys. Res.*, **94**, 15099, 1989b.
- Scholer, M., and F. Jamitzky, Particle orbits during the development of plasmoids, *J. Geophys. Res.*, **92**, 12181, 1987.
- Scholer, M., F. M. Ipavich, G. Gloeckler, D. Hovestadt, and B. Klecker, Leakage of magnetospheric ions into the magnetosheath along reconnected field lines at the dayside magnetopause, *J. Geophys. Res.*, **86**, 1299, 1981.
- Scholer, M., D. Hovestadt, F. M. Ipavich, and G. Gloeckler, Energetic protons, alpha particles, and electrons in magnetic flux transfer events, *J. Geophys. Res.*, **87**, 2169, 1982.
- Scudder, J. D., K. W. Ogilvie, and C. T. Russell, The relation of flux transfer events to the magnetic reconnection, in *Magnetic Reconnection in Space and Laboratory Plasmas*, ed. by E. W. Hones, Jr., p153, Geophysical Monograph 30, AGU, Washington, D.C., 1984.
- Shi, Y., and L. C. Lee, Structure of the reconnection layer at the dayside magnetopause, *Planet. Space Sci.*, **38**, 437, 1990.
- Shi, Y., C. C. Wu, and L. C. Lee, A study of multiple X line reconnection at the dayside magnetopause, *Geophys. Res. Lett.*, **15**, 295, 1988.
- Sibeck, D. G., R. W. McEntire, A. T. Y. Lui, R. E. Lopez, S. M. Krimigis, R. B. Decker, L. J. Zanetti, and T. A. Potemra, Energetic magnetic ions at the dayside magnetopause: Leakage or merging, *J. Geophys. Res.*, **92**, 12097, 1987.

- Smith, M. F., D. J. Rodgers, R. P. Rijnbeek, D. J. Southwood, A. J. Coates, and A. D. Johnstone, Plasma and field observations with high time resolution in flux transfer events, in *Solar Wind-Magnetosphere Coupling*, ed. by Y. Kamide and J. A. Slavin, p. 321, Terra Scientific, Tokyo, 1986.
- Song, Y., and R. L. Lysak, Evaluation of twist helicity of flux transfer event flux tubes, *J. Geophys. Res.*, **94**, 5273, 1989.
- Sonnerup, B. U. Ö., Magnetic reconnection in a highly conducting incompressible fluid, *J. Plasma Phys.*, **4**, 161, 1970.
- Sonnerup, B. U. Ö., Adiabatic particle orbits in a magnetic null sheet, *J. Geophys. Res.*, **76**, 8211, 1971.
- Sonnerup, B. U. Ö., The reconnecting magnetosphere, in *Magnetospheric Physics*, ed. by B. M. McCormac, p. 23, D. Reidel, Dordrecht, Holland, 1974.
- Sonnerup, B. U. Ö., Magnetic field reconnection, in *Solar System Plasma Physics*, Vol. 3, ed. by L. T. Lanzerotti, C. F. Kennel, and E. N. Parker, p. 45, North-Holland, Amsterdam, 1979.
- Sonnerup, B. U. Ö., Magnetic field reconnection at the magnetopause: An overview, in *Magnetic Reconnection in Space and Laboratory Plasmas*, ed. by E. W. Hones, Jr., p. 92, Geophysical Monograph 30, AGU, Washington, D.C., 1984.
- Sonnerup, B. U. Ö., Magnetic field reconnection in cosmic plasmas, in *Unstable Current Systems and Plasma Instabilities in Astrophysics*, ed. by M. R. Kundu and G. D. Holman, D. Reidel Publ. Co., Dordrecht, Holland, 1985.
- Sonnerup, B. U. Ö., G. Paschmann, I. Papamastorakis, N. Sckopke, G. Haerendel, S. J. Bame, J. R. Asbridge, J. T. Gosling, and C. T. Russell, Evidence for magnetic field reconnection at the Earth's magnetopause, *J. Geophys. Res.*, **86**, 10049, 1981.
- Sonnerup, B. U. Ö., I. Papamastorakis, G. Paschmann, and Lühr, Magnetopause properties from AMPTE/IRM observations of the convection electric field: Method development, *J. Geophys. Res.*, **92**, 12137, 1987.
- Southwood, D. J., The hydrodynamic stability of the magnetospheric boundary, *Planet. Space Sci.*, **11**, 587, 1968.
- Southwood, D. J., Theoretical aspects of ionosphere-magnetosphere-solar wind coupling, *Adv. Space Res.*, **5**, 4, 1985.

- Southwood, D. J., The ionospheric signature of flux transfer events, *J. Geophys. Res.*, **92**, 3207, 1987.
- Southwood, D. J., M. A. Saunders, M. W. Dunlop, W. A. C. MierJedrzejowics, and R. P. Rijnbeek, A survey of flux transfer events recorded by the UKS spacecraft magnetometer, *Planet. Space Sci.*, **34**, 1349, 1986.
- Southwood, D. J., C. J. Farrugia, and M. A. Saunders, What are flux transfer events?, *Planet. Space Sci.*, **36**, 503, 1988.
- Speiser, T. W., Particle trajectories in model current sheet, 1. Analytical solutions, *J. Geophys. Res.*, **70**, 4219, 1965.
- Speiser, T. W., Particle trajectories in model current sheet, 2. Applications to auroras using a geomagnetic tail model, *J. Geophys. Res.*, **72**, 3919, 1967.
- Speiser, T. W., Conductivity without collision noise, *Planet. Space Sci.*, **18**, 613, 1970.
- Speiser, T. W., and D. J. Williams, Magnetopause modeling: Flux transfer events and magnetosheath quasi-trapped distributions, *J. Geophys. Res.*, **87**, 2177, 1982.
- Speiser, T. W., and L. R. Lyons, Comparison of an analytical approximation for particle motion in a current sheet with precise numerical calculations, *J. Geophys. Res.*, **89**, 147, 1984.
- Stern, D. P., Adiabatic particle motion in a nearly drift-free magnetic field: Applications to the geomagnetic tail, *J. Geophys. Res.*, **83**, 1079, 1978.
- Stern, D. P., The role of O-type neutral lines in magnetic merging during substorms and solar flares, *J. Geophys. Res.*, **84**, 63, 1979.
- Stern, D. P., and P. Palmadesso, Drift free magnetic geometries in adiabatic motion, *J. Geophys. Res.*, **80**, 4244, 1975.
- Sweet, P. A., The neutral point theory of solar flares, in *Electromagnetic Phenomena in Cosmical Physics*, ed. by B. Lehnert, p. 123, Cambridge University Press, London, 1958.
- Swift, D. W., Numerical simulation of the interaction of the plasma sheet with the lobes of the Earth's magnetotail, *J. Geophys. Res.*, **87**, 2287, 1982.

- Swift, D. W., A two-dimensional simulation of the interaction of the plasma sheet with the lobes of the earth's magnetotail, *J. Geophys. Res.*, **88**, 125, 1983.
- Swift, D. W., Numerical simulations of tearing mode instabilities, *J. Geophys. Res.*, **91**, 219, 1986.
- Swift, D. W., Particle simulation of plasma processes in the Earth's magnetotail, *Computer Phys. Commun.*, **49**, 173, 1988.
- Swift, D. W., and J. J. Ambrosiano, Boundary conditions which lead to excitation of instabilities in plasma simulations, *J. Comput. Phys.*, **44**, 302, 1981.
- Swift, D. W., and C. Allen, Interaction of the plasma sheet with the lobes of the Earth's magnetotail, *J. Geophys. Res.*, **92**, 10015, 1987.
- Tajima, T., *Computational Plasma Physics: With Applications to Fusion and Astrophysics*, Addison-Wesley, New York, 1989.
- Tanaka, M., Macroscale implicit electromagnetic particle simulation of magnetized plasmas, *J. Comput. Phys.*, **80**, 209, 1988.
- Taylor, J. B., Relaxation of toroidal plasma and generation of reverse magnetic fields, *Phys. Rev. Lett.*, **33**, 1139, 1974.
- Taylor, J. B., Relaxation and magnetic reconnection in plasmas, *Rev. Mod. Phys.*, **58**, 741, 1986.
- Terasawa, T., Numerical Study of explosive tearing mode instability in one-component plasmas, *J. Geophys. Res.*, **86**, 9007, 1981.
- Thomsen, M. F., J. A. Stansberry, S. J. Bame, S. A. Fuselier, and J. T. Gosling, Ion and electron velocity distributions within flux transfer events, *J. Geophys. Res.*, **92**, 12127, 1987.
- Ting, A. C., W. H. Matthaeus, and D. Montgomery, Turbulent relaxation processes in magnetohydrodynamics, *Phys. Fluids*, **29**, 3261, 1986.
- Todd, H., B. J. I. Bromage, S. W. H. Cowley, M. Lockwood, A. P. van Eyken, and D. M. Willis, EISCAT observations of bursts of rapid flow in the high latitude dayside ionosphere, *Geophys. Res. Lett.*, **13**, 909, 1986
- Tsurutani, B. T., A. L. Brinca, E. J. Smith, R. T. Okida, R. R. Anderson, and T. E. Eastman, A statistical study of ELF-VLF plasma waves at the magnetopause, *J. Geophys. Res.*, **94**, 1270, 1989.

- Ugai, M., Dependence of fast magnetic reconnection on electrical resistivity in an isolated current sheet system, *Phys. Fluids*, **26**, 1569, 1983.
- Ugai, M., Self-consistent development of fast magnetic reconnection with anomalous plasma resistivity, *Plasma Phys. Contr. Fusion*, **26**, 1549, 1984.
- Vasyliunas, V. M., Theoretical models of magnetic field line merging, 1, *Rev. Geophys. Space Phys.*, **13**, 303, 1975.
- Vasyliunas, V. M., Steady state aspects of magnetic field line merging, in *Magnetic Reconnection in Space and Laboratory Plasmas*, ed. by E. W. Hones, Jr., p25, Geophysical Monograph 30, AGU, Washington, D.C., 1984.
- Wagner, J. S., J. R. Kan, and S-I. Akasofu, Particle dynamics in the plasma sheet, *J. Geophys. Res.*, **84**, 891, 1979.
- Wagner, J. S., P. C. Gray, J. R. Kan, T. Tajima, and S-I. Akasofu, Particle dynamics in reconnection field configurations, *Planet. Space Sci.*, **29**, 391, 1981.
- Walén, C., On the theory of sunspot, *Ark. Mat. Astron. Fys.*, **30A**, 1, 1944.
- Wei, C. Q., and L. C. Lee, Ground magnetic signatures of moving elongated plasma clouds, *J. Geophys. Res.*, **95**, 2405, 1990.
- White, R. B., Resistive instabilities and field line reconnection, in *Handbook of Plasma Physics Vol. I: Basic Plasma Physics*, ed. by A. A. Galeev and R. N. Sudan, p. 611, North-Holland Publishing Co. Amsterdam, 1983.
- White, R. B., Resistive reconnection, *Rev. Mod. Phys.*, **58**, 183, 1986.
- Wu, C. C., Kelvin-Helmholtz Instability at the Magnetopause Boundary, *J. Geophys. Res.*, **91**, 3042, 1986.
- Yeh, T., and W. I. Axford, On the reconnection of magnetic field lines in conducting fluids, *J. Plasma Phys.*, **4**, 207, 1970.